FOLATE-TARGETED PROTEOLYTIC NANOBEACONS: TOWARDS SELECTIVE, IMAGED DELIVERY IN SOLID TUMORS

By

Ian D. McFadden

Dissertation

Submitted to the Faculty of the

Graduate School of Vanderbilt University

in partial fulfillment of the requirements

for the degree of

DOCTOR OF PHILOSOPHY

in

Interdisciplinary Materials Science

December, 2014

Nashville, Tennessee

Approved:

J. Oliver McIntyre

Todd D. Giorgio

Barbara Fingleton

Wellington Pham

Thomas Yankeelov

Craig Duvall

DEDICATION

To my parents, David and Andrea, for teaching me the value of education,

for instilling in me the virtues necessary to pursue mine,

and for always believing that I could achieve my aspirations.

To my friends, new and old, for the memories,

for the times good and bad, and for the comic relief always.

And above all to my wife, Elaine, for her inexhaustible patience,

for having the lovingest heart, for believing in me always,

for sharing our sense of humor,

for giving birth to our beautiful son, Tristan,

for any children we may welcome in the future,

and for whom I will fight through fear and self doubts

in order to be a better man

because I love her so very much.

ACKNOWLEDGEMENTS

This work would not have been possible without the financial, moral, and practical support of countless institutions and individuals. I wish to thank all who aided me in various ways during my graduate career, through seeming Hell and literal high-water.

Each of my committee members provided me with a unique form of mentoring that contributed to the completion of this dissertation and my development as a scientist. I am grateful to Dr. Oliver McIntyre and Dr. Todd Giorgio, my co-primary research advisors, for their often-sought guidance regarding research and career directions. Dr. Wellington Pham demonstrated his dedication to mentorship through his unfaltering willingness to provide me research training as well as personal and professional development advice. The generosity of Dr. Tom Yankeelov and his genuine concern for my personal welfare were reassuring and truly humbling. Dr. Craig Duvall's frank honesty in looking out for my professional best interests were appreciated more than I may have let on at times.

I am especially indebted to one particular committee member, Dr. Barbara Fingleton, with whom I credit the resurrection and resuscitation of my graduate school career. In a time of potential crisis, she volunteered to mentor me and thereafter assumed many of the responsibilities of primary advisor to me with no requirement for recognition. Her keen insights and ability to indentify research priorities proved invaluable in the completion of this work. For this and so much more I have immense respect and will be forever grateful.

The past and present members of the Matrisian, Fingleton, and Giorgio laboratories have my deepest gratitutde for the roles they have played in the completion of this work and my doctorate, from training and mentoring to listening and commiserating.

Much of the experimental work presented here was either instructed by or performed by members of other laboratories, as well. Brian Evans, Kelsey Beavers, and Lucas Hofmeister of the Vanderbilt University (VU) Biomaterials Laboratories and Dr. Ian Tomlinson of the Rosenthal Laboratory aided greatly in the development of the chemical synthesis strategies discussed herein. My thanks also go out to Dr. Kelly Hines of the McLean Laboratory and Dr. Don Stec of the VU Small Molecule NMR Facility for their fine work characterizing peptides from my syntheses. I especially appreciate the many hours or training and troubleshooting provided me by Dr. Wade Calcutt of the VU Mass Spectrometry Research Core.

The administrators of the Interdisciplinary Materials Science (IMS) program are beyond deserving of recognition. I am particularly grateful to Sarah Satterwhite for her unwavering dedication to the IMS students and unconditional professional and personal support throughtout my time at Vanderbilt. I must also thank Dr. Sandra Rosenthal, who not only opened he laboratory to me, but generously and voluntarily paid members of the VU Rowing Team to assist in the mitigation of damages to my home caused by the May 2010 flooding in Nashville.

Funding for my research and education was provided by the Interdisciplinary Graduate Education and Research Traineeship from the National Science Foundation, the Department of Defense Breast Cancer Research Program, the VU In Vivo Cellular and Molecular Imaging Center, and the VU Interdisciplinary Graduate Program in Materials Science.

Finally, I thank my incomparable friends and family, without whom I would neither have endeavored nor persevered to complete my doctoral dissertation. I love you all.

REPORTABLE OUTCOMES

The data, troubleshooting procedures, and research findings presented in this dissertation have achieved or directly contributed to:

- elucidation of the effects of fluorophore bulkiness and substrate length on the proteolytic cleavage and MMP selectivity of designed MMP substrates with FRET-paired fluorophores for optical sensing of MMP activity.
- modification and application of an inhibitor titration assay using GM6001 tight binding inhibitor of MMPs to characterize active MMP concentrations.
- development of a robust synthesis scheme for solid phase synthesis of FRET-equipped substrate peptides with attachment of folic acid to N-termini and functional groups at C-termini for bioconjugation with nanoparticles. This strategy is adaptable to the production of any number of peptides with no fewer than 4 covalent attachment sites for linking to fluorophores, therapeutics, targeting ligands and/or particles or surfaces. Such peptides may be designed as substrates for any proteolytic enzymes of interest by modifying the central primary amino acid sequence.
- reporting on the modification of the optical properties of TAMRA dye by exposure to 2% hydrazine solution or para-phenylenediamine (pPDA), rendering the modified TAMRA unsuitable for FRET with fluorescein-based dyes at physiologic pH.
- elucidation of the causes for interference with bioconjugation chemistry for attaching FRET peptides to nanoparticles or surfaces including absence of

functional groups, modification of functional groups by chemical adducts, and steric hindrance of the reaction. A strategy to overcome these interferences was designed and executed successfully.

- successful conjugation of folate-linked, FRET-equipped MMP substrate peptides to PAMAM nanoparticles to produce folate-targeted proteolytic nanobeacons (FTPNBs) and subsequent validation of the MMP-responsiveness of FTPNBs.
- preliminary *in vitro* characterization of the dependence of cellular internalization of FTPNBs on folate-targeting and MMP activation.
- development of a new cell line variant of MDA-MB-468 human metastatic breast cancer cells expressing decreased levels of folate receptor, i.e. 40-75% of control.
- development of methods to manipulate folate receptor expression in cells by culture in folate-deficient medium and to assess folate binding capacity by indirect flow cytometry.

TABLE OF CONTENTS

LIST OF FIGURES

LIST OF TABLES

LIST OF ABBREVIATIONS

HCTU: 2-(6-Chloro-1H-benzotriazole-1-yl)-1,1,3,3-tetramethylaminium hexafluorophosphate, 23
HD: Hydrodynamic diameter, 13
HMBC: heteronuclear multiple bond correlation, 67
HPLC: High pressure liquid chromatography, 24
LCMS: tandem liquid chromatography mass spectrometry, 24
M/z: mass-to-charge ratio, 49
MALDI: Matrix-assisted laser desorption/ionization, 65
MeCN: acetonitrile, 29
MeOH: Methanol, 25
MMP: Matrix metalloproteinase, 3
MMPI: Matrix metalloproteinase inhibitor, 4
MPS: monocyte phagocytic system, 15
MRI: Magnetic resonance imaging, 5
MW: molecular weight, 76
NIR: near-infrared, 5
NMM: N-methylmorpholine, 32
NMP: N-methyl-2-pyrrolidone, 32
NMR: Nuclear magnetic resonance, 67
NMWL: Nominal molecular weight limit, 151
pB2v: peg-Broad2-vis peptide, 32
PBs: Proteolytic beacons, 5
PBS: Phosphate buffered saline, 28
PEG: poly(ethylene glycol), 15
PET: Positron emission tomography, 5
PMSF: phenylmethanesulfonylfluoride, 26
pPDA: para-phenylenediamine, 135; p-phenylenediamine, 135, 156
PXL: Paclitaxel, 129
PyClock: 6-Chloro-benzotriazole-1-yloxy-tris-pyrrolidinophosphonium hexafluorophosphate, 23
QD: Quantum dot, 13
Qdot(605)NH_2: Qdot® 605 ITK™ Amino (PEG) Quantum Dots, 139
qPCR: Quantitative RealTime PCR, 250
RBCs: Red blood cells, 16
rcf: relative centrifugal force, 134
RES: Reticuloendothelial system, 13
RFC: reduced folate carrier, 10
RT: room temperature, 25
RT-PCR: Reverse transcription polymerase chain reaction, 249
S/R: Sensor-to-reference emission ratio, 6
shRNA: short hairpin ribonucleic acid, 255
SIA: Succinimidyl iodoacetate, 23
SPECT: Single-photon emission computed tomography, 5
SPPS: Solid phase peptide synthesis, 22
Sulfo-SMPB: Sulfosuccinimidyl-4-(p-maleimidophenyl)butyrate, 143
TAMRA: tetramethylrhodamine, 23

TCEP: tris(2 carboxyethyl)phosphine, 143; Tris(2-carboxyethyl)phosphine, 143
TEA: triethylamine, 70
TEM: Transmission electron microscopy, 130
TFA: Trifluoroacetic acid, 24
TIMPs: Tissue inhibitors of metalloproteinases, 4
TIPS: triisoproylsilane, 32
TLC: thin-layer chromatography, 70
TNF-α: Tumor necrosis factor alpha, 14
TOCSY: Total Correlation Spectroscopy, 67
TOF: time-of-flight, 65
Trt: Trityl, triphenylmethane, 141
VEGF: Vascular endothelial growth factor, 14

CHAPTER I

INTRODUCTION

It goes almost without saying that cancer, a group of over 200 different diseases that are classified as malignant neoplasms, presents a world health concern that demands the attention of biomedical researchers and clinicians. These diseases altogether comprise the second leading cause of death in the United States trailing heart disease by less than one percent and outpacing the next most prevalent cause by nearly eighteen percent[1]. The death rate due to cancer is not declining as quickly as heart disease[1], though, and may therefore become the overall most common cause of death in the near future. This is especially concerning as the average life expectancy continues to increase[1], and deaths from cancer are more prevalent in persons over age 45[2]. Excluding basal cell and squamous cell skin cancers and most *in situ* carcinomas, an estimated 1.66 million new cancer diagnoses and 586,000 cancer deaths will be counted in 2014 in the United States alone[3].

Many of these cancer cases will present as solid tumor malignancies in bodily organ tissues such as breast, prostate, lung, colon, kidney, or liver, among others. Despite success stories of modern chemotherapies and even newer molecularly-targeted treatments for some hematologic malignancies such as imatinib (marketed by Novartis Pharmaceuticals as Gleevec) for chronic myelogenous leukemia[4], equally effective chemotherapeutic interventions for most non-resectable solid tumors have remained elusive. The anatomies and physiologies of these dysplastic growths present significant challenges to treatment, often owing to difficulty in selectively delivering diagnostic or

cytotoxic reagents to tumors primarily because they arise by clonal evolution from normal cells and tissues. The ultimate goal in cancer chemotherapy is the specific eradication of malignant cells while sparing normal ones. However, despite the currently available menu of tumoricidal compounds, many chemotherapy approaches fail to halt or reverse tumor progression due to dose-limiting off-target or systemic toxicities. Even targeted therapies have failed in this respect either because of a lack of true tumor specificity, ineffective delivery to solid tumors, or both. For example, monoclonal antibodies, which may have great specificity and affinity for a biomarker of interest, succumb to the physiological barriers that prevent systemic delivery of many potentially therapeutic agents to tumors. Studies have found that systemically administered antibodies fail to accumulate in solid tumors, resulting in tumor retention of less than 1% of the injected dose in rodents and less than 0.01% in humans[5,6]. As explained by Dvorak et al, the target tumor cells are generally some distance removed from leaky tumor blood vessels, separated by stromal cells and other tumor cells that collectively constitute significant barriers to tumor penetration by extravasated monoclonal antibodies[5].

Therefore a global research objective must be to understand and exploit the emergent properties of tumor cells and the solid tumor microenvironment. Mortality from cancer is strongly associated with metastatic disease rather than with primary lesions. For example, the 5-year survival rate of women diagnosed with localized breast cancer is 99% whereas for women diagnosed with distant metastases this rate is only 24%[3]. But which molecules are important at which stages of tumor progression and metastasis? Are these molecules clinically relevant therapeutic targets? Such questions have provided the impetus for entire fields of cancer and disease research that have provided vast amounts of

knowledge in recent decades about the biomolecular mechanisms of carcinogenesis and cancer progression. An improved understanding of who, what, and when with respect to biomarker expression, cellular secretions, enzymatic activities, and host-tumor interactions in the tumor microenvironment is leading to development of new strategies to target diagnostic and therapeutic agents to solid tumor malignancies.

I.1. Matrix Metalloproteinases in Cancer Research

The first of the strategies our research seeks to employ in order to target solid tumors is to exploit the proteolytic activities of tumor-associated matrix metalloproteinases (MMPs). MMPs are a family of at least 24 different zinc-dependent endopeptidases, altogether capable of degrading all components of the extracellular matrix (ECM) as well as other cell surface substrates important in tumor progression[7,8]. Likely because of their great diversity of substrates and the roles of MMPs in normal physiology such as embryogenesis, tissue remodeling, angiogenesis, inflammation, and wound healing, MMPs are tightly regulated at multiple biological levels. Transcription of MMP genes is modulated by transcription factors downstream of extracellular and intracellular signaling networks which are in some cases themselves influenced by MMP activity[9]. Upon transcription and translation, MMPs are expressed as zymogens requiring proteolytic processing to become active and exert their own specific proteolytic activities[10]. These enzymes are then further regulated by an endogenous class of inhibitors known as tissue inhibitors of metalloproteinases (TIMPs)[10]. Interestingly, TIMPs also have roles in facilitating the activation of MMPs, such as activation of pro-MMP2 by the complex of MMP14 and TIMP-2[10,11]. Given the myriad intermolecular interfaces and regulatory components involved, it is not surprising that dysregulation or altered expression of

MMPs is associated with many different disease states including atherosclerosis[12], arthritis[13], emphysema[14], and cancer [15,16].

The expression patterns and enzymatic activities of MMPs have been used to distinguish benign from malignant tumors and to identify aggressive tumors associated with poor outcome, as reviewed extensively elsewhere[15,17]. Identification of the ECM-degrading functions of MMPs and association of MMP expression with invasion and metastasis in some malignancies led to rapid development and clinical testing of small molecule matrix metalloproteinase inhibitors (MMPIs) in the 1990s. The unexpected and disappointing failure of most MMPI clinical trials, particularly those employing non-selective MMPIs, resulted in the abandonment of MMPs as therapeutic targets by many pharmaceutical companies, though it also gave researchers pause to develop new perspectives about the roles of MMPs in cancer. MMP experts have since posited that perhaps the most important roles for MMPs in tumor progression have not to do with ECM degradation but instead with the plethora of other substrates and signaling cascades with which MMPs interact[8,18,19]. Furthermore, different MMP family members have been shown to have either positive or negative prognostic significance in different diseases at various phases of tumor development[19,20]. In combination with follow-up studies that indicated that treatment with marimastat could improve survival of an appropriately selected population of gastric cancer patients[21], these insights suggest that MMPs may yet be viable therapeutic targets in the diagnosis and treatment of cancer. A better understanding of which MMPs play what roles at which stages of disease progression, along with development of reagents that are selective for those enzymes, is imperative in the development of effective anti-cancer therapies. However, *in vivo* assessment of the

efficacy of MMPIs both as inhibitors of MMPs and as tumor cell cytostatic agents has been a challenge. The lack of appropriate endpoints and surrogate markers was criticized following reports of the MMPI clinical trial outcomes[18,19]. In the time since, though, advances in biomedical and molecular imaging in parallel with bioconjugate chemistry have shown a promising potential to develop tools that enable the requisite measurement of MMP activity and response to therapy *in vivo*.

The development of probes to noninvasively visualize and quantify MMP activity *in vivo* has steadily progressed for over a decade, now encompassing several imaging modalities including optical imaging[22–28], magnetic resonance imaging (MRI)[29,30], positron emission tomography (PET)[31–33], and single-photon emission computerized tomography (SPECT)[34], as reviewed by Scherer et al (2008)[35]. Importantly, in 2001 following the development of a protease-activated near-infrared (NIR) fluorescent probe[28], Bremer et al were the first to demonstrate optical detection of MMP activity *in vivo* using a probe that allowed visualization of MMP2 inhibition in response to treatment with Prinomastat[26]. Also of interest are the optical MMP probes that were developed by Tsien et al to include a latent polycationic cell penetrating peptide to effect cellular internalization of attached payloads following activation by MMPs[25,36].

An important limitation of the first MMP imaging probes was the inability to quantitatively measure the specific enzymatic activity of MMPs. To address this issue, our laboratory developed dendrimer-based MMP-responsive fluorogenic macromolecules referred to as proteolytic beacons (PBs)[37]. A distinct advantage introduced in these probes was the inclusion of a "reference" fluorophore that quenches the sensor fluorophore by intramolecular Förster Resonance Energy Transfer (FRET), but also

fluoresces with an emission distinct from the sensor. This enabled semi-quantitative measurement of MMP activity by assessment of the sensor-to-reference fluorescence emission ratio (S/R), as proteolytic activation by MMPs disrupts FRET, resulting in dequenching and dramatic increase in emission of the sensor fluorophore while emission from the reference fluorophore remains relatively unchanged[37]. PBs employing this design were further developed by our laboratory and applied to *in vivo* and *ex vivo* measurement of MMP7 activity in mouse models of colon cancer by optical imaging of "PB-M7NIR" (structure shown in Figure I-1)[24].

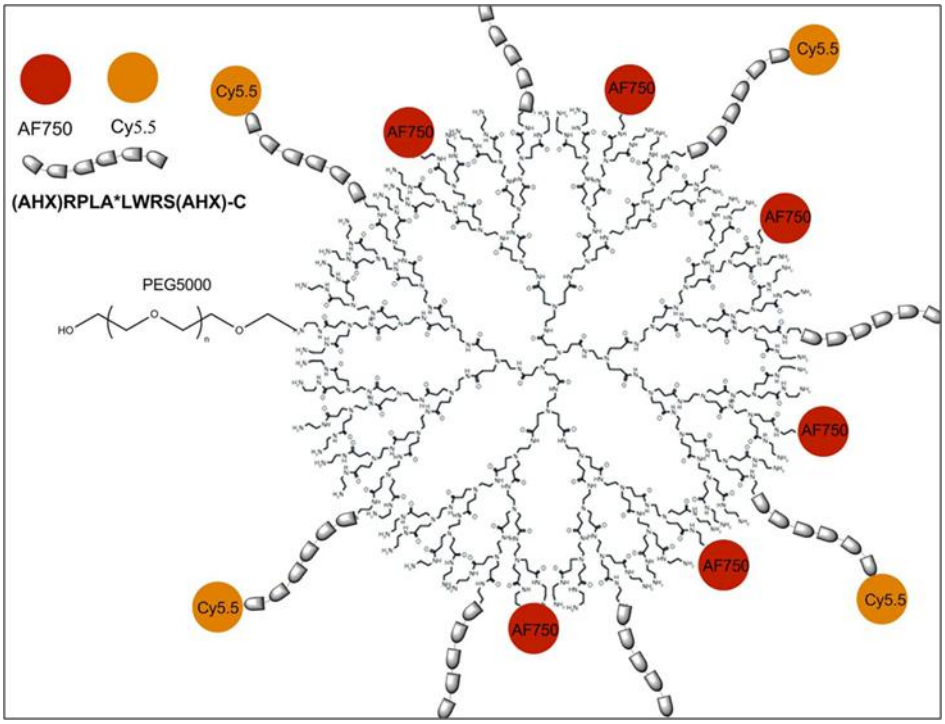

Figure I-1: **Structure of PB-M7NIR**[24]
A Cy5.5 optical sensor is linked via AHX to the N-terminus of the matrix metalloproteinase-selective cleavable peptide (RPLA*LWRS, cleavage site denoted by an asterisk) that is coupled via a second AHX and cysteine with the PAMAM. The internal reference, AF750, of PB-M7NIR is linked directly to the dendrimer (Starburst PAMAM dendrimer, Generation 4). The structure is not drawn to scale. Figure reproduced with permission[24].

While PBs of this design have clearly demonstrated the ability to assess tumor-associated MMP7 activity *in vitro*[24,37,38] and *in vivo*[24], they leave room for adaptation and further development. As alluded to above, a growing body of evidence suggests that the contributions of the various MMPs are tissue-, disease-, and stage-specific (reviewed elsewhere[15,19,20]), suggesting that proteolytically-activated diagnostics and therapeutics could be customized to best combat specific malignancies. In theory, PBs can be modified for selectivity of any protease of interest (e.g. another MMP) by substituting the appropriate amino acid sequence in the structure of the substrate peptide that tethers the sensor fluorophore to the dendrimer. An MMP family member that has attracted much attention particularly in the study of metastatic disease is MT1-MMP (also known as MMP14), so-named because it is the first identified member of a subfamily of MMPs that is membrane-bound, exerting its proteinase activity at the cell surface as opposed to being secreted into the surrounding ECM. MMP14 undergoes proteolytic processing in the trans-Golgi complex prior to trafficking to the cell surface in active form, providing spatial restrictions on substrate recognition and possibly affording protection from circulating proteinase inhibitors[11,39,40]. Nonetheless, MMP14 has demonstrated processing of diverse substrates including collagens types I-IV, fibronectin, vitronectin, laminin, fibrin, proteoglycan, some chemokines and downstream secreted proteinases such as proMMPs (2, 8, and 13)[11,20,40]. Importantly, MMP14 expression has been reported to correlate with the malignancy of various tumor types and is thought to be an essential mediator of cell migration, invasion, and expansion of solid tumors through ECM[41,42]. It has been shown to concentrate at the leading edges of various migrating cells[39,41] and has been demonstrated to contribute to migration of MCF-7 breast cancer

cells on vitronectin[43]. Furthermore, invasive potential can be reconstituted in non-invasive COS cells by expressing MT1-MMP, even in the absence of downstream MMPs (MMP2 and MMP13), resulting in degradation of type I collagen, invasion of three-dimensional type I collagen gels, and traversing of a chick chorioallantoic membrane [39,40]. Hotary et al found that MMP14 modulated invasive and morphogenic responses requiring remodeling of type I collagen matrices by stimulated Madin-Darby canine kidney epithelial (MDCK) cells, whereas secreted MMPs did not[42]. Taken together, a plethora of published data suggests that MMP14 plays a critical role in conferring cells with invasive and metastatic properties *in-vivo* via remodeling and penetrating of extracellular matrix (ECM) barriers and processing of multiple classes of extracellular molecules. MMP14 therefore presents an attractive target for enzyme-activated selective delivery of therapeutic and imaging agents to malignant tumor cells.

A limitation of the aforementioned design of PBs is the lack of a tumor cell-specific uptake mechanism for intracellular delivery of imaging or therapeutic agents released by proteolytic activation. Various targeting ligands such as transferrin, riboflavin, Arg-Gly-Asp (RGD) and other peptides, carbohydrates such as mannose, and folic acid have been employed for endocytic delivery of macromolecular compounds to tumor cells, as reviewed elsewhere[44–46]. Interestingly, Tsien et al very recently reported that dual targeting of MMP2 activity and integrin $\alpha_v\beta_3$ via an RGD motif to expose a latent nonspecific cell penetrating peptide (CPP) was successful at amplifying tumor targeting beyond levels attained by either mechanism alone[47].We hypothesized that attachment of an appropriately chosen ligand to the terminus of a substrate peptide distal to the

nanobeacon core could enable selective internalization of PB cleavage products by tumor cells.

I.2. Folate Targeting in Cancer Chemotherapy

As a second strategy working in conjunction with proteolytic activation by MMPs, our research focused on the incorporation of folic acid (FA) as a tumor cell-selective targeting ligand in the design of modified PBs. The α- and β- isoforms of the folate receptor (FR) are glycosylphosphatidylinositol-anchored membrane proteins involved in the endocytosis of FA and its analogues. Because naturally occurring folates are vitamins required for *de novo* synthesis of nucleotides including thymidine and purines as well as the amino acid methionine, folate metabolism is a critical process during rapid cycles of cell division and growth such as those of proliferating tumor cells[48,49]. This pathway has been understood and exploited for chemotherapy since the introduction of aminopterin, an antifolate, in 1947 by Dr. Sidney Farber who is also known as the "Father of Modern Chemotherapy". The research conducted by Farber and his colleagues demonstrated that aminopterin could induce remission in childhood leukemias[50,51]. Antifolates are analogues of folic acid that act as inhibitors, several of which bind the intracellular enzyme dihydrofolate reductase (DHFR) to prevent the processing of folic acid to a necessary intermediate form for nucleotide synthesis and effectively halt cell replication. Methotrexate and pemetrexed, a more recently developed antifolate, are currently prescribed as adjuvant therapies for malignancies including breast, lung, head and neck cancers, non-Hodgkin lymphoma, osteosarcoma, bladder cancer, and choriocarcinoma[52]. While many antifolates face limitations with respect to systemic delivery to tumors because they are endocytosed by the ubiquitously expressed reduced folate carrier (RFC)

protein, development of modified antifolates and folate conjugates with improved tumor selectivity is ongoing[52]. Folic acid is not internalized by the RFC, but rather by the isoforms of FR, which exhibit a much more favorable expression pattern for selective delivery to tumor cells.

Increased significance of FR-α as a tumor marker was discovered in 1991 when a protein enriched on the surface of a human ovarian carcinoma cell line was shown by amino acid analysis to be FR[53,54]. In the time since, many studies have yielded a wealth of literature regarding FR and folate-targeting of directed therapeutic and imaging agents[55–63]. FR-α is now recognized as an established tumor marker with elevated expression in many epithelial cancers but limited or negligible expression in normal tissues. One study of normal and malignant tissues showed that 86% of primary human breast carcinomas tested showed appreciable levels of FR[54], while other studies reported that FR over-expression was associated with poor patient outcomes as measured by recurrence and overall survival rates in cancers of the breast[64] and colon[65].

Probably the most significant advantage to emerge from studies of FR-mediated delivery has been the surprisingly low level of toxicity to normal tissues. Studies by Leamon et al. indicate that folate-targeted drugs that fail to bind FR are rapidly ($t^{1/2} < 10$ min) excreted via the kidneys, reducing nonspecific delivery and contributing to patient convenience during administration[66]. Nonetheless, the concern persists that FR is expressed in some normal tissues such as brain, lung and especially kidney[49,66,67]. In each case though, the FR expression is limited to the apical membrane of polarized epithelial cells[54], unavailable to folates in systemic circulation. It is well known that FR is present on the proximal tubule cells of human and mouse kidney tissue, and in fact folate-

targeted imaging agents are readily observed in the kidneys[49,68]. However, data suggests that captured folate-conjugates in the kidneys do not harm the proximal tubules because they are endocytosed at the apical cell surface and then transported in endocytic vesicles to the basolateral side of the epithelium[69]. Thus, the kidney FR appears to serve as a salvage receptor that captures folate (and its drug conjugates) in the urinary filtrate and transcytoses the vitamin back to the blood[54,67].

In addition to the favorable expression pattern of FR, several properties of the FA molecule itself make folate-targeting of solid tumors attractive. FA is small (441 Da) and innately non-immunogenic, facilitating its rapid and complete penetration of solid tumors without induction of an adverse immune or inflammatory reaction[67]. A quantitative analysis of folate biodistribution *in vivo* revealed that essentially every cell in a breast malignancy was bathed by FA-linked imaging agent within minutes of intravenous injection[66], corroborating the ability of FA conjugates to diffuse throughout a solid tumor. FR has high affinity (K_d ~ 0.1-1.0 nM) for FA and therefore relatively low doses of folates are sufficient to saturate the folate binding capacity of FR-expressing cells[48,66]. Previous studies have shown that attachment of large macromolecules to FA has not significantly reduced this affinity (for a review of such conjugates, see Xia and Low, 2010[70]).

A variety of folate-conjugated imaging and therapeutic agents have already been developed[55–58,60,61,68,71–77] and have been extensively reviewed elsewhere[49,66,70]. Importantly, several have shown efficacy *in vitro* and most have displayed improved potency with reduced toxicity when tested *in vivo*. In fact, at least four folate-targeted therapeutics have proceeded to human clinical trials (phase II) and several folate-targeted

imaging agents are in pre-clinical development. One folate-targeted imaging agent, ^{99m}Tc-EC20, has been introduced into the clinic, where as of 2008 it had been used to image more than 200 cancer patients and showed excellent agreement with computerized tomography (CT) scans with no reports of adverse events[66]. The same company that produces ^{99m}Tc-EC20 recently reported that its folate-vinca alkaloid drug conjugate (vintafolide) in combination with docetaxel extended overall survival (OS) for patients with FR-positive recurrent non-small cell lung cancer (NSCLC) compared to patients receiving monotherapy docetaxel in its TARGET Phase 2b clinical trial[78].

Together with the biochemically amenable properties of FA and significance of FR in many solid tumor malignancies, these results suggest that folic acid is an attractive molecule for extending the design of PBs to include a targeting ligand that may enable selective intracellular delivery of PB cleavage fragments to tumor cells. Interestingly, Vlahov and Leamon, among the foremost experts in the field of folate-targeted therapies, recently concluded that enzymatically cleavable folate conjugates represent an area of future potential for delivery to cancer cells[79].

I.3. Rational Design of Nanoparticles for Delivery in Solid Tumors

While targeting of tumor-associated MMP activity and folate receptor expression is intended to provide selective imaging and delivery by PBs in the tumor microenvironment, one must also consider the ability of PBs to reach and accumulate in solid tumors or metastases via systemic delivery. The failure of even targeted chemotherapies to eradicate such malignancies, often due to dose-limiting off-target toxicities, emphasizes the importance of an engineered system for selective delivery that spares normal tissues. Over the past quarter-century, advances in the understanding of the

biological barriers to cancer drug delivery *in vivo* and the development of multifunctional nanoparticles to overcome such barriers has offered much promise to improve detection and chemotherapeutic treatment of solid tumors.

The size, hydrophobicity, and surface charge of systemically delivered nanoparticles play important roles during vascular circulation. Upon introduction into circulation, adsorption of proteins and electrolytes by hydrophobic and electrostatic interactions contributes to the hydrodynamic diameter (HD) of a particle that is somewhat larger than the unhydrated diameter or may even be different than the diameter measured in non-biological suspensions. Molecules with HD less than 5 nm are rapidly removed from circulation owing to glomerular filtration in the kidneys[80]. Molecules with HD between 6 nm and 8 nm are typically filtered at a rate inversely correlated with size, whereas molecules with HD greater than 8 nm are typically not filtered[80]. For example, renal clearance studies in mice have shown that quantum dots (QDs) with HDs ranging 4.36-5.52 nm were subject to renal excretion whereas QDs with HD greater than 8 nm were not, but rather exhibited uptake in the reticuloendothelial system (RES) and lungs[81].

An emergent "gold standard" for 21st century tumor targeting of compounds is the use of nanoparticulate (HD: 10-100 nm) formulations that may selectively accumulate in solid tumors upon intravenous injection[82,83]. The predominant mechanism of size-selective accumulation of macromolecules in tumors was first described in 1986 and later termed the enhanced permeability and retention (EPR) effect by Maeda et al[84,85]. In normal vasculature, tight junctions between adjacent endothelial cells prohibit passive trafficking of all but the smallest molecules (HD less than about 5 nm)[81] across the endothelium, as reviewed by Bazzoni (2006)[86]. In many tumors, though, a host of altered

chemical and physiological factors such as bradykinin, nitric oxide, prostaglandins, carbon monoxide, peroxynitride, MMPs, vascular endothelial growth factor (VEGF), tumor necrosis factor alpha (TNF-α), and heat, among others, contribute to the rapid formation of "leaky" neovasculature during tumor angiogenesis[87,88]. The resulting tortuous and fenestrated vessels in some tumors permit extravasation of macromolecules up to 500 kDa[82] that does not occur in tissues with normal vasculature. A lack of functional lymphatic vessels in many solid tumors further contributes to selective accumulation of macromolecules as filtration by lymphatic drainage would otherwise clear many such molecules. In fact, it has been shown that this retention is the key mechanism enabling the EPR effect in solid tumors, as low-molecular weight molecules may return to circulation by diffusion[89]. Recently, Tang et al showed that despite better tumor penetration by 20 nm-diameter nonporous spherical silica nanoparticles as compared with either 50 nm or 200 nm particles[90], 50 nm drug-conjugated particles were retained in tumors in the highest concentrations over time and were more effective at reducing tumor size *in vivo*[91]. Particles larger than 100-200 nm it seems may be too large to either extravasate in tumors or be effectively endocytosed by cells[91].

Even though the EPR effect has been observed and confirmed reproducibly *in vivo* in murine models of cancer[82,84,89,92], the application of nanoparticulate formulations to significantly improve the overall proportion of injected drugs delivered to human tumors has not translated readily to the clinic[45]. Several researchers including Maeda have pointed out that the EPR effect is not solely sufficient for delivery or even universally applicable to solid tumors, owing to heterogeneity between individuals, between tumor types, and even within a tumor itself[93,94]. A thorough analysis of the strategies that have

been employed to overcome the heterogeneity of the EPR effect or augment it in tumor targeting is beyond the scope of this work, but has been reviewed elsewhere[88]. Many of these strategies focus on either increasing blood pressure within and around tumors or normalizing the distribution of neovasculature in tumors by regulating angiogenesis. With any of these strategies, though, careful control and optimization of nanoparticle size is nonetheless critical for efficacious delivery to solid tumors.

In addition to size, the surface characteristics of systemically administered nanoparticles are critically important for circulation time, clearance route, and delivery. The body's first line of defense against foreign bodies and substances introduced to the bloodstream is the innate immune system. To achieve a rapid response to unidentified potential pathogens without reliance on the slower specific recognition mechanisms involved in adaptive immunity, the innate immune system has evolved to recognize potential pathogens highly conserved molecules and non-specific threatening molecular patterns[95]. Hydrophobic moieties and overall hydrophobicity such as might be encountered in a bacterial cell membrane thusly trigger the innate immune system, resulting in much greater likelihood of adsorption of opsonins such as complement proteins, immunoglobulins, albumin, fibrinogen, and apolipoproteins[96]. Opsonized nanoparticles are efficiently removed from circulation by phagocytes[97] such as circulating monocytes, splenic macrophages, alveolar macrophages, or Kupffer cells in the liver that are collectively known as the Monocyte Phagocytic System (MPS)[98]. Hence a common strategy to prevent nanoparticle clearance by the MPS is to encapsulate or decorate the nanoparticle surface with hydrophilic macromolecules such as poly(ethylene glycol) (PEG). These are commonly referred to as "stealth" nanoparticles, and the technique has

been applied to liposomes, inorganic metal nanoparticles, quantum dots, and polymer-based nanoparticles alike[24,63,99–103]. Bioconjugation of PEG to nanoparticles can both improve water-solubility and sterically hinder adsorption of opsonins to prevent complement activation and undesired clearance by the MPS, thereby increasing the circulation half-life of PEGylated particles. Other MPS avoidance strategies have included mimicking the outward appearance of circulating red blood cells (RBCs), either by bioconjugation of immune-halting proteins such as CD47 to nanoparticles or by encapsulation of particles in natural RBC membrane bilayers[97].

The charge resulting from the surface composition of a nanoparticle also greatly influences its suitability for systemic delivery. The zeta potential (ζ) of a particle is defined as the electrical potential in the interfacial double layer where a stationary layer of fluid adhered to the particle meets the dispersion medium. In other words, it is the outwardly perceived difference in electrical potential between the dispersed or solvated particle and the solution in which it is dispersed. Several studies have indicated that particles with highly-positive ζ (cationic) or highly-negative ζ (anionic) are more rapidly cleared from circulation than electrostatically neutral particles[104–107]. While both types of charged surfaces may contribute to interactions with serum proteins and eventual uptake by the MPS, cationic particles have been found to interact nonspecifically with many cell types due to regions of negative charge (e.g. sialic acid) in the lipid bilayers of cell membranes. As such, polycationic particles may exhibit especially high levels of off-target and systemic toxicity owing to this interaction with normal cells that often results in translocation across the plasma membrane. Like hydrophobic surfaces, the charged surfaces of nanoparticles may be shielded by encapsulation or bioconjugation with

macromolecules such as PEG or pairing of charged molecular regions with counter-ions. In fact, reversible shielding strategies have been employed to effect selective cellular internalization via multiply-charged cell penetrating peptides[25] or "proximity-activated" nanoparticles[108] that reveal a polycationic surface only upon enzymatic activation by tumor-associated enzymes (e.g. MMPs).

Altogether, the above considerations contribute to a set of generalized axioms of biocompatibility and suitability for systemic delivery of tumor-targeted nanoparticles. As illustrated in Figure I-2, nanoparticles for this purpose should be approximately 8-100 nm in HD, as hydrophilic as possible, and should exhibit ζ of the smallest magnitude feasible during systemic vascular circulation. As indicated above, PEGylation of nanoparticles may aid in the optimization of each of these parameters.

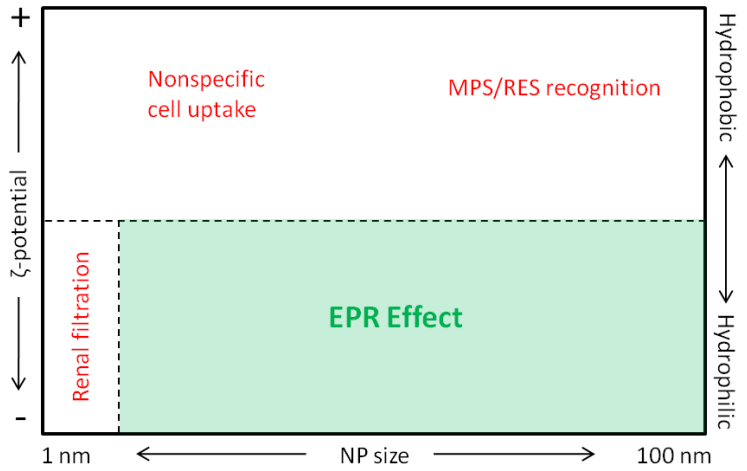

Figure I-2: **Nanoparticle biocompatibility and tumor-targeting axioms**
To take advantage of the EPR effect for selective accumulation in solid tumors, systemically administered nanoparticles should be approximately 8-100 nm in HD, as hydrophilic as possible, and should exhibit ζ of the smallest magnitude feasible during systemic vascular circulation. Figure adapted from a conference presentation by Scott E. McNeil, Ph.D. of the Nanotechnology Characterization Laboratory within the National Cancer Institute.

I.4. Hypotheses and Goals of This Dissertation

The above considerations regarding the physiological properties of solid tumors and the strategies that have been developed to selectively deliver imaging and therapeutic agents to them lead us to believe that the design of PBs developed in our laboratory (see Figure I-1) can be extended to include folic acid as a targeting ligand to effect selective delivery of payloads to malignant cells within solid tumors. We hypothesize that nanoparticles conforming to the biocompatibility and tumor-selective delivery axioms described above and featuring folate-targeted conjugates tethered to their surfaces by MMP-cleavable linker peptides will prove more selective for delivery into tumor cells than macromolecular constructs employing any one of these elements. Optical imaging enabled by the fluorescent switch as designed in the previous iteration of PBs is a logical tool for measuring activation of and delivery by these particles that we have termed "folate-targeted proteolytic nanobeacons" (FTPNBs). The majority of this dissertation focuses on refining the design and reducing to practice the synthesis and characterization of FTPNBs, thereby enabling the study of the effects that the employed targeting mechanisms have on each other and on selective delivery when applied in concert.

CHAPTER II

SELECTION OF AN MMP SUBSTRATE FOR CLEAVABLE CONJUGATION TO CARRIER NANOPARTICLES

II.1. INTRODUCTION

Our laboratory has previously developed proteolytic nanobeacons with demonstrated applicability to the detection of tumor-associated MMP7 or MMP9 activity *in vitro*, *ex vivo*, and *in vivo*[24,37,38,109]. In the prototypical design of a proteolytic nanobeacon (Figure I-1), MMP substrate peptides, each with a "sensor" fluorophore attached to the N-terminus, were covalently linked to an organic PAMAM dendrimer core. The PAMAM core was also decorated with "reference" fluorophores designed to quench the sensor via intramolecular FRET and linear PEG molecules to improve water solubility and biocompatibility of the overall construct. The reference fluorophore provided constitutive fluorescence emission associated with the nanoparticle core, while emission from the sensor fluorophore was attenuated until proteolytic cleavage of the substrate peptide would eliminate intramolecular FRET and increase the sensor fluorescence. As such, semi-quantitative assessment of proteolysis was achieved by calculating the sensor-to-reference emission ratio (S/R) in solutions, fluorescence microscopy images, or photographic images representative of proteolytic nanobeacons[37].

Building upon this design, the research presented hereafter was focused on developing two primary modifications for the synthesis of a newer generation of proteolytic nanobeacons: (1) incorporation of a linker substrate peptide selective for MMP14; and (2) covalent attachment of folic acid to the N-terminus of the substrate

peptide in addition to the sensor fluorophore. Selective activation of proteolytic nanobeacons by MMP14 would be advantageous for selective delivery and imaging of tumor-associated proteolysis in solid tumors owing to the pleiotropic roles of MMP14 in tumor progression. MMP14 has been reported to be relevant to all stages of tumor progression, as it can cleave a variety of substrates including but not limited to the pro-enzyme forms of other MMPs, ECM proteins, cell surface proteins such as cell adhesion molecules, and soluble molecules involved in cell signaling[11]. Importantly, expression of MMP14 has been shown to be required for invasion and migration of tumor cells through extracellular matrices where matrix remodeling is necessary to allow cellular mobility[42,110], a critical component of tumor metastasis. A potential pitfall of designing proteolytic nanobeacons selective for MMP14 is the spatial confinement of MMP14 to the cell membrane that limits its availability for extracellular proteolysis of nanobeacons in the tumor microenvironment. On the other hand, there is evidence suggesting that the extracellular domains of MMP14 may be either shed from the cell membrane[111] or secreted in microvesicular exosomes[112]. Theoretically, modification of the PB-M7 design (Figure I-1) to employ a peptide with a different amino acid sequence could impart selectivity for MMP14 instead of MMP7. However, as demonstrated by the data that follow in this chapter, development of substrates that are both efficiently cleaved and highly selective for MMP14 is non-trivial in practice.

The second modification, attachment of folic acid to the N-termini of the linker substrate peptides distal to the nanoparticle cores, provides a new dimension to proteolytic nanobeacons in the form of a targeting ligand. Folic acid binds with and is internalized along with any conjugates by the folate receptor, the alpha isoform of which

has been reported to be overexpressed in many solid tumors but expressed at very low levels (if at all) in most normal tissues[49,54]. Therefore in addition to the selective activation of nanobeacons in the MMP-rich tumor microenvironment imparted by the substrate peptide, folate targeting may provide a mechanism for selective uptake of nanobeacons and released folate conjugates by malignant tumor cells. Covalent attachment of folic acid to substrate peptides in addition to the sensor fluorophore while preserving the capacity for bioconjugation with nanoparticles presented a technical challenge. Attachment of folic acid to conjugates in an orientation that permits subsequent binding with folate receptors requires linking through one or both of carboxylic acid functional groups at the same end of the molecule. Covalent bonding employing these carboxylic acid groups is most readily achieved with primary amine groups, but the PB-M7 design made use of the N-terminal primary amine of the substrate peptide for attachment of the sensor, leaving no suitable functional group for reaction with folic acid near the N-terminus. Substrate peptide designs were therefore modified to implement lysine residues possessing two primary amine groups, the α-amine as part of the peptide backbone and the ε-amine of the side chain. Assuming successful inclusion of folic acid, the hydrophobicity and extremely low solubility of folic acid in aqueous solutions at physiological pH was still of concern for the necessary function of the resulting peptides as MMP substrates.

With the above considerations in mind, the primary objective of the research that follows was to develop methods for the synthesis and characterization of proteolytic nanobeacons that were dually-targeted to the folate receptor and proteolysis by MMP14 and could generate an optical signal for detection of MMP activity. One of the

requirements, then, was to determine whether folic acid conjugation to substrate peptides would interfere with MMP cleavage. Shown below, the design of proteolytic nanobeacons was further modified to incorporate both the sensor and reference dyes by attachment to amino acid side chains of the substrate peptide. Troubleshooting of FRET-equipped MMP substrate synthesis led to insights regarding steric hindrance, eschewing of an MMP14-selective substrate in favor of a broadly MMP-cleavable one, and ultimately to development of a robust method for preparing FRET substrates with visible-spectrum fluorophores by solid phase peptide synthesis (SPPS). An optical switch was observed in folated substrates, though not upon treatment with MMPs. MMP cleavage of folated substrates not inclusive of fluorophores was confirmed by mass spectrometry.

A number of peptide structures will be presented in the chapters that follow. For the ease of discernment by the reader, presented in Table II-1 are selected names, amino acid sequences, and design intentions of the central MMP-cleavable domains. Throughout this dissertation, to discriminate between L-amino acids and other chemical functional groups, amino acid residues are represented by capital letters corresponding to their conventional single-letter notations while other chemical functional groups are indicated using lowercase letters, e.g. amine groups as "-nh_2" or carboxyl groups as "-cooh."

Table II-1: MMP substrate peptides nomenclature and intent

Name/Identifier	MMP Cleavage Sequence	Design Intent	Origin
Peptide #13	RIGF * LRTA	MMP14 selective	Kridel et al [113]
Peptide #14	PLA * XWAR	MMP14 selective	Mucha et al [114]
Weiss	ESSN * LFVL	MMP14 selective	Outyang et al [39]
Hybrid	WSLN * LFVL	MMP14 selective	Amalgam of Mucha/Weiss [39,114]
Broad2	RPLG * LWAR	Broadly MMP cleavable	Knight et al [115]
PEPDAB1001	GPLG * MRGC	ADAM/MMP cleavable	Rasmussen et al[116]
M9	AVRW * LLTA	MMP9 selective	Chen et al [117]

* designates scissile bond

II.2. MATERIALS AND METHODS

II.2.1. General Methods

Materials. All chemicals and biochemicals were reagent-grade or HPLC-grade and solutions were prepared in filtered deionized water (dH_2O) (Milli-Q, Billerica, MA, USA). Unless otherwise noted, all chemicals were purchased from either Sigma Aldrich (St. Louis, MO, USA) or Thermo Fisher Scientific (Waltham, MA, USA). 5(6)-carboxytetramethylrhodamine succinimidyl ester (TAMRA-SE), 5(6)-tetramethylrhodamine maleimide (TAMRA-mal), 5(6)-carboxyfluorescein succinimidyl ester (FAMSE), 5-fluorescein maleimide (FL-mal), and Fmoc-PEG_1-CH_2-COOH were purchased from Anaspec (Fremont, CA, USA). Succinimidyl iodoacetate (SIA) and phenylmethanesulfonylfluoride (PMSF) were purchased from Pierce Chemical (Rockford, IL, USA). Dye-quenched gelatin (DQG), Alexa Fluor 700™ (AF700), and Alexa Fluor 750™ (AF750) were obtained from Molecular Probes (Eugene, OR, USA). GM6001 broad-spectrum MMP inhibitor was purchased from Chemicon International (Temecula, CA, USA). Standard Fmoc-protected amino acids, Rink Amide AM LL resin (100-200 mesh), and 6-Chloro-benzotriazole-1-yloxy-tris-pyrrolidinophosphonium hexafluorophosphate (PyClock) were obtained from EMD Chemicals (Billerica, MA, USA). Fmoc-Lys(5/6-FAM)-OH and Fmoc-Lys(5/6-TAMRA)-OH were purchased from AAT Bioquest (Sunnyvale, CA, USA). 2-(6-Chloro-1H-benzotriazole-1-yl)-1,1,3,3-tetramethylaminium hexafluorophosphate (HCTU) was obtained from ChemPep (Wellington, FL, USA). Broadly MMP-cleavable fluorogenic substrate peptide "PEPDAB1001" [dab-GPLGMRGC(fitc)-$conh_2$, where dab is Dabcyl] was generously donated by Dr. Marcia Moss of BioZyme (Apex, NC, USA).

HPLC. High pressure liquid chromatography (HPLC) was generally performed using an Agilent Infinity 1260 HPLC system (Agilent, Santa Clara, CA, USA) with a photodiode array detector and analytical-scale fraction collector. HPLC columns for analytical scale (Polaris C18-A, 4.6 x 250.0 mm, 3 µm pore size) and semi-preparative scale (Polaris C18-A, 10 x 250.0 mm, 5 µm pore size) separations were obtained from Varian (Palo Alto, CA, USA). Mobile phases for chromatography gradients were water and acetonitrile (MeCN) with 0.1% trifluoroacetic acid (TFA) unless otherwise noted.

LCMS. Liquid chromatography mass spectrometry (LCMS) separations were performed with an Acquity UPLC system in tandem with a Synapt Q-TOF high resolution mass spectrometer (Waters, Milford, MA, USA) in positive ion, V mode for determination of accurate masses. Mobile phases used for chromatography gradients were 95:5 H_2O:MeCN (A) and 5:95 H_2O:MeCN (B) with 0.2% formic acid and packed columns were C18, 4.6 x 100 mm with 1.7 µm pore size unless otherwise specified. The applied gradient was 0% to 90% (B) over 7 minutes unless otherwise noted.

Spectrophotometry. UV-visible spectrophotometry was recorded using a Shimadzu UV-2501 PC spectrophotometer (Shimadzu, Kyoto, JP). Samples were diluted at least 1:1 with 0.1M phosphate buffer (pH 7.0-7.5) and measured against identical solvent mixture as a baseline reference unless otherwise specified.

II.2.2. Synthesis of PAMAM-based proteolytic nanobeacons from FITC-labeled peptides

Peptide #13 [fitc{Ahx}RIGFLRTA{Ahx}C-cooh, where {Ahx} is aminohexanoic acid] and Peptide #14 [fitc{Ahx}PLAXWAR{Ahx}C-cooh] (see Appendix A) were obtained as custom syntheses from Genscript Corporation (Piscataw, NJ, USA). Generation 3 Starburst® polyamido amine dendrimer (PAMAM3) was purchased from

Sigma Aldrich (St. Louis, MO, USA). Methoxyl PEG succinimidyl ester, MW 1000 (PEG1000-NHS) was purchased from Nanocs (Boston, MA, USA). BHQ-10 carboxylic acid, succinimidyl ester (BHQ-10SE) was purchased from Biosearch Technologies (Petaluma, CA, USA). To 50 µL PAMAM3 (1.14 µmol, 20 wt% in MeOH) was added 50 µL (3.43 µmol) PEG1000-NHS to afford PAMAM3-PEG following 30 minutes incubation at room temperature (RT). 20 µL (228 nmol) of either PAMAM3 or PAMAM3-PEG in MeOH was then activated by addition of 62 µL (2.19 µmol) SIA in 50/50% MeOH/DMF and reaction for 30 minutes at RT. To 36 µL (100 nmol) activated PAMAM3 or PAMAM3-PEG was then added 55 µL (330 nmol) of either Peptide #13 or Peptide #14 in 50/50% MeOH/DMF and reaction allowed to proceed overnight at RT with rocking. 7 µL (700 nmol) cysteine in MeOH was added to each of the four reactions to block any remaining iodoacetyl groups. Reaction mixes were diluted with 8 volumes 1 mM EDTA solution (pretreated with 1 mM PMSF) and 1 volume EtOH and concentrated by ultrafiltration in Centriprep YM3 devices (EMD Millipore, Darmstadt, DE). Retentates were diluted again with 9 volumes 1 mM EDTA and reconcentrated. 20 nmol of PAMAM-equivalent from each of the resulting retentates were subsequently adjusted to pH 9.0 by addition of 1/9 volume 0.5 M Na_2CO_3 and reacted with either 14 µL (200 nmol) or 11 µL (200 nmol) TAMRA-SE in DMF to give 8 final reaction mixes. Reactions proceeded overnight at RT under argon gas with gentle rocking. Concentration by ultrafiltration was applied as before to these reaction mixes to give 8 final product retentates, as listed in II.3.1 (final wash in deionized water pretreated with 1 mM PMSF).

II.2.3. FRET switch assay

The ability of peptides and constructs to develop an increase in fluorescence as a result of disruption of FRET proximity by proteolytic enzymes was assessed according to previously published techniques [24,116]. MMPs were purchased as recombinant human catalytic domains from either Calbiochem (La Jolla, CA, USA) or Enzo Life Sciences (Farmingdale, NY, USA). Analytes and enzymes were diluted into common assay buffer (50 mM Tris pH 7.5, 200 mM NaCl, 5 mM CaCl2, 2 µM ZnSO4, 0.01% Brij 35) treated with 1 mM PMSF approximately 10 minutes prior to assay to inhibit the activity of any contaminating serine proteases. Fluorescence was monitored in opaque white 96-well plates in a top-reading fluorescence plate reader. Final volumes of assay wells were generally either 100 µL or 80 µL with intraplate conformity.

II.2.4. Synthesis and characterization of 2-color Peptides #13,14 via reactive dyes

72 µL (1500 nmol) TAMRA-mal in DMF was added to 75 µL (305 nmol) of either Peptide #13 or Peptide #14 in 67/33% DMF/MeOH and reacted overnight at RT with gentle rocking to afford products "F13T" and "F14T." 100 µL each of the resulting reaction mixes were diluted 1:1 with deionized water and dialyzed against 100 mL deionized water to remove unbound TAMRA-mal. Dialyzed F13T and F14T were subsequently diluted into tricine buffer (50 mM tricine pH 7.4, 200 mM NaCl, 10 mM $CaCl_2$, 50 µM $ZnSO_4$, 0.005% Brij 35) and treated overnight with trypsin (0.02 mg/mL), pronase (0.02 mg/mL), or EDTA for analysis by the FRET switch assay (see II.2.3, above) to determine maximum potential fluorescence fold change upon proteolysis (hereafter referred to as "FRET switch"). Dye quenched gelatin (DQG) was included as a control substrate. F14T was subsequently incubated with pronase (0.02 mg/mL), trypsin

(0.02 mg/mL), MMPs-2,7,9,14 (20 ng total enzyme per well, each separately), or EDTA and FRET switch monitored continuously over approximately 2 hours.

II.2.5. Generalized synthesis of 2-color FRET peptides via dual fluorophore conjugation

Peptides containing unmodified lysine and cysteine residues were dissolved to 10 mg/mL in DMF and reacted with 2 molar equivalents of dithiolthreitol (DTT) in deionized water to reduce disulfide bonds that may have formed due to oxidation of cysteine. Reduced peptides were then precipitated 3 times in 10 volumes of ice cold acetone to remove DTT and finally dried under nitrogen gas flow. 2 molar equivalents (relative to starting peptide) of sulfhydryl-reactive dye (FL-mal or TAMRA-mal) in DMF was then added to dry reduced peptide and allowed to react 2 hours to overnight at RT with gentle rocking. Acetone precipitation and nitrogen drying was repeated to remove unreacted fluorescent dye. 2 molar equivalents of amine-reactive dye (FAMSE or TAMRA-SE) was then added to dry fluorescent peptide product and allowed to react 2 hours to overnight at RT to afford a mixture of non-, singly-, and dually-fluorescent peptides. A final acetone precipitation and nitrogen drying procedure was used to remove unreacted fluorescent dye molecules and yield peptide product(s).

II.2.6. Novel MMP14-selective FRET peptides

Non-fluorescent peptides Ac-KWSLNLFVLC-cooh and Ac-K{Ahx}WSLNLFVL{Ahx}C-cooh (where Ac represents acetyl, $COCH_3$) were obtained commercially as custom syntheses from American Peptide Company (Sunnyvale, CA, USA). Attachment of FL-mal and TAMRA-SE dyes was performed as outlined above (see II.2.5) to synthesize FRET peptides

[Ac-K(tamra)WSLNLFVLC(fam)-cooh and Ac-K(tamra){Ahx}WSLNLFVL{Ahx}C(fam)-cooh]. These peptides were then subjected to FRET switch assay with pronase or EDTA to determine suitability as a 2-color FRET substrate.

II.2.7. Synthesis and characterization broadly MMP-cleavable 2-color FRET substrates

Broadly MMP-cleavable "Broad2" [h_2n-RPLGLWARC-cooh] and "Ahx-Broad2" [h_2n-{Ahx}RPLGLWAR{Ahx}C-cooh] peptides were obtained as custom syntheses from Biomer Technology (Pleasanton, CA, USA). Unless otherwise noted, "phosphate buffer" hereafter refers to 100 mM potassium phosphate buffer (pH 7.3) and all chemical reactions were performed at RT with gentle rocking, protected from light.

A 2-color Broad2 FRET peptide [tamra-RPLGLWARC(fam)-cooh] was synthesized as described above with minor modifications. To 1.1 mg (1.03 µmol) Broad2 peptide was added 51 µL sterile-filtered PBS with 0.2 M DTT, 1 mM PMSF. Reduced Broad2 peptide was then precipitated by addition of 500 µL ice cold acetone and dried under nitrogen gas flow prior to resuspension in 51 µL phosphate buffer. 88 µL (2.05 µmol) FL-mal in DMF was then added and allowed to react for 3 hours to give the intermediate product, "Broad2-FL." Broad2-FL was then precipitated and dried as before with 1 mL ice cold acetone and nitrogen gas to give a yellow solid that was reconstituted in 100 µL phosphate buffer. To 70 µL of Broad2-FL solution was added 76 µL (1.44 µmol) TAMRA-SE in DMF and left overnight. Acetone precipitation was then performed twice in 1 mL volume with final reconstitution of product, "TMR-Broad2-FL," in 75 µL DMF. TMR-Broad2-FL was then diluted 1:100 in phosphate buffer for spectrophotometry and

1:100 in standard assay buffer for FRET switch assay with trypsin (0.02 mg/mL) or EDTA (25 mM).

Another FRET peptide based on the Broad2 substrate sequence, "FL-Broad2-TMR" [fam-RPLGLWARC(tamra)-cooh], was synthesized with oppositely reactive fluorescent dyes to reverse the N-terminal and C-terminal attachment sites. 168 µL (3.55 µmol) FAMSE in DMF was added to 190 µL (1.77 µmol) Broad2 in phosphate buffer and allowed to react 3 hours. To 338 µL of this reaction mix was added 7 µL (3.5 µmol) DTT in deionized water. After 2 hours, the reaction mixture was precipitated in 1 mL ice cold acetone to afford a reduced yellow solid intermediate, "FL-Broad2." 141 µL (3 µmol) TAMRA-mal in DMF and 282 µL phosphate buffer were added to the yellow solid. Due to incomplete dissolution, the mixture was again precipitated in acetone and dissolved in acetonitrile (MeCN) to give a completely dissolved solution. Another 141 µL (3 µmol) TAMRA-mal was then added and allowed to react 3 hours. Following a final acetone precipitation, the product (FL-Broad2-TMR) was reconstituted in 500 µL DMF and subsequently diluted 1:500 in standard assay buffer for FRET switch assay with trypsin (0.02 mg/mL) or MMPs-2,3,9,13,14 using 20 nM active MMP concentration per assay well as calculated from inhibitor titration assay (see Appendix B), and/or EDTA (25 mM).

A similar FRET substrate with flexible hydrophobic spacers designed to alleviate steric hindrance of the MMP cleavage site,"Ahx-Broad2-vis" [fam-{Ahx}RPLGLWAR{Ahx}C(tamra)-cooh, see Appendix A], was synthesized in a 1-pot series of sequential dye-addition reactions. 73 µL (1.54 µmol) FAMSE in DMF was added to 50 µL (770 nmol) freshly reconstituted Ahx-Broad2 peptide. 12 µL

phosphate buffer was added and the reaction mix left shaking for 3 hours. To 100 µL of this reaction mix was added 64 µL (1.15 µmol) TAMRA-mal in DMF and 6 µL phosphate buffer. Following overnight (approximately 18 hours) reaction, peptide products were precipitated by addition of 1 mL ice cold acetone and reconstituted in 150 µL DMF. Dissolved Ahx-Broad2-vis was then diluted in standard assay buffer and FRET switch assay repeated as with FL-Broad2-TMR above.

II.2.8. Investigation of substrate steric hindrance via FRET switch assay

"Peptide 13c" [tamra-RIGFLRTRK(fitc)R-cooh], "Peptide 13e" [tamra-SGRIGFLRTAK(fitc)R-conh$_2$], "Peptide 13g" [tamra-{Ahx}SGRIGFLRTAK(fitc)R-conh$_2$], and "Peptide 13i" [dab-SGRIGFLRTAK(fitc)R-conh$_2$, where dab represents Dabcyl] were obtained as custom syntheses from Biomer Technology (Pleasanton, CA, USA). All substrate peptides were reconstituted from lyophilized powder to 5 mM concentration in dH2O or 50% MeCN and diluted to final assay concentration of 8.75 µM in standard assay buffer for FRET switch assays with pronase (17 nM), MMPs-2,14 (5 nM) and/or EDTA (250 µM).

II.2.9. Synthesis and characterization of M9 and M9-Folate FRET peptides

"M9" peptide [h$_2$n{Ahx}AVRWLLTA{Ahx}C-cooh] was purchased as a custom product from Genscript (Piscataway, NJ, USA). "M9-Folate" peptide [fa-K{Ahx}AVRWLLTA{Ahx}C-cooh, where fa is folic acid] was obtained as a custom synthesis from Biomer Technologies (Pleasanton, CA, USA). "M9-vis" and "M9-Folate-vis" were synthesized using a procedure analogous to FL-Broad2-TMR (see II.2.7, above). Chemical reactions were performed at RT with gentle rocking, protected

from light.52 µL (1.1 µmol) and 72 µL (1.6 µmol) FAMSE in DMF were added to 50 µL each of M9-Folate (553 nmol) and M9 (795 nmol) in DMF, respectively. 10% volume 0.1 M phosphate buffer (pH 7.3) was added to each reaction mix and the reactions were allowed to proceed overnight. 10 µL (1 µmol) and 15 µL (1.5 µmol) DTT in dH_2O were added to M9F and M9 reaction mixes, respectively and reacted 60 minutes. Reduced peptide intermediates were precipitated in ice cold acetone, dried under nitrogen gas flow, and reconstituted in 100 µL DMF each with vortexing and sonication. 48 µL (997 nmol) and 69 µL (1.43 µmol) TAMRA-mal in DMF and 10% volume phosphate buffer were added to M9F and M9 reaction mixes, respectively, and allowed to react overnight. Each peptide product was precipitated and dried as before, then reconstituted in 33/67% 1 mM phosphate buffer (pH 7.5)/DMF to yield M9-Folate-vis and M9-vis FRET peptides. FRET switch assays were carried out as described earlier either with trypsin (0.02 mg/mL) or MMPs-3,9,14 (20 nM active MMP).

M9 and M9F peptides were incubated with and without MMP9 in assay buffer (see II.2.3) and then analyzed by LCMS to determine qualitatively whether or not proteolysis was occurring in the absence of attached fluorophores. Briefly, 4 µL (80 µg) of each peptide was dissolved in 200 µL total volume of assay buffer with or without MMP9 (20 nM active MMP) and incubated overnight. The resulting mixtures were analyzed by LCMS (see general procedure, II.2.1).

II.2.10. Commercially produced Broad2 FRET peptides

"GG-B2-vis" [h_2n-GGK(fam)GGRPLGLWARGGK(tamra)G-cooh] and "fa-GG-B2-vis" [fa-GGK(fam)GGRPLGLWARGGK(tamra)G-cooh] peptides were obtained as custom syntheses from Biomer Technologies (Pleasanton, CA, USA).

II.2.11. Synthesis and characterization of peg-Broad2-vis FRET peptide

Conventional Fmoc-protected solid phase peptide synthesis (SPPS) was performed using a PS3 automated peptide synthesizer (Protein Technologies, Tucson, AZ, USA) according to manufacturer instructions to synthesize "peg-Broad2-vis" FRET peptide [Fmoc-{peg_1}K(fam){peg_1}RPLGLWAR{peg_1}K(tamra)G-$conh_2$]. Rink amide AM LL (100-200 mesh) low-substitution resin was used in amount equivalent to 50 µmol substitution. All Fmoc-protected monomer residues were portioned to 200 µmol per coupling, combined with 190 µmol HCTU, and double coupled with the exception of Fmoc-Lys(5/6-X)-OH (200 µmol per coupling), where X is FAM or TAMRA, where coupling was performed using 250 µmol PyClock instead of HCTU used in the standard single coupling reactions. The solvents employed for automated synthesis were N-methyl-2-pyrrolidone (NMP) as primary solvent, 20% piperidine in NMP for Fmoc deprotection cycles, and 0.4 M N-methylmorpholine (NMM) in NMP for residue activation solution. Final peptide products were simultaneously deprotected and cleaved from solid phase resin support by vigorous vortexing in cleavage cocktail B [88% TFA, 5% H_2O, 5% phenol, 2% triisoproylsilane (TIPS)] for 2 hours and recovered by filtration and precipitation in ice cold diethyl ether (Et_2O).

Molecular weights of the products of SPPS were determined by LCMS (general method, see II.2.1). Attempted purification of the intended peg-Broad2-vis (pB2v) peptide by semi-preparative HPLC was performed on a Waters Breeze 2 HPLC system (Waters, Milford, MA, USA) with monitoring of eluted chemical species at 550 nm that is characteristic of TAMRA dye. Collected fractions were diluted with dH_2O, lyophilized, and reconstituted in dH_2O prior to analysis by LCMS and further purification by HPLC.

After three rounds of iterative purification, peptide product "peg-Broad2-vis_2.2.1" (pB2v_2.2.1) was lyophilized and reconstituted in 100 µL dH_2O. The concentration of the resulting aqueous solution was estimated to be 334 µM in pB2v by measuring absorbance at 550 nm on a Nanodrop 1000 instrument (Thermo Scientific, Wilmington, DE, USA) and applying the Beer-Lambert Law with a molar extinction coefficient for TAMRA dye of 80,000 $M^{-1}cm^{-1}$. This solution was diluted 80-fold in standard assay buffer for FRET switch assays with either trypsin (0.02 mg/mL) or MMPs-2,9,14 (varying active concentrations, as determined by inhibitor titration assay, see Appendix B).

II.3. RESULTS

II.3.1. Attachment of FITC-labeled MMP14 substrate peptides to PAMAM dendrimers

In order to develop proteolytic nanobeacons with selectivity for MMP14, custom peptides based on published substrates with demonstrated susceptibility to enzymatic cleavage selectively by MMP14[113,114] were designed and obtained. As seen in Figure II-1, Peptide #13 and Peptide #14 each feature an N-terminal FITC moiety for quenchable fluorescence ("sensor"), a C-terminal cysteine residue for bioconjugation with PAMAM nanoparticles, and Ahx groups spatially separating these functional groups from the central MMP cleavage site.

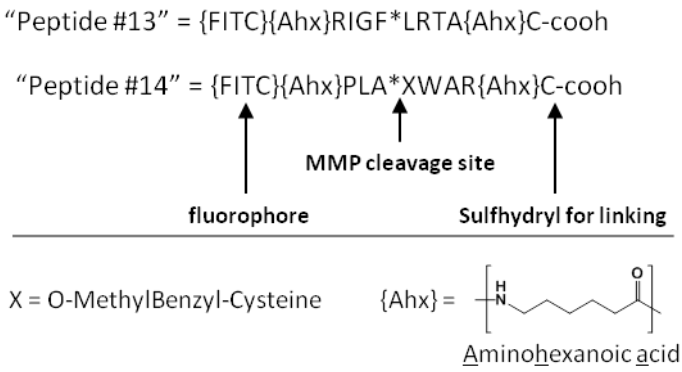

Figure II-1: **1-color MMP14 substrate peptides**
Peptide substrates for MMP14 shown above were designed based upon literature reporting on the effects of primary amino acid sequence on substrate efficiency for MMP14 and other enzymes [113,114]. "Peptide #13" and "Peptide #14" were designed to be selectively cleavable by MMP14 and to utilize the sulfhydryl-containing side chain of a C-terminal cysteine for attachment to a core nanoparticle decorated with a moiety to quench FITC fluorescence when in proximity.

A series of eight proteolytic nanobeacons was synthesized based on a previously established technique[24,37] using Peptide #13 and Peptide #14 with generation-3 PAMAM dendrimers, with or without PEGylation, and with either TAMRA of BHQ-10 to quench FITC fluorescence, as schematically diagrammed in Figure II-2.

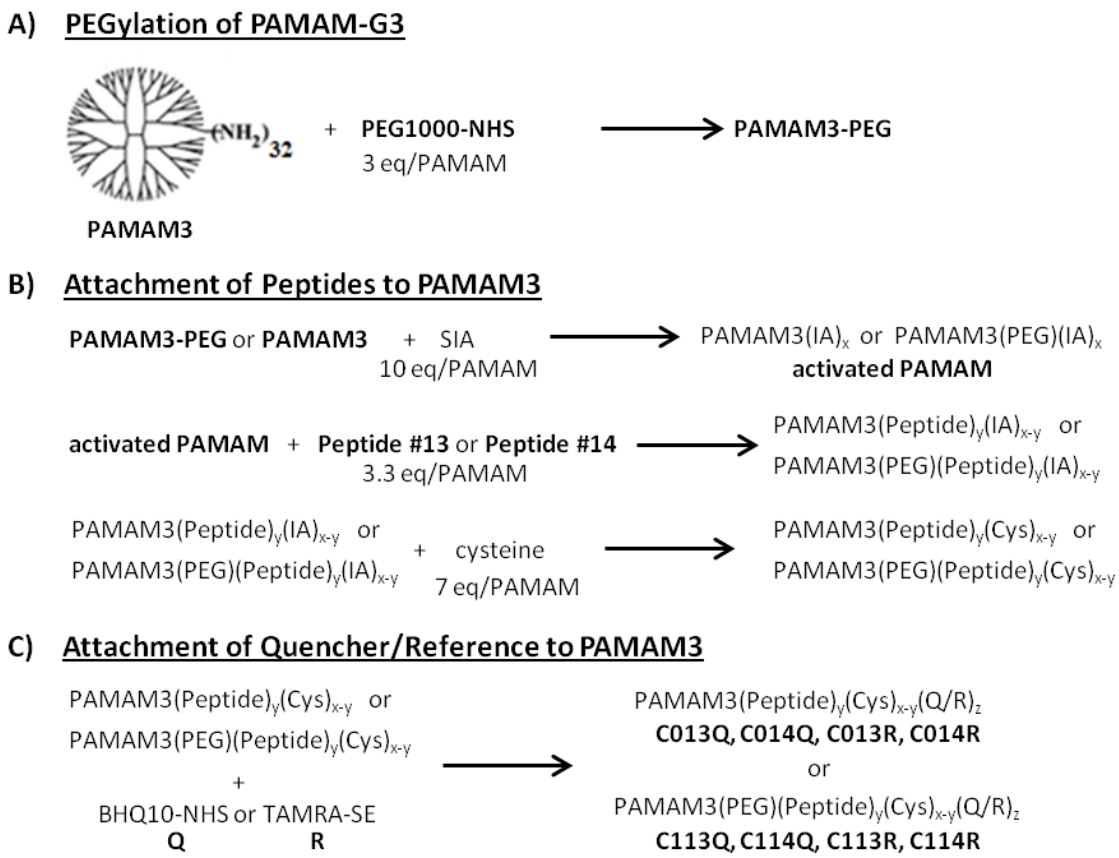

Figure II-2: **Scheme, synthesis of PAMAM-based proteolytic nanobeacons from 1-color peptides** MMP-14 substrate peptides (Peptide #13 and Peptide #14, see Figure II-1) were attached to PAMAM3 dendrimers via a multi-step synthesis to generate MMP14-selective proteolytic nanobeacons. Eight products were generated; number scheme as follows: PEGylated (C1xxx), non-PEGylated (C0xxx), bearing Peptide #13 (Cx13x) or Peptide #14 (Cx14x), and bearing BHQ10 (CxxxQ) or TAMRA (CxxxR).

The proteolysis sensing ability of the synthesized products was assessed by measurement of the sensor-to-reference fluorescence ratio (S/R) following overnight incubation with trypsin. None of the PNBs synthesized demonstrated a greater than 2-fold change in S/R upon treatment (Figure II-3a), and only C113R and C114Q (Figure II-2, above) displayed a change greater than 1.5 fold. Incubation of C113 and C114Q with MMPs yielded similar changes in S/R relative to control (EDTA) and possessed no obvious selectivity for MMP14, though it was noted that MMP14 cleaved DQG less effectively than other MMPs in this assay (Figure II-3b).

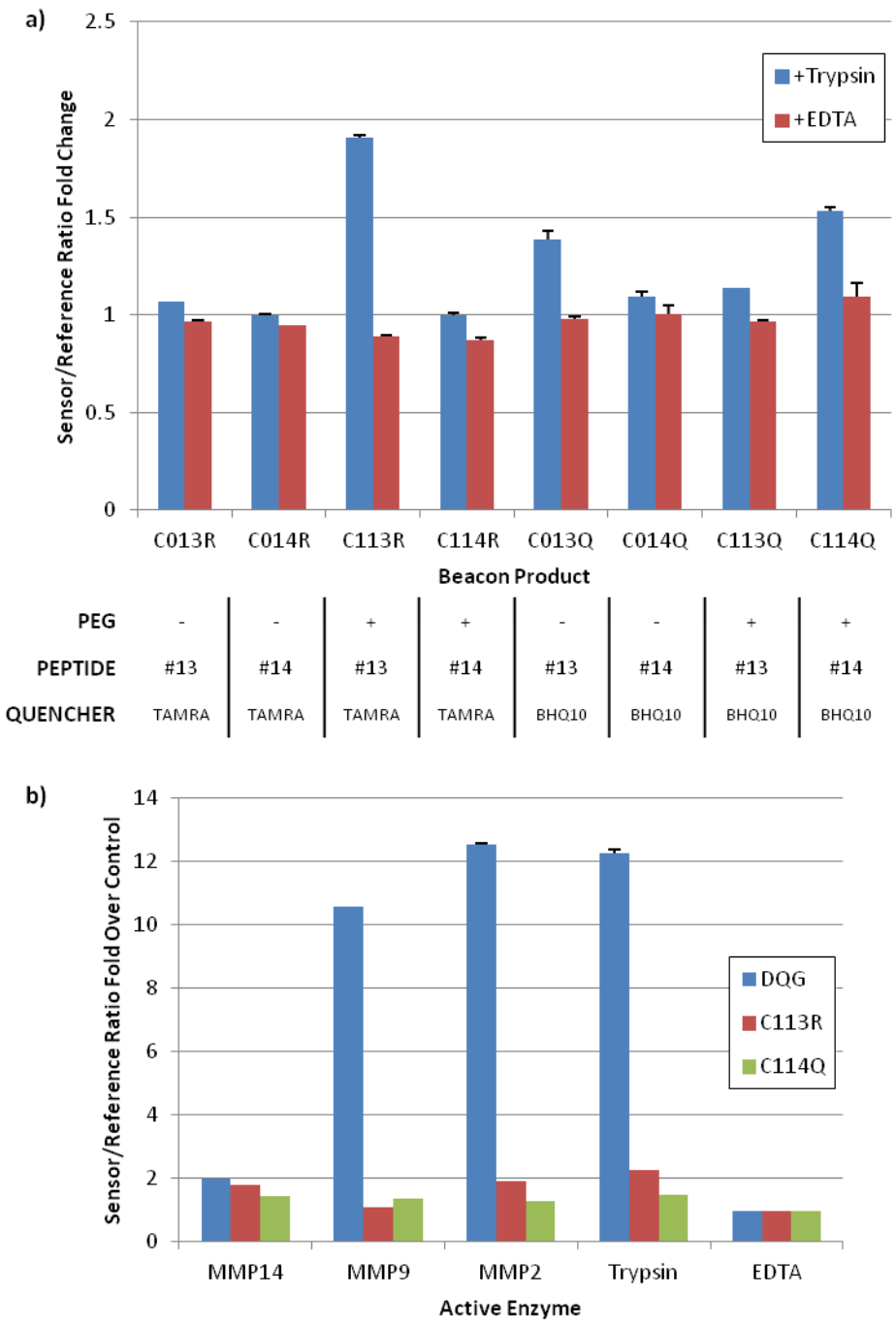

Figure II-3: **Fluorescent (FRET) switch of MMP14-cleavable proteolytic nanobeacon series** A series of 8 PAMAM-based proteolytic nanobeacons with or without PEG, utilizing Peptide #13 or #14 and either TAMRA dye or BHQ10 as noted were incubated with trypsin or EDTA overnight at 37°C and the sensor-to-reference fluorescence emission ratio calculated before and after incubation (a). Emission bandwidths for sensor and reference fluorescence correspond to FITC and TAMRA dyes, respectively. C113R and C114Q were similarly incubated with MMPs (b). Dye-quenched gelatin (DQG) was included as a control. Values represent average of triplicates. Error bars: standard deviation.

II.3.2. MMP cleavability and FRET switch of 2-color (FRET) MMP14 substrates

We hypothesized that intramolecular FRET of PNBs could be made more robust, both in terms of proportion of energy transferred ("quenching") and batch-to-batch reproducibility, by incorporating paired fluorophores directly into the substrate peptide rather than attaching the quenching fluorophore to the PAMAM surface. We therefore synthesized dually labeled substrate peptides ("F13T" and "F14T") by attaching sulfhydryl-reactive TAMRA dye to Peptide #13 and Peptide #14 (Figure II-4), leaving the C-terminal carboxyl functional groups available for attachment to nanoparticles.

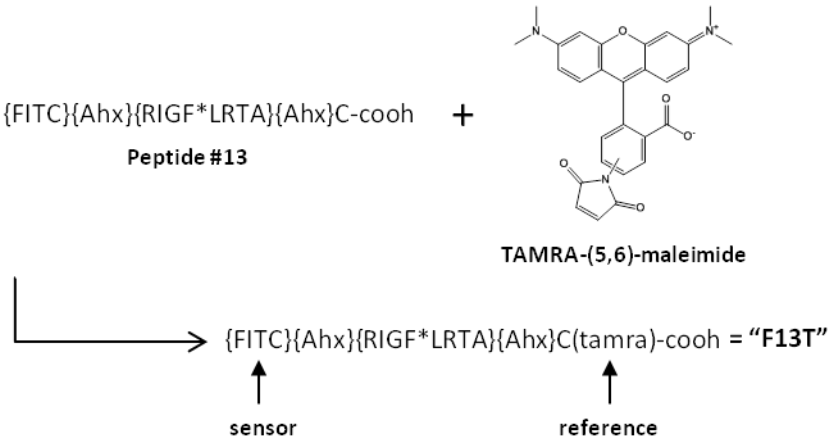

Figure II-4: Scheme, FRET peptides synthesized via maleimide-to-sulfhydryl reaction
The sulfhydryl-reactive dye, TAMRA-(5,6)-maleimide, was used to label peptides on the side chain of their cysteine residues, generating peptides equipped with FITC ("sensor") and TAMRA ("reference") fluorophores which constitute a well-studied FRET pair. This strategy was extended to Peptide #14 to synthesize "F14T," as well.

FITC (sensor) fluorescence of both F13T and F14T increased dramatically following overnight incubation with trypsin and pronase (Figure II-5a), while TAMRA (reference) fluorescence remained mostly unchanged (Figure II-5b). Because treatment with pronase elicited a nearly 24-fold increase in the sensor fluorescence of F14T, the FRET switch of F14T upon treatment with MMPs was also assessed. While sensor fluorescence increased

with exposure to MMP14, other MMPs (MMP2, MMP7, MMP9) were also able to generate modest FRET switches in F14T (Figure II-5c).

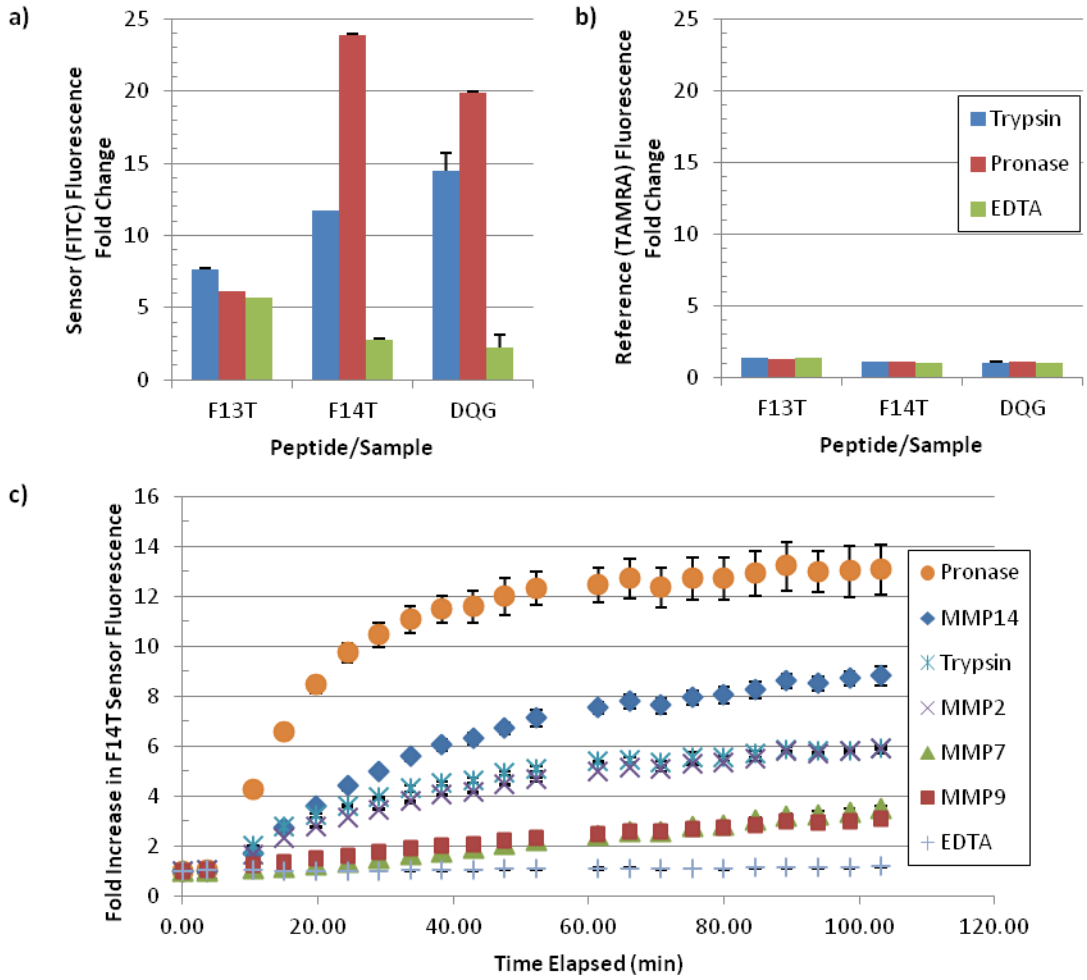

Figure II-5: **FRET switch of 2-color MMP14 substrate peptides**
F13T and F14T 2-color peptides were incubated with trypsin, pronase, or EDTA overnight at 37°C and the sensor and reference fluorescence emission measured before and after incubation (a,b). F14T was incubated with proteolytic enzymes or EDTA and fluorescence measured over time (c). Values represent average of duplicates (a,b) or triplicates (c, except MMP2: duplicates). Error bars: standard deviation.

II.3.3. Synthesis and characterization of novel MMP14 substrates

In order to improve selectivity of PNBs for MMP14 over other MMPs, substrate peptides were designed based upon MMP14-selective substrate sequences reported in the literature. As depicted in Figure II-6, the amino acid sequence published by Ouyang et

al[39] was modified, taking into consideration the insights outlined by Mucha et al[114] to generate novel "hybrid" peptides.

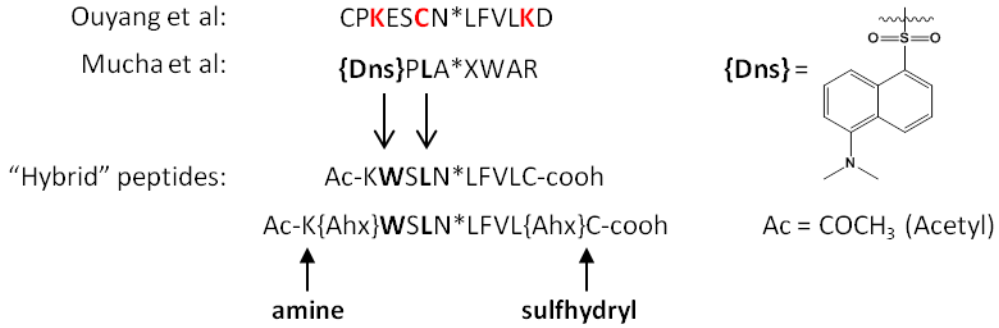

Figure II-6: Scheme, redesigned "hybrid" MMP14 substrates
MMP14 substrate peptides were designed based upon reported MMP14-selective substrate sequences in the literature [39,114]. Residues in red presented problems for fluorophore attachment due to their reactive side chains. Residues from the sequence presented by Mucha et al were substituted to generate new potential MMP14 substrates. Tryptophan (W) was chosen to replace the fluorescent dansyl (Dns) moiety due to structural similarity.

Ac-KWSLNFLVC-cooh and Ac-K{Ahx}WSLNLFVL{Ahx}C-cooh were obtained as custom syntheses without any included fluorophores. To assess the suitability of these novel hybrid peptides as FRET substrates for MMP14, sequential attachment of sulfhydryl reactive FL-mal and amine reactive TAMRA-SE dyes was attempted, as schematically diagrammed in Figure II-7.

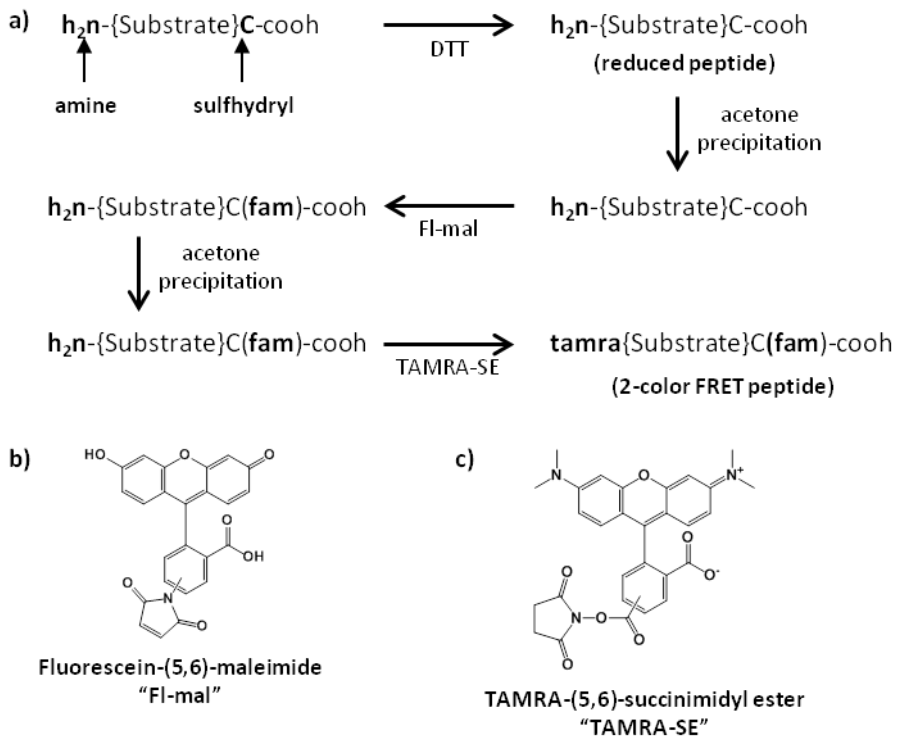

Figure II-7: **Scheme, synthesis of 2-color FRET peptides using reactive dyes**
The general stepwise procedure (a) used to produce 2-color FRET peptides for visualizing MMP activity. Steps included reduction of disulfide dimers by reducing agent DTT, acetone precipitation to remove unreacted materials, and reaction with sulfhydryl-reactive fluorescein (b) as well as amine-reactive TAMRA (c) dyes.

Unfortunately, handling of these peptides was generally difficult, often owing to insolubility in aqueous and organic solvents. When analysis was possible, products of synthesis generally reflected poor coupling of one dye or the other and afforded unsatisfactory FRET switch when treated with proteolytic enzymes (data not shown, outcomes summarized in Table II-2).

Table II-2: **Outcomes of MMP14-selective substrate trials**

Name	Sequence	Outcomes/Properties
#13 (Kridel)	FITC{Ahx}RIGF * LRTA{Ahx}**C**-cooh	Poor switch
#14 (Mucha)	FITC{Ahx}PLA * XWAR{Ahx}**C**-cooh	Poor switch on dendrimer, non-selective
Weiss	Ac-**C**SGESSN * LFVL{Ahx}-conh$_2$	Solubility/dye conjugation issues
Hybrid	Ac-**K**WSLN * LFVL**C**-cooh	Solubility/dye conjugation issues
Hybrid-Ahx	Ac-**K**{Ahx}WSLN * LFVL{Ahx}**C**-cooh	Solubility/dye conjugation issues

II.3.4. Troubleshooting synthesis and MMP-cleavability of FRET peptides

The challenges associated with synthesis of FRET substrates using unlabeled peptides and reactive dyes highlighted the need to characterize MMP cleavage efficiency following dye attachment. Therefore a broadly MMP-cleavable peptide (h_2n-RPLGLWARC-cooh, hereafter referred to as "Broad2," see Appendix A) with high sensitivity and previously characterized relative efficiencies with various MMPs[115] was obtained. A 2-color FRET substrate, "TMR-Broad2-FL," was synthesized by sequential addition of FL-mal and TAMRA-SE as depicted in Figure II-7, above. TMR-Broad2-FL possessed an absorbance spectrum characteristic of FAM and TAMRA dye inclusion (Figure II-8a), and upon incubation with trypsin demonstrated an increase in sensor (FAM) fluorescence over several minutes (Figure II-8b). The FRET switch potential of TMR-Broad2-FL was also assessed with MMP2 and MMP14, however only meager increases in sensor fluorescence were observed after 90 minutes (data not shown). Labeling of Broad2 peptide was repeated using the same synthetic strategy with several FRET-partnered dye pairs including TAMRA/FAM and AF700/AF750, however none of the substrates generated demonstrated a greater than 1.5-fold increase in sensor fluorescence upon proteolysis by trypsin (data not shown).

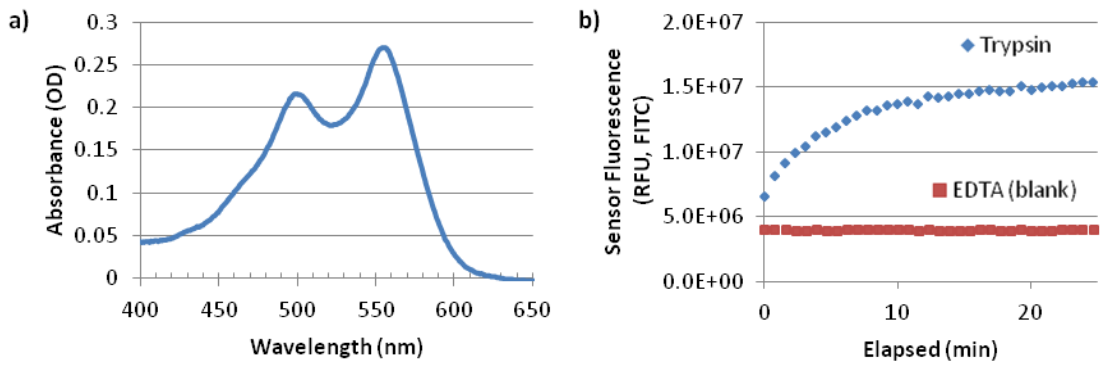

Figure II-8: **Absorbance and FRET switch of 2-color Broad2 peptide**
2-color Broad2 FRET peptide was synthesized as diagrammed in Figure II-7 and analyzed by spectrophotometry (a) to confirm fluorophore attachment and fluorescence following treatment with trypsin or EDTA (b) to confirm proteolytic FRET switch.

In an effort to troubleshoot the synthesis and consequent preteolysis sensing ability of FRET peptides, another 2-color substrate based on the Broad2 peptide was synthesized by sequential dye addition. "FL-Broad2-TMR" was synthesized by first attaching N-terminal FAMSE and subsequently attaching C-terminal TAMRA-mal, as diagrammed in Figure II-9. This represented both a change in the positions of each dye and the order of reactions with succinimidyl ester- and maleimide-containing reactive dye species with respect to the previously synthesized TMR-Broad2-FL. Interestingly, the FRET switch of FL-Broad2-TMR reflected approximately a 17-fold increase in sensor fluorescence upon proteolysis by trypsin, however almost no difference from control with MMPs-2,3,9,13,14 (Figure II-10).

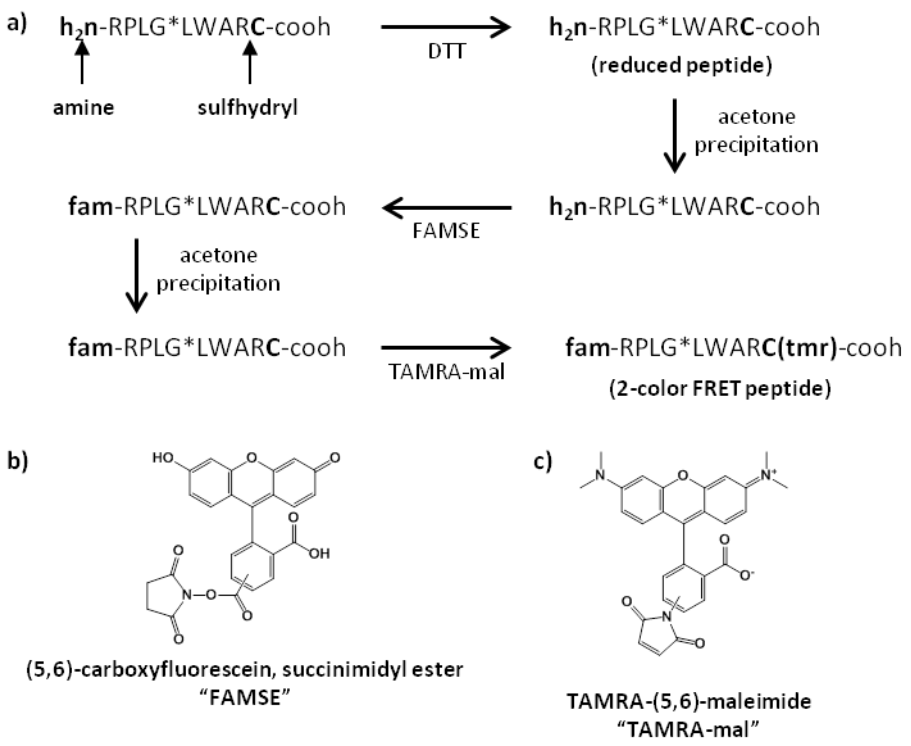

Figure II-9: **Scheme, synthesis of 2-color Broad2 FRET peptide using reactive dyes**
The stepwise procedure (a) used to produce 2-color "Broad2" FRET peptide for visualizing MMP activity. Steps included reduction of disulfide dimers by reducing agent DTT, acetone precipitation to remove unreacted materials, and reaction with amine-reactive fluorescein (b) as well as sulfhydryl-reactive TAMRA (c) dyes.

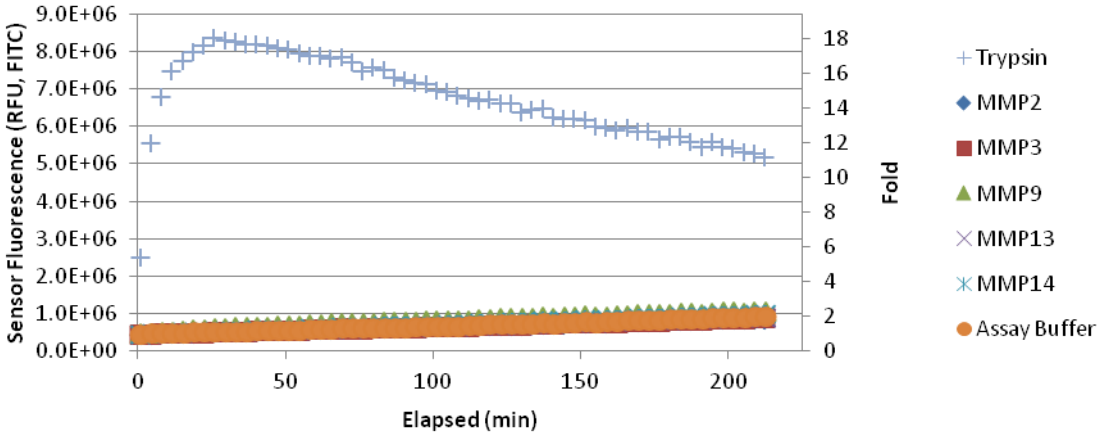

Figure II-10: **FRET switch of 2-color Broad2 with proteolytic enzymes**
2-color Broad2 peptide with N-terminal fluorescein and C-terminal TAMRA, FL-Broad2-TMR, was synthesized as diagrammed in Figure II-9 and subjected to incubation with proteolytic enzymes with monitoring of sensor (FITC) fluorescence. Fold indicates multiple of initial fluorescence emission intensity (note: blank values were not subtracted prior to calculation of fold). Values represent average of duplicates.

To interrogate whether the lack of FRET switch with MMPs could be due to the carboxyl terminus or conformation of the peptide in solution, FL-Broad2-TMR was attached to PAMAM4 via EDAC-mediated coupling and the products recovered by ultrafiltration (technique analogous to II.2.2). FRET switch of the resulting PNBs demonstrated the same pattern as free peptide, with trypsin generating an increase in sensor fluorescence and MMPs generating no such increase (data not shown).

We hypothesized that the synthetic route of dye addition in solution phase as well as steric hindrance of the MMP cleavage site may have been interfering with the ability of substrate peptides to be cleaved by MMPs following synthesis. Therefore a series of peptides based on the previously described MMP14 substrate, Peptide #13, were obtained with FRET-partnered dyes attached during solid phase synthesis by the manufacturer (Peptide -13c, -13e, -13i, -13g, see Appendix A) and tested for FRET switch. The sensor fluorescence of Peptide 13c increased approximately 15-fold with exposure to pronase over 120 minutes, whereas MMP2 effected a modest 5-fold increase and other MMPs (3, 7, 9 and 14) caused less than a 2-fold increase over the same time span (Figure II-11).

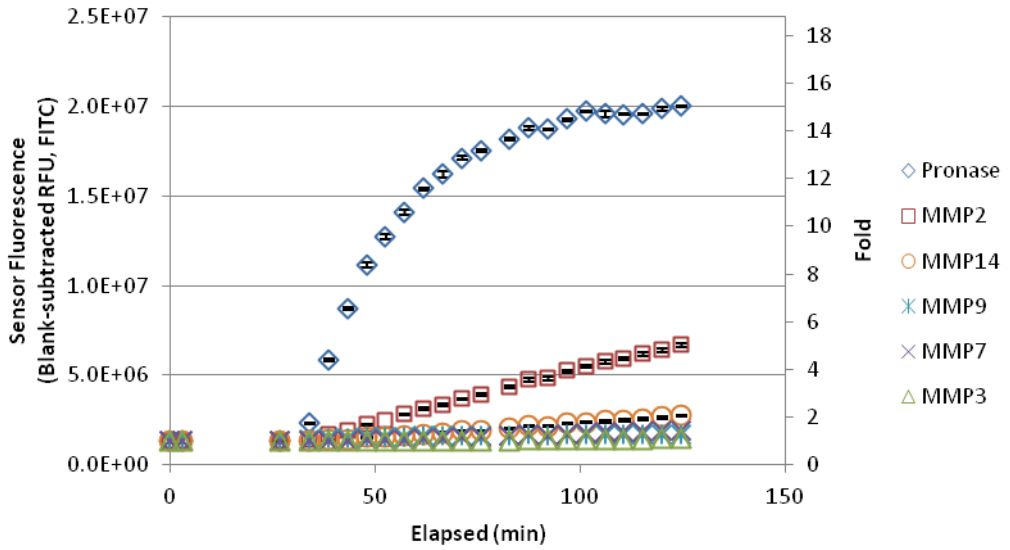

Figure II-11: FRET switch of Peptide 13c with proteolytic enzymes
2-color Peptide 13c was incubated with proteolytic enzymes (50 nM active enzyme) with monitoring of sensor (FITC) fluorescence. Fold indicates multiple of initial fluorescence emission intensity after subtracting plate blank. Values represent average of triplicates. Error bars: SEM.

To further investigate the role of steric hindrance of the cleavage site in preventing FRET switch, the series of Peptide 13-based 2-color substrates (Figure II-12a) were each incubated with pronase, MMP2, MMP14, or EDTA and sensor fluorescence monitored over time. All substrates exhibited rapid increases in sensor fluorescence when digested with pronase (Figure II-12b), however only Peptide 13i, which contained dabcyl instead of TAMRA, was apparently cleaved by both MMP2 and MMP14. Interestingly, only Peptide 13e, with two more amino acids between the dye-conjugated residues than Peptide 13c, demonstrated some selectivity for MMP14 over MMP2, an effect that was abrogated by the addition of an Ahx spacer in Peptide 13g (Figure II-12c,d). Baseline fluorescence from incubation of peptides with EDTA was subtracted from all other panels to calculate the increases in fluorescence with proteolytic enzymes (Figure II-12e).

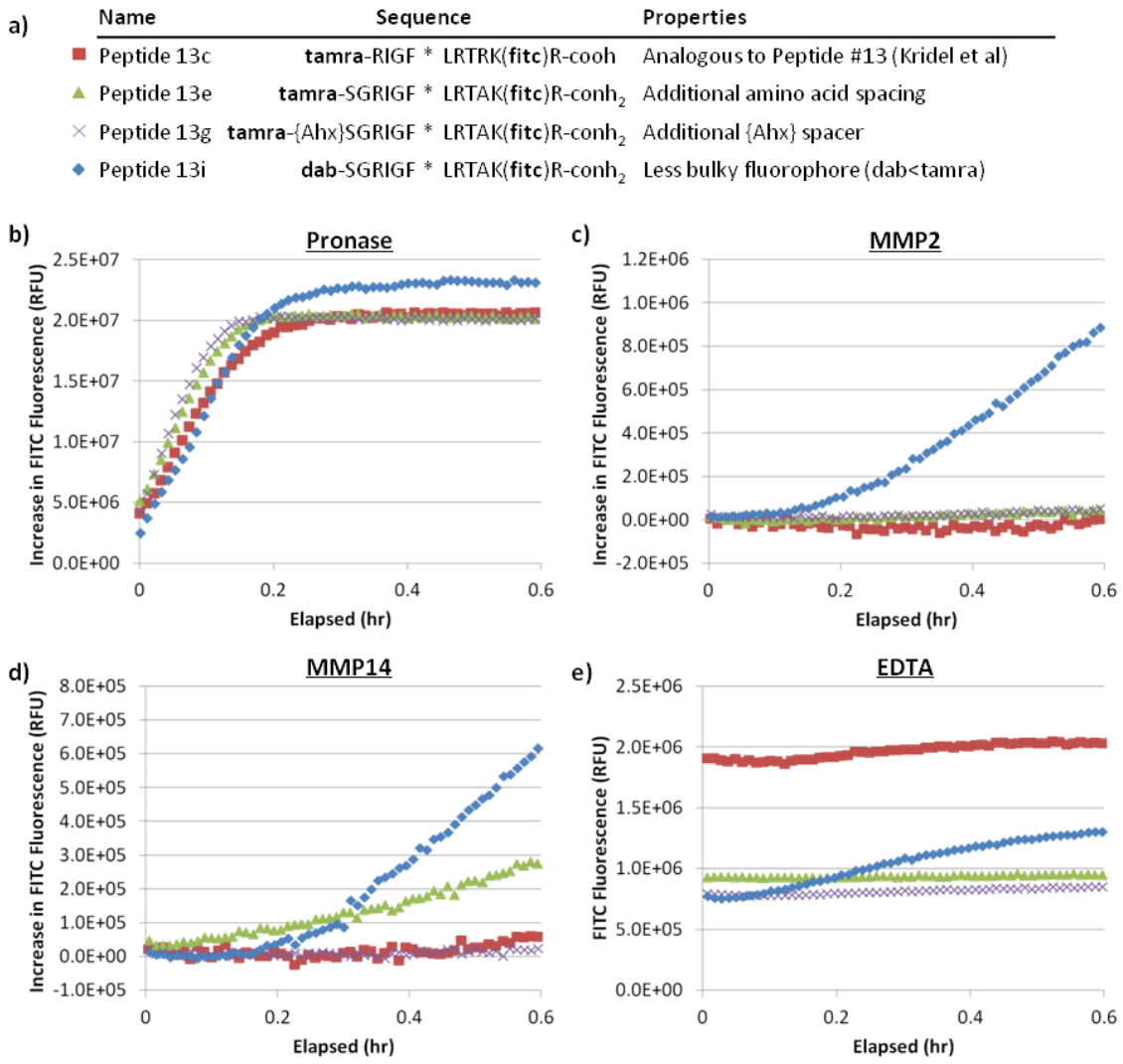

Figure II-12: Investigation of Peptide #13 cleavage site steric hindrance
A series of FRET peptides (a) based on the MMP14-selective cleavage sequence of Peptide #13 (Kridel et al) were purchased and subjected to incubation with pronase (b), MMP2 (c), MMP14 (d), or EDTA (e). The increase in FITC fluorescence generated due to incubation with enzymes (b-d) was calculated by subtracting the fluorescence of the EDTA control sample (e) at each timepoint. Values represent average of triplicates.

To examine whether steric hindrance could explain the lack of MMP cleavage of FL-Broad2-TMR despite demonstrated FRET switch potential, "Ahx-Broad2" [h_2n-{Ahx}RPLGLWAR{Ahx}C-cooh, see Appendix A], a peptide design based on the Broad2 cleavage sequence with additional Ahx spacers to alleviate possible steric hindrance of the central MMP cleavage site, was obtained commercially. "Ahx-Broad2-

vis" was synthesized in a 1-pot reaction analogous to the synthesis of FL-Broad2-TMR (Figure II-9), omitting the DTT reduction step and acetone precipitation between reactive dye attachment reactions. Measurable FRET switches resulted from proteolysis of Ahx-Broad2-vis by MMP9, MMP2, and MMP14, in order of decreasing magnitude (Figure II-13). The increase in sensor fluorescence over time induced by MMPs was abrogated by the inclusion of EDTA in assay conditions.

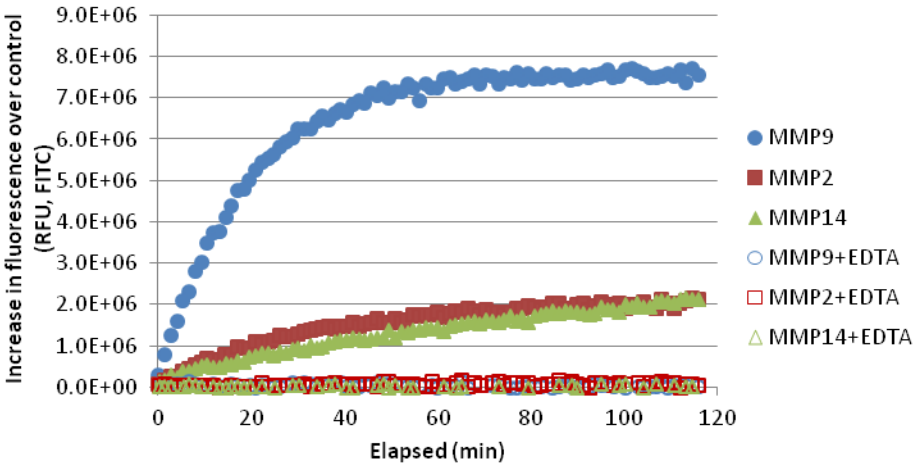

Figure II-13: **FRET switch of Ahx-Broad2-vis with MMPs**
2-color Ahx-Broad2-vis peptide analogous to 2-color Broad 2 (Figure II-10) with additional Ahx spacers was subjected to incubation with MMPs (20 nM active concentration, each) with or without inclusion of EDTA and monitoring of sensor (FITC) fluorescence. Fluorescence of sample with buffer only was subtracted at each timepoint to calculate the enzyme-associated increase in fluorescence. Values represent single measurements.

II.3.5. MMP-cleavability of folated substrate peptides

Incorporation of folic acid as a targeting ligand tethered to nanoparticles by an MMP-cleavable linker is integral to our dual-targeted nanoparticle design. It was therefore necessary to determine whether the covalent attachment of folic acid would prohibitively interfere with MMP proteolysis of dual-targeted constructs. Our laboratory has previously demonstrated FRET switch with 2-color variants of a substrate designed for

MMP9 cleavage, a peptide termed "M9" [h2n-{Ahx}AVRWLLTA{Ahx}C-cooh][109] (unpublished data, Scherer and McIntyre). A folated version of this peptide, "M9-Folate" or "M9F" [fa-{Ahx}AVRWLLTA{Ahx}C-cooh] was obtained commercially for direct comparison of MMP cleavage and consequent FRET switch with M9. See Appendix A for detailed structures.

2-color FRET peptides were synthesized from M9-Folate and M9 peptides (M9-Folate-vis and M9-vis, respectively) via DTT reduction and sequential addition of FAMSE and TAMRA-mal, analogous to the synthesis of FL-Broad2-TMR, as diagrammed in Figure II-9. The resulting FRET peptides were analyzed for FRET switch potential and MMP cleavability by incubation with either trypsin or MMPs (3, 9, and 14). As seen in Figure II-14, the sensor fluorescence of both peptides increased rapidly over 30 minutes of exposure to trypsin, however incubation with MMPs did not result in substantial increases in sensor fluorescence. The folation of M9F had no apparent effect on relative efficiencies of trypsin or MMP cleavage compared to M9.

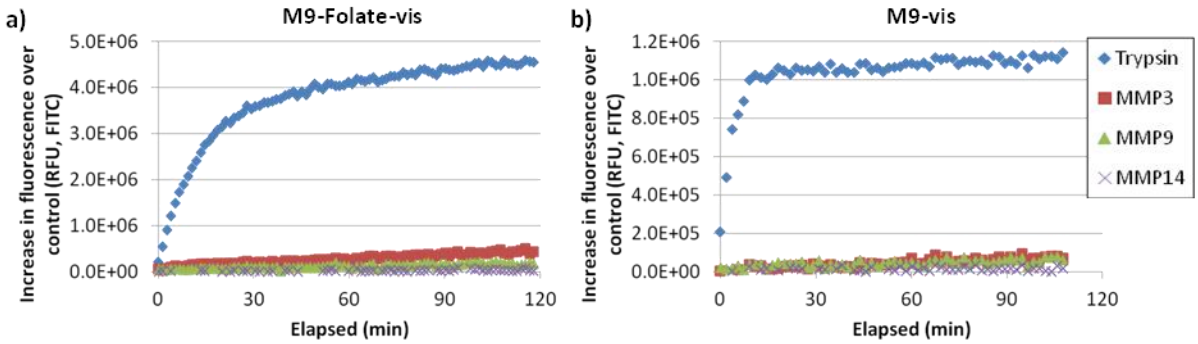

Figure II-14: FRET switch of M9-Folate-vis and M9-vis with proteolytic enzymes
2-color FRET peptides were synthesized from M9-folate (a) and M9 (b) peptides via sequential dye addition with DTT reduction as diagrammed in Figure II-9 and subjected to incubation with proteolytic enzymes and monitoring of sensor (FITC) fluorescence. Fluorescence of sample with buffer only was subtracted at each timepoint to calculate the enzyme-associated increase in fluorescence. Values represent single measurements.

Because the FRET switch results with M9F and M9 mirrored those of FL-Broad2-TMR and because there exists evidence of thiol-based inhibition of MMP activity[118–120], the use of DTT in the synthesis of 2-color FRET substrates was questioned. Synthesis of M9-Folate-vis and M9-vis was therefore repeated employing a 1-pot reaction analogous to the synthesis of Ahx-Broad2-vis (see II.3.4) but with TAMRA-maleimide in the first reaction and FAMSE in the second. This had so significant impact either on the maximum potential FRET switch with trypsin or on the relative MMP cleavability for either peptide (data not shown).

To further investigate whether the presence of the folate moiety was affecting peptide cleavage by MMPs, unlabeled M9-Folate peptide was subjected to incubation in buffer with and without MMP9 for proteolysis and analyzed by LCMS. The most substantial ions detected in the non-cleaved control sample corresponded to the expected molecular weight of disulfide dimers of the intact M9-Folate peptide (Figure II-15a,d). The MMP9-treated sample, however, contained ions with M/z corresponding to doubly-charged states of the N-terminal fragment and disulfide dimers of the C-terminal fragment expected from MMP cleavage of M9-Folate (Figure II-15b-d), thereby confirming proteolysis of the folated peptide by MMP9.

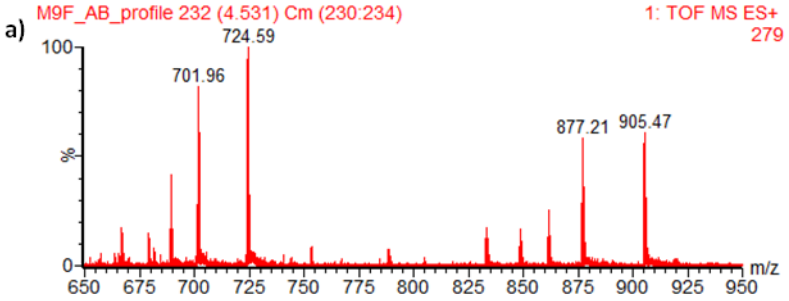

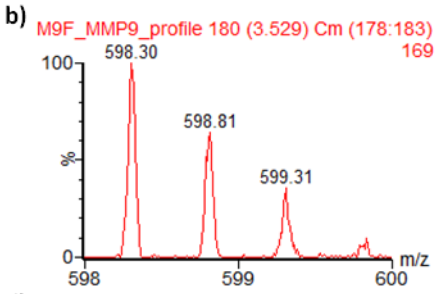

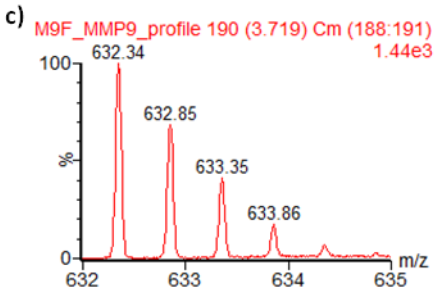

d)

Chemical Species	Mass	M+2H	M+4H	M+5H
M9F Dimer (S-S)	3615.88		904.98	724.18
M9F N-term. MMP9 Cleavage Fragment	1194.60	598.31		
M9F C-term. MMP9 Cleavage Fragment Dimer (S-S)	1262.68	632.35		

Figure II-15: LCMS analysis of M9-Folate peptide and MMP9 cleavage products
M9-Folate (M9F) peptide was analyzed by LCMS before (a) and after (b,c) treatment with MMP9 to obtain mass spectra. M/z of ions detected in untreated M9F sample (a) corresponded to disulfide dimers of the intended structure. The MMP9-treated sample contained ions with M/z peaks corresponding to the N-terminal product (b) and disulfide dimers of the C-terminal product of MMP9 cleavage. Detected ions and corresponding chemical species are tabulated (d).

To obviate the sequential dye addition synthesis as a potential confounding reason for lack of MMP cleavage of FRET substrates, two custom peptides with amino acid sequences based on the broadly MMP-cleavable Broad2 peptide and with fluorescein and TAMRA dyes incorporated as part of solid phase synthesis by the manufacturer were obtained. "GG-Broad2-vis" [h_2n-GGK(fam)RPLGLWARGGK(tamra)G-cooh] and "FA-GG-Broad2-vis" [fa-GGK(fam)RPLGLWARGGK(tamra)G-cooh] (see Appendix A) were analyzed by FRET switch assay with either trypsin or MMPs (2, 9, and 14). Unfortunately, neither peptide demonstrated greater than 3-fold increase in sensor (FAM)

fluorescence over 30 minutes of incubation with any enzyme, though surprisingly GG-Broad2-vis developed a nearly 5-fold increase in reference (TAMRA) fluorescence during incubation with trypsin (data not shown). Subsequent UV-visible spectrophotometry comparing (FA-)GG-Broad2-vis with 2-color peptides previously acquired from the same supplier revealed low TAMRA absorbance relative to that of FAM (data not shown). The supplier confirmed difficulty in the coupling chemistry for attachment of the TAMRA fluorophore.

II.3.6. Synthesis and characterization of a broadly MMP-cleavable FRET peptide by SPPS

Due to the inconsistencies encountered with 2-color FRET peptides both from sequential fluorophore attachment to peptides in solution phase and from commercial sources, I explored the possibility of synthesizing a peptide using conventional Fmoc-SPPS. In addition to traditional amino acids, several reagents were commercially available for synthesis of unusual and modified peptide structures, including fluorophore-bearing lysine residues (Figure II-16a,b) and short polyethylene glycol (PEG) residues (Figure II-16c). As such, we designed and synthesized a broadly MMP-cleavable substrate bearing FAM and TAMRA dyes and flexible hydrophilic PEG spacers using an automated peptide synthesizer for conventional Fmoc-SPPS (Figure II-16d). Refer to Appendix A for chemical structure of "peg-Broad2-vis (pB2v)."

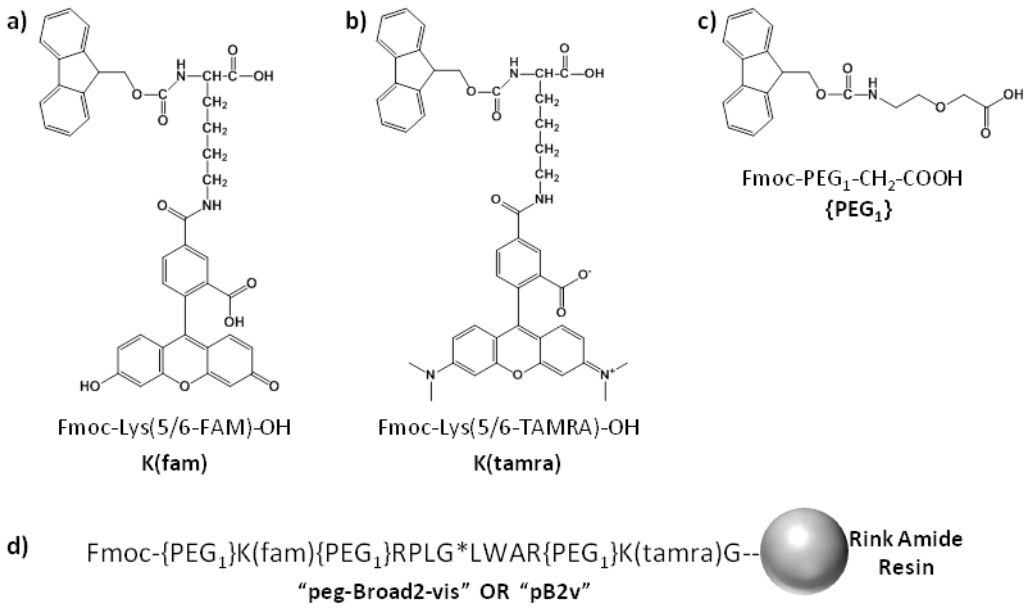

Figure II-16: Schema for solid phase peptide synthesis of peg-Broad2-vis
Reagents for SPPS of fluorescent peptides, Fmoc-Lys(5/6-FAM)-OH (a) and Fmoc-Lys(5/6-TAMRA)-OH (b), as well as hydrophilic spacer residue Fmoc-PEG_1-CH_2-COOH (c) were acquired commercially (shorthand representations in bold). "peg-Broad2-vis (pB2v)" peptide was synthesized on a rink amide resin using a PS3 automated peptide synthesizer to yield a C-terminally amidated peptide (d).

LCMS performed on the crude peptide mixture recovered from final deprotection and cleavage of pB2v from the solid support resin indicated a heterogeneous mixture of chemical species partially resolved by chromatography (Figure II-17a). However, ions with M/z corresponding to the triply-charged state (Figure II-17b) as well as other charge states (Figure II-17c) of the expected structure of pB2v were identified within the LCMS analytes.

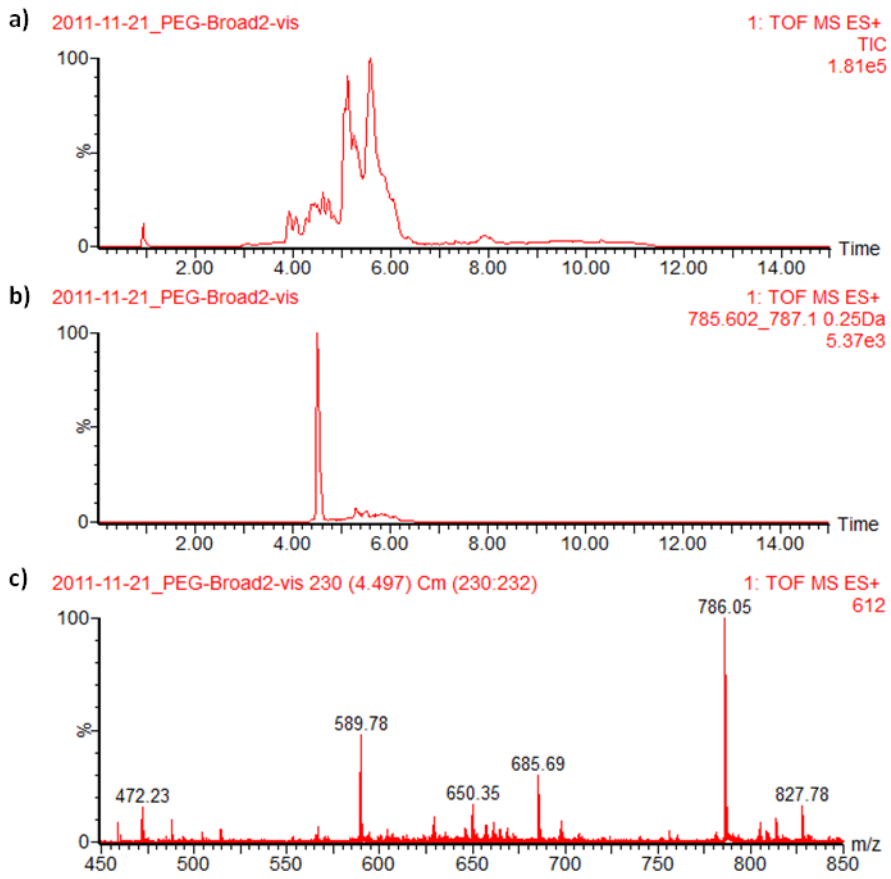

Figure II-17: **LCMS of peg-Broad2-vis crude peptide mixture from SPPS**
The crude peptide mixture from SPPS of pB2v peptide (Figure II-16d) was characterized by LCMS to give total ion counts (a). A chromatogram representing the ions with M/z corresponding to the triply-charged state of the expected peptide was extracted (b) and the mass spectrum of the peak integrated (c). Ions with M/z corresponding to the multiple charge states of expected pB2v structure (472, 589, 786) were detected.

As such, semi-preparative HPLC separation and recovery of the pB2v crude peptide mixture were performed and three separate fractions collected for further workup (Figure II-18a). LCMS analysis of each collection confirmed the presence of ions with M/z corresponding to pB2v in the second fraction collected, although "pB2v_2," indicated a still heterogeneous mixture of chemical species (data not shown). pB2v_2 was therefore separated again by semi-preparative HPLC with a focused solvent gradient to afford three further subdivided collections: pB2v_2.1, _2.2, and _2.3 (Figure II-18b). LCMS analysis was repeated with each of the collected fractions to confirm the presence of pB2v in

pB2v_2.2 (data not shown), which was then purified again by semi-preparative HPLC to afford a single peak, collected as pB2v_2.2.1 (Figure II-18c).

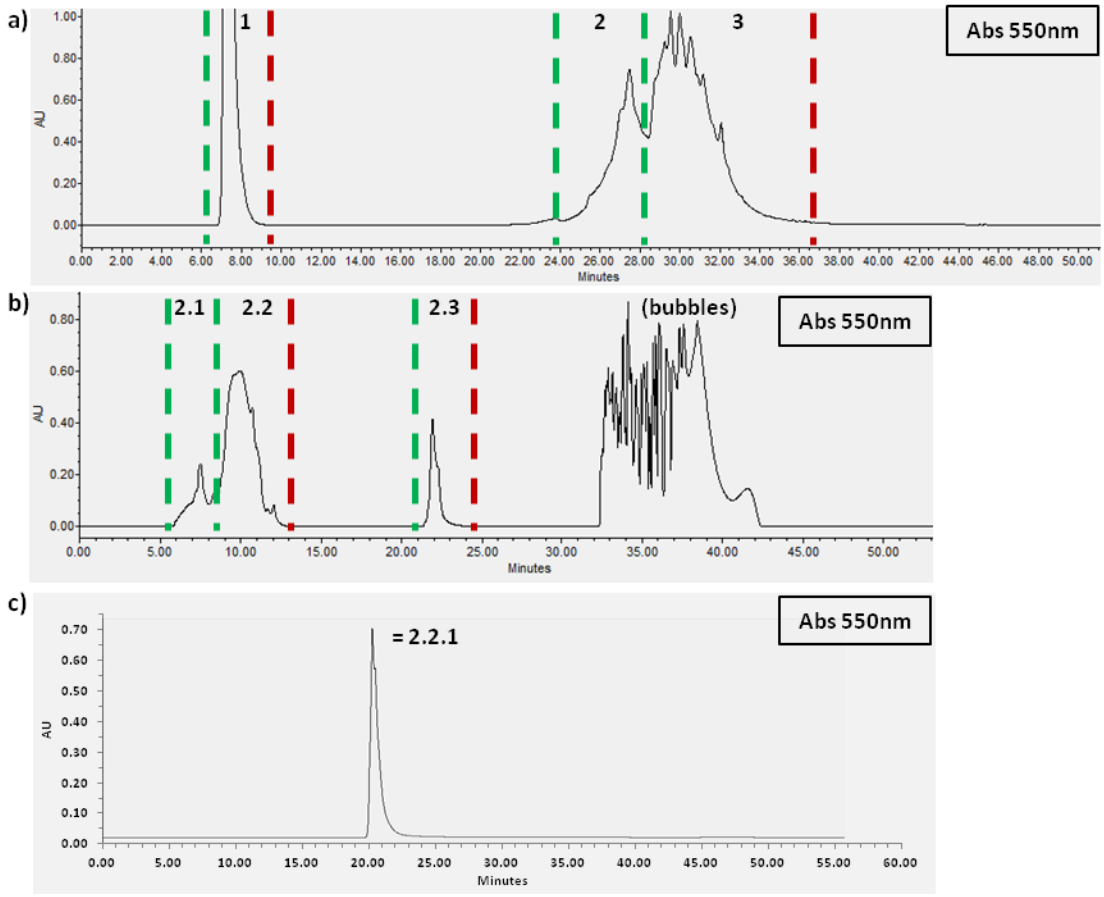

Figure II-18: Iterative HPLC purification of pB2v
pB2v peptide mixture from SPPS was separated by semi-preparative RP-HPLC with monitoring of eluent absorbance at 550 nm (TAMRA) and fractions collected (a). This process was iterated to further purify Fractions #2 (b) and# 2.2 (c) as labeled to ultimately yield a product fraction labeled "pB2v_2.2.1." Green and red dashed lines indicate approximate start and end of fraction collection, respectively.

The purified peptide, pB2v_2.2.1, was then incubated with either trypsin or MMPs (2, 9, or 14) to assess FRET switch potential and relative cleavage efficiency. Importantly, sensor fluorescence of pB2v_2.2.1 increased upon proteolytic cleavage by trypsin and each MMP (Figure II-19), though direct comparison of rates of fluorescence increase is

inappropriate because in this experiment the concentrations of active MMPs varied from enzyme to enzyme.

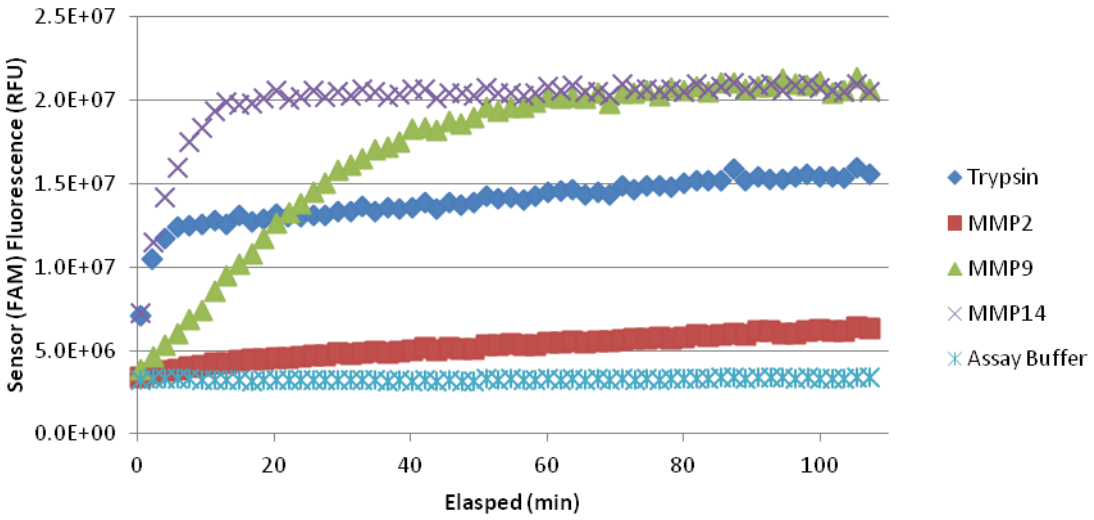

Figure II-19: FRET switch of purified pB2v_2.2.1 peptide
Following iterative purification by semi-preparative RP-HPLC, pB2v_2.2.1 peptide product was incubated with proteolytic enzymes and the fluorescence of the sensor moiety (FAM) monitored over time. Note: plot represents raw fluorescence measurements; plate blank was not subtracted from values. Values represent single measurements.

The efficiency of enzymatic cleavage of pB2v_2.2.1 by MMPs was determined by calculating the specificity constants, k_{cat}/K_m, as follows:

$$\frac{k_{cat}}{K_m} = \frac{M}{F_e C_e},$$

where M is the initial rate of fluorescence increase, F_e is the maximum fluorescence increase for a particular enzyme-substrate pair and C_e is the concentration of active enzyme as determined by inhibitor titration assay (see Appendix B)[116]. From the results depicted in Figure II-19, peg-Broad2-vis_2.2.1 is roughly 1.5 times more efficient a substrate for MMP14 than for MMP2, and approximately twice as efficient for MMP9 as for MMP14 (Table II-3), which is in general agreement with published relative

efficiencies for substrates with a very similar amino acid sequence in the MMP cleavage site (P_4-P_4')[115].

Table II-3: Enzyme specificity values for pB2v_2.2.1 with MMPs

Enzyme	k_{cat}/K_m (M^{-1} s^{-1})
MMP2	6.51E+03
MMP9	1.96E+04
MMP14	9.57E+03

II.4. Discussion and Conclusions

The work presented above was initially focused on the development of proteolytic nanobeacons to provide optical sensing of MMP14 activity and targeting of the optical sensor to folate receptors for cellular internalization. To this end, proteolytic nanobeacons and FRET-equipped peptide substrates were synthesized and characterized for their optical properties and MMP-cleavability.

Based upon the relatively small and inconsistent FRET switches observed from proteolytic nanobeacons synthesized with MMP14 substrate peptides derived from previously published studies (Figure II-3), we hypothesized that attachment of FRET-paired fluorophores directly to the substrate peptide would provide a more robust optical switch than attachment of the quenching/reference fluorophore to the nanoparticle core, both in terms of proportional energy transfer and batch-to-batch reproducibility. To test this hypothesis we synthesized "2-color" peptides decorated with both FITC and TAMRA dyes, well-characterized visible-spectrum fluorophores that participate in FRET. "F14T" 2-color MMP14 substrate exhibited excellent optical switch potential when digested by the bacterial protease, pronase, and to a lesser degree with MMP14, however was not as selective for MMP14 as desired, as shown in Figure II-5. "F13T," on

the other hand, demonstrated a smaller maximum optical switch, but was somewhat more selective for MMP14, corroborating previously published findings that a proline residue in the P3 substrate position is favorable for cleavage efficiency by the MMP family broadly, whereas an arginine residue in the P4 position seems to provide some degree of selectivity for MMP14 [113,114]. In general, cleavage efficiency and enzyme selectivity of substrates present a trade-off that must be managed to provide an effective sensor that is not promiscuous for other metalloproteinases or proteases.

To provide an effective sensor for MMP14-selective proteolytic nanobeacons, several published amino acid sequences with either high selectivity[39] or high efficiency[114] of cleavage by MMP14 were amalgamated to generate novel MMP14 substrate peptides with side chains compatible with the chemistry of 2-color peptide synthesis. These peptides were obtained as unlabeled peptides, requiring the bioconjugation of FAM and TAMRA dyes to facilitate FRET and the consequent optical switch. Unfortunately, handling of these peptides was challenging due to insolubility in aqueous and organic solvents and multi-step processes to attach both fluorophores. As such, the products of our syntheses lacked sufficient optical switch for MMP activity sensing applications, as indicated in Table II-2.

Revisiting the conceptual design of folate-targeted proteolytic nanobeacons and the current understanding of the tumor microenvironment, the use of a substrate peptide selective for MMP14 was questioned. Although MMP14 has been shown to possess pleiotropic roles as a proteinase capable of hydrolyzing several classes of proteins, including activation of MMP2 and MMP8[8,11], and has been shown to play vital roles in tumor cell invasion and metastasis[42,110], its confinement at the cell surface as a

membrane-type MMP could present a limitation to the extracellular processing of proteolytic nanobeacons prior to folic acid-mediated cellular internalization. On the other hand, the extracellular milieu of a solid tumor may often be rich in secreted MMPs[15,16], especially near the leading edges of invasive malignant cells[121–123]. As such, the use of a broadly MMP-cleavable substrate as the scissile linker for proteolytic nanobeacons was investigated as a more promising approach to effect dual-targeted delivery.

The chemistry of FAM and TAMRA labeling of substrate peptides was therefore troubleshot using a broadly MMP-cleavable substrate peptide termed Broad2. This peptide was derived from a published substrate with high cleavage efficiency with MMPs[115,124] in order to provide the most robust means for evaluation of the optical switch resulting from fluorescent substrate hydrolysis. Interestingly, as demonstrated in Figure II-8 and Figure II-10, attachment of FAM and TAMRA was confirmed by UV-visible absorbance and FRET switch upon proteolysis with trypsin, however no concordant increase in sensor (FAM) fluorescence emission was observed upon treatment with MMPs. These results suggest that this particular fluorophore-labeled peptide forms a conformation unfavorable for proteolytic cleavage by MMPs.

In order to obviate peptide handling and the synthetic route of dye addition as confounding reasons for lack of an optical switch with MMPs in 2-color MMP substrates, peptides with FRET-paired fluorophores attached as part of synthesis in solid phase were acquired commercially. These substrates, all based on a core amino acid sequence with reported enzyme selectivity for MMP14 ("Peptide #13")[113], differed from one another either in the type or number of residues separating the fluorophores or in the fluorophore used to accept energy from FITC, as specified in Figure II-12. FRET was confirmed in all

peptides of the series, as each substrate exhibited a substantial increase in FITC fluorescence upon proteolysis by pronase. However only Peptide 13i, which featured a less bulky FITC quenching moiety in dabcyl instead of TAMRA, exhibited some fluorescence enhancement upon treatment with either MMP2 or MMP14 to indicate cleavage. This result suggests that steric hindrance of the MMP cleavage site may inhibit MMP cleavage of substrate peptides comparable in length and number of residues separating fluorophores. Furthermore, while Peptide 13c was not well-cleaved by MMPs, Peptide 13e possessing two additional amino acids between FITC and TAMRA was cleaved by MMP14 but not MMP2. Interestingly, Peptide 13g, longer still by the addition of a hydrophobic Ahx spacer, was not cleavable by MMPs, indicating that hydrophobic residues near the MMP cleavage site may also inhibit proteolysis by MMPs. These findings corroborate the documented crystal structures of MMPs and the proposed mechanism of proteolysis by metalloproteinases. MMP2 is reported to possess a shallower substrate binding pocket than MMP14[125] and in each case the hydrolysis of the scissile peptide bond in the substrate requires water[10].

To isolate steric hindrance as the intervening problem in MMP cleavage of the aforementioned Broad2 peptide, an analogous peptide with an additional N-terminal Ahx group, Ahx-Broad2, was obtained commercially and labeled with FAM and TAMRA fluorophores as with Broad2, previously. The resulting Ahx-Broad2-vis peptide was cleaved by MMPs (2, 9, and 14) resulting in FRET switches with each MMP, as shown in Figure II-13. Proteolysis was confirmed to be attributable to metalloproteinase activity by the abrogation of FRET switch in samples including both MMPs and EDTA to chelate free metal ions. Taken together with the evident inability of MMPs to cleave dye-labeled

Broad2 and the Peptide 13-based series of substrates to varying degrees, this finding indicates that steric hindrance of the MMP cleavage site due to proximity of FITC and TAMRA is an important consideration in the design of fluorescent substrate peptides for proteolytic nanobeacon synthesis. Nonetheless, the results reported here demonstrate that synthesis of MMP substrate peptides with visible-spectrum fluorophores for optical imaging of MMP-associated proteolytic activity is feasible.

Given the obstacles to proteolytic cleavage presented by the relatively bulky organic dye molecules, FITC/FAM and TAMRA, we hypothesized that N-terminal attachment of folic acid, another quite hydrophobic molecule, could also inhibit MMP-dependent proteolysis of substrate peptides. Because incorporation of folic acid as a targeting ligand tethered to nanoparticles by an MMP-cleavable linker is integral to our dual-targeting design, we assessed proteolysis of a folated analogue of an MMP9-selective substrate, M9, that was found previously to exhibit FRET switch from 2-color variants exposed to MMP9[109] (unpublished data, Scherer and McIntyre). M9 and M9-Folate were obtained commercially as non-fluorescent peptides and initially labeled with FAMSE and TAMRA according to the same procedure used for 2-color Broad2 that incorporated DTT for reduction of intermolecular disulfide bonds that may have formed in solution (see Figure II-9). FRET switch was observed from both constructs (M9-vis and M9-Folate-vis) upon treatment with trypsin, but surprisingly neither construct was cleaved by MMPs, as shown in Figure II-14. As a result, no conclusion could be drawn from this experiment regarding the effect, if any, of N-terminal folation on MMP cleavage efficiency.

The FRET switch results with M9-vis and M9-Folate-vis mirrored those of FL-Broad2-TMR and other peptides synthesized using DTT as a reducing agent. Given that thiol-based inhibition of MMP activity has been sparsely reported[118–120], synthesis of M9-Folate-vis and M9-vis was repeated employing a 1-pot reaction analogous to the synthesis of Ahx-Broad2-vis, a peptide that exhibited FRET switch upon MMP cleavage (see II.3.4). The revised synthetic route had no significant impact either on the maximum potential FRET switch with trypsin or on the relative MMP cleavability for either peptide, M9-vis or M9-Folate-vis (data not shown). Neither folate alone nor the use of DTT alone accounted for the inability of MMPs to cleave 2-color M9 peptides.

To focus on the N-terminal attachment of folic acid as a possible interferent with MMP cleavage of substrate peptides, unlabeled M9-Folate peptide was incubated with MMP9 and the resulting reaction mix analyzed by LCMS. While ions with M/z corresponding to disulfide dimers of M9-Folate peptides were found in both the MMP9-treated and control samples, the detection of ions corresponding to the expected MMP9 cleavage products of M9-Folate in the MMP9-treated sample (Figure II-15) suggests that N-terminal folation alone does not block MMP-dependent proteolysis of substrate peptides.

To obviate the sequential dye addition synthesis as a potential confounding reason for lack of MMP cleavage of FRET-equipped substrates, two peptides based on Broad2 with fluorescein and TAMRA dyes incorporated in solid phase synthesis by the manufacturer were obtained and analyzed by FRET switch assay with trypsin and MMPs (2, 9, and 14). Unfortunately, neither peptide demonstrated greater than 3-fold increase in sensor (FAM) fluorescence over 30 minutes of incubation with any enzyme. UV-visible

spectrophotometry comparing these peptides with 2-color peptides previously acquired from the same supplier revealed low absorbance by TAMRA relative to that of FAM (data not shown), suggesting that the lack of FRET switch from these peptides may have been attributable to insufficient quenching of fluorescein. A significant fraction of these particular peptide batches probably lacked the TAMRA quencher required for intramolecular FRET.

Due to the challenges and inconsistencies encountered with 2-color FRET peptides both from sequential fluorophore attachment to peptides and from completely commercially prepared peptides, I designed and synthesized a 2-color peptide using conventional Fmoc-SPPS. Taking into consideration the potential inhibition of MMP cleavage by steric hindrance and/or hydrophobic spacers discussed above, we designed a FRET-equipped, broadly MMP-cleavable substrate peptide with hydrophilic spacers based on Broad2 and PEG, peg-Broad2-vis (pB2v), as diagrammed in Figure II-16. LCMS analysis of the crude peptide mixture produced by SPPS of pB2v (Figure II-17) indicated a heterogeneous mixture, although ions with M/z indicative of the intended macromolecular structure were detected, corroborating some degree of successful pB2v synthesis by SPPS. This synthetic route was further validated by assessing the FRET switch of pB2v_2.2.1, a peptide sample purified by iterative HPLC with collection of eluted analytes. Sensor (FAM) fluorescence of pB2v_2.2.1 increased at differing rates upon incubation of pB2v_2.2.1 with trypsin, MMP2, MMP9, or MMP14, as shown in Figure II-19. The calculated relative enzyme specificities of pB2v_2.2.1 with MMPs (Table II-3), show that synthesis of FRET-equipped substrate peptides by SPPS yielded an MMP-cleavable peptide with a FRET switch sufficient for optical sensing of MMP

activity. Furthermore, SPPS of FRET-equipped peptides provides the benefit of adaptability to any desired amino acid sequence that constitutes a substrate for an enzyme of interest and could therefore prove useful in many areas of biomedical research in which proteolytic degradation plays a key role. Indeed, over 570 individual proteases have been identified in the human proteome and linked to over 114 different hereditary diseases[126]. Subsequent studies were performed with beacon peptides produced by SPPS.

CHAPTER III

SYNTHESIS AND CHARACTERIZATION OF FOLATE-CONJUGATED, FRET-EQUIPPED, MMP-CLEAVABLE LINKER PEPTIDES

III.1. INTRODUCTION

The previous chapter focused on the design of proteolytic nanobeacons and synthesis and characterization of FRET-equipped MMP substrate peptides as precursors for proteolytic nanobeacon synthesis. Importantly, it was found that attachment of FAM and TAMRA directly to the substrate peptide can lead to robust FRET switch upon proteolysis. However, this strategy can also present significant challenges in the chemistry to attach fluorophores while preserving MMP cleavability as well as ability to attach folic acid and conjugate peptides to nanoparticles. Ultimately, SPPS presented a synthesis technique that could achieve all of these aims simultaneously by incorporating FAM and TAMRA attached to the side chains of lysine residues, leaving the N-terminus and C-terminus of peptides available for reaction.

Neither attachment of dyes nor attachment of folic acid alone were found to block substrate cleavage by MMPs, yet FRET switch with a folated MMP substrate peptide cleaved by MMPs was not demonstrated above. A purified product of SPPS demonstrated sufficient FRET switch upon treatment with MMPs to optically sense MMP activity, however it represented a small fraction of the product of synthesis. As such, the scope of this chapter is two-fold. The research that follows focuses both on the optimization of SPPS techniques to produce FRET-equipped MMP substrate peptides in sufficient yields and the development of an appropriate chemical synthesis technique for

N-terminal folation of such peptides. The results below elucidate the development of a robust protocol for SPPS of folated MMP substrate peptides exhibiting FRET switch upon cleavage by MMPs and with the potential for conjugation to nanoparticles via appropriate chemical functional groups. We specifically demonstrate that a folation of a broadly MMP-cleavable peptide yields a substrate that is cleavable by MMPs, the sensor (FAM) fluorescence emission of which is amplified upon treatment with MMPs.

III.2. Materials and Methods

III.2.1. General Methods

All chemicals and biochemicals were reagent-grade or HPLC-grade and solutions were prepared in filtered deionized water (dH_2O) (Milli-Q, Billerica, MA, USA). Unless otherwise noted, all chemicals were purchased from either Sigma Aldrich (St. Louis, MO, USA) or Thermo Fisher Scientific (Waltham, MA, USA). B16-F10 mouse melanoma cells and MDA-MB-468 human breast adenocarcinoma cells were obtained from ATCC (Manassas, VA, USA). CT26 mouse colon carcinoma cells were a gift from the Pozzi Laboratory (Vanderbilt University School of Medicine, Nashville, TN, USA). R221A mouse mammary tumor cells were isolated previously by our laboratory as described elsewhere[127].

III.2.2. Chromatography and mass spectrometry

HPLC and LCMS were performed as described above (see II.2.1) unless otherwise specified. HPLC traces where chromatograms monitoring absorbance at 495 nm are shown were collected using mobile phases 50 mM phosphate buffer (pH 7.0) in HPLC-grade water (A) and HPLC-grade MeOH (B) for chromatography. Matrix-assisted laser desorption/ionization time-of-flight (MALDI-TOF) mass spectrometry was performed

using a Voyager-DE™ STR Workstation (Applied Biosystems, Foster City, CA, USA). Samples were diluted 1:1 in a saturated solution of α-Cyano-4-hydroxycinnamic acid (CHCA) in 60% MeCN with 0.1% TFA and dried as 1.0-1.5 µL spots on gold-plated MALDI plates.

III.2.3. Analysis of pB2v SPPS products by mass spectrometry

HPLC-purified product of SPPS, pB2v_2.2.1, was analyzed by LCMS and MALDI-TOF MS (1:100 dilution in dH_2O prior to dilution into CHCA solution) to determine the molecular weight of constituent chemical species. pB2v_2.2.1 was subsequently diluted in assay buffer (see section II.2.3) and treated with trypsin, MMP2, or MMP14 overnight to allow for proteolysis. 10 µL from each protolysis sample was then desalted by repeated pipetting through u-C18 ZipTip (EMD Millipore, Darmstadt, DE) and analyzed by MALDI-TOF MS.

III.2.4. Qualitative Ninhydrin assay (Kaiser test)

Resin samples for analysis were transferred to glass test tubes, washed repeatedly with EtOH and air dried. To dried resin beads, equal parts of three solutions were added: 1.4 M Ninhydrin reagent in EtOH, 21 M phenol in EtOH, and 100 µM potassium cyanide in pyridine. The resulting mixture was heated to 100 °C for 5 minutes in a stirring oil bath and visually inspected for development of blue-violet hue characteristic of formation of Ruhemann's purple in the presence of amine functional groups.

III.2.5. Troubleshooting of pB2v produced by SPPS

Monitored synthesis. SPPS of pB2v peptide was repeated as before (see II.2.11), interrupting automated synthesis to assess completeness of residue coupling by

qualitative Ninhydrin assay (III.2.4, above) at suspect coupling steps. MALDI-TOF MS and FRET switch assay with trypsin and MMPs-2,9,14 were repeated as with previously synthesized pB2v.

Mass spectrometry. Electrospray ionization quadrupole ion-mobility time-of-flight (ESI-Q-IM-TOF) mass spectrometry and MS-MS were performed on a Synapt G2 HDMS (Waters, Milford, MA, USA) by Kelly Hines of the McLean Laboratory (Vanderbilt University, Nashville, TN, USA). The crude pB2v peptide mixture from SPPS was analyzed by ESI-Q-TOF MS and MS-MS. Following separation of pB2v by analytical-scale HPLC, ESI-Q-TOF MS was repeated on recovered HPLC fractions.

NMR. Nuclear magnetic resonance (NMR) spectra were acquired by Don Stec (Small Molecule NMR Facility Core, Vanderbilt University, Nashville, TN, USA) using a 14.0 T Bruker magnet equipped with a Bruker AV-III console operating at 600.13 MHz. All spectra were acquired in 3mm NMR tubes using a Bruker 5 mm TCI cryogenically cooled NMR probe. Chemical shifts were referenced internally to D_2O (4.70 ppm) which also served as the 2H lock solvents. For 1D 1H NMR, typical experimental conditions included 32K data points, 13 ppm sweep width, a recycle delay of 1.5 seconds and 64 scans. Total Correlation Spectroscopy (TOCSY) experiments were acquired using a 2048 x 512 data matrix with a 120 ms DIPSI spinlock, 2 seconds recycle delay and 8 scans per increment. The data was processed using a $\pi/2$ shifted squared sine window function and displayed in absorption mode. J1(C-H) filtered heteronuclear multiple bond correlation (HMBC) experiments were acquired using a 2048 x 256 data matrix, a J(C-H) value of 9 Hz for detection of long range couplings resulting in an evolution delay of 55ms, J1(C-H) filter delay of 145 Hz (34 ms) for the suppression of one-bond couplings, a recycle delay

of 1.5 seconds and 128 scans per increment. The HMBC data was processed using a π/2 shifted squared sine window function and displayed in magnitude mode.

MTT assay. B16 melanoma, CT26 colon cancer, and R221A breast cancer cells were seeded at 5,000 cells per well in wells of a clear 96-well plate and allowed to adhere in Dulbecco's Modified Eagles Medium (DMEM, Life Technologies, Carlsbad, CA, USA). Unpurified pB2v peptide including the unidentified 56-Da adduct was dissolved in dH_2O to an undetermined concentration and serially diluted in DMEM to give concentrations of 100%, 33%, 10%, 3.3%, 1%, and no peptide (dH_2O and medium). Cell culture medium was aspirated from wells containing cells and replaced with medium containing the serial dilutions of peptide. After overnight incubation, fresh medium was added to cells and a standard MTT Assay protocol performed. 20 µL Methylthiazolyldiphenyl-tetrazolium bromide (MTT reagent, 5 mg/mL in dH_2O) was added to each well and incubated for 1 hour at 37 °C. Media was then aspirated from wells and replaced with 100 µL isopropyl alcohol and the absorbance of each well at 570 nm measured.

D-pB2v. Fmoc-D-amino acids were purchased from Anaspec (Fremont, CA, USA). A peptide homologous to pB2v with the exception of the inclusion of biologically inactive D-amino acids in place of L-amino acids in the cleavage sequence (RPLGWLAR) was synthesized by SPPS (method, see II.2.11). Preparation of analytical samples, MALDI-TOF MS, FRET switch assay with either trypsin or MMPs-9,14, and UV-visible spectrophotometry were carried out in parallel with pB2v (L-amino acids) as described previously (see II.2.11, II.2.3, III.2.2).

III.2.6. Synthesis and characterization of N-terminally folated MMP substrate peptides

The broadly MMP-cleavable substrate peptide, "Ahx-Moss" [{Ahx}GPLGMRGS{Ahx}C-conh$_2$], was obtained as a custom synthesis from Biomer Technologies (Pleasanton, CA, USA). pB2v peptide was synthesized by SPPS as described previously (see II.2.11, III.2.5) and remained attached to solid support resin.

DCC coupling in solution. Attachment of folic acid to the N-terminus of the peptide was first attempted by carbodiimide carboxyl-to-amine coupling. 1.2 mg (2.72 µmol) folic acid (FA) was added to the manufacturer's glass ampule containing 2 mg (1.81 µmol) Ahx-Moss peptide, followed by 70 µL dimethylsulfoxide (DMSO), 42 µL pyridine, 60 µL DMF, and a small magnetic stir bar. The ampule was then sealed and purged of atmospheric air by nitrogen gas bubbling for 15 minutes. 20 µL (3.63 µmol) dicyclohexylcarbodiimide (DCC) was injected, preserving air-free conditions, and reacted with continuous stirring for 3 days. Aliquots were removed at 0, 1, 2, and 72 hours and analyzed by HPLC.

FA-NHS coupling in solution. Succinimidyl ester of folic acid (FA-NHS) was a gift from Dr. Wellington Pham (Institute of Imaging Science, Vanderbilt University, Nashville, TN, USA). To 2 mg (1.81 µmol) Ahx-Moss peptide in the manufacturer's glass ampule were added 300 µL of buffer [50% MeCN in dH_2O adjusted to pH 7.5 using sodium carbonate (Na_2CO_3) and 1 N hydrochloric acid (HCl)] and a small magnetic stir bar. The ampule was then sealed and purged of atmospheric air by argon gas flow, maintaining positive pressure throughout addition of remaining reagents. 20 µL (495 nmol) FA-NHS in DMSO was injected and the reaction stirred at RT. At 0, 1, and 2 hours following reaction start, aliquots of reaction mix and reactants at matched concentration

were spotted on disposable plates for thin-layer chromatography (TLC). Mobile phase used for all TLC was 35% MeOH in dichloromethane (DCM) with 1% 1 N HCl. TLC spots were visualized with iodine vapor staining. After overnight stirring at RT, 100 µL (2.25 µmol) freshly-dissolved FA-NHS in DMSO was injected into the reaction mixture. Following 80 minutes further reaction, reaction mix and reactants were spotted for TLC. Due to formation of a turbid solution, 500 µL buffer was added and the entire reaction mix centrifuged to separate phases. Pelleted solute was resuspended in 100 µL DMSO and both phases analyzed by TLC and MALDI-TOF MS. Pelleted products of Ahx-Moss peptide and FA-NHS reaction were purified by semi-preparative HPLC (general method, see II.2.1) and lyophilized to yield an oily yellow solid. This recovered product was then analyzed by MALDI-TOF before and after overnight incubation with MMP9 in standard assay buffer (see II.2.3) at RT.

FA-NHS coupling on solid phase. 31.9 mg (estimated 6 µmol peptide equivalent) of pB2v peptide-resin was weighed into a 10 mL round-bottom Pyrex flask. 6.5 mg (14.7 µmol) FA-NHS, 1.0 mL DMSO, and 10 µL triethylamine (TEA) were then added to the flask and reacted overnight with stirring, protected from light. The reaction slurry was then filtered over a glass-fritted filter (Büchner funnel) and the solid peptide-resin washed thoroughly with DMF and EtOH prior to drying under vacuum. Final deprotection, cleavage from solid support, and precipitation of peptide was performed as before (see II.2.11), substituting cleavage cocktail K [82.5% TFA, 5% H_2O, 5% phenol, 5% thioanisole, 2.5% ethanedithiol (EDT)] for cocktail B. After removing trace solvents by rotary evaporation, dried crude peptide mixture was reconstituted in HPLC-grade water and analyzed by MALDI-TOF MS (general method, see III.2.2).

HCTU coupling on solid phase. 360 µL (16.7 µmol) HCTU in SPPS activator solution was combined with 360 µL (16.3 µmol) FA in NMP and vortexed 10 minutes (Note: in general, this procedure was subsequently performed with 95:100 molar equivalents HCTU:FA). 405 µL (9.2 µmol FA equivalent) of the resulting activated FA solution was added to 10 mg (1.83 µmol estimated peptide equivalent) dry pB2v peptide-resin and reacted at RT, vortexting, overnight. Folated peptide resin was washed over a glass Büchner funnel with DMF followed by EtOH, shell frozen in dH_2O, and lyophilized prior to further workup. Final deprotection, cleavage from solid support, and precipitation of folated peptide was performed as before using cleavage cocktail R (95% TFA, 5% thioanisole, 3% EDT, 2% anisole). The resulting crude FApB2v peptide mixture was shell frozen in dH_2O and lyophilized. Lyophilized peptide was reconstituted in 50% MeCN and analyzed by LCMS, purified by semi-preparative HPLC (general methods, see II.2.1), and characterized by FRET switch assay with either trypsin or MMPs-2,9,14.

III.2.7. General procedures for folation and acetylation of peptides in solid phase

Folation. Peptide-resins from SPPS were N-terminally deprotected as described previously (II.2.11), rinsed thoroughly with DMF and EtOH, and dried under vacuum. 11.4 molar equivalents HCTU in SPPS activator solution and 12 molar equivalents FA in NMP (95:100 HCTU:FA) relative to the moles of peptide N-termini (calculated from the weight of dry peptide-resin) were combined and vortexed 10 minutes. The entirety of the resulting activated FA solution was added to dry peptide-resin and reacted at RT, vortexting, overnight.

Acetylation. Peptide-resins from SPPS were N-terminally deprotected as described previously (II.2.11), rinsed thoroughly with DMF and EtOH, and dried under vacuum.

Dry peptide-resin was submerged in a solution of either [10% acetic anhydride, 10% diisopropylethylamine (DIPEA), 80% DMF] or (25% acetic anhydride, 25% pyridine, 50% NMP) and reacted with vortexing at least 1 hour to effect acetylation of peptide N-termini.

III.2.8. Synthesis and characterization of FRET peptides for oxime ligation

Fmoc-Dpr(Boc-Aoa)-OH and Fmoc-Lys(ivDDE)-OH were purchased from EMD Chemicals (Billerica, MA, USA). Synthesis of "pB2vAoa" FRET peptide [Fmoc-{peg_1}K(fam){peg_1}RPLGLWAR{peg_1}K(tamra)G{DprAoa}-$conh_2$] bearing a C-terminal aminooxy moiety for chemoselective attachment to carbonyl functional groups by oxime ligation was performed by SPPS as described previously (see II.2.11) with modifications for optimization of yield.

SPPS using K(fam). pB2vAoa was initially synthesized using a procedure analogous to pB2v (see II.2.11) with single-coupling of Fmoc-Lys(5/6-X)-OH (where X is FAM or TAMRA) mediated by HCTU (instead of PyClock) to impart K(tamra) and K(fam) in the peptide structure. Analytical samples were prepared using cleavage cocktail R (see III.2.6) to yield crude peptide mixture and were assessed by LCMS, purified by HPLC, and reassessed by LCMS.

SPPS using K(ivDDE). pB2vAoa was synthesized by an alternative route employing SPPS with a protected lysine residue followed by selective deprotection and reaction with amine-reactive FAMSE. Precursor peptide, [Fmoc-{peg_1}K(ivDDE){peg_1}RPLGLWAR{peg_1}K(tamra)G{DprAoa}-$conh_2$], was synthesized by SPPS as described above with double coupling of Fmoc-Lys(ivDDE)-OH mediated by HCTU. Analytical samples of this precursor were prepared as described

previously (see II.2.11) by cleavage and deprotection in cleavage cocktail B and assessed by HPLC and LCMS. Because the Fmoc protecting group is labile in the conditions required to remove the ivDDE protecting group (but not *vice versa*), the precursor peptide on resin (approximately 25 µmol peptide equivalent) was also N-terminally folated or acetylated (general procedure, see III.2.7, above) and examined by LCMS prior to proceeding to FAM attachment. Folated precursor peptide on resin was subsequently deprotected by three repetitions of submersion in 2% hydrazine solution in DMF, standing for 3 minutes, and removal of supernatant to effect removal of ivDDE from the side chain of lysine (confirmed by qualitative Ninhydrin assay, see III.2.4). 2.87 mL (60 µmol) FAMSE in DMF was added to the resin and allowed to react overnight at RT with shaking, protected from light. After removing the supernatant, the resin sample was rinsed repeatedly with DMF followed by EtOH and dried under vacuum. Cleavage cocktail B (II.2.11) was applied to generate analytical samples of crude "FApB2vAoa" peptide [fa{peg$_1$}K(fam){peg$_1$}RPLGLWAR{peg$_1$}K(tamra)G{DprAoa}-conh$_2$] mixture for subsequent analysis by LCMS and spectrophotometry.

SPPS using triple-coupling. pB2vAoa was synthesized using a procedure analogous to pB2v (see II.2.11) with triple-coupling of the second introduced arginine (N-terminal to MMP cleavage site) and triple-coupling of Fmoc-Lys(5/6-FAM)-OH with 2 molar equivalents relative to peptide N-termini per coupling, with all couplings mediated by HCTU. Final deprotection and cleavage from solid support resin was performed according to general procedures (II.2.11) using cleavage cocktail R (III.2.6). Crude peptide mixture was purified by analytical scale HPLC and subsequently characterized by

LCMS and FRET switch assay with trypsin and MMPs-9,14 (see general methods, II.2.3 and III.2.2).

FApB2vAoa. pB2vAoa on resin (from triple-coupling technique) was N-terminally deprotected, folated (see III.2.7), and cleaved from resin with cleavage cocktail R to yield FApB2vAoa which was then characterized by LCMS and FRET switch assay with trypsin and MMP14 with and without inclusion of EDTA. FApB2vAoa was also purified by analytical-scale HPLC and recovered fractions again analyzed by LCMS.

AcpB2vAoa. pB2vAoa on resin (from triple-coupling technique) was N-terminally deprotected, acetylated (see III.2.7), and cleaved from resin with cleavage cocktail R to yield AcpB2vAoa peptide [Ac{peg$_1$}K(fam){peg$_1$}RPLGLWAR{peg$_1$}K(tamra)G{DprAoa}-conh$_2$]. AcpB2vAoa was similarly purified by analytical-scale HPLC and purified fractions analyzed by LCMS and FRET switch assay with MMPs-2,9,14 with and without inclusion of EDTA.

III.2.9. Validation of FRET peptide function with endogenous MMPs in vitro

Unpurified AcpB2vAoa FRET peptide was incubated with a human metastatic breast cancer cell line, MDA-MB-468, in the presence or absence of GM6001 broad-spectrum MMP inhibitor. Briefly, MDA-MB-468 cells were seeded at approximately 250,000 cells per well of 6-well plastic tissue culture plates in RPMI1640 medium and allowed to expand for 18 hours. Lyophilized AcpB2vAoa crude peptide mixture (from SPPS triple-coupling method) was reconstituted in DMF to a concentration of 10 mg/mL (3.92 mM, validated by spectrophotometry using empirically determined extinction of TAMRA dye, data not shown). Media containing approximately 5 µM AcpB2vAoa or DMF (sham) and approximately 10 µM GM6001 or DMSO (sham) were added to assigned wells of the

tissue culture dish. At several intervals following medium additions, aliquots of conditioned media were removed and diluted with equal volumes fresh medium containing EDTA to prevent further metalloproteinase activity. The sensor (FAM) fluorescence of all samples was measured simultaneously at the endpoint (24 hours) by plate reader assay.

III.3. RESULTS

III.3.1. Analysis of peg-Broad2-vis (SPPS products) by mass spectrometry

To confirm successful synthesis and characterize yields, the products of SPPS of pB2v peptide were purified by semi-preparative HPLC (Figure II-18) and analyzed by LCMS. While LCMS confirmed the presence of ions with M/z corresponding to the intended structure of pB2v, it also revealed that multiple chemical species were present in recovered products (Figure III-1a). The most abundant peak contained ions with M/z corresponding to multiple charge states of a parent ion with a mass of 1940 Da (Figure III-1b) that was smaller than the expected mass of pB2v (2354 Da). MALDI-TOF MS was performed to corroborate LCMS results with pB2v_2.2.1 wherein the most abundantly detected ions had M/z values of approximately 1941 and 2438 (Figure III-1c), indicating that the sample included a second unidentified product larger than the intended peptide.

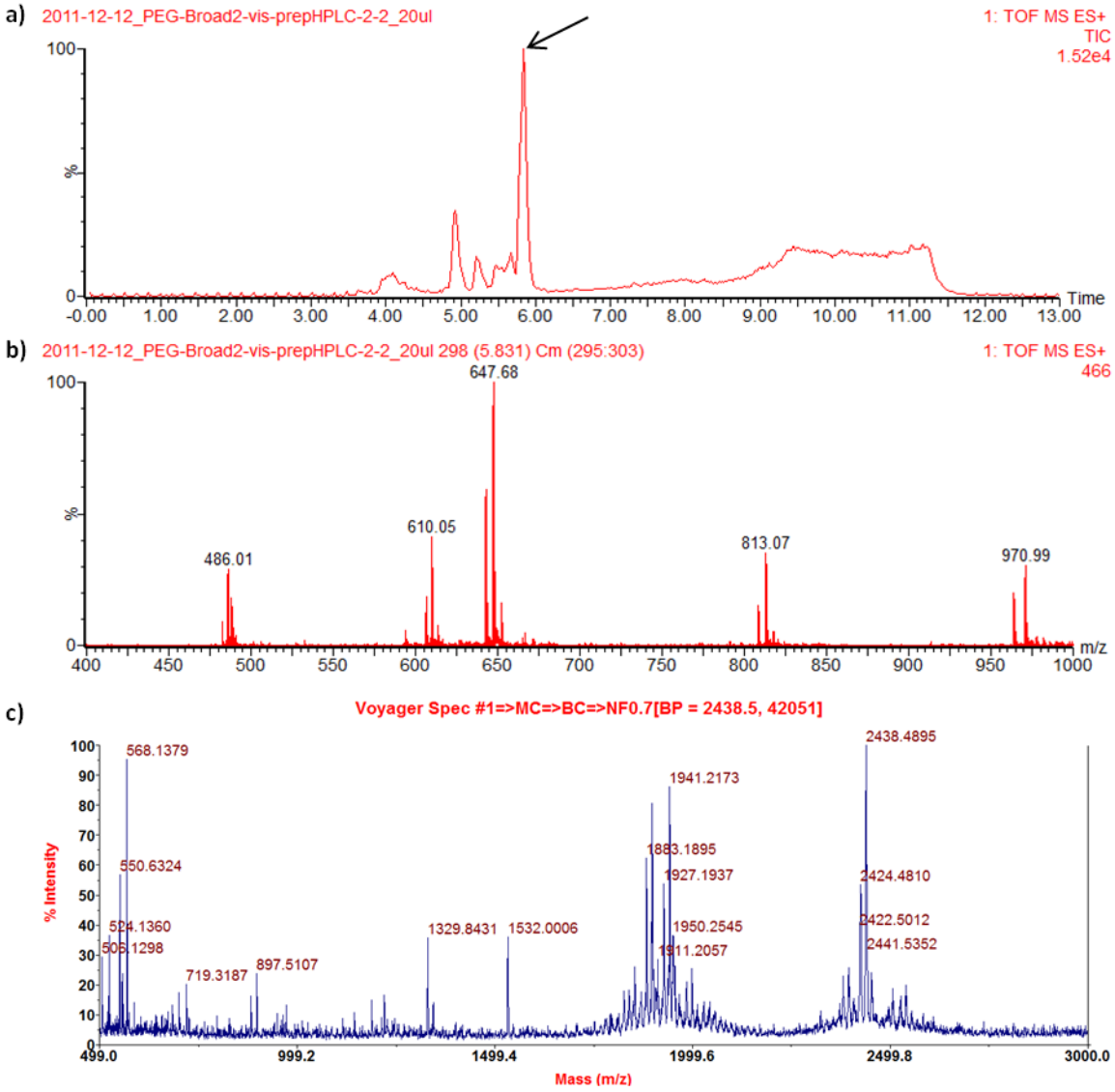

Figure III-1: **Mass spectrometry analysis of purified pB2v_2.2**
Chromatogram (a) represents total ion counts in ESI+ mode following reversed-phase liquid chromatography of pB2v sample collected from iterative HPLC separation. Mass spectrum (b) represents the integration of the most abundant peak, indicated by a black arrow in (a). Detected peaks (486, 647, 970 M/z) correspond to multiply charged states of a parent ion with mass ~1940 Da, as depicted in MALDI-TOF mass spectrum (c).

To aid in identification of the majority products in pB2v_2.2.1 with unexpected MW, pB2v_2.2.1 was incubated with trypsin, MMP9, or MMP14 to proteolytically cleave peptides and the resulting mixtures were analyzed by MALDI-TOF MS. Analysis of a buffer-only sample confirmed the presence of one of the previously detected ions with

M/z of 2438. In all samples containing proteolytic enzymes, ions with M/z corresponding to intact forms of the previously detected species were not detected (Figure III-2b-d). MMP-treated samples had in common an ion with M/z of 1144.9, corresponding to an unpredicted, unidentified cleavage fragment. In all, proteolysis of the peptide products contained in pB2v_2.2.1 was confirmed, however a predicted chemical structure was not corroborated.

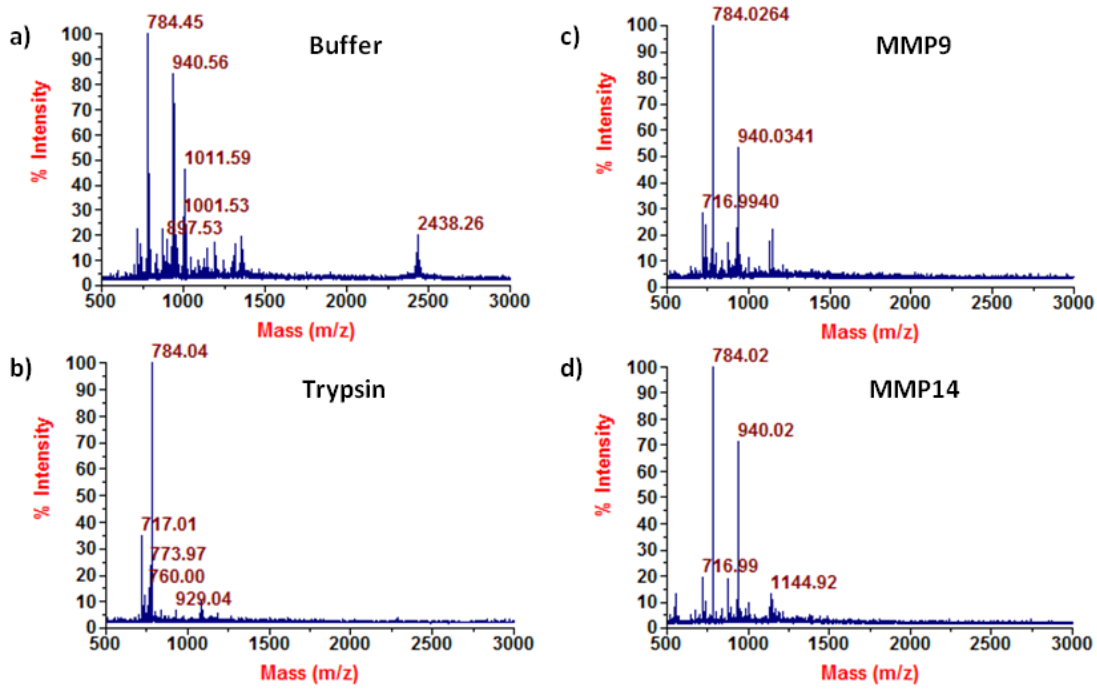

Figure III-2: MALDI-TOF MS of cleaved pB2v_2.2.1 peptide
Enzymatic cleavage fragments of purified pB2v peptide (pB2v_2.2.1) were analyzed by MALDI-TOF MS following incubation with buffer (a), trypsin (b), MMP9 (c), or MMP14 (d) and desalting.

III.3.2. Investigation of unidentified products of SPPS

Because SPPS of pB2v yielded MMP-cleavable substrates with measurable FRET switch but initial synthesis yielded mostly unidentified products, pB2v was synthesized again by SPPS with the inclusion of checkpoints at residues suspected to couple inefficiently. Qualitative Ninhydrin testing of peptides on solid support resin at these

checkpoints indicated the presence of available amines following attempted couplings of the C-terminal Fmoc-PEG_1-CH_2COOH residue and Fmoc-Lys(5/6-FAM)-OH (Figure III-3).

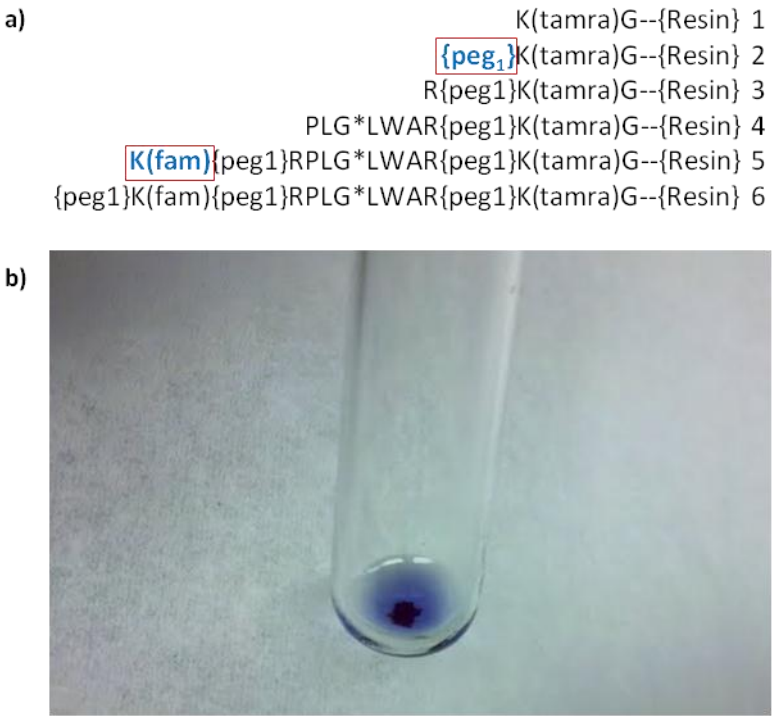

Figure III-3: Resynthesis of pB2v with Ninhydrin analysis of suspect couplings
Growing peptides on resin were sampled after 6 selected couplings (a) during the synthesis of pB2v. Highlighted couplings gave positive qualitative results by Ninhydrin test as depicted in (b).

Following final deprotection and cleavage from the solid support, crude pB2v peptide mixture was analyzed by MALDI-TOF MS. The majority products detected possessed M/z of 1925 and 2412, corresponding to parent ions with masses of 1924 Da and 2411 Da, respectively (Figure III-4). These findings corroborated the qualitative results of Ninhydrin testing during SPPS (above), as the masses observed correspond to either the intact pB2v structure with a 56 Da adduct (2411 Da) or a structure omitting the FAM-bearing lysine residue, also with a 56 Da adduct (1924 Da). The peptide mixture was

desalted and analyzed by LCMS that confirmed the presence of products with the same MW (data not shown).

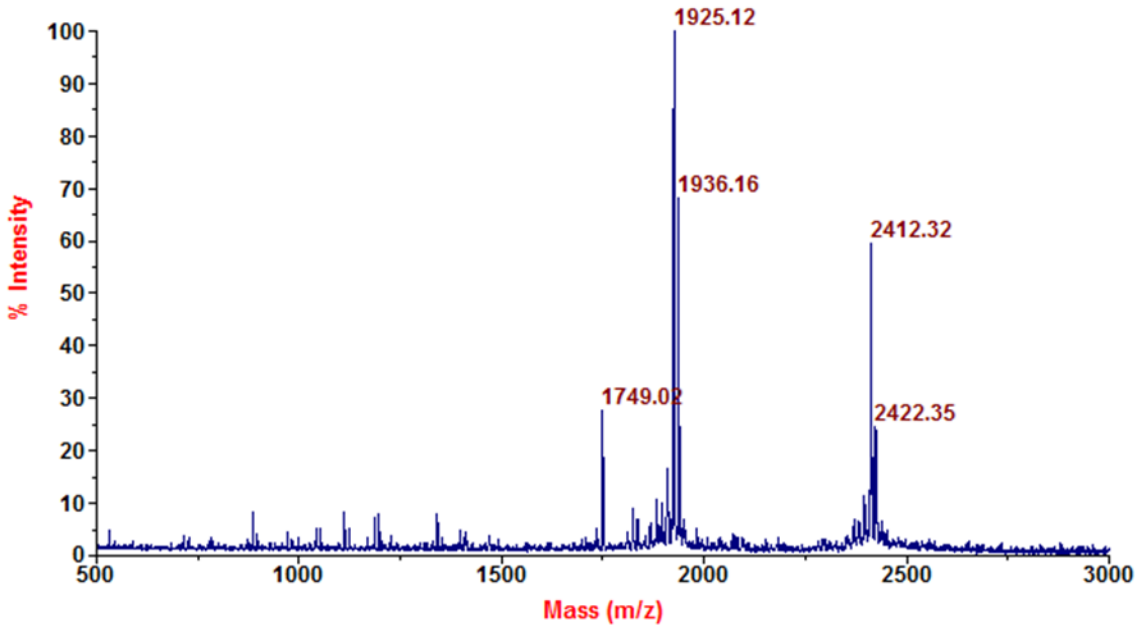

Figure III-4: MALDI-TOF MS of resynthesized pB2v peptide

To confirm MMP-cleavability and FRET switch potential, crude pB2v peptide mixture was incubated with either trypsin or MMPs (2, 9, or 14) with monitoring of sensor fluorescence, as before (see II.3.6). Similar to the previously synthesized batch of pB2v, sensor fluorescence intensity of the crude mixture rapidly increased within a 10-20 minutes of exposure to each proteolytic enzyme and continued to increase up to 110 minutes (Figure III-5), confirming the inclusion of the FAM-bearing lysine residue in some proportion.

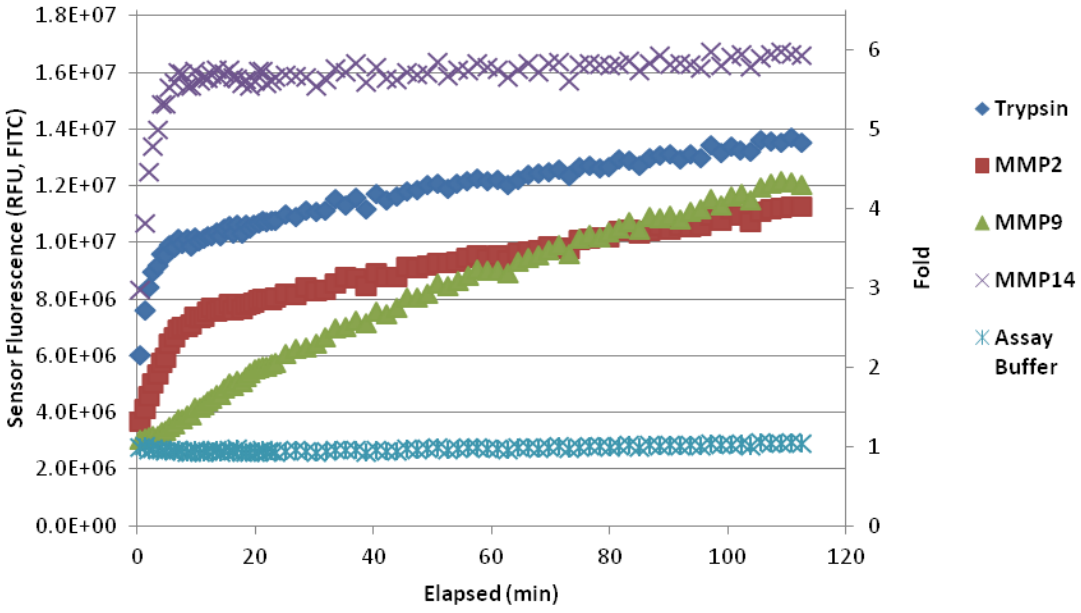

Figure III-5: **FRET switch of resynthesized pB2v peptide with MMPs**
Sensor (FAM) fluorescence emission of pB2v peptide from SPPS increased upon treatment with proteolytic enzymes. Fold indicates increase over initial fluorescence intensity of control sample. Values represent single measurements.

To confirm the biological relevance of pB2v cleavability by MMPs and to provide a non-cleavable control for biological experiments, a peptide with amino acid sequence identical to pB2v but substituting D-amino acids for all conventional L-amino acids ("D-pB2v") was synthesized by SPPS. MALDI-TOF MS analysis of crude D-pB2v peptide mixture following final deprotection and detachment from solid support in cleavage cocktail confirmed the same majority product masses (1924 Da, 2411 Da) detected from SPPS of (L-)pB2v (data not shown). A FRET switch assay was performed comparing (L-)pB2v and D-pB2v in the presence of trypsin or MMPs (9 or 14). Similar to previous observations, sensor fluorescence of (L-)pB2v increased rapidly over several minutes with either trypsin or MMP14, whereas there was no concordant increase in sensor fluorescence of D-pB2v with any enzyme (Figure III-6).

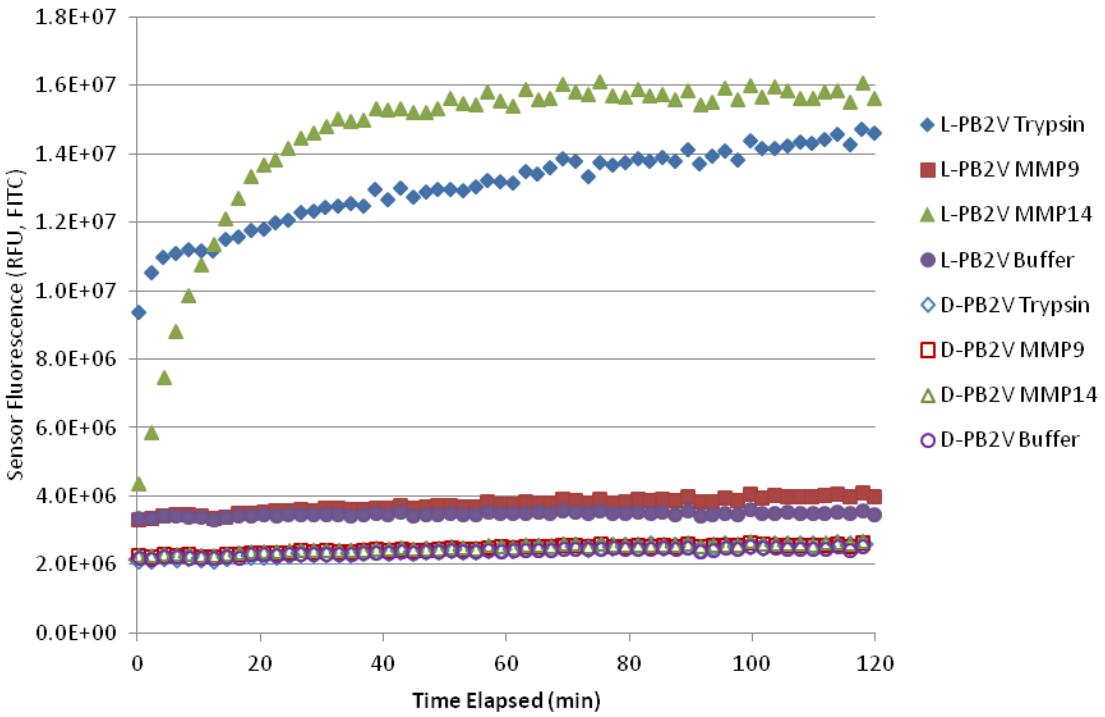

Figure III-6: **FRET switch assay of D-pB2v versus L-pB2v peptides**
Sensor (FAM) fluorescence of pB2v peptides synthesized by SPPS with either L-amino acids or D-amino acids upon incubation with proteolytic enzymes. Values represent average of duplicates.

To ensure that D-pB2v lacked a FRET switch not because of a lack of fluorophore inclusion but because of inability of biological enzymes to proteolytically cleave it, the UV-visible absorbances of D-pB2v and (L-)pB2v were compared by spectrophotometry. Both peptides exhibited absorbance spectra characteristic of FAM and TAMRA dye inclusion, as shown in Figure III-7. The lower FAM absorption relative to TAMRA absorption in (L)-pB2v was indicative of inefficient coupling of the K(fam) residue during SPPS. On the other hand, the relatively equal peak heights in the spectrum of D-pB2v confirms the inclusion of both dyes and suggests that D-pB2v was not cleaved in the FRET switch assay (Figure III-6) by proteinases specific for L-amino acids.

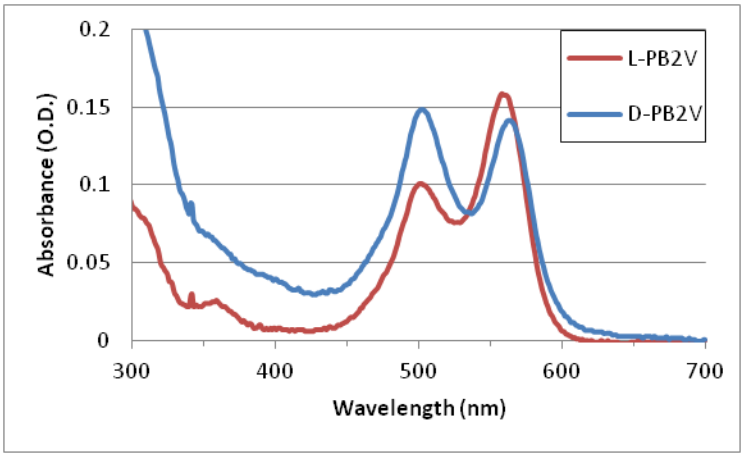

Figure III-7: Absorbance of pB2v peptides from SPPS
UV-vis absorbance spectra of pB2v vis peptides synthesized with either l-amino acids (blue) or d-amino acids (red) in SPPS. Peaks at 495 nm and 560 nm correspond to characteristic absorbance maxima of FAM and TAMRA dyes, respectively.

In order to further characterize the constituent chemical species produced by the repeated SPPS of pB2v and to troubleshoot the apparent chemical adduct, crude pB2v peptide mixture was desalted and analyzed by ESI-Q-IM-TOF MS by Kelly Hines of the McLean Laboratory (Dept. of Chemistry, Vanderbilt University). As seen in Figure III-8, the mass spectrometer detected ions with M/z representative of multiple charge states of pB2v peptide structures inclusive and exclusive of K(fam), each with and without a 56 Da addition, corroborating the previous findings from MALDI-TOF MS (Figure III-4) and LCMS but also confirming the presence of the intended pB2v structure without the adduct.

a)

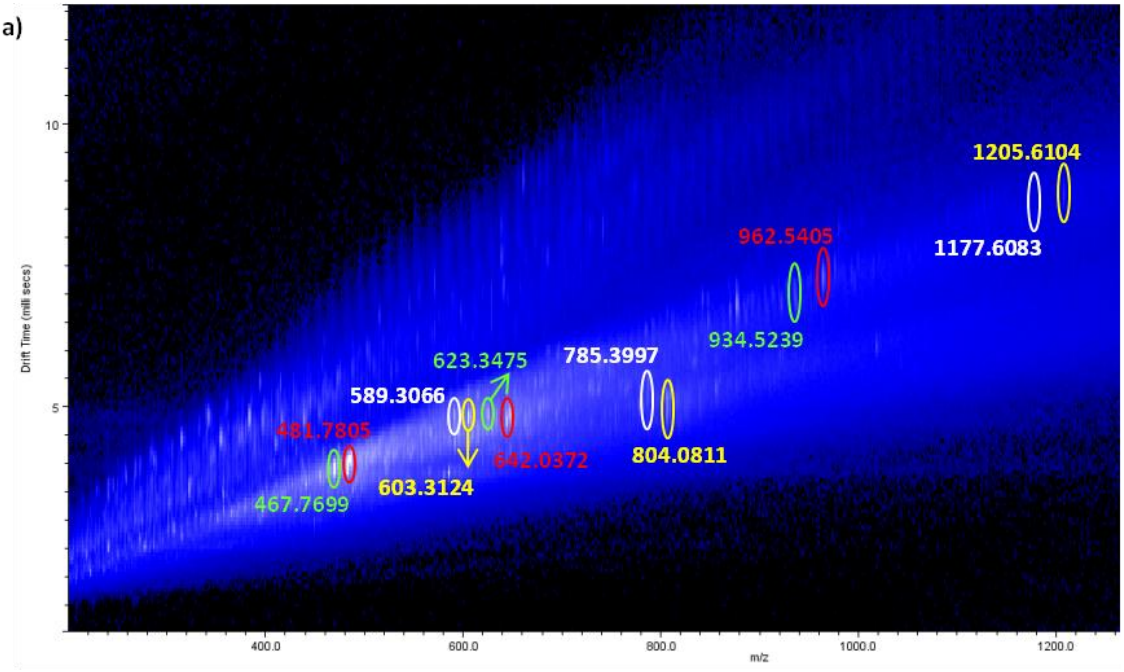

b)

Charge State	Peptide	Peptide+56	Peptide-k(fam)	Peptide-k(fam)+56
+1	2354.1398	2410.1320	1867.9971	1923.9971
+2	1177.5738	1205.5699	934.3376	962.4986
+3	785.3852	804.0492	623.3376	641.9990
+4	589.2908	603.2889	467.7552	481.7493
+5	471.6342	482.8326	374.4057	385.5994

Figure III-8: ESI-Q-IM-TOF MS of pB2v
Masses of detected ions in ESI-Q-IM-TOF MS of pB2v (a) are encircled and color coded to correspond with the table of expected M/z for each chemical species and charge state (b). Data and figure courtesy of Kelly Hines of the McLean Laboratory in the Department of Chemistry at Vanderbilt University.

Because mass spectrometry indicated the presence of the intact structure of pB2v in an unknown proportion in the crude peptide mixture from SPPS, analytical-scale HPLC with collection of detection peak fractions was performed to determine whether the products of SPPS could be separated and identified. Eluents were monitored for absorbance at 280 nm and 550 nm (representative of tryptophan and TAMRA peak

absorbance, respectively) to automate collection of four eluted chemical species (Figure III-9).

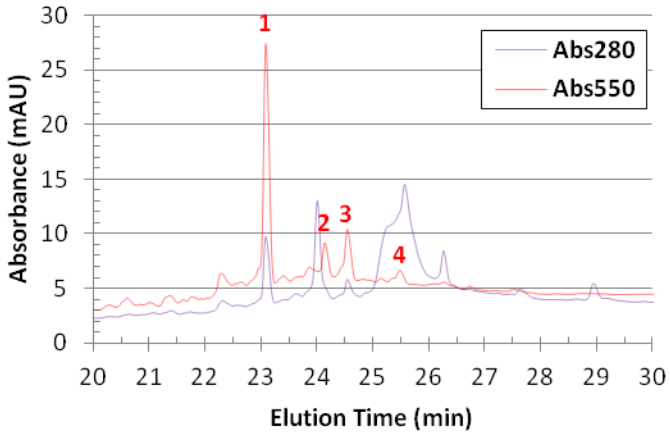

Figure III-9: HPLC separation of pB2v
Crude pB2v peptide from SPPS was separated by analytical-scale HPLC. Material peaks collected during analyte elution indicated by red numerals.

The separated products collected from HPLC of pB2v crude peptide were analyzed separately by ESI-Q-IM-TOF MS to determine the identities of chemical species contained therein. The four products previously identified by mass spectrometry were partially resolved by HPLC separation, as indicated in Table III-1, below. The most intense MS signal in the sample collected from the most abundant HPLC peak (Peak 1 in Figure III-9, above) corresponded to the peptide product omitting K(fam), with some signal also representative of the same chemical structure with the additional 56 Da adduct (data not shown). Each of the other three samples similarly contained ions corresponding to two of the previously identified products of SPPS, with one signal being greater than the other. These results confirmed attachment of the adduct to some portion of the products and /or absence of K(fam) and partial separation of these products by chromatography.

Table III-1: Detected chemical species in ESI-Q-IM-TOF MS of pB2v HPLC Fractions

HPLC Fraction	-K(fam)	-K(Fam)+56	Expected	Expected+56
1	++	+		
2	+	++		
3			++	+
4			+	++

The specific site of attachment of the 56 Da adduct was interrogated by reassessing the desalted crude pB2v peptide mixture with fragmenting ESI-Q-IM-TOF MS-MS. Interestingly, Figure III-10 shows that the detectable ions with a 56 Da addition included expected fragments of pB2v as short as a peptide composed of only the four C-terminal residues of pB2v [h_2n-{peg_1}K(tamra)G-$conh_2$ (+56 Da)].

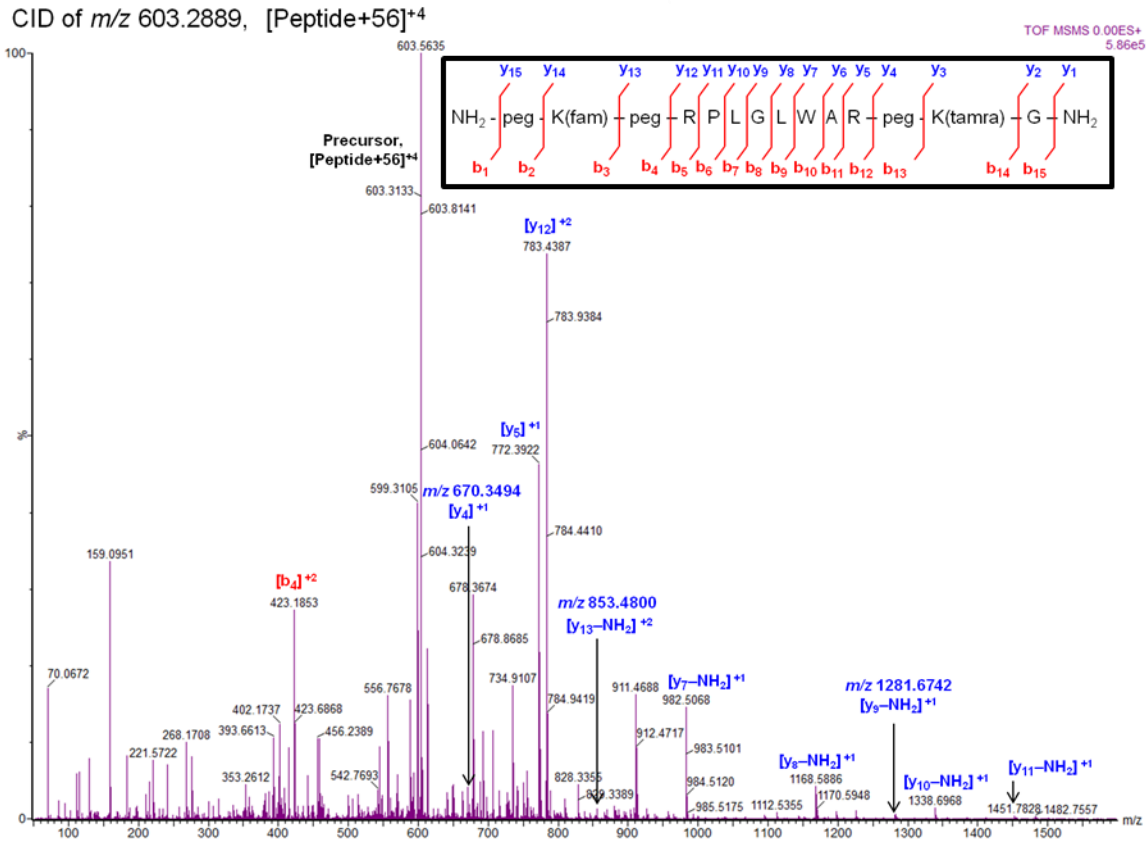

Figure III-10: Fragmenting ESI-Q-TOF MS-MS of pB2v peptide
Detected C-terminal (red) and N-terminal fragments of pB2v peptide from SPPS are overlaid on mass spectrum of detected ions. Inset: schematic indicating nomenclature of detected fragments. Data and figure courtesy of Kelly Hines of the McLean Laboratory in the Department of Chemistry at Vanderbilt University.

To investigate the chemical structure of the 56 Da adduct repeatedly detected in products of SPPS by mass spectrometry, 2D NMR experiments correlating protons with other protons separated by as many as three bonds (TOCSY) and correlating protons with carbon atoms (HMBC) were performed by Don Stec of the Small Molecule NMR Facility Core at Vanderbilt University. TOCSY detected four groups of unique methyl peaks correlating with branched alkyl structures, two of which are represented in the expected structure of pB2v and two of which are not (Figure III-11a). HMBC also indicated a proton-carbon correlation not accounted for in the expected structure of pB2v (Figure III-11b). While the molecular weight of the adduct detected by MS and the NMR spectra jointly corroborated the structure of a t-butyl attachment to pB2v, neither MS nor the NMR correlation spectra definitively identified its structure or intramolecular site of attachment.

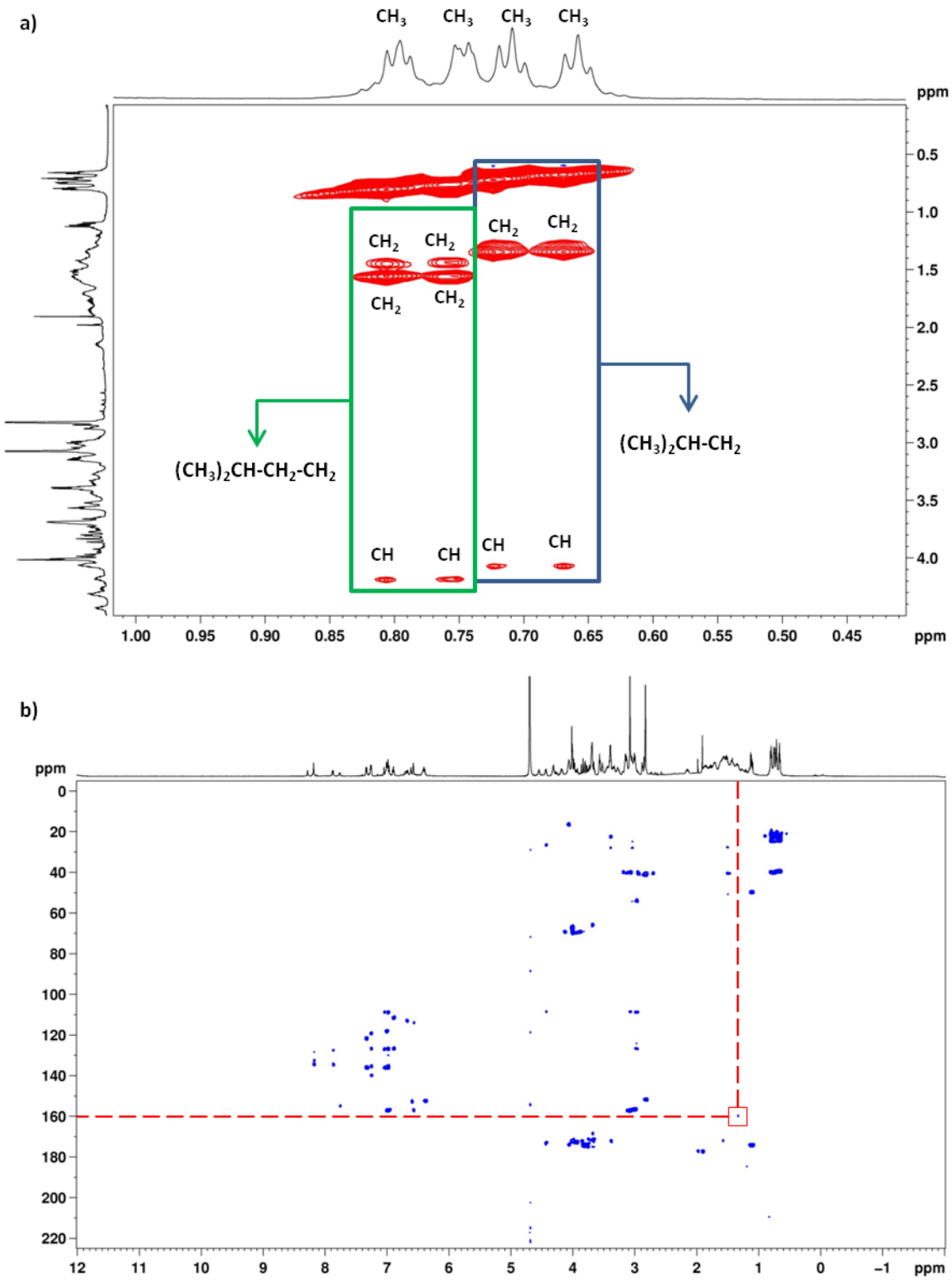

Figure III-11: 2D-NMR Spectra of pB2v peptide
TOCSY (a) and HMBC (b) 2D-NMR spectra of pB2v peptide. Correlating peaks either corresponding (boxed, blue) or not corresponding (boxed, green) to the expected molecular structure are indicated in (a). Red box and dashed lines in (b) indicate HMBC correlation not accounted for in expected peptide structure.

Because the above analyses corroborated the postulate that the adduct could be caused by the release of t-butyl cations from Boc and other protecting groups during final peptide deprotection, a common occurrence in SPPS[128], several strategies designed to mitigate t-butyl release and/or attachment were attempted. Protection of pB2v amino acid residues with trityl chloride or selective removal of Boc protecting groups by treatment of peptide-resin with bismuth (III) trichloride (confirmed successful by qualitative Ninhydrin test) prior to TFA-based deprotection and cleavage from resin were performed. Final deprotection and detachment of pB2v peptide from solid phase resin was performed in cleavage cocktail K and cleavage cocktail R (see III.2.5). Crude pB2v peptide mixture was treated with formic acid to remove t-butyl groups and reprecipitated in Et_2O. Unfortunately, none of the above processes eliminated the presence of the adduct in analytical samples. Analysis by ESI-Q-IM-TOF, LCMS, and/or MALDI-TOF MS reproduced earlier results, indicating similar relative abundance of the unidentified 56 Da adduct (data not shown).

With the aid of Jenn Duan, an undergraduate student in the Dept. of Biomedical Engineering at Vanderbilt University, a short peptide representative of the C-terminus of pB2v [h_2n-WAR{peg_1}KG-$conh_2$] was synthesized and confirmed to possess a 56 Da adduct by LCMS (data not shown). 2D NMR analysis of this simpler structure was attempted as with full-length pB2v above, but provided no further insights as to the identity and attachment site of the adduct (data not shown).

To determine whether pB2v peptide including the unidentified 56 Da would be toxic to cells, as might be the case for TFA-derived salts, an MTT viability assay with three mouse cancer cell lines was performed following overnight incubation with pB2v (+56

Da) crude peptide mixture at concentrations covering a range of two orders of magnitude. While the different cell lines metabolized MTT reagent at slightly different rates, there were no significant changes in cell viability with changes in peptide concentration (Figure III-12).

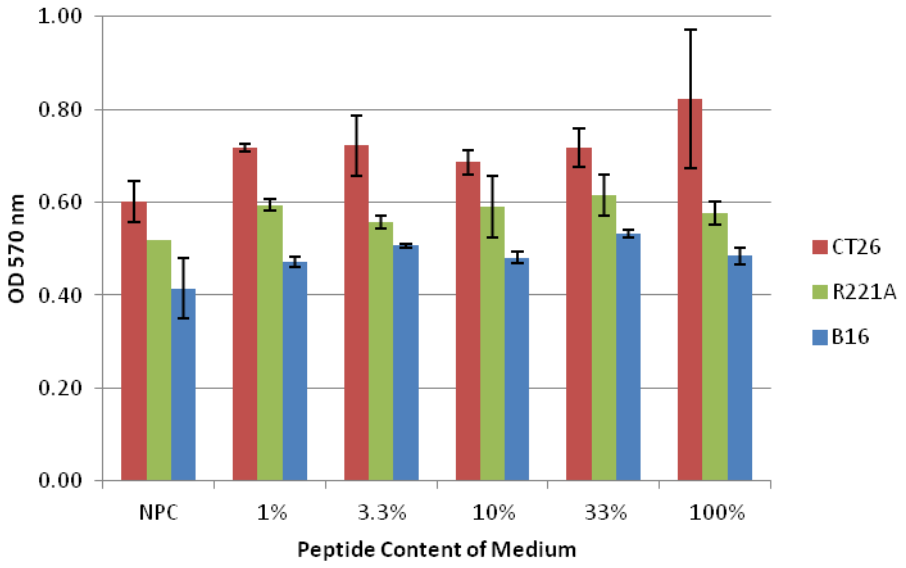

Figure III-12: MTT assay of mouse cell lines incubated with pB2v(+56) peptide
Percentages reflect serial dilution to establish concentration range from medium containing peptide at undetermined absolute concentration. NPC sample represents medium alone with no peptide. Values represent average of duplicates. Error bars: standard deviation.

III.3.3. Development of a protocol for N-terminal folation of peptides

In the analyses above, the feasibility of producing MMP-cleavable peptides endowed with measurable FRET switch potential by SPPS was confirmed despite the unintended inclusion of an unidentified, non-toxic 56 Da chemical adduct. To move forward the synthesis of dual-targeted constructs, several strategies were tested to facilitate and optimize N-terminal attachment of folic acid to peptides.

Because the chemical structure of folic acid presents two carboxylic acid function groups in an orientation favorable for preserving ligand function following conjugation,

the commonly used technique of carbodiimide-mediated amide bond formation with primary amines was attempted using DCC as a reactant to form amine-reactive intermediates with folic acid. A commercially-sourced, broadly MMP-cleavable substrate peptide [h_2n-{Ahx}GPLGMRGS{Ahx}C-conh$_2$] was reacted with folic acid and DCC overnight with monitoring by HPLC (data not shown), as schematically diagrammed in Figure III-13. After overnight reaction, the reaction mix was compared with unreacted peptide by gel permeation chromatography (GPC). Unfortunately, distinctive shifts in GPC peaks detected by the in-line refractive index detector were not observed, therefore successful attachment of folic acid to peptides was not confirmed.

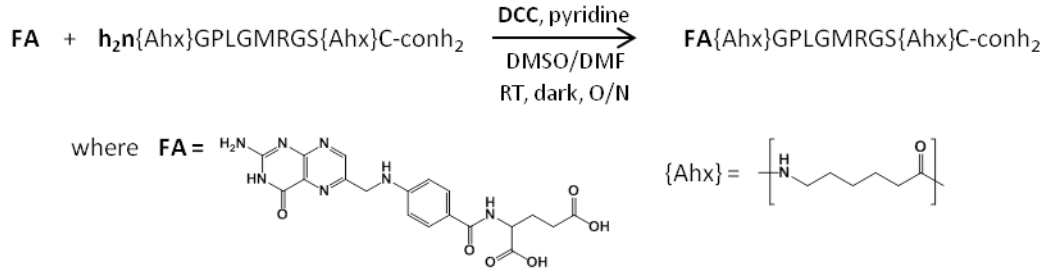

Figure III-13: Scheme, synthesis of folated peptide by DCC coupling
A known-cleavable MMP peptide substrate was reacted with folic acid and DCC to effect carboxyl-to-amine amide bonding.

A second strategy for N-terminal folation of peptides relied on the well-known reactivity of succinimidyl esters with primary amines[129]. Succinimidyl ester of folic acid (FA-NHS) was provided by Dr. Wellington Pham in the Vanderbilt Institute of Imaging Science. Dr. Pham oversaw the reaction of FA-NHS with aforementioned peptide (above) in buffered solution (diagrammed in Figure III-14) as well as development of a method to monitor the reaction by TLC.

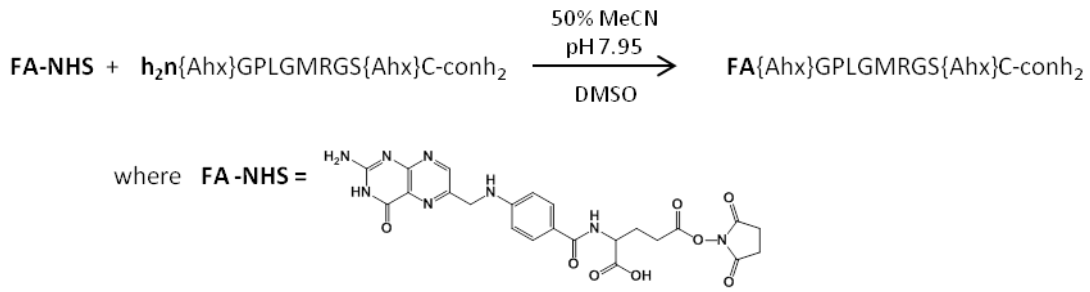

Figure III-14: Scheme, synthesis of folated peptide by NHS-ester of folic acid

TLC monitoring of the amide-forming reaction was begun with FA-NHS as the limiting reactant and analyzed immediately following reaction start. Iodine staining of the chromatographically separated reaction mix indicated a reduction in the intensity of the spot representing FA-NHS reactant (Figure III-15a). After 1 hour of reaction, reaction mix appeared to contain a diminished though still observable amount of FA-NHS, although the two spots representative of peptide remained indistinguishable from peptide reactant alone (Figure III-15b). The same pattern was observed following 2 hours of reaction with a slight reduction observed in the intensity of peptide-associated spots in the reaction mix sample (Figure III-15c). As such, the reaction was allowed to proceed overnight, then excess FA-NHS was added to the reaction mix and analyzed by TLC after 80 minutes further reaction. As seen in Figure III-15d, the spot associated with FA-NHS was apparent in this reaction mix sample while one of the two peptide-associated spots was not observable. Because precipitates formed as reaction of peptide with excess FA-NHS proceeded, the precipitate and supernatant phases were separated by centrifugation and reassessed separately by TLC. One immobile and one FA-NHS-associated spot appeared in the supernatant sample, whereas the pellet sample appeared to contain only one spot that was immobile in the TLC conditions used (Figure III-15e).

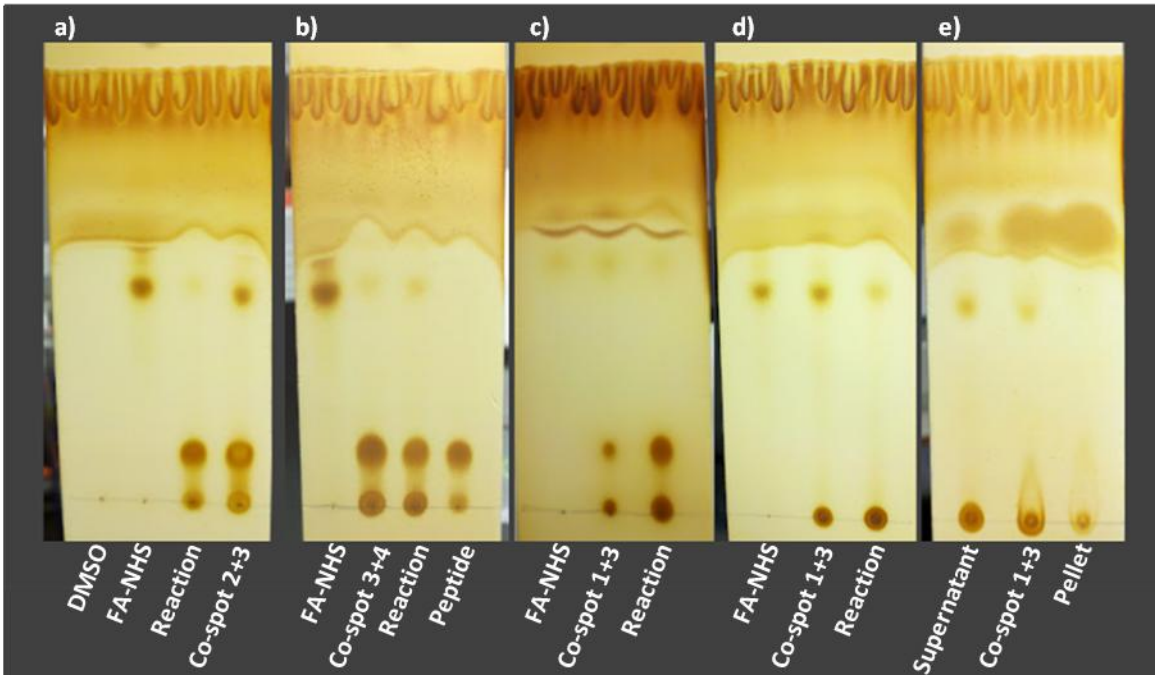

Figure III-15: Thin layer chromatography tracking folation of peptide by FA-NHS
Peptide with sequence {Ahx}GPLGMRGS{Ahx}C-conh$_2$ was reacted with limiting FA-NHS and analyzed at 0 (a), 1 (b), and 2 (c) hours following reaction start. Excess FA-NHS was subsequently added to the reaction mix (d). Precipitates formed during reaction were separated by centrifugation and each phase reanalyzed (e).

The pelleted components of the reaction mix were analyzed by MALDI-TOF MS to characterize the chemical species contained therein. As seen in Figure III-16a, the prevalent ions detected corresponded to four predicted chemical structures: unreacted peptide, a disulfide dimer of the starting peptide, folated peptide, or (singly) folated disulfide dimer (molecular weights tabulated in Figure III-16b).

a)

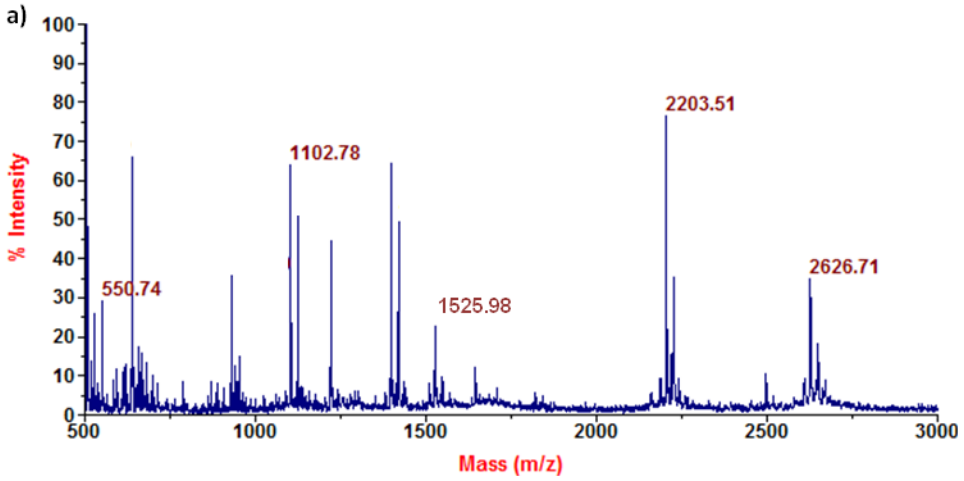

b)

Species	Expected MW	Detected MW
Peptide	1102.4	1102.78
Peptide Dimer (S-S)	2203.2	2203.51
FA-Peptide	1525.8	1525.98
FA-Peptide Dimer (S-S)	2626.3	2626.71

Figure III-16: MALDI-TOF MS of pelleted FA-peptide reaction mix
Mass spectrum (a) from MALDI-TOF MS analysis of pelleted precipitates of reaction between FA-NHS and {Ahx}GPLGMRGS{Ahx}C-conh$_2$ peptide. Labeled peaks correspond to masses of folated and non-reacted peptides as well as disulfide-dimerized analogues of each (b).

The pelleted products of peptide and FA-NHS reaction were subsequently purified by semi-preparative HPLC. TLC analysis of purified material indicated a chemical structure with composition distinct from reactants (either FA-NHS or peptide, data not shown). Purified material was then incubated with MMP9 to determine whether or not attachment of folic acid using succinimidyl ester chemistry would interfere with proteolytic cleavage. As Figure III-17 shows, MALDI-TOF analysis of the incubation mixture detected ions representative of both folated and non-folated N-terminal products of MMP9 peptide cleavage as well as singular and disulfide dimerized C-terminal products of MMP9 pepitde cleavage (predicted molecular weights in inset), but very little if any signal

corresponding to intact peptides. These results confirmed near-complete proteolysis of folated peptide by MMP and corroborated previous findings that non-folated peptides remained after reaction with excess FA-NHS.

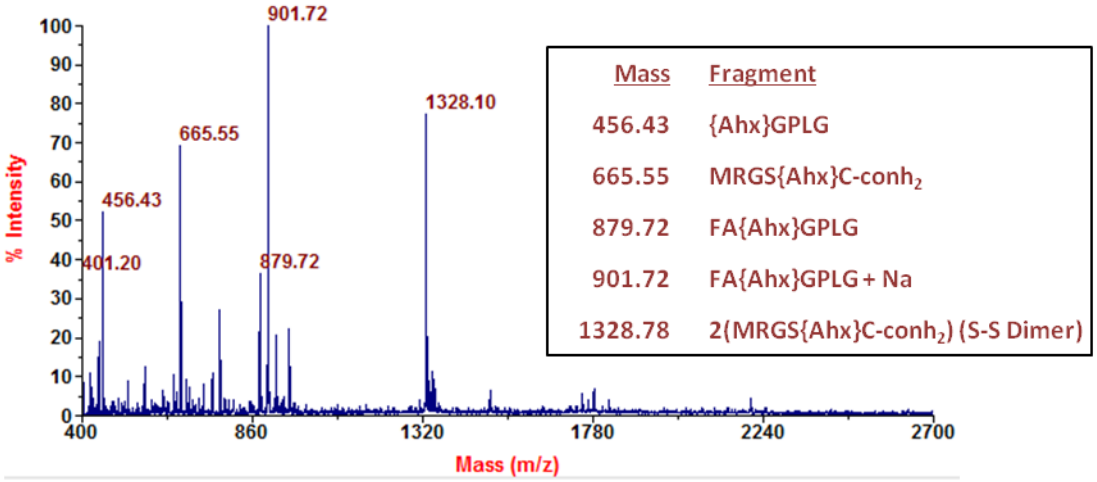

Figure III-17: MALDI-TOF MS of folated, MMP9-cleaved peptide
HPLC-purified product of peptide folation by FA-NHS was incubated with MMP9 and the proteolytic cleavage fragments thereof analyzed by MALDI-TOF MS. Labeled mass peaks correspond to molecular weights (inset) of expected MMP cleavage fragments.

To provide flexibility in the design and modification of peptides produced by Fmoc-protected SPPS, it was desirable to folate peptides on resin as part of solid phase synthesis. Given the above evidence of at least partial yield of folated peptides from succinimidyl ester reaction with peptide N-termini in solution, folation of pB2v on solid support resin was attempted using FA-NHS. Subsequent analysis by MALDI-TOF MS and analytical HPLC provided no evidence of successful folic acid attachment to pB2v under these conditions (data not shown).

Due to the demonstration of incomplete folation in the presence of excess reactant and lack of evidence for folation in solid phase using FA-NHS, a strategy adapting the coupling reagent used in each coupling of automated SPPS to couple folic acid in solid phase was tried. As schematically diagrammed in Figure III-18, folic acid was reacted

with HCTU to form amine-reactive intermediates and applied to N-terminally deprotected pB2v peptide on resin to generate "FApB2v" peptide [fa-{peg$_1$}K(fam){peg$_1$}RPLGLWAR{peg$_1$}K(tamra)G-conh$_2$] on resin.

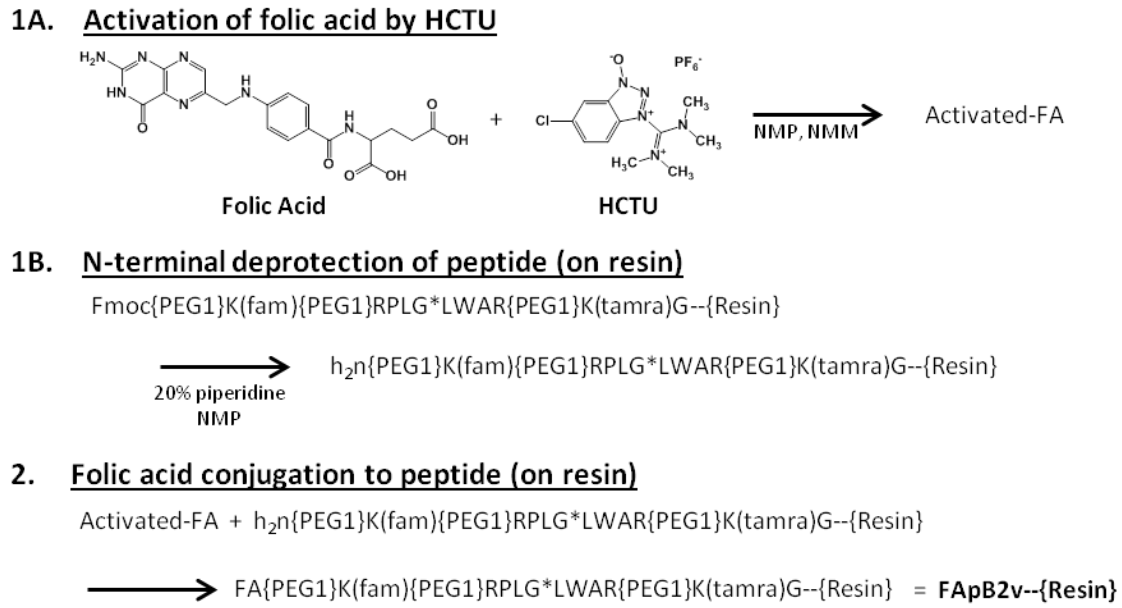

Figure III-18: Scheme, synthesis of folated peptide in solid phase using HCTU activator

FApB2v peptide was simultaneously deprotected and detached from solid support in cleavage cocktail R using conditions similar to those used for pB2v (see III.2.5), and the resulting crude peptide mixture analyzed by LCMS. The majority of detectable ions were represented by two partially-resolved majority peaks, as depicted in Figure III-19a. The integrated mass spectrum of the first peak (Figure III-19b) shows the M/z of multiple charge states of a chemical species resembling the expected structure of FApB2v but omitting K(fam) and including a 56 Da adduct. The mass spectrum of the second peak (Figure III-19c) represents multiple charge states of intact FApB2v, again with a 56 Da adduct. Importantly, ions with M/z corresponding to predicted pB2v structures lacking folic acid were not detected.

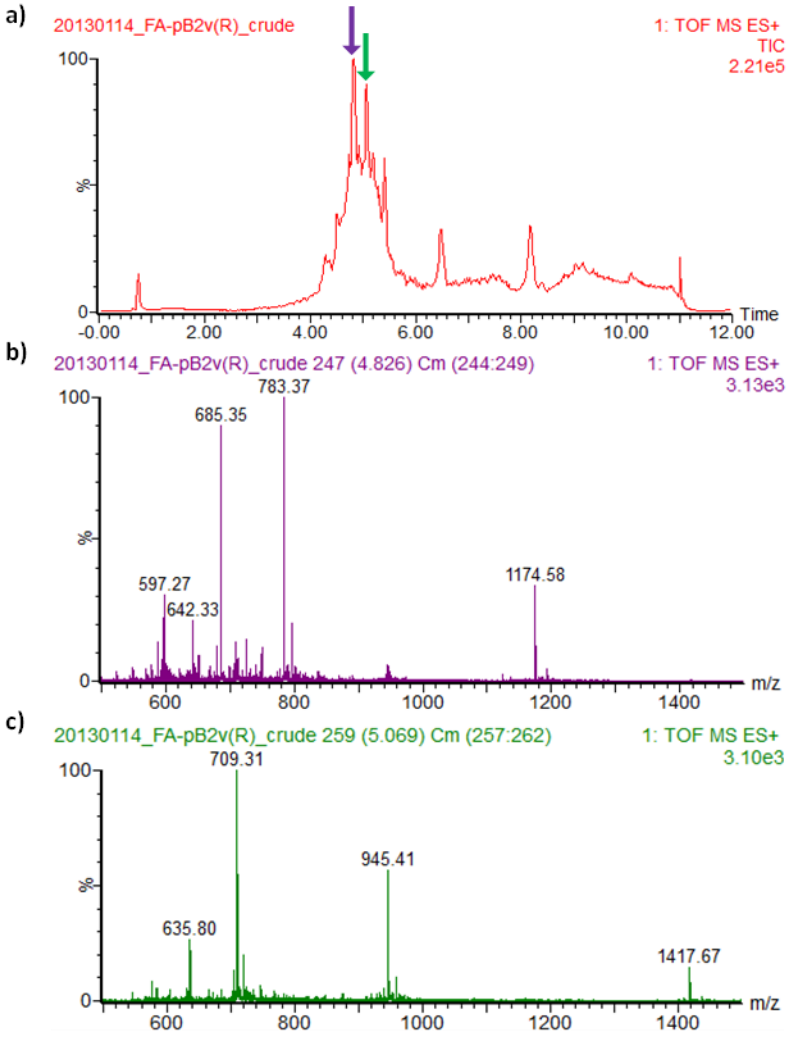

Figure III-19: LCMS of FApB2v peptide from HCTU-activation synthetic route
Total ion counts (a) following LC of FApB2v crude peptide mixture from solid phase synthesis route employing HCTU activation to conjugate FA. Arrows are color-coordinated with mass spectra (b,c) corresponding to the integrated ion peaks. Detected ion masses correspond to multiple charge states of peptide including FA and a 56 Da adduct but lacking K(fam) (b: 685, 783, 1174) or complete peptide including FA and 56 Da adduct (c: 709, 945, 1417).

FApB2v peptide was purified by semi-preparative HPLC and the collected fractions analyzed by LCMS. As seen in Figure III-20, a substantial though non-majority peak contained ions with M/z representing multiple charge states of the designed FApB2v peptide prepared by SPPS.

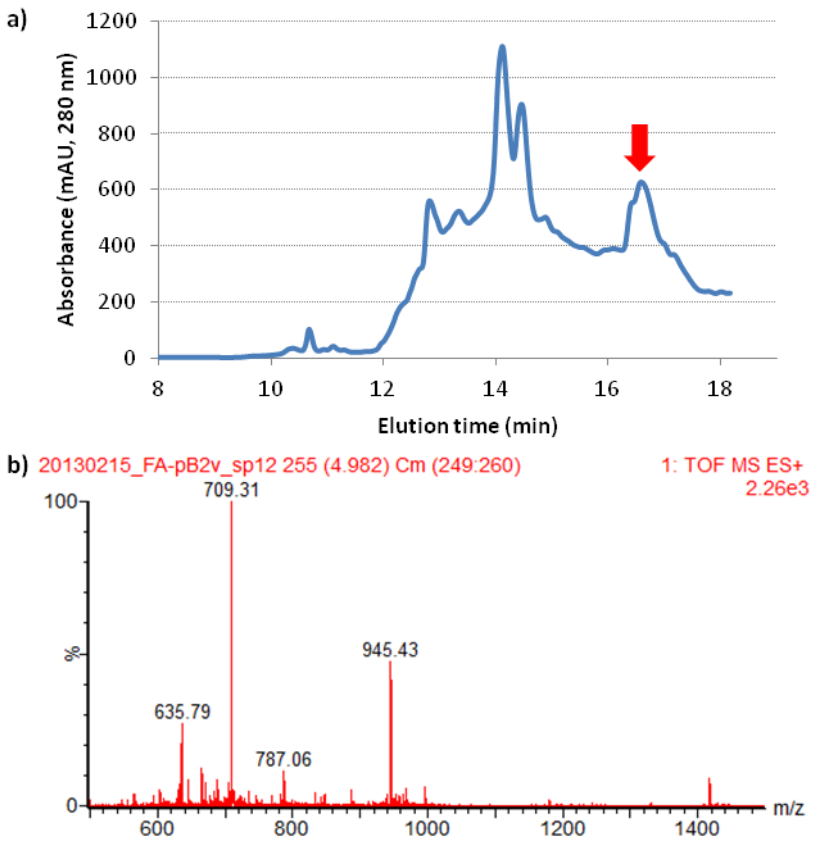

Figure III-20: Purification of FApB2v
Semi-preparative HPLC (a) was used to purify FApB2v peptide from SPPS employing HCTU activation of FA for folate conjugation. Arrow indicates the peak containing the intended product, as identified by the detected ions in LCMS (b, mass spectrum). M/z of 709, 945, 1417 represent charge states of a chemical species with molecular weight matching expected FApB2v structure.

To confirm that FApB2v was cleavable by MMPs and had a FRET switch suitable for sensing proteolytic activity, purified FApB2v was incubated with trypsin or MMPs (2, 9, or 14) and monitored for sensor (FAM) fluorescence. The fluorescence of sample wells containing trypsin or MMP14 increased 8-fold over 120 minutes and displayed a trend towards continued increase (Figure III-21). Notably, this represents a conservative estimate of FRET switch because the background fluorescence intensity due to the microplate and assay milieu was not subtracted. Sensor fluorescence increased modestly

with MMP2 and MMP9, as well, although assay wells with different MMPs were not standardized for active MMP concentration.

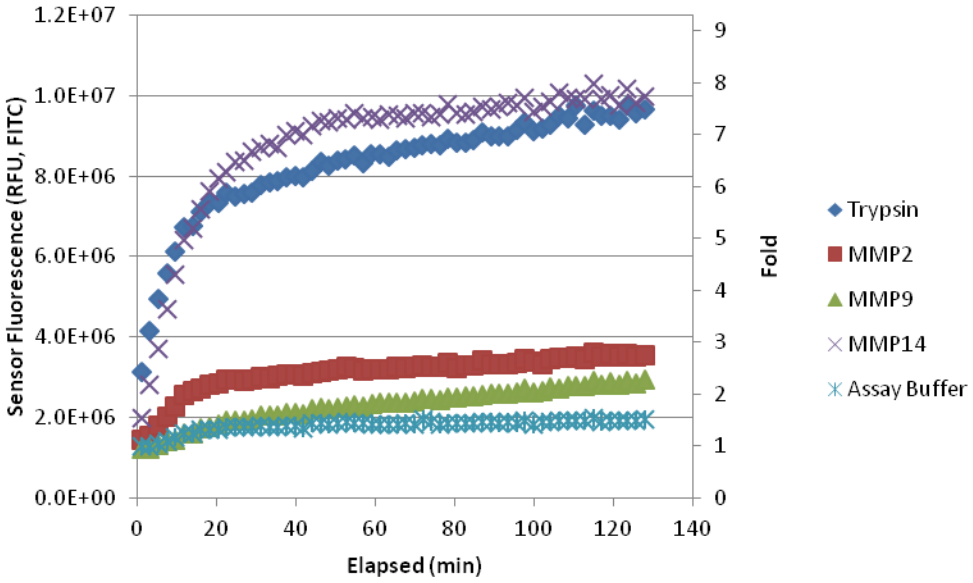

Figure III-21: FRET switch of purified FApB2v
FApB2v peptide purified by semi-preparative HPLC was incubated with proteolytic enzymes. Sensor fluorescence increase due to dequenching of FAM dye upon proteolytic cleavage was monitored. Note that fold-change in sensor fluorescence does not account for background fluorescence subtraction in this case.

Given the lack of evidence for FA coupling with peptides via carbodiimide chemistry, the evident lack of FA-NHS coupling to peptides in solid phase, and the apparent success of HCTU-mediated FA coupling in synthesizing folated peptides capable of generating FRET switch upon cleavage by MMPs, the synthetic route of SPPS followed by HCTU-mediated coupling of FA in solid phase was established as the standard protocol for producing folated MMP-FRET substrates presented hereafter.

III.3.4. Synthesis and characterization of peptides suitable for oxime ligation

To enable our design of dual-targeted nanoparticles based upon bioconjugation of MMP-cleavable, FRET-equipped substrate peptides to nanoparticle surfaces, we required

a chemistry that provided efficient coupling and chemoselectivity in mild conditions. Dirksen et al reported the ability to site-specifically ligate peptide fragments in the presence of unprotected amino acid side chains via oxime ligation with nucleophilic catalysis[130] (see Figure III-22). This technique was also previously demonstrated effective for attaching MMP9 substrate peptides to aldehyde-presenting polyester dendrons (Scherer and McIntrye, unpublished).

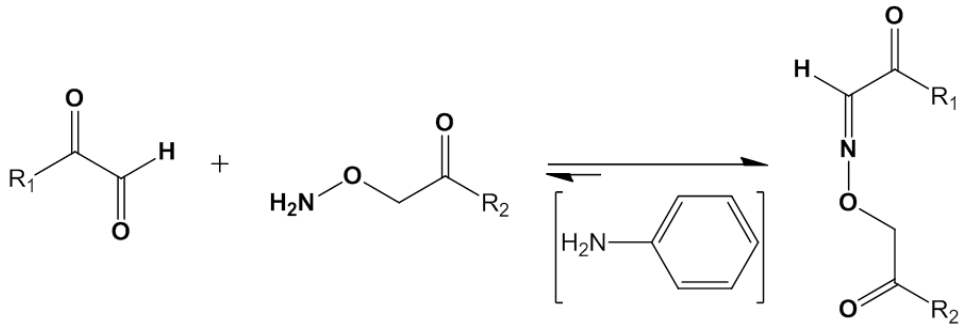

Figure III-22: Scheme, chemoselective oxime ligation (adapted from Diksen et al[130])
Oxime ligation between R_1-glyoxylyl (an aldehyde) and aminooxyacetyl-R_2 performed in either the absence or the presence of aniline as a catalyst. Reactive groups (aldehyde, aminooxy) and oxime bond are indicated in bold.

As such, the design of broadly MMP-cleavable pB2v peptide was modified to include an C-terminal aminooxy functional group for use in oxime ligation chemistry by utilizing the protected residue, Fmoc-Dpr(Boc-Aoa)-OH, as the first residue in SPPS of "pB2vAoa" [h_2n-{peg_1}K(fam){peg_1}RPLGLWAR{peg_1}K(tamra)G{DprAoa}-$conh_2$] (chemical structure in Appendix A). Following SPPS of pB2vAoa, crude peptide mixture from peptide-resin cleavage was analyzed by LCMS to assess relative yield and identity of products. The trace of total ions detected subsequent to LC (Figure III-23a) indicated the presence of multiple chemical species. As in previous syntheses using the same SPPS strategy, the majority of ions detected corroborated a predicted chemical structure corresponding to the intended peptide construct but without the K(fam) residue (Figure

III-23b,c), although ions with M/z representative of intact pB2vAoa were also detected (Figure III-23d,e). Ions with and without an unidentified 67 Da adduct were also detected, constituting a pair of structures for each case. Most importantly, DprAoa was present in the corresponding predicted molecular structures and masses (tabulated in Figure III-23f).

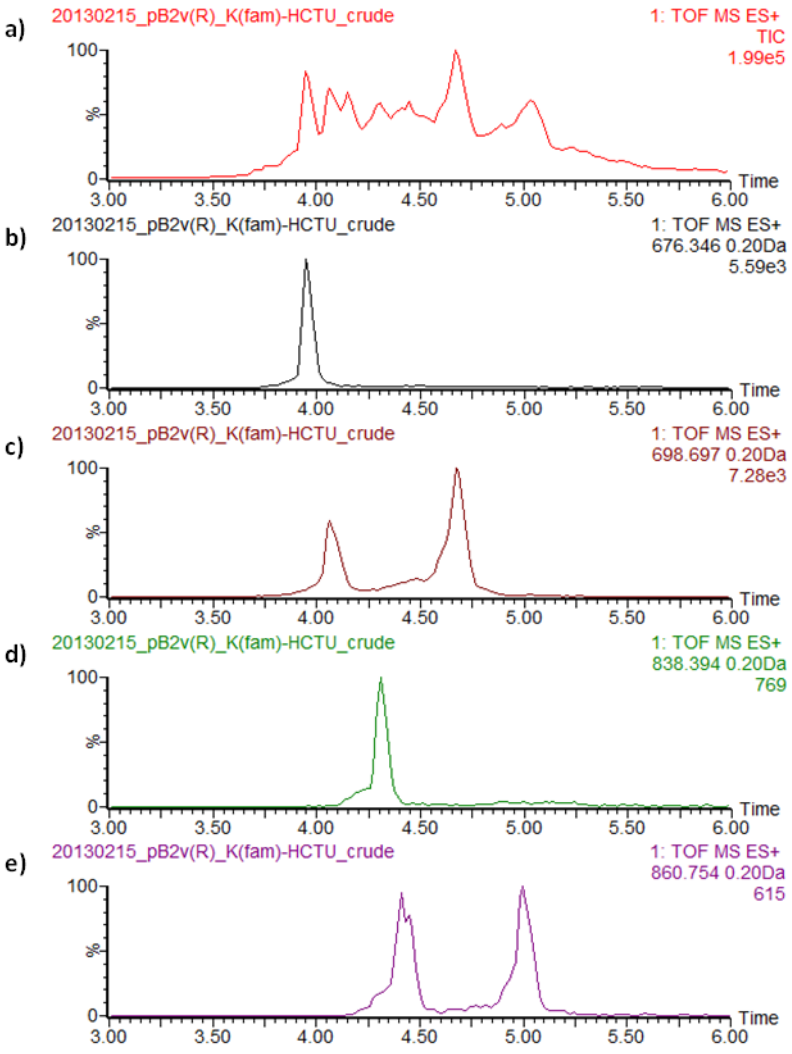

f)

Molecule	Mass	M/z (M+3H)
{PEG1}_{PEG1}RPLGLWAR{PEG1}K(tamra)G{DprAoa}-conh2	2026.05	676.36
+67 Da	2093.05	698.69
{PEG1}K(fam){PEG1}RPLGLWAR{PEG1}K(tamra)G{DprAoa}-conh2	2512.20	838.41
+67 Da	2579.20	860.74

Figure III-23: LCMS of unpurified pB2vAoa from SPPS
Total ion counts in ESI+ MS (a) following LC of pB2vAoa crude peptide mixture from SPPS. Chemical species eluting at distinct times (b-e) corresponded to intended structure omitting (b,c) or including (d,e) K(fam) residue as well as including an unidentified 67-Dalton adduct (c,e), as tabulated (f).

To validate the LCMS indications of the relative abundance of peptide products in pB2vAoa crude mixture, semi-preparative HPLC was performed with monitoring of tryptophan (280 nm) and TAMRA (550 nm) peak absorbance to automate eluent

collection and LCMS was repeated on separately collected fractions. As depicted in Figure III-24, the HPLC eluent peak containing the intended pB2vAoa structure represented a minority product of the synthesis. The majority peaks in HPLC corroborated the LCMS findings that a predicted structure lacking K(fam), with or without additional chemical adducts, contributed to the majority of SPPS products (data not shown).

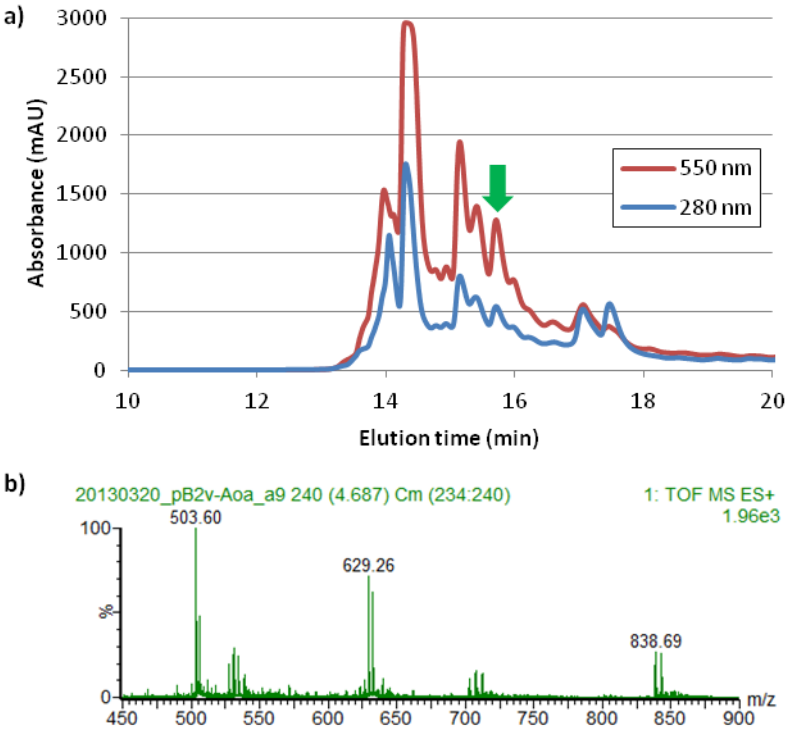

Figure III-24: Purification of pB2vAoa
Semi-preparative HPLC (a) was used to purify pB2vAoa peptide from SPPS. Arrow indicates the peak containing the intended product, as identified by the detected ions in LCMS (b, mass spectrum). M/z of 503, 629, 838 represent charge states of a chemical species with molecular weight matching expected pB2vAoa structure. Note that the most abundant peak (a, 14.2 mins) contained ions with mass corresponding to a product omitting the K(fam) residue (data not shown).

III.3.5. Attempt to improve yield from SPPS by substitution of K(ivDDE) for K(fam)

Because incomplete coupling of K(fam) appeared to be a persistent cause of unintended product yield from SPPS of FRET peptides, a strategy employing a lysine

residue with a protecting group less bulky than fluorescein in SPPS was explored with the purpose of providing more efficient coupling for higher yields and preserving the ability to later attach fluorescein via a reaction with a relatively inexpensive amine-reactive dye. This strategy also presented the potential to extend applications of SPPS of MMP substrate peptides to include moieties not commercially available as lysine conjugates or that are intolerant of the acid-base conditions required for SPPS, such as NIR dyes or drug molecules. Fisher et al demonstrated that the (4,4-dimethyl-2,6-dioxocyclohex-1-ylidine)ethyl (DDE) group could be removed from peptides in SPPS on rink amide resin by application of 2% hydrazine solution in DMF (a basic solution) without affecting acid-labile protecting groups[131]. As such, the design for SPPS of pB2vAoa was modified to substitute Fmoc-Lys(ivDDE)-OH, a more recently developed analogue of DDE-protected lysine that generates less side-reactive byproducts during deprotection, in place of Fmoc-Lys(5/6-FAM)-OH, as schematically diagrammed in Figure III-25.

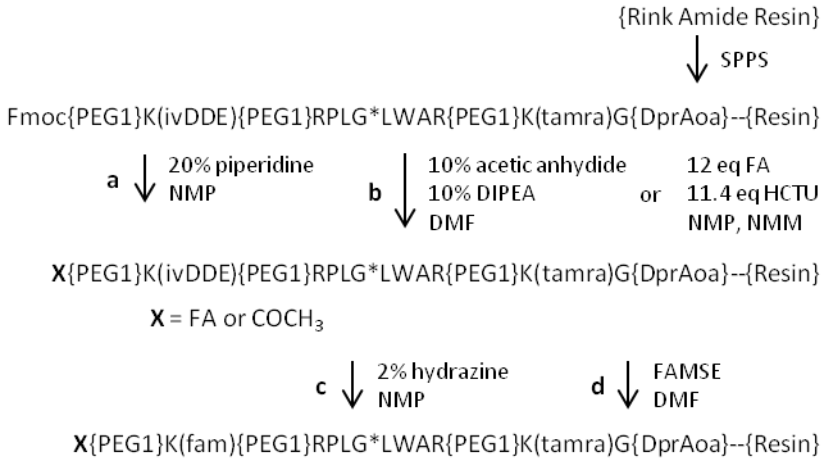

Figure III-25: Scheme, synthesis of (FA/Ac)pB2vAoa peptides via K(ivDDE) route
The peptide containing protected lysine K(ivDDE) in place of K(fam) was produced in SPPS, then the N-terminus terminated by removal of Fmoc (a) and acylation with either FA or acetyl group (b). The ivDDE protecting group was then removed (c) and the side chain of lysine reacted with FAMSE (d) to introduce FAM as the sensor dye.

Following synthesis of ivDDE-protected pB2vAoa by SPPS, the crude peptide mixture was analyzed by HPLC and LCMS to elucidate relative product purity and identity. Monitoring the peak absorbance of tryptophan at 280 nm, three substantial eluent peaks from HPLC were detected, as can be seen in Figure III-26a. Interestingly, only one of these peaks was accompanied by a substantial peak in 550 nm absorbance, representative of TAMRA dye. Concordantly, LCMS also indicated the presence of a predicted ion corresponding to the intended peptide lacking K(tamra), however also indicated an abundance of ions representing the intact intended peptide structure with or without a 67 Da adduct (Figure III-26b,c). All structures corroborated by MS contained K(ivDDE), indicating robust coupling of Fmoc-Lys(ivDDE)-OH during SPPS.

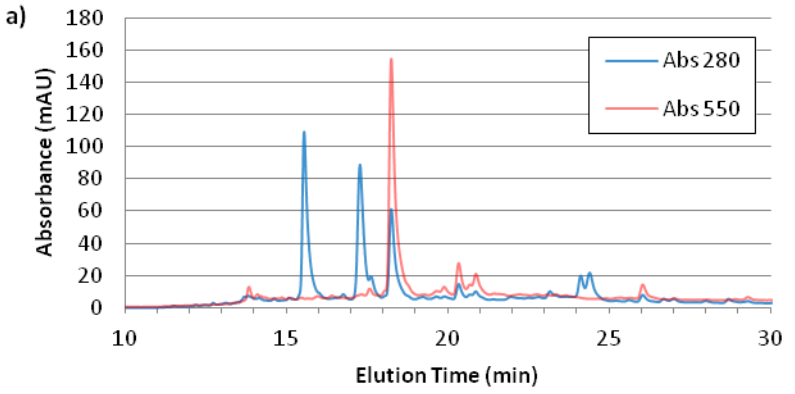

c)

Peak #	Chemical Species	Mass (Da)
1	{PEG1}K(ivDDE){PEG1}RPLGLWAR{PEG1}_G{DprAoa}-conh$_2$	1820.04
2	{PEG1}K(ivDDE){PEG1}RPLGLWAR{PEG1}K(tamra)G{DprAoa}-conh$_2$	2360.28
3	(2) + 67 Da	2427.28

Figure III-26: HPLC and LCMS of ivDDE-protected pB2vAoa peptide
A peptide with sequence analogous to pB2vAoa substituting K(ivDDE) for K(fam) was synthesized by SPPS as diagrammed in Figure III-25 and analyzed by analytical scale HPLC (a). LCMS was subsequently performed, wherein total ion counts (b) were correlated with predicted products of SPPS (c). Peak numbers in (b) correspond to chemical species (c) with masses detected in each peak.

To validate the applicability of the protected lysine strategy to the synthesis of folated FRET peptides, the folate-conjugated, ivDDE-protected peptide depicted in Figure III-25b was synthesized via SPPS terminating with the previously demonstrated HCTU-mediated method of FA attachment. As seen in Table III-2, LCMS of the resulting crude peptide mixture detected ions with M/z corresponding to the multiple charge states of the intended product of SPPS as well as adducts similar to those observed previously (40, 67,

107 Da). Importantly, molecules smaller than the folated peptide (i.e. not folated) were not detected, suggesting that the coupling of folic acid to peptides was robust.

Table III-2: Detected ions via LCMS of folated, ivDDE protected pB2vAoa peptide

Molecule	Mass	M/z, M+ 2H	3H	4H
FA{PEG1}K(ivDDE){PEG1}RPLG*LWAR{PEG1}K(tmr)G{DprAoA}-conh$_2$	2783.41	1392.71	928.81	696.86
+40 Da	2823.41	1412.71	942.14	706.86
+67 Da	2850.41	1426.21	951.14	713.61
+107 Da	2890.41	1446.21	964.48	723.61

To complete the synthesis of a folated and FRET-equipped peptide, the ivDDE protecting group was removed with 2% hydrazine solution and the resin-bound peptide subsequently reacted with FAMSE to generate "FApB2vAoa" [fa-{peg$_1$}K(fam){peg$_1$}RPLGLWAR{peg$_1$}K(tamra)G{DprAoa}-conh$_2$], as diagrammed in Figure III-25, above. Notably, peptide-resin was observed by visual inspection to change color from intense pink-magenta to yellow-brown during treatment with hydrazine and finally to orange upon removal of hydrazine and washing in organic solvents (DMF, EtOH, NMP). LCMS analysis of the resulting crude peptide mixture detected ions corresponding to the expected FApB2vAoa structure with adducts of 67 and 107 Da (Figure III-27). Ions representing structures smaller than the expected construct were not detected, indicating successful coupling of the fluorescein moiety.

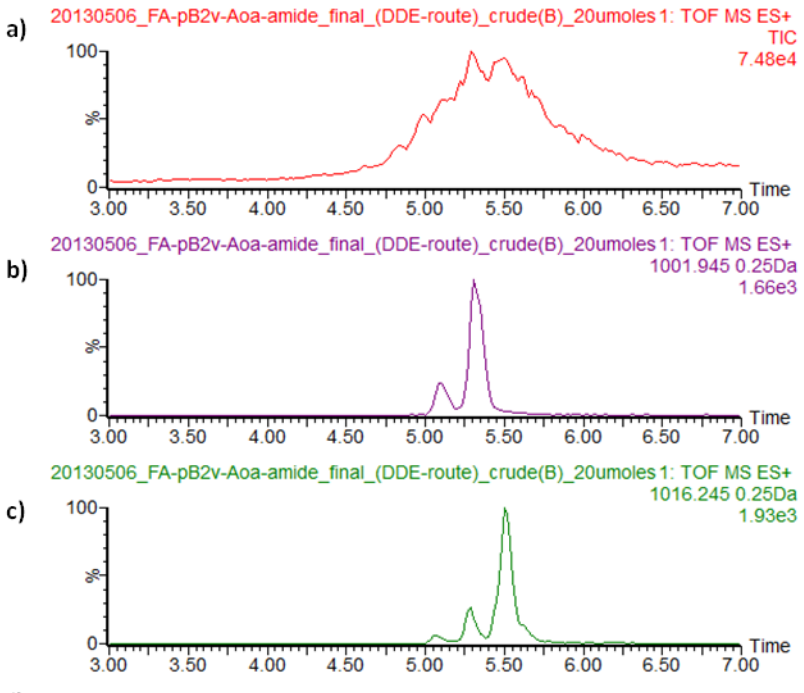

d)

Molecule	Mass	M/z, M+ 2H	3H	4H
FA{PEG1}K(fam){PEG1}RPLG*LWAR{PEG1}K(tmr)G{DprAoA}-conh$_2$	2935.33	1468.67	979.45	734.84
+67 Da	3002.33	1502.17	1001.78	751.59
+107 Da	3042.33	1522.17	1015.12	761.59

Figure III-27: LCMS of FApB2vAoa via ivDDE-route
FApB2vAoa peptide was synthesized by SPPS employing K(ivDDE) residue, hydrazine deprotection, and subsequent reaction with FAMSE as diagrammed in Figure III-25. Total ion counts (a) following HPLC were collected and ions corresponding to FApB2vAoa peptide with additional adducts of +67 Da (b) and +107 Da (c) were detected, as tabulated (d).

The observation that FApB2vAoa synthesized in SPPS by the aforementioned K(ivDDE) route appeared to have anomalous optical properties (yellow in pH7 buffer by visual inspection instead of the expected pink hue characteristic of TAMRA dye) was conspicuous. To investigate, crude peptide mixture was diluted in buffered solutions ranging in pH from 3.5 to 7.0 and assessed for UV-visible absorbance by spectrophotometry. While FAM and TAMRA dyes are known to exhibit reversibly pH-sensitive optical properties, each should absorb visible light with comparable peak molar extinction coefficients at neutral pH. However, as seen in Figure III-28, FApB2vAoa

synthesized according to the scheme in Figure III-25 had absorbance characteristic of FAM (495 nm maximum) but not TAMRA (560 nm maximum) at pH 7.0. The presence of TAMRA dye was indicated by its characteristic absorbance in acidic buffers, but this absorbance was attenuated with increasing pH and practically absent at pH 7.0. On the other hand, FAM absorbance was reversibly quenched in acid, as expected.

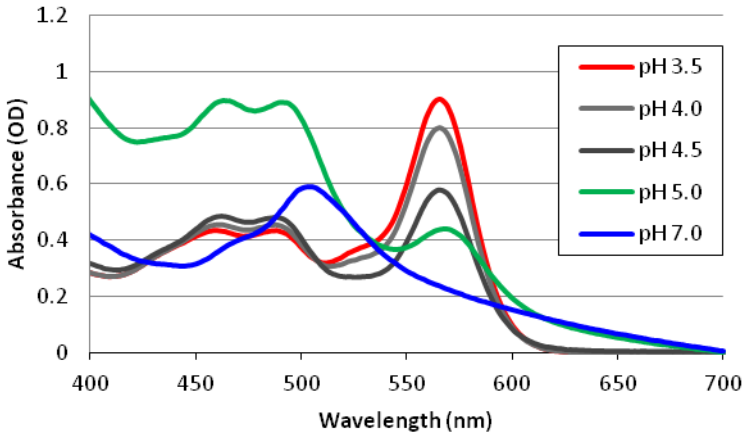

Figure III-28: pH-dependent absorbance of FApB2vAoa via ivDDE-route
Aliquots of FApB2vAoa peptide synthesized via SPPS including K(ivDDE), hydrazine deprotection, and FAMSE coupling as diagrammed in Figure III-25 were diluted to equivalent concentrations in pH buffers and analyzed by spectrophotometry.

Because the ability of proteolytic nanobeacons hinges on the optical properties of the constituent fluorophores at physiologic pH, an alternative synthesis strategy was necessary. Based upon the unusual observations of color change during treatment of peptide-resin with hydrazine solution, deprotection of K(ivDDE) was attempted using hydroxylamine hydrochloride and imidazole according to a published technique[132]. Subsequent spectrophotometric analysis reproduced pH sensitivity of FApB2vAoa treated with 2% hydrazine solution but did not demonstrate this property with hydroxylamine/imidazole-treated peptide. However, deprotection of K(ivDDE) with hydroxylamine/imidazole was found to be very inefficient at best as determined by

qualitative Ninhydrin assay (data not shown). Further troubleshooting to optimize synthesis of FRET peptides in SPPS using protected lysine residues was not explored.

III.3.6. Capping and triple coupling in SPPS to improve yield of FRET peptides

While the coupling efficiency of K(ivDDE) in SPPS was apparently superior to that of K(fam), the complications of the additionally required deprotection and dye conjugation steps limited the feasibility of this approach to synthesis of FRET peptides. As such, the coupling of K(fam) was revisited. pB2vAoa peptide was synthesized following the originally devised scheme for SPPS of pB2v (see II.2.11), using HCTU as the carboxyl activating reagent for all couplings rather than using PyClock for Fmoc-Lys(5/6-X)-OH (where X is FAM or TAMRA). Importantly, Fmoc-Lys(5/6-FAM)-OH was reacted with triple-coupling of 2 molar equivalents of residue relative to resin substitution in each coupling and an acetic anhydride capping step was added immediately after this step to terminate any peptide products not successfully conjugated with K(fam) prior to proceeding with the remaining N-terminal residue couplings.

Crude pB2vAoa peptide mixture from SPPS was analyzed by analytical-scale HPLC with a mobile phase gradient composed of 50 mM potassium phosphate buffer (pH 7.0) and MeOH to allow monitoring of eluent absorbance at 495 nm attributable to FAM in addition to 280 nm (tryptophan) and 560 nm (TAMRA). As seen in Figure III-29a, the resulting chromatograms reflect a less heterogeneous mixture of products, with most of the integrated signal belonging to a closely grouped set of eluted product peaks. Importantly, each of these peaks was coincident in each of the three chromatogram channels (280 nm, 495 nm, 560 nm) with magnitudes suggestive of incorporation of both fluorescent dyes. Eluents represented by these peaks were collected jointly and analyzed

by LCMS, in which ions with M/z representative of multiple charge states of two predicted chemical structures were detected: the intended Fmoc-pB2vAoa product with a 40 Da addition (as was seen with previously analyzed pB2v analogues from SPPS) and a peptide product missing the DprAoa residue with no adduct (Figure III-29b). The identification of only two different molecular weights from the multiple co-collected peaks in HPLC was not wholly unexpected. Both of the fluorophores, FAM and TAMRA were present as a mixture of two isomers each. The slightly different attachments of these isomers may contribute to different retention times in HPLC, leading to the possibility of four analyte peaks representative of molecules with identical molecular weights.

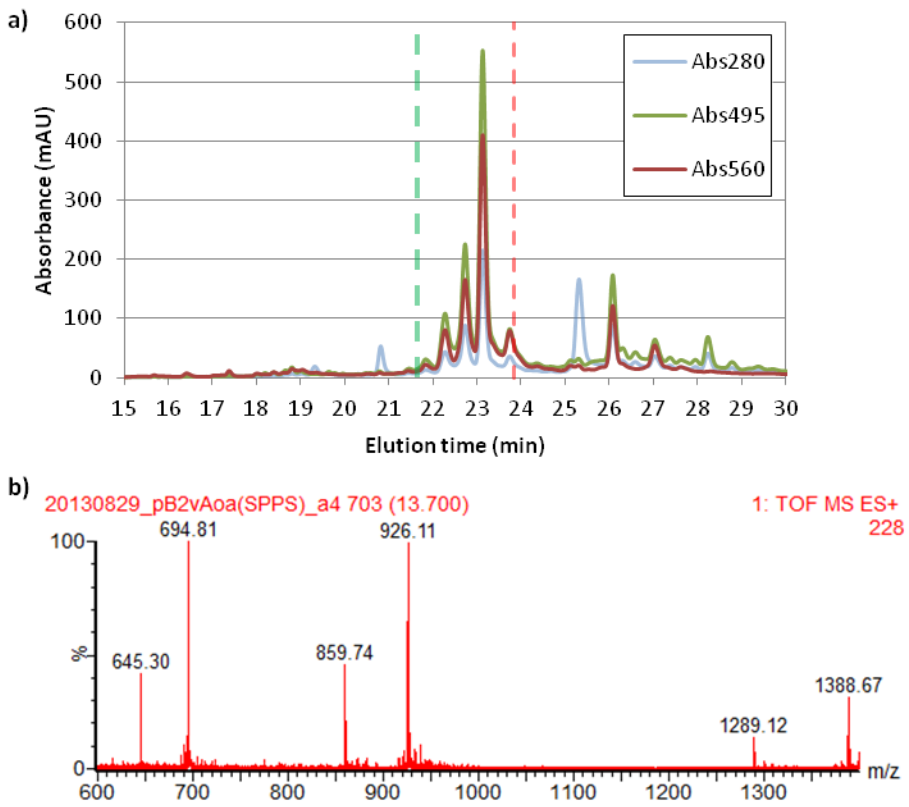

Figure III-29: HPLC and LCMS of pB2vAoa via triple-coupling SPPS
pB2vAoa peptide was synthesized via SPPS with triple coupling of 2 molar equivalents each K(fam) residue and left Fmoc-protected at the N-terminus. Material was recovered from analytical scale HPLC (a) of crude peptide product as indicated by dashed lines and subsequently analyzed by LCMS to yield a mass spectrum (b). M/z of ions detected correspond to multiple charge states of Fmoc-pB2vAoa with a +40 Da adduct (694, 926, 1388) or an analogous structure lacking the C-terminal DprAoa residue (645, 859, 1289).

To confirm successful coupling of all residues and consequent optical properties of Fmoc-pB2vAoa from triple-coupling SPPS, the partially purified peptide solution recovered from analytical-scale HPLC was analyzed by FRET switch assay, incubating peptides with either trypsin or MMPs (9 or 14). Sensor (FAM) fluorescence of Fmoc-pB2vAoa increased rapidly upon cleavage by MMP14 or trypsin, reaching the end of the linear stage of fluorescence amplification within 5 minutes, as plotted in Figure III-30. A 15-fold increase in sensor fluorescence attributable to MMP14 activity was observed in less than 25 minutes.

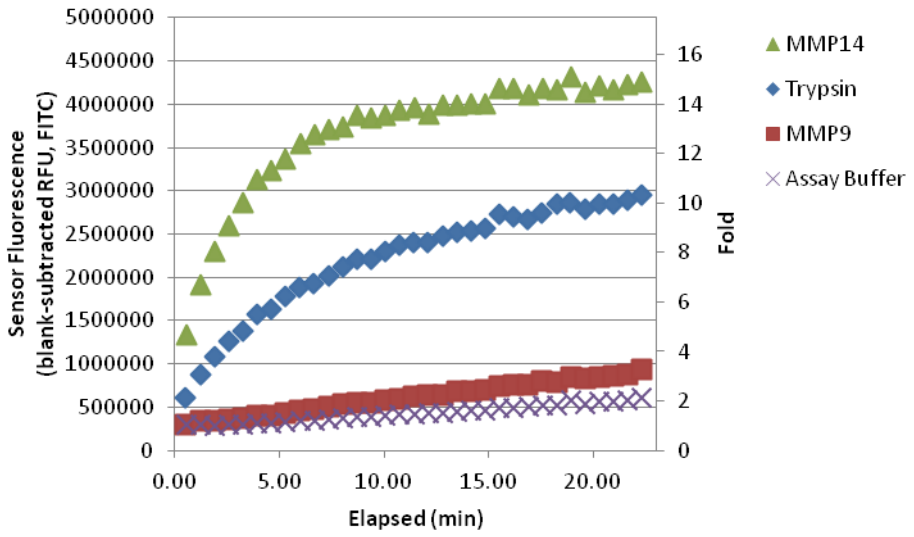

Figure III-30: FRET switch of purified Fmoc-pB2vAoa from triple-coupling SPPS
Sensor (FAM) fluorescence emission from HPLC-purified Fmoc-pB2vAoa peptide from SPPS with triple-coupling of K(fam) residue increased upon treatment with proteolytic enzymes. Values represent single measurements.

Given the provision of peptides with demonstrated MMP-inducible FRET switch from triple-coupling SPPS, the peptide-resin material from synthesis of Fmoc-pB2vAoa (above) was deprotected and reacted in solid phase as diagrammed in Figure III-25 to acylate the N-terminus with either FA or the acetyl group ($COCH_3$, "Ac"), yielding FApB2vAoa or "AcpB2vAoa", respectively.

Crude peptide mixture from synthesis of FApB2vAoa was incubated with trypsin or MMP14, with and without EDTA to inhibit metalloproteinase activity. As with the parental peptide, a FRET switch developed rapidly from FApB2vAoa with both trypsin and MMP14 in the absence of EDTA, reaching a 6-fold increase in sensor emission intensity within 20 minutes (Figure III-31). Notably, this FRET switch is representative of an unpurified peptide mixture, whereas the FRET switch of Fmoc-pB2vAoa (above) was measured with partially purified peptide. EDTA abrogated the amplification of

sensor fluorescence with MMP14 but had no effect on the increase caused by trypsin cleavage.

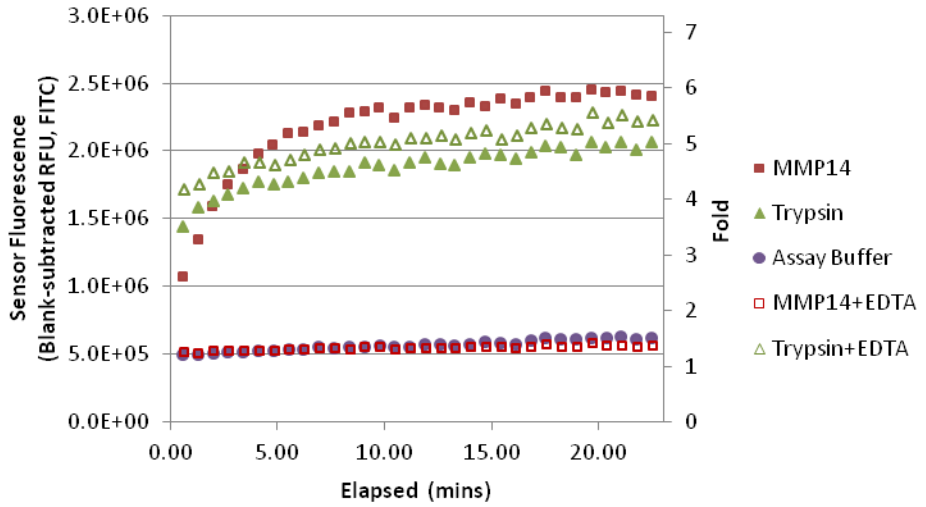

Figure III-31: FRET switch of unpurified FApB2vAoa from triple-coupling SPPS
Sensor (FAM) fluorescence emission from unpurified FApB2vAoa peptide from SPPS with triple-coupling of K(fam) residue increased upon treatment with proteolytic enzymes. EDTA was included in control samples to inhibit metalloproteinase activity. Values represent single measurements.

As with previously synthesized peptides, FApB2vAoa was analyzed by HPLC with automated fraction collection and LCMS of the collected eluents. Chromatograms of the absorbance channels employed for fraction collection (Figure III-32a) reflect slightly poorer resolution of the folated peptide than the parental Fmoc-protected pB2vAoa (Figure III-29a). Nonetheless, the majority of integrated absorbance was recorded within a group of clustered peaks corresponding to separately collected eluent volumes, two of which were found by LCMS to contain ions with M/z representative of the multiple charge states of FApB2vAoa with a 40 Da adduct (Figure III-32b,c). Corroborating the results of previous peptide folation reactions (see III.3.3, III.3.5), ions representative of

non-folated products were not detected, indicating successful attachment of folate to peptides.

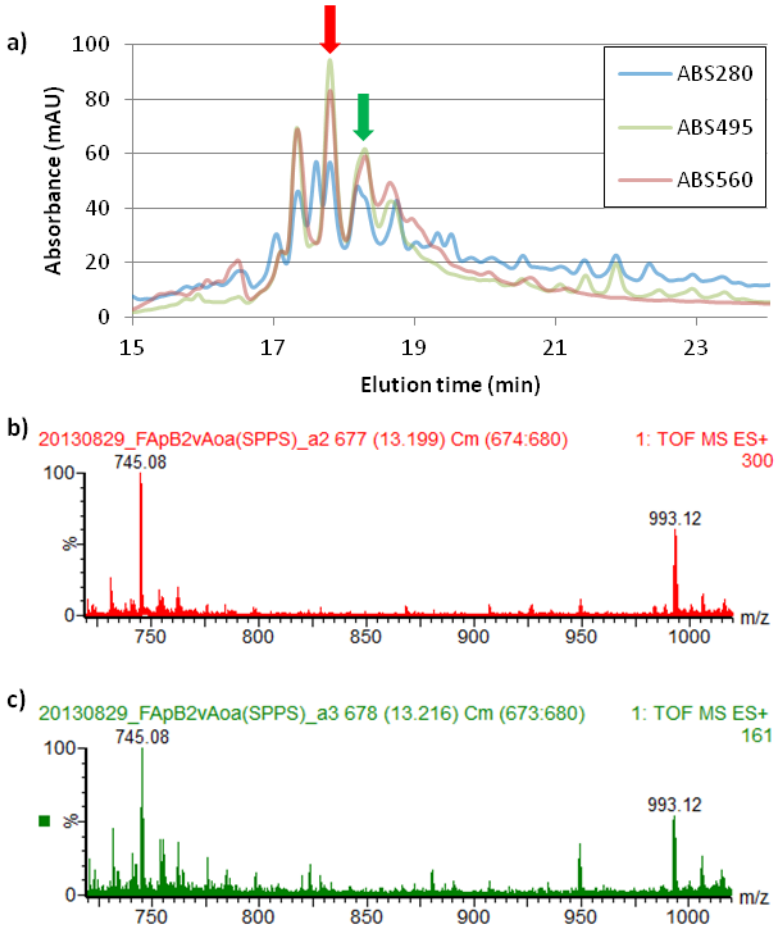

Figure III-32: HPLC and LCMS of FApB2vAoa from triple-coupling SPPS
Crude peptide mixture from SPPS of FApB2vAoa with triple-coupling of K(fam) residue was analyzed by analytical scale HPLC, recording absorbance of eluted analytes at 280 nm, 495 nm, and 560 nm (a). Color-coordinated arrows in (a) indicate material peaks collected from HPLC that were subsequently characterized by LCMS to give mass spectra (b,c). M/z of detected ions (745, 993) correspond to multiple charge states of the expected structure of FApB2vAoa with a +40 Da adduct.

AcpB2vAoa, the MMP-cleavable but non-folate-targeted counterpart to FApB2vAoa (for detailed structure see Appendix A), was similarly characterized by HPLC and LCMS. As seen in Figure III-33a, the crude product of SPPS appeared relatively homogeneous compared to either Fmoc-pB2vAoa or FApB2vAoa, with the majority of

integrated absorbance signals assigned to only two peaks. As shown in Figure III-33, LCMS of the HPLC eluents collected based upon these peaks detected ions representing the expected structure of AcpB2vAoa with a chemical adduct of similar weight (42 Da) to that found on FApB2vAoa (40 Da).

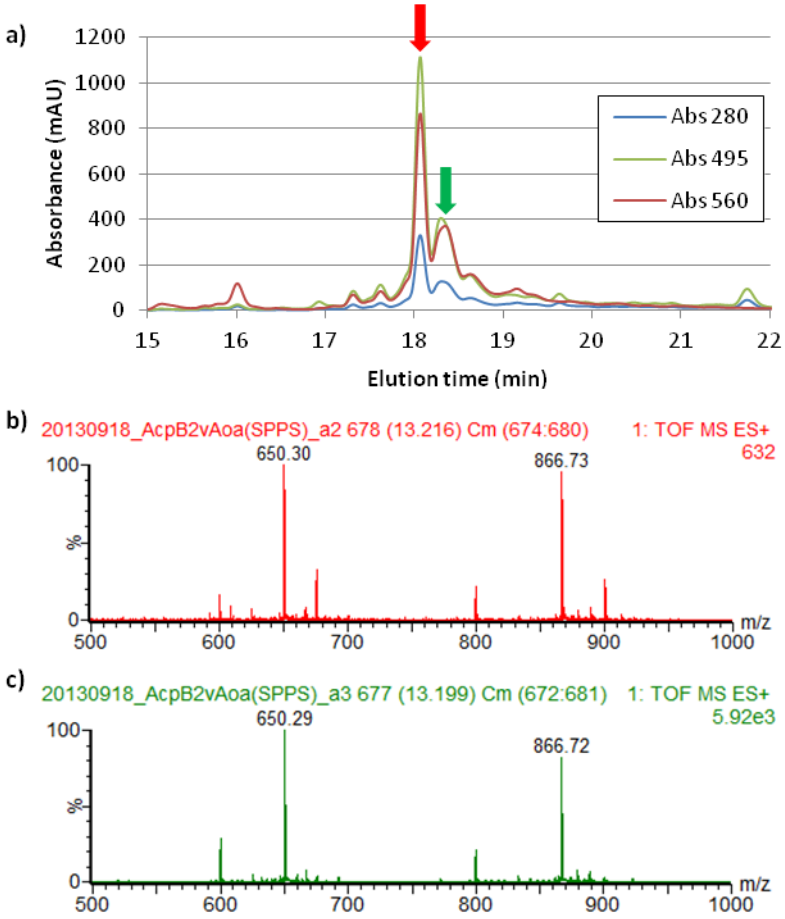

Figure III-33: HPLC and LCMS of AcpB2vAoa from triple-coupling SPPS
Crude peptide mixture from SPPS of AcpB2vAoa with triple-coupling of K(fam) residue was analyzed by analytical scale HPLC, recording absorbance of eluted analytes at 280 nm, 495 nm, and 560 nm (a). Color-coordinated arrows in (a) indicate material peaks collected from HPLC that were subsequently characterized by LCMS to give mass spectra (b,c). M/z of detected ions (650, 866) correspond to multiple charge states of a structure 42 Da larger than the intended AcpB2vAoa peptide.

To validate its FRET switch potential and MMP-cleavability, purified AcpB2vAoa collected from analytical-scale HPLC (Figure III-33a, eluent peak indicated by red arrow) was mixed with MMPs (2, 9, or 14) in the presence and absence of EDTA to inhibit

metalloproteinase activity. Sensor (FAM) fluorescence increased with each MMP in the absence of EDTA, reaching greater than 25-fold the starting intensity upon treatment with MMP14 in less than 10 minutes (Figure III-34). FRET switch continued to increase with MMPs past 100 minutes of reaction. These effects were nearly completely abrogated by the inclusion of EDTA in the assay buffer.

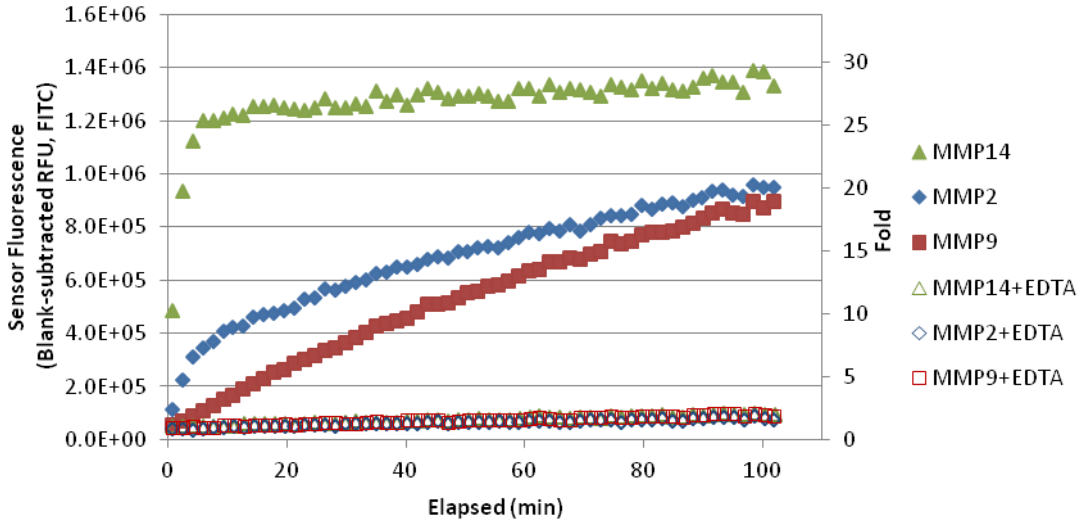

Figure III-34: FRET switch of purified AcpB2vAoa from triple-coupling SPPS
Sensor (FAM) fluorescence emission from HPLC-purified AcpB2vAoa peptide from SPPS with triple-coupling of K(fam) residue increased upon treatment with proteolytic enzymes. EDTA was included in control samples to inhibit metalloproteinase activity. Values represent single measurements.

Further validation of AcpB2vAoa peptide as a biosensor for MMP-associated proteolytic activity was performed in vitro by incubating MDA-MB-468 human breast cancer cells with cell culture media containing AcpB2vAoa either with or without broad spectrum MMP inhibitor GM6001. Because HPLC and LCMS results (above) indicated that most of the product of SPPS represented the intended structure of AcpB2vAoa, crude peptide was employed in this experiment. Conditioned media were sampled at several intervals over a 24-hour period and diluted into medium containing EDTA to halt

metalloproteinase activity prior to analysis by plate reader fluorescence spectroscopy. Sensor (FAM) fluorescence increased through 24 hours in conditioned media from culture conditions containing cells and AcpB2vAoa in the absence of inhibitor, exhibiting a greater than 10-fold increase in media sampled after 24 hours of incubation, whereas fluorescence of AcpB2vAoa in the absence of cells remained constant (Figure III-35). Interestingly, the inclusion of GM6001 partially abrogated the increase in sensor fluorescence, as only a 4-fold increase in sensor emission intensity was observed at the endpoint in this condition.

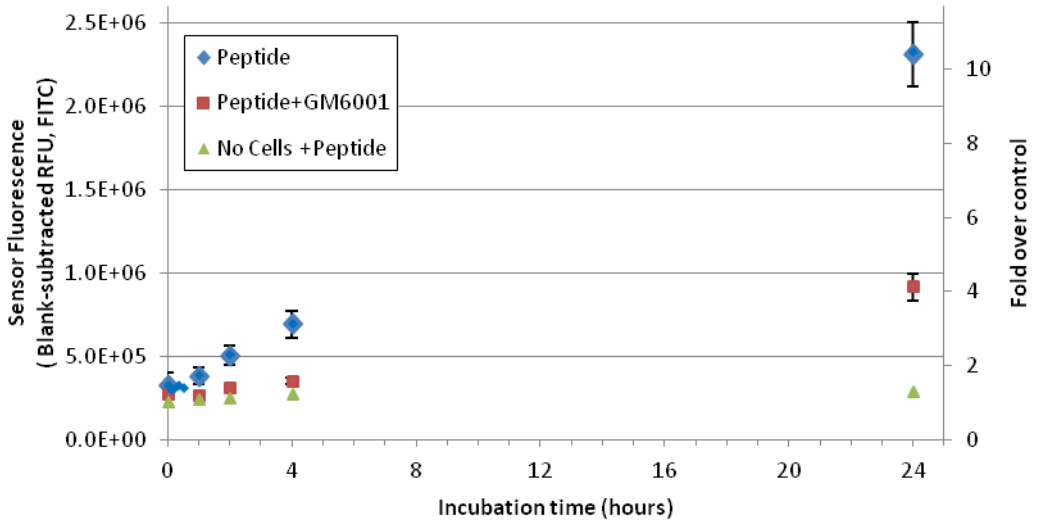

Figure III-35: FRET switch of AcpB2vAoa in cell culture
Unpurified AcpB2vAoa peptide was incubated with MDA-MB-468 human breast cancer cells. Medium samples were collected at timepoints and sensor (FAM) fluorescence assessed. GM6001 was added to control samples to inhibit MMP activity. Fold change expressed as multiple of no cell control sample initial fluorescence intensity. Values represent average of duplicates (except no cell control, single measurements). Error bars: standard deviation.

Altogether, the findings above with FApB2vAoa and AcpB2vAoa indicated that peptides possessing all the requisite components for folate targeting, optical sensing of proteolytic activity, and oxime ligation with nanoparticles were produced by SPPS.

III.4. Discussion and Conclusions

The results presented in this chapter have detailed the development of a robust protocol for solid phase synthesis of folate-targeted, MMP-sensing substrate peptides with C-terminal aminooxy functional groups for attachment to nanoparticles via oxime ligation. Troubleshooting of SPPS and chemical analyses of SPPS products yielded insights into the efficiencies of residue coupling in automated SPPS and incompatibility of organic dyes with the reaction conditions required for deprotection of protected amino acid side chains in SPPS. Together, these insights led to the development of a revised triple-coupling strategy to improve yields of expected products from SPPS.

Mass spectrometric analysis of pB2v, the broadly MMP-cleavable substrate peptide bearing FAM and TAMRA dyes for FRET and including monomeric PEG residues as hydrophilic spacers produced by SPPS (see II.3.6), indicated the presence of multiple chemical species with unexpected molecular weights, even in the sample iteratively purified by HPLC (Figure III-1). The masses of detected ions corroborated multiple possible products of SPPS, such as a peptide omitting both arginine residues and one PEG_1 residue from the intended structure. However, because mass spectrometry provides no structural information and NMR data would have been confounded by the presence of multiple structures, no definitive structures of the products of SPPS could be identified from these data and samples.

To provide additional insight into the chemical identities of peptides produced, SPPS of pB2v was repeated with qualitative interrogation of suspect coupling reactions during automated SPPS by Ninhydrin assay as indicated in Figure III-3, revealing uncoupled primary amines following attempted coupling of the K(fam) residue. Combined with the finding that the molecular weights of two of the most abundantly detected ions by mass

spectrometry differed by 56 Da each from either the expected MW of pB2v or of pB2v without K(fam), these data suggested that coupling of K(fam) was incomplete during synthesis. The majority of the final products of SPPS contained this unidentified 56 Da adduct. However, as seen in Figure III-5, incubation of the crude peptide mixture from the repeated SPPS of pB2v with MMPs confirmed the MMP-induced FRET switch seen previously with purified pB2v_2.2.1 from the first synthesis (Figure II-19). Furthermore, the dependence of the observed FRET switch on biologically relevant MMPs and incorporation of FAM dye was confirmed by assessing the FRET switch (Figure III-6) of D-pB2v, a peptide analogous to pB2v but synthesized with D-amino acids. D-pB2v did not exhibit a FRET switch upon treatment with MMPs, however like (L-)pB2v did possess an absorbance spectrum representative of FAM and TAMRA dye inclusion (Figure III-7). Therefore the K(fam) residue was necessarily coupled in some proportion during SPPS of pB2v peptides and the unidentified 56 Da adduct did not block MMP cleavage or the consequent sensor (FAM) fluorescence amplification upon peptide hydrolysis.

Further characterization of the 56 Da adduct seen in repeated SPPS of pB2v peptides was attempted by advanced mass spectrometry and NMR techniques in collaboration with other laboratories at Vanderbilt University. Detection of ions corresponding to the intended pB2v structure with and without incorporation of K(fam) and/or the 56 Da adduct by ESI-Q-IM-TOF MS in a desalted crude peptide sample, as seen in Figure III-8, both confirmed the previous findings and suggested that the adduct could not be removed by desalting, such as might be the case with an ionic adduct such as iron (^{56}Fe). Rather, the adduct was likely covalently bonded, as could be the case if a t-butyl cation was

liberated from a protecting group and reattached at another molecular site, a common occurrence during TFA-mediated deprotection of protected amino acid side chains following Fmoc-SPPS[128]. Covalent attachment of the 56 Da adduct was further corroborated by the finding that the four products of SPPS identified above [pB2v +/- K(fam), +/-56 Da] were partially separable by HPLC (Figure III-9), but all detected by ESI-Q-IM-TOF MS (Table III-1) following separation. To determine possible site of adduct attachment on the peptide, fragmenting ESI-Q-IM-TOF MS-MS was performed focusing on an ion representative of the intact pB2v structure including the adduct. Shown in Figure III-10, the predicted fragments represented in the mass spectrum suggested that the 56 Da adduct was likely attached within the three or four residues nearest the C-terminus. Additional efforts to identify the structure and location of the adduct by 2D NMR experiments with HPLC-purified pB2v(+56) (Figure III-11) corroborated the covalent attachment of a branched alkyl group with two methyl groups that are not present in the predicted structure of pB2v. Ultimately, the NMR spectra could not resolve the exact location of adduct attachment. The TAMRA fluorophore, while a probable candidate for modification owing to an unprotected carboxylic acid functional group, was probably not the site of covalent attachment, as a short peptide representative of a C-terminal portion of pB2v [h_2n-WAR{peg_1}KG-$conh_2$] was also found to have the 56 Da adduct (data not shown).

Given the evidence in agreement with covalent attachment of a branched alkyl cation that could be the result of inadequate scavenging during TFA-mediated deprotection and cleavage of pB2v from the solid support resin, several strategies involving protection, deprotection, or scavenging of liberated protecting groups by organic molecules were

attempted to either mitigate or remove the adduct following SPPS. Unfortunately, none of these strategies generated peptide products free of the 56 Da adduct as determined by mass spectrometry (data not shown, see III.2.5), suggesting that transfer of t-butyl cations from protected amino acid side chains to other moieties might not have been the source of the adduct.

As documented above, SPPS of pB2v peptide and variants thereof repeatedly produced peptide mixtures that possessed the same 56 Da adduct that was not readily prevented nor removed, and peptide mixtures containing the adduct nonetheless exhibited FRET switches upon treatment with MMPs. Therefore to determine whether the adduct could be considered an inert artifact of synthesis, the toxicity of crude pB2v(+56) peptide mixture to cells was assessed *in vitro*. A colorimetric MTT assay, the results of which are shown in Figure III-12, indicated no toxicity to three different mouse cancer cell lines upon 24 hours of exposure to a range of peptide concentrations spanning two orders of magnitude. Taken together, the experiments characterizing pB2v validate the requisite optical and biological functions of peptides produced by SPPS for use in proteolytic nanobeacons, even with the inclusion of an unidentified adduct. As such, further studies to identify the origin and structure of the common 56 Da adduct were not pursued.

Having confirmed the feasibility of using SPPS to produce MMP-cleavable peptides endowed with measurable FRET switch potential, the production of dual-targeted peptide constructs further required development and testing of an efficient synthesis technique for the attachment of folic acid to the N-termini of peptides. Despite the presence of two carboxylic acid functional groups in the structure of folic acid and the published use of carbodiimide chemistry to attach folic acid to amine-terminated nanoparticles[57,63,133],

DCC-mediated coupling of folic acid to the N-terminal primary amines of peptides in solution could not be demonstrated effective in our hands (see III.3.3). Reaction of the NHS ester of folic acid (FA-NHS) with peptides in solution was shown by TLC (Figure III-15) and MALDI-TOF MS (Figure III-16) to provide partial but incomplete coupling of folic acid despite the use of excess FA-NHS reactant. Importantly, MALDI-TOF MS of the products of reaction of FA-NHS and broadly MMP-cleavable peptides following treatment with MMP9 (Figure III-17) detected predicted cleavage products but not intact peptides, validating the findings in the previous chapter that folation of substrate peptides does not block MMP cleavage. However, attempts to incorporate N-terminal folation of peptides in SPPS by reacting peptides on solid support resin with FA-NHS were not shown by HPLC or MALDI-TOF MS to induce the expected changes in HPLC retention time or molecular weight (data not shown).

Labeling of peptides with folic acid during as part of solid phase synthesis, while peptides are attached to solid support resin and the side chains of constituent residues are protected from undesired side reactions by acid-labile protecting groups, provides flexibility and extensibility in the design of multifunctional peptides produced by SPPS. The application of HCTU, the aminium-based carboxyl-to-amine coupling mediator used in most couplings during automated SPPS of pB2v, was shown by LCMS (Figure III-19 and Figure III-20) to successfully mediate attachment of folic acid to resin-bound protected pB2v peptide. Importantly, while the resulting peptide mixture contained products including or omitting the K(fam) residue and/or a 56 Da adduct, characteristic of the previous SPPS of pB2v, ions corresponding to peptides absent folic acid were not detected. Furthermore, as seen in Figure III-21, a purified product of HCTU-mediated

folation of pB2v (FApB2v) exhibited up to an 8-fold increase in sensor (FAM) fluorescence upon treatment with MMPs, confirming again that neither attachment of folic acid nor the synthetic steps preceding prohibitively interfered with the fluorescence or MMP-cleavability of substrate peptides produced by SPPS. It should also be noted that the sensor fold-changes up to 8-fold shown in Figure III-21 reflect a conservative calculation of the effect on sensor fluorescence attributable to cleavage of FApB2v, as they do not account for the background emission intensity inherent to the assay conditions. Altogether, the above analyses confirm that folated, FRET-equipped, MMP-cleavable peptides can be produced in total solid phase synthesis and have FRET switches appropriate for optical imaging of MMP activity.

To enable our design of dual-targeted nanoparticles based upon bioconjugation of FRET-equipped MMP substrate peptides to nanoparticle surfaces, we required a synthesis technique that provided efficient coupling and chemoselectivity in mild conditions for compatibility with organic dyes and amino acid side chains. Adapting a published technique for nucleophile-catalyzed oxime ligation of unprotected peptide fragments[130], it was shown by LCMS following synthesis (Figure III-23 and Figure III-24) that incorporation of an aminooxy functional group at the C-terminus of pB2v to yield pB2vAoa peptide could be achieved by SPPS. These peptides were then endowed with a functional group with great selectivity for reaction with carbonyls (ketones and aldehydes)[130,134,135]. However, like previously discussed variations of pB2v peptides synthesized by SPPS, the pB2vAoa crude peptide mixture was found to contain a majority of peptide products lacking the intended K(fam) residue, as shown in Figure III-24. A minority of HPLC-separated synthesis products represented structures with the

predicted molecular weight of pB2vAoa, corroborating the results of previous syntheses suggesting inefficient coupling of Fmoc-Lys(fam)-OH during automated SPPS.

Because incomplete coupling of the K(fam) residue was determined to be a persistent cause of unintended yield from SPPS of FRET peptides and resulted in peptides with no sensor fluorescence to potentiate optical sensing of proteolytic activity, further optimization of pB2vAoa synthesis was necessary. Considering steric hindrance by the multiple aromatic rings of FAM a likely impediment to the coupling reaction, SPPS of pB2vAoa was repeated with substitution of Fmoc-K(ivDDE)-OH for the K(fam) residue. HPLC and LCMS of the resulting peptide, shown in Figure III-26, confirmed more efficient coupling of K(ivDDE) during automated SPPS. Despite the requirement of additional synthesis steps to remove the ivDDE protecting group and to attach FAM via amine-reactive FAMSE, the improved coupling efficiency and lower relative costs of reagents should have made this strategy more economical than the initial design employing the more expensive Fmoc-Lys(5/6-FAM)-OH precursor. LCMS following additional reactions after automated SPPS confirmed successful conjugation of folic acid and FAM, as seen in Table III-2 and Figure III-27, to provide complete synthesis of FApB2vAoa peptide. Additionally, owing to the stability of ivDDE to the conditions required for repeated deprotection of Fmoc during SPPS and its compatibility with deprotection without affecting acid labile protecting groups[131], this strategy also presented the potential to extend applications of SPPS to substrate peptides including moieties not commercially available as lysine conjugates or that are intolerant of the acid-base conditions required for SPPS, such as NIR dyes or drug molecules. However, the

2% hydrazine in NMP solution employed for removal of ivDDE in preparation for FAM attachment was found to alter the quenching fluorophore, TAMRA, as indicated by the anomalous pH-sensitive UV-visible absorbance properties of FApB2vAoa obtained by this synthetic route (Figure III-28). While TAMRA is normally reversibly pH-sensitive, absorbing maximally at 550-560 nm in acidic to neutral pH, the indicated lack of such absorbance by FApB2vAoa at pH 6.5-7.5 consequently hindered its potential FRET switch under physiologic conditions, as quenching of FAM emission was compromised. As such, an alternative ivDDE deprotection scheme employing hydroxylamine hydrochloride and imidazole[132] was attempted and was shown compatible with desired optical properties of TAMRA. However, this strategy was minimally effective at removing ivDDE from the protected lysine residue (data not shown, see III.3.5). As such, further attempts to produce pB2vAoa peptides using K(ivDDE) residue were not pursued.

Instead, I sought to improve yields of pB2vAoa by altering the coupling scheme for Fmoc-Lys(5/6-FAM)-OH during automated SPPS. pB2vAoa peptide was synthesized following the originally devised scheme for SPPS of pB2v (see II.2.11), with the important modifications that: i) Fmoc-Lys(5/6-FAM)-OH was reacted with triple-coupling of 2 molar equivalents of residue relative to resin substitution in each coupling; and ii) an acetic anhydride capping step was added immediately after the third coupling to terminate any peptide products not successfully conjugated with K(fam) prior to coupling the remaining residues. This synthesis strategy was found by HPLC and LCMS analysis of crude peptide mixture (shown in Figure III-29) to produce a much less heterogeneous mixture of peptide products, the majority of which had molecular weights corroborating the inclusion of K(fam). The products of this synthesis also contained an

unidentified 40 Da adduct. Furthermore, the important optical and biological functions of pB2vAoa from triple-coupling SPPS were validated by the demonstration of greater than 15-fold increase in FAM fluorescence after 20 minutes incubation with MMP14 (Figure III-30). Paradoxically, triple-coupling using 2 molar equivalents (relative to resin substitution sites) per coupling required less of the relatively expensive Fmoc-Lys(5/6-FAM)-OH reactant than the previously employed double-coupling using 4 molar equivalents per coupling. Interestingly, as seen in Figure III-29, a minority product corresponding to the structure of pB2vAoa omitting the C-terminal DprAoa residue but not inclusive of any adduct was also detected.

HPLC and LCMS were again used to confirm successful acylation of pB2vAoa from triple-coupling SPPS with either folic acid or acetic anhydride (as described in III.2.7) to yield FApB2vAoa (Figure III-32) or AcpB2vAoa (Figure III-33), respectively. FRET switch was confirmed in an unpurified sample of FApB2vAoa crude peptide (Figure III-31) as well as in HPLC-purified AcpB2vAoa (Figure III-34). The MMP-associated FRET switches in each case were abrogated by the inclusion of EDTA in the assay media, confirming the dependence of the observed fluorescence enhancement on metalloproteinase activity. Additionally, the sensor (FAM) fluorescence emission of cell culture medium containing crude AcpB2vAoa peptide mixture was also shown to increase during 24 hours incubation with human breast cancer cells, as seen in Figure III-35. This effect was partially inhibited by the addition of GM6001, a broad-spectrum MMP inhibitor, suggesting that AcpB2vAoa was cleaved by MMPs in the cell culture medium to generate the increase in FAM emission.

Altogether, the above results validate the triple-coupling SPPS and subsequent N-terminal modification protocol as a robust set of techniques for total solid phase synthesis of folate-targeted, FRET-equipped, MMP-cleavable peptides suitable for oxime ligation reactions for the synthesis of proteolytic nanobeacons. This SPPS protocol is adaptable to any amino acid sequence of interest to generate substrates for other proteolytic enzymes as well as to the inclusion of many other targeting ligands and chemical functional groups for subsequent bioconjugation reactions, and may therefore be of interest to many researchers studying the plethora of human diseases in which protein or peptide degrading enzymes play key roles[126].

CHAPTER IV

SYNTHESIS AND CHARACTERIZATION OF FOLATE-TARGETED PROTEOLYTIC NANOBEACONS

IV.1. INTRODUCTION

The preceding chapters have detailed the design, synthesis, and characterization of beacon peptides exhibiting a detectable increase in visible-spectrum fluorescence upon cleavage by MMPs. The peptides feature N-terminal attachment to either folic acid as a targeting ligand or an acetyl group for inertness, and a C-terminal aminooxy functional group for bioconjugation to nanoparticles or surfaces. The intent of this design is that the portion of a peptide on the N-terminal side of a scissile bond, presenting either folic acid or an acetyl group in addition to the sensor fluorophore (e.g. FAM), should be liberated from the nanoparticle surface upon cleavage by an MMP or MMPs for which the peptide is a selective substrate. In the case of a folate-targeted proteolytic nanobeacon, the liberated peptide fragment represents a folate conjugate that should be readily internalized by cells displaying membrane-anchored folate receptors[136,137].

With a robust protocol for the synthesis of these multifunctional peptide linkers established, selection of a suitable nanoparticle core for proteolytic nanobeacons was also required. As discussed earlier (see I.3), nanoparticles for tumor-targeted proteolytic nanobeacons should have at least one dimension greater than about 10 nm and no dimensions much larger than 100 nm to avoid rapid secretion in the kidneys, avoid undesired diffusion throughout body tissues, and to take advantage of the EPR effect in solid tumors. Additionally, the nanoparticle cores of nanobeacons must present a suitable

functional group for bioconjugation with peptides and other molecules important for biocompatibility (e.g. PEG). Finally, the nanoparticles themselves must ultimately be relatively non-toxic in the form injected for systemic administration.

Several candidate classes of nanoparticles meeting these criteria were considered. Our laboratory previously reported detection of MMP7 activity using proteolytic nanobeacons based on PAMAM dendrimers[24]. PAMAMs are well-studied, commercially available in several nominal sizes with different numbers of surface functional groups, and amenable to several types of bioconjugation reactions. However, prepared PAMAM solutions are typically relatively polydisperse due to the divergent generational synthesis employed in the production of PAMAMs. Furthermore, the primary amines at branch termini effectively present a polycationic surface with a high-positive Zeta potential that may lead to nonspecific cell uptake and potentially undesirable elimination from circulation *in vivo*[138]. A substantial fraction of the amine termini must be functionalized or terminated with neutral or anionic groups to abrogate this effect and improve biocompatibility.

Fréchet-style polyester dendron nanoparticles have also been employed previously by our laboratory for the synthesis of MMP9-responsive carriers of near-infrared fluorophores and/or paclitaxel (PXL)[109]. Dendrons of this type can be synthesized rapidly and efficiently[139] with defined sizes and near monodispersity by convergent synthesis schema[140]. The diversity of available terminal cores for organic dendrons also provides the ability to mix-and-match differently equipped dendrons for multiplexed conjugates of imaging agents and drug molecules (Scherer et al, unpublished). However, *in vivo* imaging studies with nanodendron-based proteolytic nanobeacons indicated substantial accumulation of dendrons in mouse livers following parenteral administration

(Sameulson et al, unpublished). The cause(s) of this accumulation have not be elucidated, but there is very likely a size-dependent influence on biodistribution of dendrons[104,106,138].

We also considered partially inorganic nanoparticles for use as multifunctional cores in proteolytic nanobeacon design. Iron oxide (FeOx) nanoparticles have been increasingly used for biomedical imaging applications and are commercially available or easily synthesized with biocompatible surface coatings amenable to several types of bioconjugation reactions. For example, dextran-coated FeOx nanoparticles may be synthesized with either amine or carboxylic acid functional groups on their surfaces and typically have hydrodynamic diameters ranging 20-45 nm[141], a size range that has been reported to be optimal for the EPR effect and cellular internalization with other spherical inorganic nanoparticles[142]. Unlike the organic nanoparticles discussed above, FeOx nanoparticles innately enable additional imaging modalities such as magnetic resonance contrast, transmission electron microscopy (TEM) without additional staining, and histology of tissue sections by Prussian blue staining. Separation and recovery of FeOx-based nanoparticles may also be simplified owing to the superparamagnetic property of Fe_3O_4 (magnetite) and its oxidized analogue, γ-Fe_2O_3 (maghemite). However, strong absorbance in the UV-visible region of the electromagnetic spectrum by iron is a concern for spectrophotometric analyses of such nanoparticles, though fluorescein-labeled FeOx imaging agents have been reported in the literature [66,143–146]. Conceivably, this absorbance could serve as a quencher of sensor (FAM) in addition to TAMRA in intact nanobeacons, leading to the potential for even greater relative FRET switch and S/R ratio increase upon MMP cleavage.

The research that follows documents the development and troubleshooting of strategies to covalently attach peptides and other molecules to nanoparticles for the purpose of synthesizing folate-targeted proteolytic nanobeacons. Weighing the advantages and potential pitfalls of each class of nanoparticle described above, FeOx nanoparticles were chosen as the principal candidates for bioconjugation with FRET-equipped MMP substrate peptides. Despite several attempts at nanobeacon synthesis using FeOx-based nanoparticles and data suggesting attachment of peptides to FeOx nanoparticles, FRET switches indicative of proteolytic cleavage were not observed from nanobeacons of this type. The results of i) troubleshooting of the reaction conditions and each of the reactants for oxime ligation; ii) revisited analysis of the peptide-nanoparticle linking chemistry; and iii) synthesis of nanobeacons using a peptide with a lengthier hydrophilic spacer at its C-terminus collectively indicated steric hindrance and impurities in peptide mixtures from SPPS as the probable causes for ineffective bioconjugation reactions. To address these issues, a peptide with a flexible, hydrophilic spacer group near the C-terminus was synthesized and used for nanobeacon synthesis. Ultimately, the successful synthesis of folate-targeted proteolytic nanobeacons on organic PAMAM dendrimers as well as preliminary evidence of folate-dependent nanobeacon uptake *in vitro* is presented below.

IV.2. Materials and Methods

IV.2.1. General Methods

Materials. All chemicals and biochemicals were reagent-grade or HPLC-grade and solutions were prepared in filtered deionized water (dH_2O) (Milli-Q, Billerica, MA, USA). Unless otherwise noted, all chemicals were purchased from either Sigma Aldrich

(St. Louis, MO, USA) or Thermo Fisher Scientific (Waltham, MA, USA). Chemical reactions were performed protected from light and at RT with rocking unless otherwise specified. Dextran-coated iron oxide nanoparticles ("IDX"), with 5 nm iron-oxide cores and 30 nm hydrodynamic diameter according to the manufacturer's quality assessments were purchased from Ocean Nanotech (Springdale, AR, USA). mPEG-SH(1k) was obtained from Creative PEGWorks (Winston Salem, NC, USA). Generation 4 Starburst® polyamido amine dendrimer (PAMAM4) was purchased from Sigma Aldrich (St. Louis, MO, USA). MDA-MB-468 human breast adenocarcinoma cells were obtained from ATCC (Manassas, VA, USA).

Mass spectrometry. LCMS was performed as described above (see II.2.1). Electrospray ionization mass spectrometry in positive ion mode (ESI+ MS) was performed using the same instrumentation as LCMS. Samples were injected using the autosampler of the UPLC system by mixture with 5:95 H_2O:MeCN with 0.2% formic acid for injector flow.

IV.2.2. Introduction of aldehydes on dextran-coated iron oxide nanoparticles

Measurement of iron content. Iron (Fe) concentration of iron oxide nanoparticle suspensions was determined according to manufacturer's recommended protocol. UV-visible spectra of suspensions were recorded and the absorbance at 500 nm used to calculate Fe mass concentration using the provided extinction coefficient of 3.25 $mg(Fe)^{-1}*mL*cm^{-1}$.

General oxidation procedure. 900 µL of sodium *meta*-periodate ($NaIO_4$) oxidant diluted to various concentrations in dH_2O was added to 100 µL (1 mg Fe equivalent) of IDX nanoparticles (nominally 10 mg/mL Fe as purchased) in Eppendorf microcentrifuge

tubes and vortexed on low speed, protected from light, for 1 hour, to afford oxidized IDX nanoparticles termed oIDX[n], where [n] indicates the concentration of $NaIO_4$ oxidant applied during oxidation. Nanoparticle suspensions were then dialyzed (1,000 MWCO) against 1-4 L dH_2O for 48 hours with several replacements of dialysate with fresh dH_2O.

Aldehyde quantitation. Amplite™ Fluorimetric Aldehyde Quantitation kit was obtained from AAT Bioquest (Sunnyvale, CA, USA). The assay was performed according to supplier instructions with minor modifications. Due to optical interference from the broad UV-visible absorption of Fe, the provided aldehyde standards solutions were spiked with IDX nanoparticle stock solution to give a final assay concentration of 1 mg/mL Fe in each well. All sample solutions were also adjusted to 1 mg/mL Fe following determination of iron content by spectrophotometry (see above). The estimated number of aldehydes per nanoparticle in each sample was calculated by dividing the interpolated aldehyde concentration by the nanoparticle number concentration that was calculated from the spectrophotometrically measured Fe concentration and expected mass of iron in each nanoparticle core based on the density of iron oxide (5.49 g/cm^3, 70% Fe)[147] and the supplier's size measurements (e.g. 1 mg/mL Fe corresponds to 6.9 nMoles/mL of IDX nanoparticles with 5 nm-diameter cores).

IV.2.3. Nanoparticle synthesis by oxime ligation

To each of two Eppendorf microcentrifuge tubes were added 246 µL (2 nmol) oIDx-500uM nanoparticles in dH_2O and 3 µL (33 µmol) aniline. Then, 18 µL (6 nmol) or 36 µL (12 nmol) FApB2vAoa in 10% DMF was added slowly to give "NP_3^{++}" and "NP_6^{++}" reaction mixes, respectively. Reactions were allowed to proceed for approximately 5 days before attempted recovery of nanoparticles. Approximately 10% of each reaction mix

was aliquotted for later analysis and the remainder of each mix was diluted to 500 µL total volume in dH_2O.

Diluted reaction mixes were transferred to Amicon Ultra 10k (NMWL 10,000) centrifugal filter devices (EMD Millipore, Darmstadt, DE) and centrifuged according to supplier instructions. To aid in recovery of aggregated samples, 450 µL dH_2O was added to filter devices and thorough sonication and repeated dispersion by pipetting performed. Mock reactions containing 18 µL (6 nmol) FApB2vAoa and 3 µL (33 µmol) aniline with or without inclusion of 246 µL (2 nmol) IDX non-oxidized nanoparticles in dH_2O ("+++ Ctl" and "++ Ctl," respectively) were assembled as controls. All containers for collection of reaction mix and recovered product components were weighed before and after collection in order to determine relative amounts of material recovered.

Recovered NP_n^{++} reaction mixes and concentrates were characterized by UV-visible spectrophotometry (general method, see II.2.1) and fluorescence spectroscopy using opaque 96-well plates in a fluorescence plate reader using excitation wavelengths of 495 nm and 555 nm. To assess the relative amount of peptide-associated FAM and TAMRA dyes in each sample, absorption spectra were corrected by scaling the spectrum of the parental (oIDX-500uM, non-reacted) nanoparticle to the sample absorbance at 400 nm (a relative minimum for the dye species) and subtracting the scaled spectrum from the sample spectrum, the difference representing added absorbance presumed attributable to the peptide-associated dyes.

Recovered NP_6^{++} concentrate from ultrafiltration (above) was subsequently pelleted by centrifugation at 14,000 relative centrifugal force (rcf), washed twice with 200 µL MeOH and centrifugation at 2,000 rcf, and resuspended in 400 µL dH_2O with sonication.

The resulting suspension was serially diluted in dH_2O to 1:3 and 1:10 dilutions and the dilution series analyzed by plate reader fluorescence spectroscopy using excitation wavelengths of 495 nm and 555 nm and emission bandwidths of 5 nm and 10 nm.

IV.2.4. Oxime ligation comparing nucleophilic catalysts

To three microcentrifuge tubes containing 182 µL (2 nmol) oIDX-1000uM nanoparticles in dH_2O, each, were added 3.3 µL (3.3 µmol) p-phenylenediamine (pPDA) and 36 µL (12 nmol), 71 µL (24 nmol), or 107 µL (36 nmol) FApB2vAoa in 10% DMF to generate "NP_6^{++} pPDA," "NP_{12}^{++} pPDA," and "NP_{18}^{++} pPDA" reaction mixes respectively. Similarly, 3 µL (33 µmol) aniline and 36 µL (12 nmol) FApB2vAoa in 10% DMF were added to a microcentrifuge tube containing 182 µL (2 nmol) oIDX-1000uM nanoparticles in dH_2O to generate "NP_6^{++} An" reaction mix. Two control reaction mixes were set up, either with no nanoparticles or with 22 µL (2 nmol) IDX (non-oxidized) nanoparticles in dH_2O. To each was added 36 µL (12 nmol) FApB2vAoa in 10% DMF to prepare "No-IDX Ctl" and "No-Rxn Ctl" reaction mixes, respectively. To all reaction mixes including controls were added 33 µL 1 M sodium phosphate buffer (pH 6.0) and dH_2O sufficient to bring total volume to 330 µL. Reactions were then allowed to proceed 24 hours before further workup.

Reaction mixes were separated and components recovered by centrifugation, precipitation, and magnetic separation. All reaction mixes were handled identically, first by centrifugation at 10,000 rcf for 10 minutes to pellet suspended inorganic nanoparticles. Supernatants were aspirated while pellets were held stationary using a 1 Tesla magnet. Pellets were then twice washed with 330 µL MeOH with vortexing and sonication and pelleted as before. Final pelleted solids were resuspended in 330 µL dH_2O

each and subsequently analyzed by UV-visible spectrophotometry and plate reader fluorescence spectroscopy, as with NP_n^{++} nanoparticles (see IV.2.3, above).

IV.2.5. Oxime ligation with fresh aniline catalyst in organic solvent

484 µL (5 nmol) oIDX-1000uM and 55 µL (5 nmol) IDX nanoparticles were each precipitated separately by increasing volume to 1.9 mL in microcentrifuge tubes with EtOH. Each nanoparticle slurry was then centrifuged at 12,000 rcf for 5 minutes and pellets held with a 1 Tesla magnet while supernatants were decanted. Pellets were air dried and resuspended in 145 µL DMSO each. 19.4 µL 1 M sodium acetate (pH 4.5) buffer was added to nanoparticle suspensions and each sonicated gently. 59.5 µL (200 nmol) FApB2vAoa in DMSO was combined with 4 µL (44 µmol) aniline from a freshly opened supplier's bottle. 31.75 µL (100 nmol FApB2vAoa equivalent) of this mixture was added to each nanoparticle suspension and reacted for 5 days.

Nanoparticle products of reactions were precipitated by pipetting reaction mixes into 1.6 mL ice cold MeOH and pelleted by centrifugation at 12,000 rcf for 10 minutes at 0 °C. Supernatants ("Supernatant 1") were collected by aspiration, holding pellets with a 1 Tesla magnet, prior to adding 200 µL ice cold MeOH to pellets. The above processes were repeated, culminating in the collection of "Supernatant 2" from each tube and air drying of each nanoparticle pellet using 1 Tesla magnet to retain drying solids. Pellets were resuspended in 145 µL DMSO each with sonication and 10 µL aliquots diluted into 1 mM phosphate buffer (pH 7.0) for UV-visible spectrophotometry.

Resuspended nanoparticles in DMSO were subsequently precipitated again by pipetting slowly into 1 mL ice cold MeOH. The resulting turbid mixtures were gently sonicated and centrifuged as above to provide "Supernatant 3" from each tube.

"Supernatant 4" was similarly obtained by washing nanoparticle pellets with 1 mL MeOH. Following air drying, pellets were once again resuspended in 135 µL DMSO each and 6 µL aliquots diluted in 1 mM phosphate buffer (pH 7.0) for UV-visible spectrophotometry.

Nanoparticles suspended in DMSO were once more precipitated by slowly pipetting into 500 µL ice cold MeOH in microcentrifuge tubes on a DynaMag™-spin magnetic separator (Life Technologies, Carlsbad, CA, USA). Supernatants were collected and transferred to empty microcentrifuge tubes on the magnetic separator. Nanoparticle pellets were resuspended in 129 µL each DMSO and 6 µL aliquots measured by UV-visible spectrophotometry as before. Because magnetically-separable solids were still discovered in the transferred solutions, the newly-formed supernatants were again collected and labeled "Supernatant 5.1". 300 µL 1 mM phosphate buffer (pH 7.0) was added to magnetically retained solutes and the resulting solutions labeled "Supernatant 5." In summary, from each of the two reactions were derived the following fractions: reaction mix, supernatants 1-5, and supernatant 5.1, and final product. Spectrophotometric measurement of the UV-visible absorbance of each fraction and a diluted sample of recovered nanoparticle products was performed after each centrifugal or magnetic separation.

IV.2.6. Peptide-focused troubleshooting of oxime ligation

Trypsin cleavage. 5 µL (1.7 nmol) FApB2vAoa in 10% DMF was combined with 40 µL dH_2O and 5 µL trypsin (0.2 mg/mL) in dH_2O and incubated several hours at RT. Molecular weights of products resulting from the cleavage reaction were determined by LCMS (general method, see II.2.1).

Diagnostic reaction. 14.9 µL (50 nmol) FApB2vAoa, 7.5 µL 4-formylbenzoic acid, and 3 µL fresh aniline (300 nmol) all in DMSO were combined and reacted for 6 hours at RT. 1 µL (3.4 nmol) FApB2vAoa and 1 µL reaction mix were each diluted with 99 µL 95:5 H_2O:MeCN with 0.2% formic acid and analyzed by ESI+ MS (see IV.2.1) to assess the extent of reaction, if any.

IV.2.7. Nanoparticle synthesis via Steglich esterification

Synthesis of carboxyl-terminated FRET peptide. Fmoc-Gly-Wang LL Resin (100-200 mesh) was purchased from EMD Chemicals (Billerica, MA, USA). A broadly MMP-cleavable FRET peptide based on the structure of pB2v, "pB2vp-cooh" [Fmoc-{peg_1}K(fam){peg_1}RPLGLWAR{peg_1}K(tamra){peg_1}G-cooh], was synthesized by SPPS on Fmoc-Gly-Wang resin with an intended maximum yield of 25 µmol in a procedure analogous to previously synthesized peptides (see II.2.11). pB2vp-cooh on resin was acetylated as described previously (see III.2.7) and final deprotection and cleavage from solid support performed using cleavage cocktail R to generate "AcpB2vp-cooh" [Ac{peg_1}K(fam){peg_1}RPLGLWAR{peg_1}K(tamra){peg_1}G-cooh].

Nanoparticle synthesis (attempted). Attachment of AcpB2vp-cooh to IDX nanoparticles displaying secondary alcohols of dextran polymers on their surfaces was attempted according to a published scheme for Steglich esterification of amino acids to starch derivatives [148]. 110 µL (10 nmol) IDX nanoparticles in dH_2O were precipitated in MeOH and resuspended in 145 µL DMSO with thorough sonication, as described in detail previously (see IV.2.5). To this were added (in order) 12.7 µL (50 nmol) AcpB2vp-cooh, 2.4 µL (15 nmol) N,N'-diisopropylcarbodiimide (DIC), and 4.0 µL (4 nmol) 4-

dimethylaminopyridine (DMAP), all in DMSO. The mixture was reacted for 20 hours in air-free conditions with continuous nitrogen bubbling before the reaction was quenched by addition of 4 µL dH_2O. Nanoparticle products were precipitated by pipetting the reaction mix into ice cold methanol on a magnetic separator device as described previously (see IV.2.5). Magnetically recovered nanoparticles were reconstituted in 150 µL DMSO and peptide attachment was characterized as described previously (see IV.2.3) by UV-visible spectrophotometry with dilution of nanoparticle solution in 100 mM phosphate buffer (pH 7.3).

IV.2.8. Nanoparticle synthesis via carbodiimide coupling to quantum dots

Qdot® 605 ITK™ Amino (PEG) Quantum Dots ("Qdot(605)NH_2," Life Technologies, Carlsbad, CA, USA) were a generous gift from the Rosenthal Laboratory (Dept. of Chemistry, Vanderbilt University, Nashville, TN, USA). 1-ethyl-3-(3-dimethylaminopropyl) carbodiimide hydrochloride (EDAC) was obtained from Calbiochem (La Jolla, CA, USA). "Borate buffer" hereafter refers to 100 mM sodium borate buffer (pH 8.5) unless otherwise specified.

Using reaction conditions recommended by Ian Tomlinson, Ph.D. (personal communication), to 10 µL (80 pmol) Qdot(605)NH_2 in 50 mM borate (pH 8.3) were added (in order) 90 µL borate buffer, 10 µL (8 nmol) Peptide 13c (see II.2.8) in DMF, 10 µL (8 nmol EDAC) in borate buffer, and100 µL additional borate buffer to give "100:100:1" (where ratios represent molar equivalents of peptide:EDAC:Qdot) reaction mix. "No EDAC Control" (100:0:1) reaction mix was generated by reproducing the above mixture but substituting 10 µL borate buffer instead of EDAC. A "No Peptide Control" sample (0:100:1) was similarly produced by substituting 10 µL DMF instead of

Peptide 13c. “1000:500:1” reaction mix was composed of 10 µL (80 pmol) Qdot(605)NH_2 in 50 mM borate (pH 8.3), 100 µL (80 nmol) Peptide 13c in DMF, 14 µL (40 nmol EDAC) in borate buffer, and 100 µL borate buffer and was reacted with stirring for approximately 65 minutes. “2000:1500:1” reaction mix consisted of 10 µL (80 pmol) Qdot(605)NH_2 in 50 mM borate (pH 8.3), 200 µL (160 nmol) Peptide 13c in DMF, and 15 µL (120 nmol EDAC) in borate buffer.

The above reaction mixes and samples were reacted with magnetic stirring in glass scintillation vials. Following 90 minutes and overnight reaction, 5 µL per well of the reaction mixes and samples were analyzed by electrophoresis in freshly cast 1% agarose gels in TAE buffer on ice, with samples migrating towards the cathode. Qdot(605)NH_2 was diluted in borate buffer to the same concentration as in reaction mixes and to serve as the reference point for electrophoretic mobility. Gels were visualized following electrophoresis by ultraviolet excitation in a BioDoc-It® Gel Imaging System (UVP, Upland, CA, USA).

IV.2.9. Nanoparticle synthesis via carbodiimide coupling to organic dendrimers

Coupling of peptides to PAMAM dendrimers was tested by combining 10 µL (56 nmol) PAMAM4 in MeOH, 147 (112 nmol) Peptide 13c in DMF, and 10 µL (223 nmol) EDAC in MeOH and allowing reaction overnight at RT with constant stirring. A non-reactive mixture (“No Rxn”) was generated in parallel by reproducing above reaction mix but substituting 10 µL MeOH for EDAC.

Following overnight reaction, 3.2 mL 2 mM EDTA in dH_2O was added to each mixture and 300 µL conserved for later analysis. Diluted reaction mixes were then concentrated by ultrafiltration in Centriprep YM3 devices (EMD Millipore, Darmstadt,

DE) according to supplier instructions. Due to adsorption of colored solutes onto YM3 filter membranes in both mixtures, 4 mL of 1 mM EDTA in 50% EtOH solution was added to devices to dissolve and recover solutes. Diluted YM3 retentates were again concentrated by ultrafiltration in Centriprep YM10 devices (MWCO 10,000 Da). Dilution and concentration of each sample was repeated in the same YM10 devices with 4 mL 1 mM EDTA in 50% ethanol solution. Retentates and effluents containing 50% EtOH from YM10 devices were recombined and concentrated using YM3 devices. All recovered solutions were subsequently diluted at least 1:2 in PBS (pH 7.1) for analysis by UV-visible spectroscopy using a Varian Cary 50 Bio spectrophotometer (Agilent, Santa Clara, CA, USA).

IV.2.10. Synthesis of a broadly MMP-cleavable FRET peptide with a flexible C-terminal linker and cysteine for bioconjugation

Fmoc-Cys(Trt)-Wang Resin was purchased from Anaspec (Fremont, CA, USA). Fmoc-NH-PEG_5-CH_2COOH was purchased from ChemPep (Wellington, FL, USA). A broadly MMP-cleavable FRET peptide based upon the design of pB2v peptide with a C-terminal hydrophilic spacer and cysteine, "pB2vp5C-cooh" [Fmoc-{peg_1}K(fam){peg_1}RPLGLWAR{peg_1}K(tamra){peg_5}C-cooh], was synthesized by SPPS on Fmoc-Cys(Trt)-Wang resin using the triple-coupling scheme developed for pB2vAoa (see III.2.8). 126 mg Fmoc-Cys(Trt)-Wang resin with 0.55 mmol/g substitution was down-loaded by coupling of 107 mg (206 µmol) Fmoc-NH-PEG_5-CH_2COOH with 81 mg (196 µmol) HCTU activator on the PS3 automated peptide synthesizer. Substitution (available N-termini for coupling) following down-loading was determined to be 0.33 mmol/g by comparing absorbance of Fmoc-deprotection solutions from untreated and down-loaded resin at 301 nm corresponding to

released Fmoc protecting groups. Resin substitution sites not coupled with PEG_5 were subsequently blocked by acetylation with 25% acetic anhydride, 25% pyridine, 50% NMP solution using the standard capping program on the PS3 instrument. Automated SPPS then proceeded as described previously with a corresponding intended scale of 40 µmol peptide based on down-loading of the resin.

pB2vp5C-cooh peptide on resin was folated as described previously (see III.2.7) to generate FApB2vp5C-cooh FRET peptide [fa-{peg_1}K(fam){peg_1}RPLGLWAR{peg_1}K(tamra){peg_5}C-cooh]. An analytical sample of FApB2vp5C-cooh was generated by submerging fa-peptide-resin in cleavage cocktail containing 90% TFA, 5% thioanisole, 2.5% TIPS, and 2.5% dH_2O, blanketing with nitrogen gas, and vortexing protected from light for 2 hours prior to precipitation in ice cold Et_2O as described previously (II.2.11). The analytical sample of uncharacterized mass/amount was dissolved in 500 µL MeOH and further diluted 1:10 in 95:5 H_2O:MeCN with 0.2% formic acid [LCMS mobile phase (A)] and characterized by ESI+ MS and LCMS (see IV.2.1).

A stock of FApB2vp5C-cooh was generated by final deprotection and detachment from solid phase resin in cleavage cocktail as before (see above), precipitated in Et_2O, and lyophilized to yield 12.1 mg of dry crude peptide mixture. 3.8 mg of unpurified FApB2vp5C-cooh was dissolved in 380 µL anhydrous DMSO and further diluted 1:100 in PBS (pH 7.1) for analysis by UV-visible spectrophotometry. The concentration of TAMRA dye, a surrogate measure of peptide concentration, was determined by absorption of the solution at 562 nm and application of the Beer-Lambert Law using an empirically determined extinction coefficient of TAMRA dye (72,110 $M^{-1}cm^{-1}$).

To assess the FRET switch of FApB2vp5C-cooh peptide, 1 µL (57 pmol) FApB2vp5C-cooh in 5:95 DMSO:PBS (pH 7.1) containing equimolar β-mercaptoethanol ("reduced FApB2vp5C-cooh") was diluted to 100 µL total volume in FRET switch assay buffer and analyzed by plate reader fluorescence spectroscopy with excitation at 494 nm and 555 nm. FApB2vp5C-cooh was also assessed by FRET switch assay with MMPs-2,9,14 by dilution of reduced FApB2vp5C-cooh solution to approximately 700 nM final assay concentration in standard assay buffer (see general method, II.2.3).

IV.2.11. Nanoparticle synthesis via heterobifunctional linker-mediated conjugation to amine-bearing iron oxide nanoparticles

SIA, sulfosuccinimidyl-4-(p-maleimidophenyl)butyrate (Sulfo-SMPB), and tris(2-carboxyethyl)phosphine hydrochloride (TCEP) were purchased from Pierce Chemical (Rockford, IL, USA). Recombinant human MMP14 catalytic domain (MMP14) was purchased from Enzo Life Sciences (Farmingdale, NY, USA). γ-Fe_2O_3 nanoparticles (FeOx) with core diameters of approximately 17 nm were synthesized and aminated with (3-aminopropyl)triethoxysilane (APTES) by Charleson Bell of the Giorgio Laboratory (Dept. of Biomedical Engineering, Vanderbilt University, Nashville, TN, USA) as described[149] to afford FeOx-NH_2 nanoparticles. Amine functionalization of FeOx-NH2 was confirmed by qualitative Ninhydrin assay (see III.2.4). Iron (Fe) and number concentrations of FeOx-NH_2 nanoparticles were characterized by measuring absorbance of suspensions at 500 nm and applying the Beer-Lambert Law with an extinction coefficient of 5 $mg^{-1}mLcm^{-1}$ and converting Fe concentration to nanoparticle number concentration using the same formula that was applied to IDX nanoparticles (see IV.2.2).

Prior to the coupling reaction, 75 µL (523 nmol) TCEP in DMSO was added to 25 µL (32 nmol) FApB2vp5C-cooh in DMSO and reacted 50 minutes to reduce any disulfide

bonds that may have formed between peptides in solution. In parallel, 100 µL (30 pmol) FeOx-NH_2 nanoparticles in DMSO were separately combined with 10 µL (37.5 nmol) of either SIA or Sulfo-SMPB in DMSO and reacted 50 minutes to generate activated "FeOx-IA" and "FeOx-mal" solutions. 47 µL (15 nmol peptide equivalent) reduced FApB2vp5C-cooh was added to FeOx-IA and FeOx-mal solutions to produce "NP^{++}_{SIA}" and "NP^{++}_{SMPB}" reaction mixes, respectively, and reaction vessels flushed with nitrogen gas prior to overnight reaction with vortexing, protected from light. 2.4 mg (2.4 µmol) mPEG-SH(1k) was dissolved in 1.07 mL (7.4 µmol) TCEP in DMSO solution to reduce and prevent oxidation of sulfhydryl functional groups. 10 µL (22.5 nmol mPEG-SH(1k) equivalent) of this solution was added to each NP^{++}_{SIA} and NP^{++}_{SMPB} reaction mixes and vortexing continued 90 minutes.

Nanoparticle products of reactions were pelleted by magnetic attraction using a 1 Tesla magnet and supernatants collected for subsequent analysis. 250 µL DMSO was added to each pellet and magnetic separation repeated. Final nanoparticle pellets were resuspended with 100 µL anhydrous DMSO. Peptide recovery and attachment to FeOx-NH_2 nanoparticles was assessed by UV-visible spectrophotometry of recovered supernatant solutions diluted in PBS (pH 7.1). Magnetic separation was used to exchange DMSO for EtOH in NP^{++}_{SIA} and NP^{++}_{SMPB} solutions prior to further 1:10 dilution in EtOH and analysis by fluorescence plate reader spectroscopy. Transmission electron microscopy (TEM) with energy-dispersive X-ray spectroscopy (EDX) of NP^{++}_{SIA} nanoparticles in EtOH was performed by Charleson Bell. FRET switch assay of FeOx-based NP^{++}_{SIA} and NP^{++}_{SMPB} was performed with MMP14 (740 ng/mL final assay concentration) by diluting nanoparticles in standard assay buffer (see II.2.3). Because

nanoparticles flocculated in assay wells, supernatants were transferred to new assay wells and the fluorescence of the iron-depleted solutions was reassessed.

IV.2.12. Nanoparticle synthesis via bioconjugation to organic dendrimers

Methoxyl PEG succinimidyl ester, MW 5000 (PEG5000-NHS) was purchased from Nanocs (Boston, MA, USA).

PAMAM4 was PEGylated by combining 145 µL (870 nmol) PAMAM4 in MeOH with 104 µL (1.74 µmol) PEG5000-NHS in MeOH and reacting 30 minutes to generate "PAMAM4(PEG5k)$_2$." Two PAMAM activation reactions were composed by reacting 10 µL (35 nmol) PAMAM4(PEG5k)$_2$ with 35 µL (438 nmol) of either SIA or Sulfo-SMPB for 40 minutes. FApB2vp5C-cooh was reduced to eliminate disulfide dimers that may have formed in solution by combining 129 µL (165.5 nmol) FApB2vp5C-cooh in DMSO with 16.5 µL (165 nmol) β-mercaptoethanol in EtOH and reacting 40 minutes. Three parallel bioconjugation reactions were performed in glass 1.0 mL Reacti-Vials (Thermo Fisher Scientific, Waltham, MA, USA) to synthesize multifunctional nanoparticles from the intermediate materials above. 44 µL (50 nmol peptide equivalent) reduced FApB2vp5C-cooh solution, 5 µL (250 nmol) EDAC, and 14.5 µL (10 nmol) PAMAM4(PEG5k)$_2$ solution were combined to form "NP^{++}_{EDAC}" reaction mix. 44 µL (50 nmol peptide equivalent) reduced FApB2vp5C-cooh solution and 11.5 µL (10 nmol) of either SIA- or Sulfo-SMPB-activated PAMAM4(PEG5k)$_2$ solutions were combined to form "NP^{++}_{SIA}" and "NP^{++}_{SMPB}" reaction mixes, respectively. Reaction vials were blanketed with Argon gas and all reactions proceeded overnight at RT with gentle rocking, protected from light. Following overnight reaction, 10 µL (75 nmol) of mPEG-

SH(1k) was added to NP^{++}_{SIA} and NP^{++}_{SMPB} reactions, each, to terminate any unreacted maleimides on nanoparticle surfaces.

The products of nanoparticle synthesis reactions above were concentrated by ultrafiltration, as described previously (see II.2.2, IV.2.9). "EDTA buffer" hereafter refers to 1 mM EDTA in dH_2O treated with 1 mM PMSF. Reaction mixes were diluted with 10 volumes EtOH and 39 volumes EDTA buffer to give final volumes of 3.2 mL each for concentration by ultrafiltration in Centriprep YM10 devices. After one round of concentration to less than 1 mL retained volume, concentrates were diluted with 600 µL EtOH and 2.4 mL EDTA buffer and again concentrated in the same YM10 devices. Concentrated retentates were collected by aspiration and combined with two washes of retentate compartments with 150 µL each of 20:80 EtOH:EDTA buffer. FApB2vp5C-cooh peptide recovery and conjugation to PAMAM nanoparticles in each reaction was assessed by UV-visible spectrophotometry of the effluents and concentrate collected from ultrafiltration diluted in PBS (pH 7.1). As with previous solution, concentrations of recovered nanoparticle solutions was determined by absorption at 562 nm and application of the Beer-Lambert Law using an empirically determined extinction coefficient of TAMRA dye (72,110 $M^{-1}cm^{-1}$) that is similar to reported values for tetramethylrhodamine-based dyes[150].

The FRET switches of NP^{++}_{EDAC}, NP^{++}_{SIA}, and NP^{++}_{SMPB} with MMP9 (nominally 5 µg/mL final assay concentration, provided by Gilead Sciences, Foster City, CA, USA) were assessed by standard assay procedures (II.2.3) with alteration of the assay buffer to account for EDTA content of nanoparticle solutions. To 1.0 mL of a 10X concentrated stock of standard assay buffer were added 10 µL (200 nmol) $ZnSO_4$ and 5 µL (1 µmol)

PMSF. Stocks of 200 mM EDTA and dH_2O were also treated with PMSF (1 mM final concentrations) prior to use in sample preparation for FRET switch assays. Final concentrations of NP^{++}_{EDAC}, NP^{++}_{SIA}, and NP^{++}_{SMPB} were estimated to be 360 nM, 370 nM, and 320 nM, respectively, based on absorbance measurements (see above). Fluorescence was recorded by plate reader every minute for 2 hours, then every 30 minutes for 12 additional hours.

IV.2.13. In vitro assessment of folate- and MMP-dependent NP^{++}_{EDAC} uptake

Phenol red-free RPMI 1640 and folate-free RPMI 1640 media were purchased from Life Technologies (Carlsbad, CA, USA). MDA-MB-231 human breast adenocarcinoma cells were purchased from ATCC (Manassas, VA, USA). Microscopy was performed using a Nikon Eclipse Ti inverted fluorescence microscope (Nikon Instruments, Melville, NY) and images analyzed using ImageJ software (NIH, Bethesda, MD, USA). Fluorescence of plated samples was measured using a TECAN Infinite F500 multimode microplate reader (Tecan Group, Männedorf, CH).

Fluorescence Microscopy. 8-chamber slides (Thermo Scientific, Waltham, MA, USA) were coated with fibronectin and seeded with 12,000 MDA-MB-231 cells per chamber in phenol red-free RPMI-1640 medium containing 1% fetal bovine serum (FBS). Cell treatment conditions were made in folate-free RPMI 1640 medium with 1% FBS, 20 μM $ZnSO_4$ and 100 nM NP^{++}_{EDAC} (except control, no beacon). Treatment media were prepared the day before cell exposure with or without approximately 700 ng/mL MMP14 and with or without 1.1 mg/mL free folic acid and baseline fluorescence determined using a microplate reader. After overnight expansion of cells, cell growth medium was removed and cells were incubated with treatment media for 4 hours.

Following treatment, media were removed to microplates for separate analysis and cells were washed and covered with PBS before imaging by fluorescence microscopy. Fluorescence of conditioned treatment media was assessed again by microplate reader.

Flow Cytometry. MDA-MB-231 cells from fluorescence microscopy were harvested using standard cell culture techniques employing 0.25% trypsin-EDTA (Life Technologies, Carlsbad, CA, USA) and suspended in sterile PBS. Flow cytometry was performed on recovered cells using a BD FACSCalibur™ flow cytometer with a single 488 nm excitation source (BD Biosciences, San Jose, CA, USA). Flow cytometry data was analyzed using FlowJo software (Tree Star, Ashland, OR, USA).

IV.3. RESULTS

IV.3.1. Introduction and quantification of aldehydes on dextran-coated iron oxide nanoparticles

In order to prepare nanoparticles for oxime ligation with multifunctional peptides from SPPS (e.g. FApB2vAoa, see III.3.4 and III.3.6), dextran-coated iron oxide nanoparticles (IDX) were oxidized with sodium *meta*-periodate ($NaIO_4$), a well-established technique to introduce aldehyde functional groups in dextran polymers[129], as schematically represented in Figure IV-1.

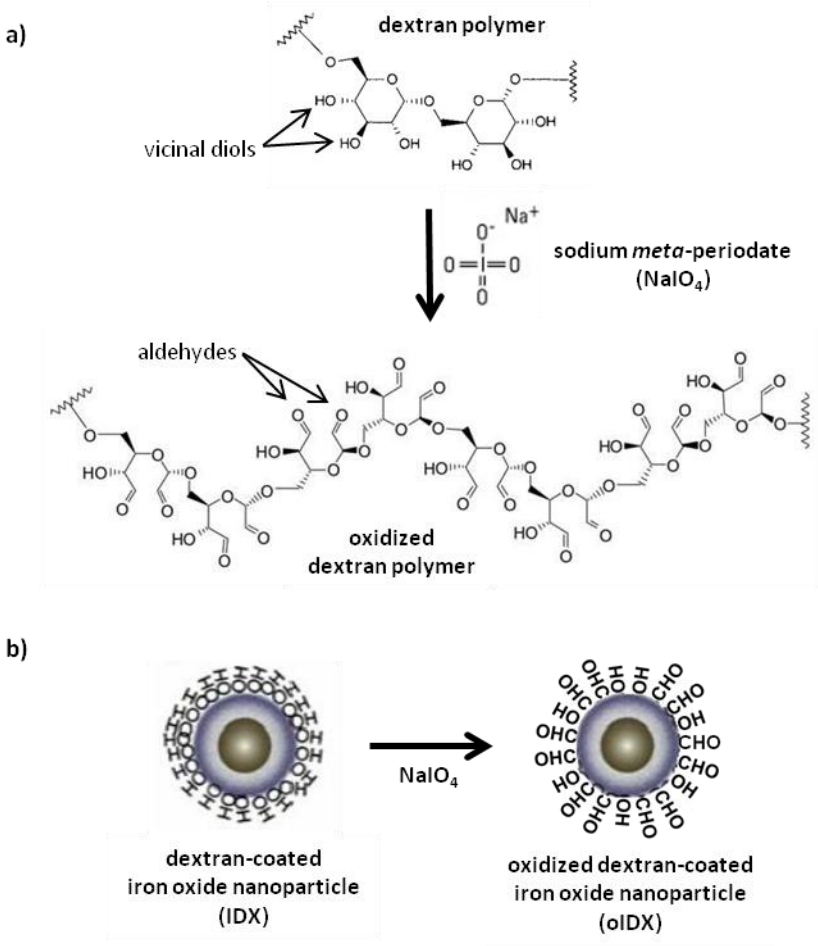

Figure IV-1: Oxidation of dextran to introduce aldehydes on IDX nanoparticles
Sodium *meta*-periodate ($NaIO_4$) can be used to oxidize dextran, thereby converting vicinal diols into two aldehyde functional groups [129] (a). This chemistry was applied to dextran-coated iron oxide nanoparticles (IDX) to introduce surface aldehydes for oxime ligation (b).

The concentration of aldehydes introduced was then measured using a commercially-obtained fluorimetric detection assay with standard solutions of known aldehyde content. 1.0 mg/mL (Fe) was introduced into each assay by titrating nanoparticle samples with assay buffer and spiking standard solutions with non-oxidized IDX nanoparticles. Standards were fit to a 4-parameter sigmoidal curve for interpolation of sample concentrations. As seen in Figure IV-2, the concentration of aldehydes measured on

nanoparticles increased in correlation with the concentration of oxidant applied during oxidation.

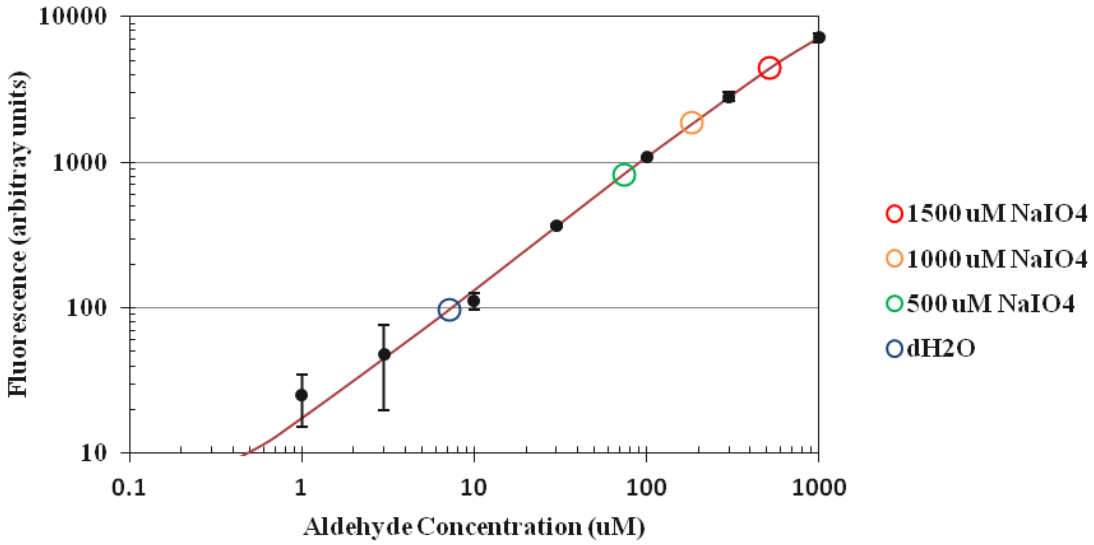

Figure IV-2: **Measurement of aldehydes on oxidized dextran-coated iron oxide nanoparticles** Black dots represent aldehyde standard solutions spiked with 1 mg/mL iron from IDX nanoparticles. Colored circles represent oxidized IDX (oIDX) samples. Values represent average of triplicates +/- SEM.

The relative numbers of aldehyde functional groups present per nanoparticle in each sample were calculated by dividing the measured aldehyde concentration by the calculated concentration of nanoparticles in each solution containing 1 mg/mL iron (determined spectrophotometrically, see IV.2.2), as tabulated in Table IV-1.

Table IV-1: **Aldehydes on oxidized dextran-coated iron oxide nanoparticles**

Sample	Aldehyde Conc. (µM)	Aldehydes/NP
dH_2O	7.2	1.0
500 µM $NaIO_4$	73.7	10.7
1000 µM $NaIO_4$	184.3	26.7
1500 µM $NaIO_4$	518.4	75.1

IV.3.2. Attempted oxime ligation of FApB2vAoa on aldehyde-bearing iron oxide nanoparticles

To synthesize folate-targeted proteolytic nanobeacons, IDX nanoparticles bearing aldehydes from oxidation with 500 µM $NaIO_4$ ("oIDX-500µM") were reacted with either 3 or 6 molar equivalents of FApB2vAoa crude peptide (relative to nanoparticles) in the presence of a catalytic amount of aniline in accordance with a published technique for oxime ligation[130], as schematically diagrammed in Figure IV-3. The term "NP^{++}" hereafter refers to a number of different proposed nanoparticle constructs, each of which is intended to be decorated with peptides bearing both a FA targeting ligand and an MMP-cleavable amino acid sequence.

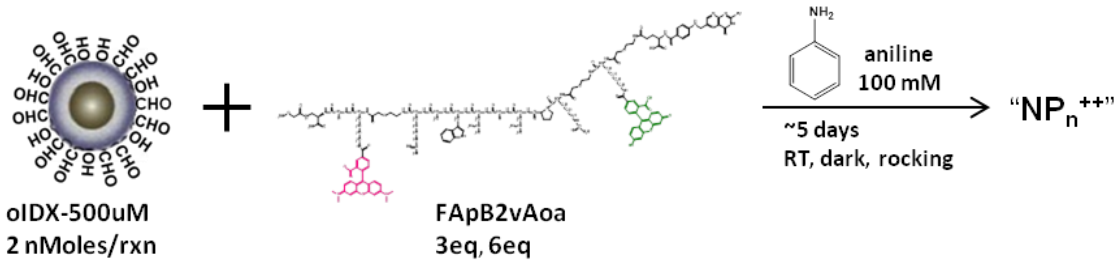

Figure IV-3: Scheme, oxime ligation reaction of FApB2vAoa peptide with oIDX-500uM nanoparticles

The resulting reaction mixes were filtered by ultrafiltration in 10 kDa (NMWL) centrifugal filter units with collection of the filtrates and concentrates for subsequent analyses. To assess the degree of peptide binding to nanoparticles, the UV-visible absorbance of the reaction mixes and their separated constituents recovered from ultrafiltration were characterized by spectrophotometry and compared with unreacted nanoparticles (Figure IV-4a). Reaction mixes and concentrates from both reactions possessed absorbance spectra with greater relative absorbance in the spectral regions characteristic of the peptide-associated FAM and TAMRA dyes (Figure IV-4b,d), though

those of from the reaction with 6 molar equivalents of peptide ("NP_6^{++}") were of greater relative deviation from the oIDX-500µM spectrum than NP_3^{++}. The absorbance of the filtrates was practically negligible, though also indicative of the presence of FAM and TAMRA dyes associated with peptide.

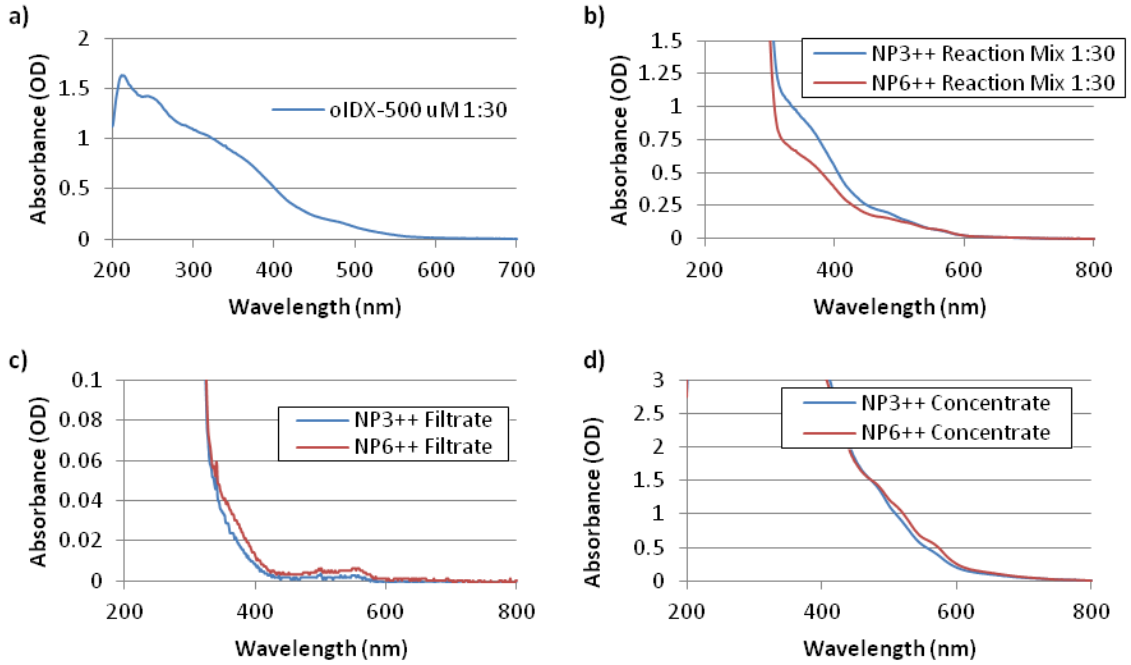

Figure IV-4: Absorbance of reactants and recovered reaction mix fractions from oxime ligation of FApB2vAoa and oIDX-500uM
UV-visible absorbance spectra were collected from aqueous solutions of oIDX-500uM nanoparticles (a) as well as diluted reaction mixes (b) and concentrates (c) and filtrates (d) following centrifugal filtration of reaction mixes through 10 kDa (NMWL) filters.

In order to quantitatively compare the amount of peptide coupled to nanoparticles by oxime ligation reactions, the absorbance spectrum of oIDX-500µM was normalized to the absorbance of each sample at 400 nm (a local minimum in absorbance of FAM and TAMRA) and subtracted from each sample. Plotted in Figure IV-5, the residual absorbance spectra of each reaction mix and concentrate were roughly representative of the characteristic peak absorbances of FAM and TAMRA dyes. Predictably, the peptide-

associated residual absorbance spectra of NP_6^{++} reaction mix and concentrate were greater in magnitude than those of NP_3^{++}, corresponding to the relative amounts of FApB2vAoa added to the reaction mixes.

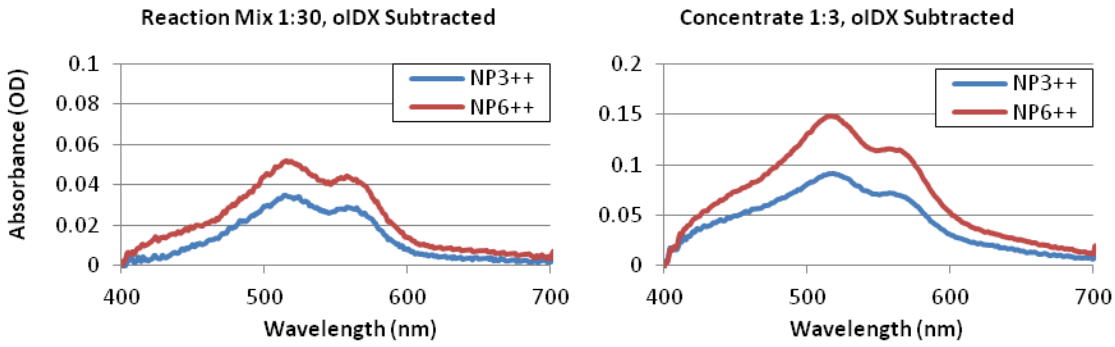

Figure IV-5: Peptide-associated absorbance of reaction mix and concentrates from oxime ligation
Spectra were generated by scaling of oIDX-500uM absorbance spectrum (Figure IV-4a) to absorbance of samples at 400 nm and subtraction from spectra of NP_n^{++} reaction mixes (Figure IV-4b, left) or concentrates from centrifugal filtration (Figure IV-4d, right).

Because very little UV-visible absorbance was observed in filtrates from ultrafiltration of NP^{++} reaction mixes (Figure IV-4c, above), the reaction mix concentrates were compared with concentrates from control solutions composed of non-oxidized (i.e. non-reactive) IDX nanoparticles, FApB2vAoa, and aniline ("+++ Ctl") or just FApB2vAoa and aniline ("++ Ctl") to determine whether fluorescence emission could be attributed solely to nanoparticle-bound peptides or if unbound peptides in solution were contributing to emission intensity. Shown in Figure IV-6, excitation at 495 nm resulted in emission with intensity maxima at 520 nm and 580 nm from all samples, confirming FRET from FApB2vAoa. Emission intensity from excitation at both 495 nm and 555 nm was greater in NP_6^{++} concentrate than NP_3^{++} (Figure IV-6a,c), however the intensities from control solutions (Figure IV-6b,d) were comparable to NP_3^{++}, indicating ineffective separation of unbound peptide from nanoparticle products by ultrafiltration.

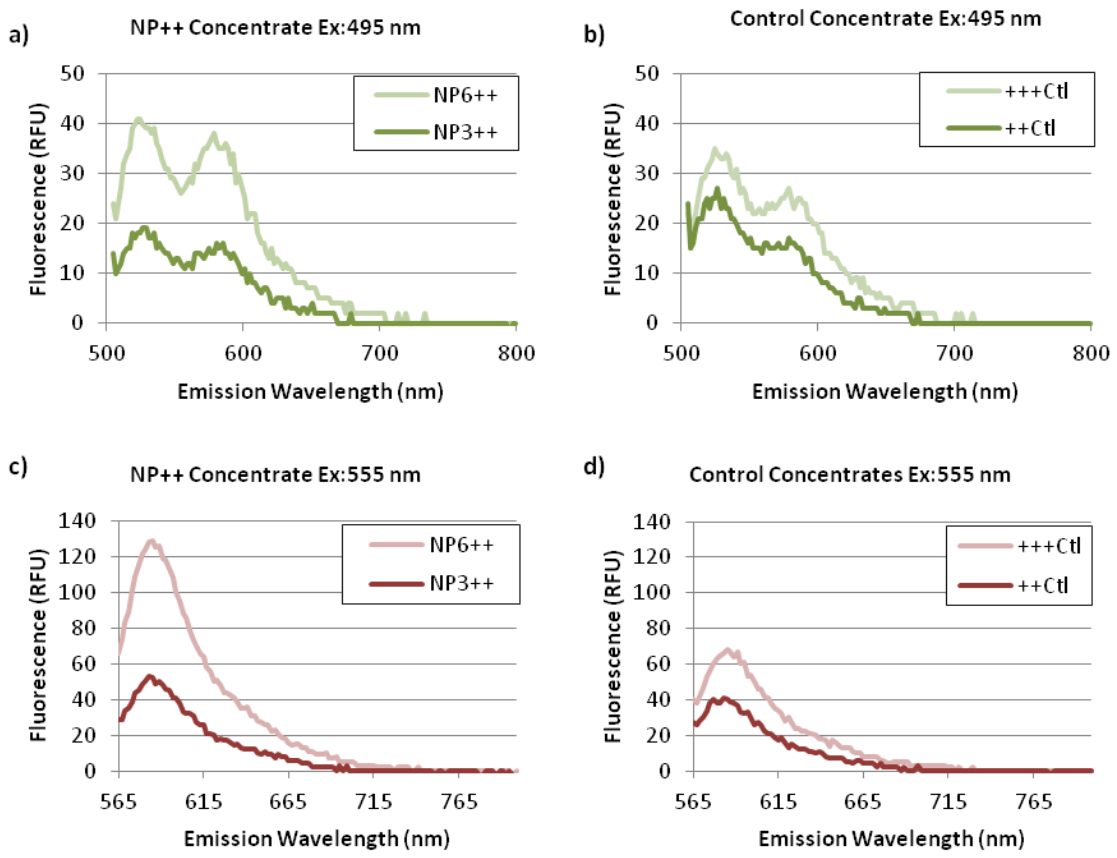

Figure IV-6: **Fluorescence of concentrates from oxime ligation**
Fluorescence of oxime ligation product (a,c) and control (b,d) concentrates from NMWL 10 kDa centrifugal filters with excitation at 495 nm (a,b) or 555 nm (c,d). "+++ Ctl" represents sample including FApB2vAoa peptide, aniline, and non-reactive IDX nanoparticles. "++ Ctl" represents sample containing FApB2vAoa and aniline only.

NP_6^{++} reaction mix concentrate was therefore precipitated in MeOH, in which FApB2vAoa was soluble, and the resulting magnetic nanoparticle pellet collected by centrifugation and magnetic attraction. Following resuspension in dH_2O, NP_6^{++} nanoparticles were serially diluted for plate reader fluorescence spectroscopy to assess whether recovered nanoparticles possessed sufficient peptide decoration for proteolysis sensing. Emission spectra from excitation of NP_6^{++} at 495 nm and 555 nm (Figure IV-7) were characteristic of FAM-TAMRA FRET, however only barely detectable above background noise of the instrument. As shown in Figure IV-7c,d, doubling the detector's

emission integration bandwidth from 5 nm to 10 nm increased sensitivity, however even the emission signal from undiluted nanoparticle solution remained noisy.

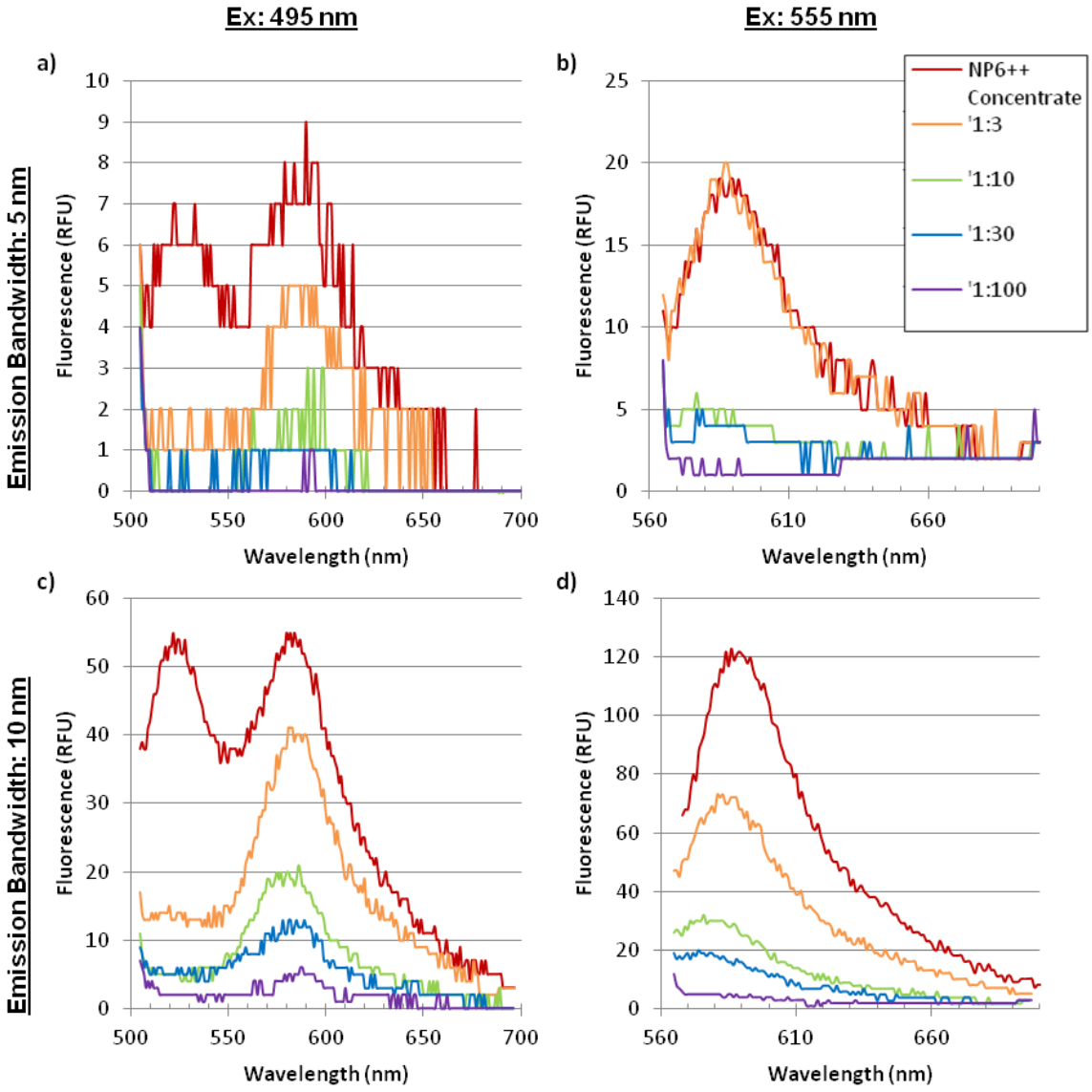

Figure IV-7: **Fluorescence emission by NP6^{++} product of oxime ligation (dilution series)**
Fluorescence emission of recovered NP6^{++} product in multiple dilutions was measured via a fluorescence plate reader with an emission bandwidth of 5 nm (a,b) or 10 nm (c,d) and excitation at 495 nm (a,c) or 555 nm (b,d).

IV.3.3. Troubleshooting reaction conditions and catalysts for oxime ligation

Based upon the insufficient fluorescence emission of NP_3^{++} and NP_6^{++} characterized above, dual-targeted nanoparticle synthesis by oxime ligation was revisited. Wendeler et al recently showed that substituted aniline derivatives, specifically p-phenylenediamine (pPDA), can offer enhanced catalysis of oxime-based bioconjugations relative to aniline across a range of pH, but most notably at pH 7[135]. As such, a series of oxime ligation reactions was performed with oIDX-1000uM nanoparticles and FApB2vAoa crude peptide in sodium phosphate buffer (pH 6.0), comparing 100 mM aniline and 10 mM pPDA as catalysts, as diagrammed in Figure IV-8. Reaction mixes were denoted "$NP_n^{++}{}_{pPDA}$" or "$NP_6^{++}{}_{An}$" to indicated the molar equivalents of FApB2vAoa relative to nanoparticles and the catalysts used in reaction. Control reactions including no nanoparticles or non-oxidized IDX nanoparticles ("No-IDX-Ctl" and "No-Rxn-Ctl," respectively) were conducted in parallel.

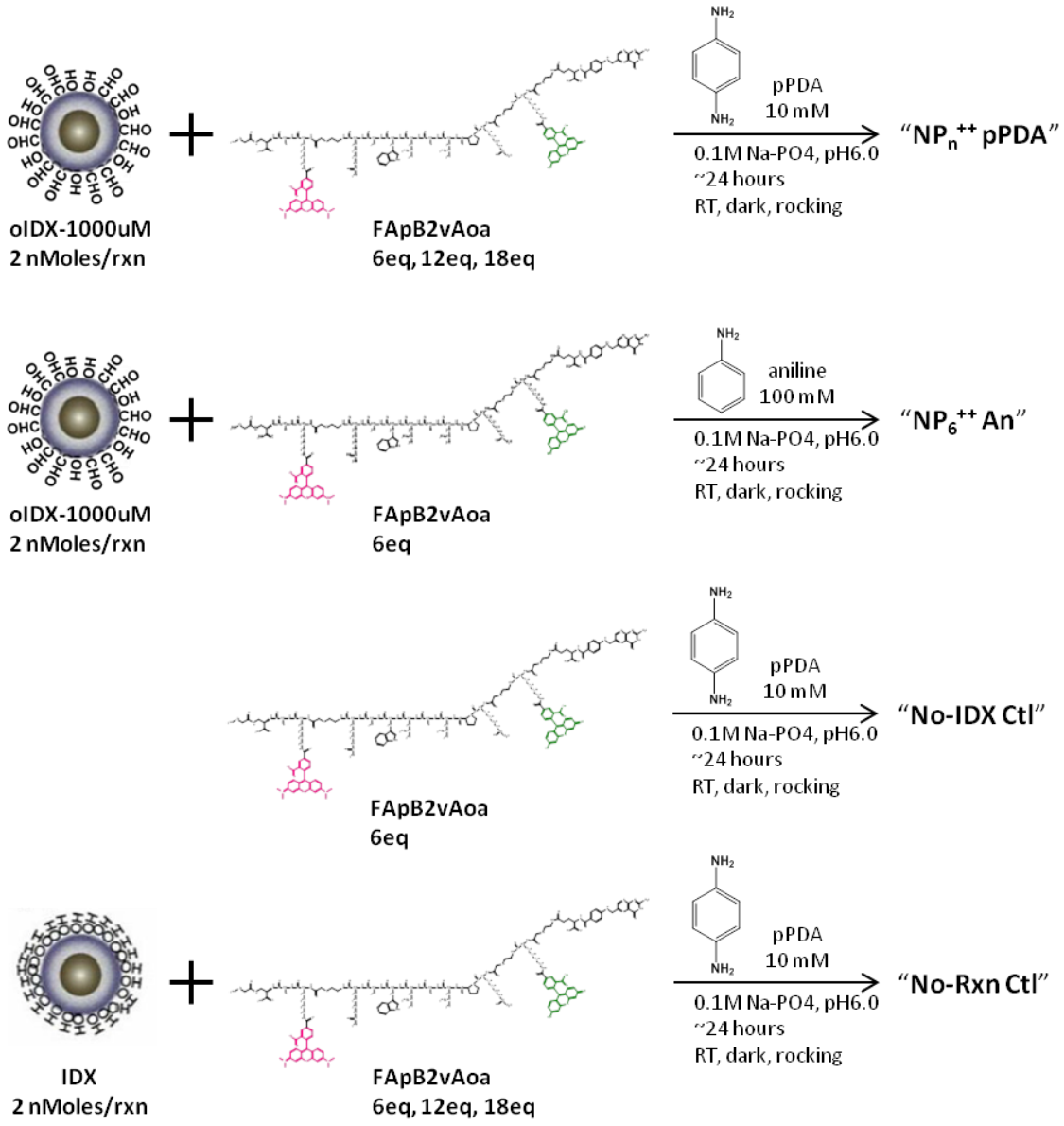

Figure IV-8: Schema, oxime ligation of FApB2vAoa and oIDX-1000uM with aniline or pPDA as catalysts

Following 24 hours of continuous rocking at RT, suspended and soluble products in reaction mixes were separated by centrifugation. As diagrammed in Figure IV-9, the resulting pellets were washed twice with MeOH to dissolve unbound FApB2vAoa peptide and precipitate FeOx-based nanoparticles, pelleting nanoparticles by centrifugation and collecting supernatants after each wash for subsequent analyses.

Nanoparticle pellets were ultimately resuspended in dH_2O prior to dilution for absorbance measurements by UV-visible spectrophotometry.

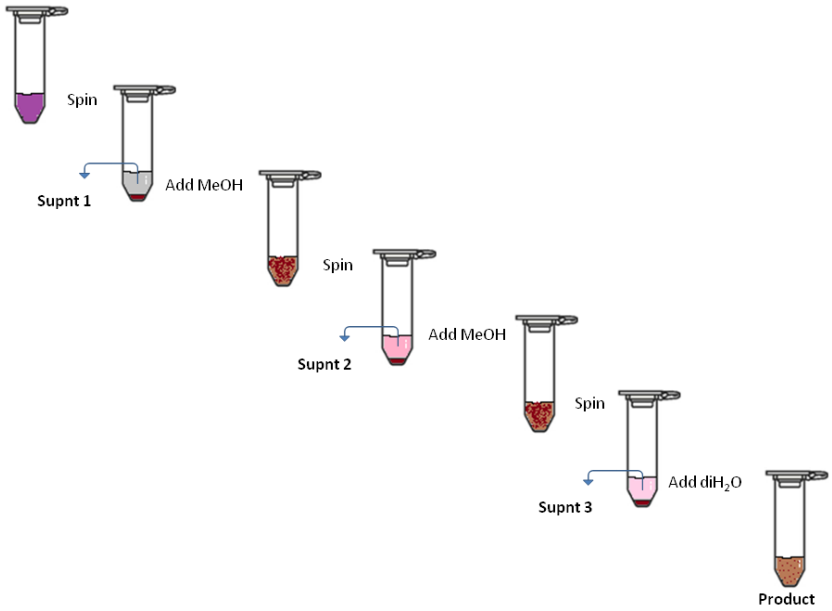

Figure IV-9: Scheme, separation of oxime ligation reactants and products by precipitation and centrifugation

In order to determine the distribution of peptide following reactions, each of the recovered supernatants and the product solutions from oxime ligations with pPDA and aniline catalysts was characterized by UV-visible spectrophotometry. With the exception of No-IDX-Ctl (which contained no nanoparticles), all of the product solutions possessed absorbance spectra (Figure IV-10) characteristic of IDX nanoparticles, with varying degrees of increased absorbance around 495 nm and 550 nm corresponding to peptide-associated absorbance. The absorbance spectrum of No-IDX-Ctl "product" was representative of FApB2vAoa, probably the result of residual peptide in the reaction vessel.

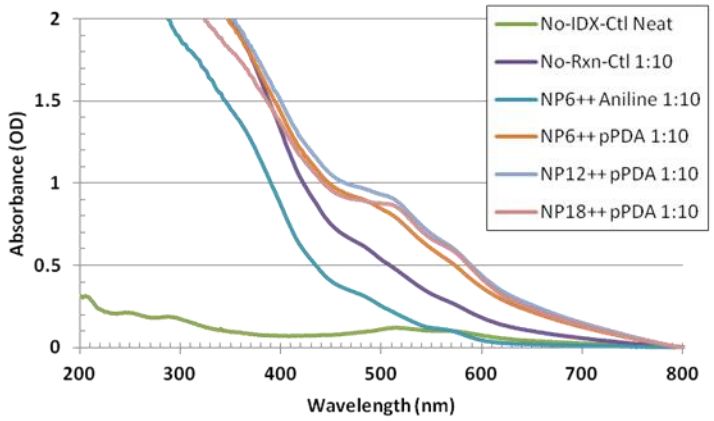

Figure IV-10: Absorbance of recovered aniline- and pPDA-catalyzed oxime ligation products FApB2vAoa peptide was reacted with oIDX-1000uM nanoparticles in the presence of pPDA or aniline as catalysts for oxime ligation. "No-Rxn Ctl" contained non-oxidized IDX nanoparticles. "No-IDX Ctl" contained peptide and pPDA but no nanoparticles (see Figure IV-8).

Interestingly, upon subtraction of the normalized absorbance spectrum of oIDX-1000uM, only the product of $NP_6^{++}{}_{An}$ possessed a residual absorbance spectrum characteristic of FAM and TAMRA dyes. As plotted in Figure IV-11, for each reaction in which FApB2vAoa was exposed to pPDA, the residual absorbance spectra of recovered products were somewhat different, decreased absorbance at 560 nm relative to 495 nm and greater absorbance in the 400-450 nm range by comparison. This result corroborated the observation that the reaction mixes, supernatants, and recovered products of reactions containing pPDA exhibited a dark violet hue by visual inspection whereas the aniline-containing reaction displayed the intensely pink color characteristic of TAMRA.

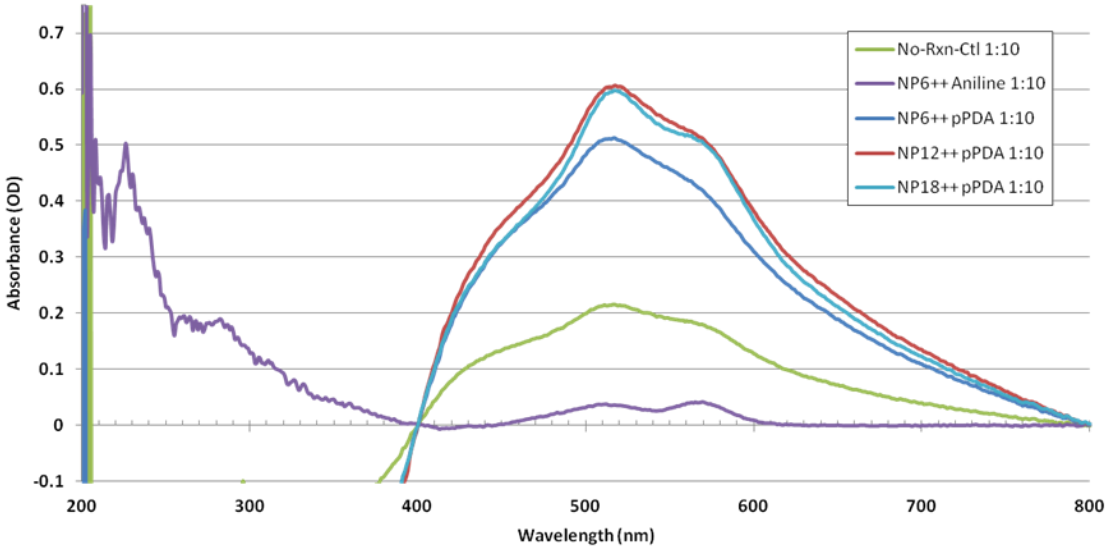

Figure IV-11: Peptide-associated absorbance of recovered aniline- and pPDA-catalyzed oxime ligation products
Spectra represent residual values after subtraction of the absorbance of parental oIDX-1000 µM nanoparticles scaled to absorbance of samples at 400 nm (as in Figure IV-5).

Furthermore, the UV-visible absorbance spectra of the supernatants collected from the separation of oxime ligation reaction mixes even more clearly demonstrated the differences between aniline and pPDA. The $NP_6^{++}{}_{An}$ supernatants possessed spectra demonstrative of FAM and TAMRA absorbance, with two distinct maxima near 495 nm and 560 nm, as seen in Figure IV-12. Supernatants from all reactions containing pPDA, however, exhibited a singular broad absorbance peak around 520 nm, uncharacteristic of FAM and TAMRA dyes despite the inclusion of FApB2vAoa peptide in the reaction mixes. This spectral abnormality suggested that pPDA might be incompatible with chemical reactions involving visible-spectrum FRET peptides.

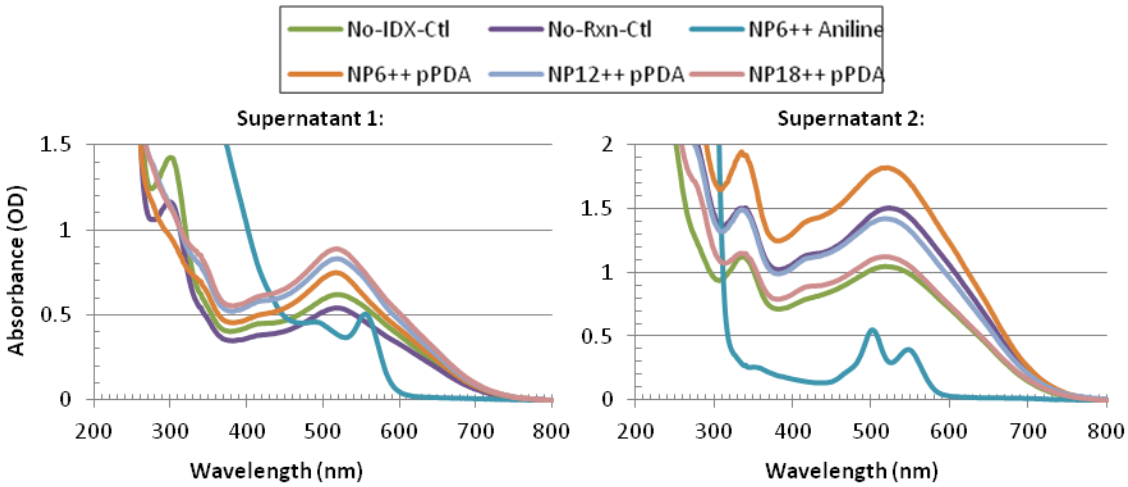

Figure IV-12: Absorbance of recovered aniline- and pPDA-catalyzed oxime ligation reaction supernatants
Supernatant 1 (left) was recovered by aspiration following centrifugation of reaction mix to pellet precipitated products. Supernatant 2 (right) was recovered by aspiration following pellet washing with methanol and subsequent centrifugation.

To determine whether the products of oxime ligation reactions involving aniline and pPDA as a catalysts exhibited the fluorescence properties critically important for optical sensing of proteolytic activity, the fluorescence spectra of the recovered nanoparticle products from each reaction were recorded by plate reader spectroscopy. As plotted in Figure IV-13, excitation at 494 nm resulted in expected FAM emission maximum around 520 nm but no emission maximum near 580 nm to indicate FRET with TAMRA, as seen previously. Greater amounts of FApB2vAoa in reactions corresponded with greater emission intensity, though no nanoparticle products emitted signal well above the noise of the instrument. Interestingly, greater signal was obtained from the products of $NP_6^{++}{}_{pPDA}$ than $NP_6^{++}{}_{An}$, despite the reaction mixes possessing equivalent proportions of FApB2vAoa, suggesting that pPDA was a more effective catalyst for peptide attachment to nanoparticles. However, combined with the peculiar absorbance spectra (above), the lack of FRET signal from sensor excitation and the practically absent emission from reference (TAMRA) excitation corroborated the incompatibility of pPDA with TAMRA

and suggested a problem with this set of oxime ligation products that prohibited use for proteolysis sensing applications.

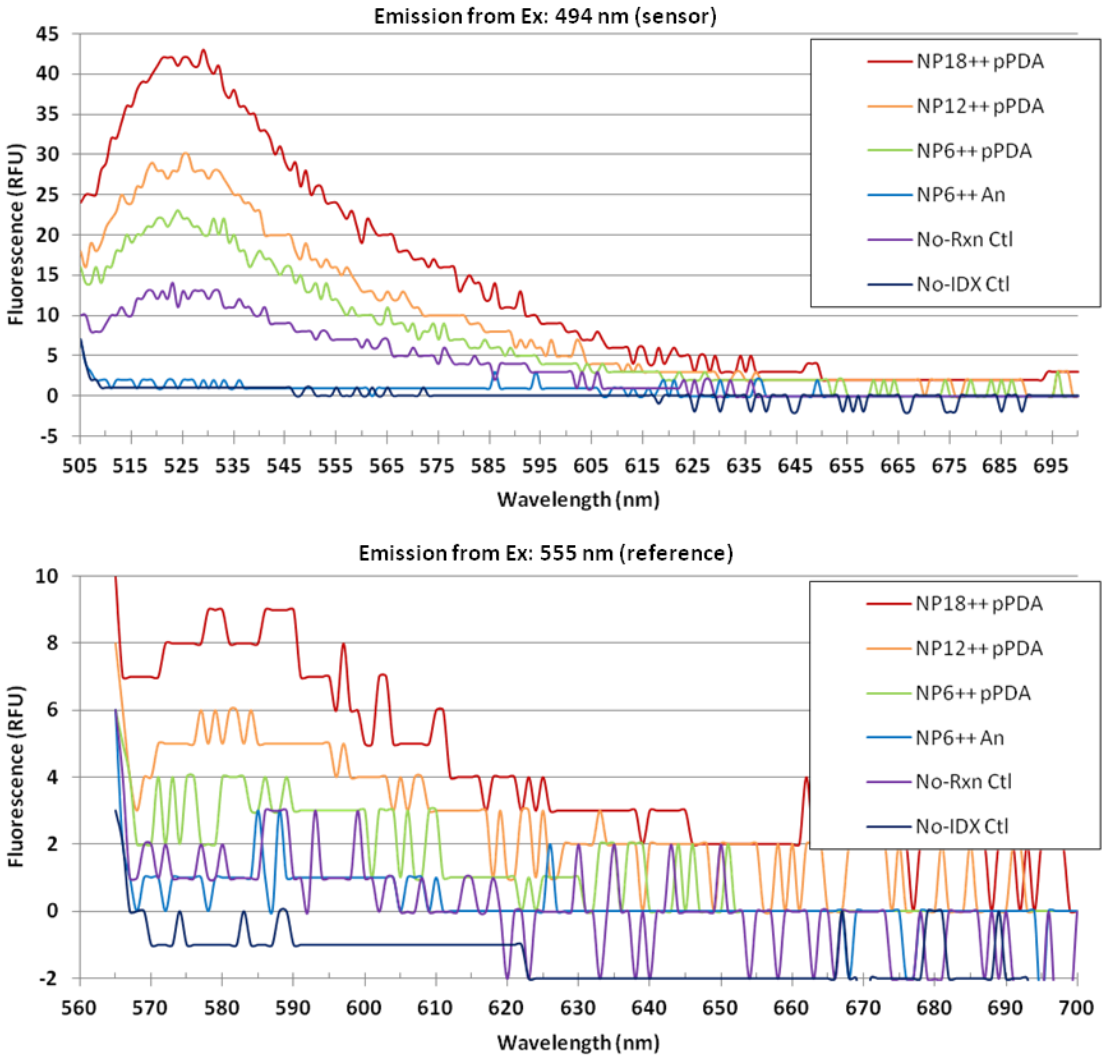

Figure IV-13: Fluorescence of products from aniline- and pPDA-catalyzed oxime ligation
Traces represent fluorescence emission stimulated by excitation at 494 nm (top) and 555 nm (bottom). FApB2vAoa peptide was reacted with oIDX-1000uM nanoparticles in the presence of pPDA (red, orange, green) or aniline (light blue) as catalysts for oxime ligation. "No-Rxn Ctl" contained non-oxidized IDX nanoparticles. "No-IDX Ctl" contained peptide and pPDA catalyst but no nanoparticles (see Figure IV-8).

IV.3.4. Re-attempt of oxime ligation in organic solvent with fresh aniline catalyst and characterization of products

The aberrant optical properties of $NP_n^{++}{}_{pPDA}$ reaction mix components with respect to the expected FApB2vAoa spectra, lacking characteristic TAMRA absorbance and FRET, effectively prohibited their use as proteolytic nanobeacons. The reaction mix components from oxime ligation reactions involving aniline, on the other hand, possessed optical spectra representative of FApB2vAoa, although analysis of peptide-associated absorbance (Figure IV-11) and fluorescence emission (Figure IV-13) indicated insufficient attachment of peptides to nanoparticles. A such, the reaction conditions for oxime ligation of oIDX-1000uM nanoparticles with FApB2vAoa using aniline as a catalyst were revised as schematically diagrammed in Figure IV-14 to include excess peptide and DMSO with 0.1 M sodium acetate buffer (pH 4.5) as the primary solvent according to previously successful reactions with non-fluorescent aminooxy-bearing peptides and aldehyde-terminated organic dendrons (Scherer and McIntyre, unpublished). Aniline was pipetted from a freshly-opened manufacturer's bottle under inert atmosphere. For comparison of final peptide attachment, a control reaction ("No-Rnx Ctl") containing non-oxidized IDX nanoparticles was conducted in parallel.

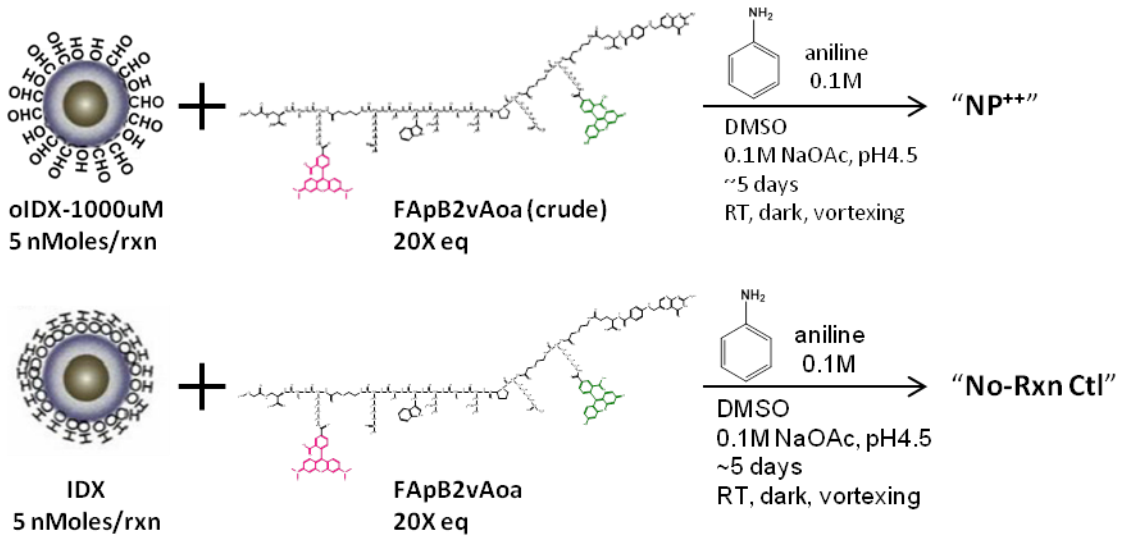

Figure IV-14: Scheme, oxime ligation of FApB2vAoa with oIDX-1000uM in DMSO with fresh aniline catalyst

After 5 days of rocking at RT, protected from light, reaction mixes were separated into nanoparticle products and supernatants by centrifugation, repeated precipitation in MeOH as before (see Figure IV-9), and resuspension in DMSO with sonication to recover NP^{++} and No-Rxn Ctl products. The FApB2vAoa peptide-associated absorbance of recovered products was calculated following UV-visible spectrophotometry by subtracting absorbance spectrum of oIDX-1000uM (scaled to product spectra at 400 nm) from product spectra, as detailed earlier (see IV.2.3 and Figure IV-5). Shown in Figure IV-15 (green traces), the resulting residual traces were characteristic of FAM and TAMRA dye absorbance spectra, representing 31.8% and 18.9% recovery of peptide from NP^{++} and No-Rx Ctl reaction mixes, respectively, by TAMRA absorbance (Table IV-2). However, following additional washing of the nanoparticle products in MeOH with centrifugal or magnetic separation and reconstitution in DMSO, peptide-associated absorbance of both NP^{++} and No-Rxn Ctl products decreased (Figure IV-15, red and blue traces).

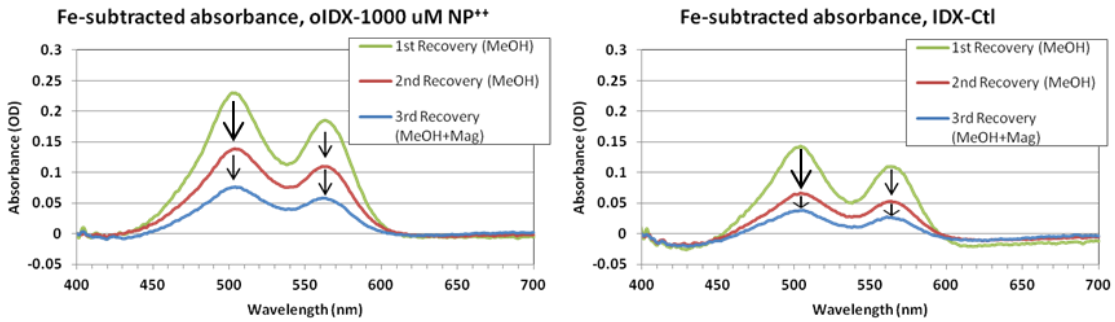

Figure IV-15: Peptide-associated absorbance of oxime ligation products decreased with each DMSO wash
FApB2vAoa peptide was reacted with either oIDX-1000 µM (left) or non-oxidized IDX nanoparticles (right, control) in the presence of aniline. The iron-subtracted absorbance of pelleted products from each reaction condition were calculated following repeated nanoparticle precipitations in methanol with centifrugal (green, red) or magnetic pelleting (blue) and reconstitution in DMSO with sonication.

Peptide recovery in nanoparticle product solutions at each phase of washing and recovery was calculated from the UV-visible absorbance spectra. The basis for recovery was established by measuring the absorbance of the FApB2vAoa reactant solution used in each reaction (data not shown) and multiplying by the volume added to reactions. The TAMRA-associated absorbance (peak optical density between 550-565 nm) of each sample was multiplied by the recovered sample volume, divided by the basis, and expressed as a percentage of TAMRA-associated absorbance in the corresponding initial reaction mix, as seen in (Table IV-2). Interestingly, MeOH supernatants collected subsequent to a previous wash in MeOH but prior to product resuspension in DMSO possessed very little TAMRA absorbance compared to MeOH supernatants from precipitation of DMSO-suspended products. This suggested that FApB2vAoa peptide might be released from association with nanoparticle products by dissolution in DMSO, indicative of a non-covalent interaction between peptides and nanoparticles.

Table IV-2: TAMRA dye recovery in separated fractions from oxime ligation of FApB2vAoa with oIDX-1000uM following multiple separations

1st Separation (MeOH, centrifuge)			
oIDX-1000 Supnt 1	66.9%	IDX-Ctl Supnt 1	77.5%
oIDX-1000 Supnt 2	0.4%	IDX-Ctl Supnt 2	0.7%
oIDX-1000 NP++ (oIDX-1000 subtracted)	31.8%	IDX-Ctl NP (oIDX-1000 subtracted)	18.9%
Cumulative Recovery	**99.2%**	Cumulative Recovery	**97.1%**
2nd Separation (MeOH, centrifuge)			
oIDX-1000 Supnt 3	4.6%	IDX-Ctl Supnt 3	7.3%
oIDX-1000-Supnt 4	0.4%	IDX-Ctl Supnt 4	0.4%
oIDX-1000 NP++ (oIDX-1000 subtracted)	25.8%	IDX-Ctl NP (oIDX-1000 subtracted)	14.2%
Cumulative Recovery	**98.1%**	Cumulative Recovery	**100.1%**
3rd Separation (MeOH, Magnet)			
oIDX-1000 Supnt 5 (oIDX-1000 subtracted)	1.2%	IDX-Ctl Supnt 5 (oIDX-1000 subtracted)	1.4%
oIDX-1000-Supnt 5.1	8.5%	IDX-Ctl Supnt 5.1	5.8%
oIDX-1000 NP++ (oIDX-1000 subtracted)	13.0%	IDX-Ctl NP (oIDX-1000 subtracted)	7.1%
Cumulative Recovery	**95.0%**	Cumulative Recovery	**100.1%**

IV.3.5. Troubleshooting oxime ligation focusing on FApB2vAoa peptide

After attempting oxime ligation of FApB2vAoa with aldehyde-bearing dextran-coated iron oxide nanoparticles in several reaction conditions, we hypothesized that FApB2vAoa might be prohibited from reacting either because of steric hindrance or blocking of requisite functional groups. Due to the known inclusion of unidentified chemical adducts in products of SPPS including FApB2vAoa, FApB2vAoa peptide was incubated with trypsin to investigate whether the adducts could be modifying the aminooxy functional group required for oxime chemistry. At least one set of proteolytic cleavage products was expected to result, as diagrammed in Figure IV-16.

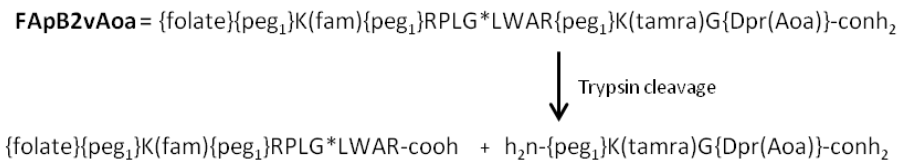

Figure IV-16: Scheme, trypsin cleavage of FApB2vAoa

LCMS of the cleavage mixture detected ions corresponding to the expected peptide fragments from trypsin cleavage of FApB2vAoa between arginine and {peg_1} residues as depicted in Figure IV-16, above. Ions representative of other possible trypsin cleavage sites, expected at the carboxyl sides of arginine or lysine residues except where followed immediately by proline, were not prevalent. The mass chromatograms from LCMS of trypsin-cleaved FApB2vAoa indicate the presence of the N-terminal cleavage fragment without any additional adducts (Figure IV-17a,f). The corresponding C-terminal portion of FApB2vAoa, however, was represented by ions with and without adducts of 28 Da and 40 Da (Figure IV-17b-g), corroborating previous analyses of pB2v peptide indicating attachment of adducts within the last four C-terminal residues (see III.3.2).

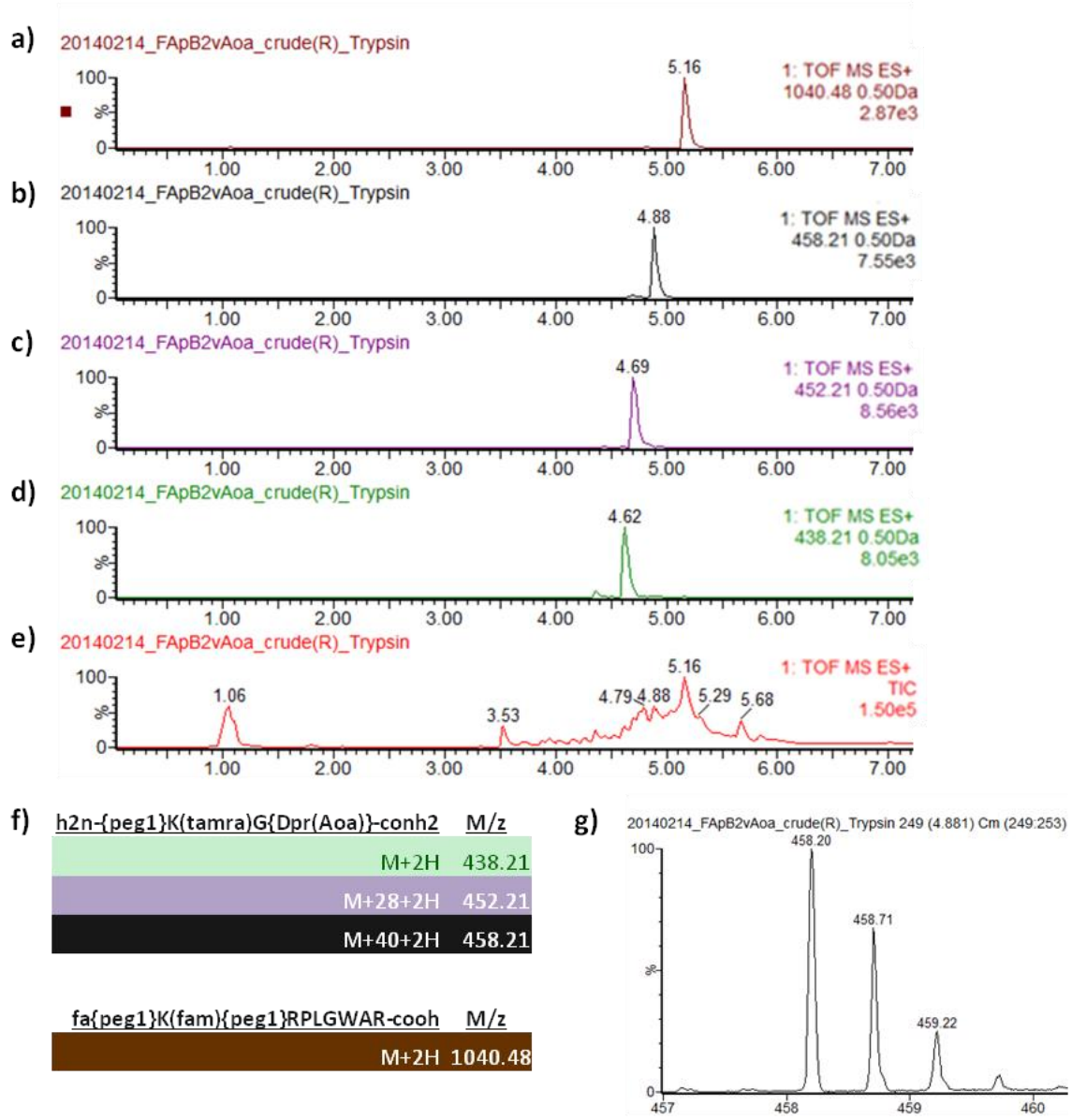

Figure IV-17: LCMS chromatograms and detected masses of cleavage products including C-terminal adducts following trypsin cleavage of FApB2vAoa
Doubly-charged ions with m/z of 1040.48 (a), 458.21 (b), 452.21 (c), and 438.21 (d) corresponding to trypsin-cleaved fragments of FApB2vAoa corresponding to expected ions with and without adducts (f) eluted separately and were detected. Total ion counts following reversed phase liquid chromatography are shown (e). A representative trace indicating the double charge of ion with M/z 458.21 is shown (g).

To directly determine whether the FApB2vAoa could form oxime bonds as intended, unpurified FApB2vAoa peptide from SPPS was reacted with 4-formylbenzoic acid, a small molecule with an aldehyde functional group and a carboxyl group attached to a

benzene ring, using the same reaction conditions attempted with FApB2vAoa and oIDX-1000uM nanoparticles, as represented in Figure IV-18.

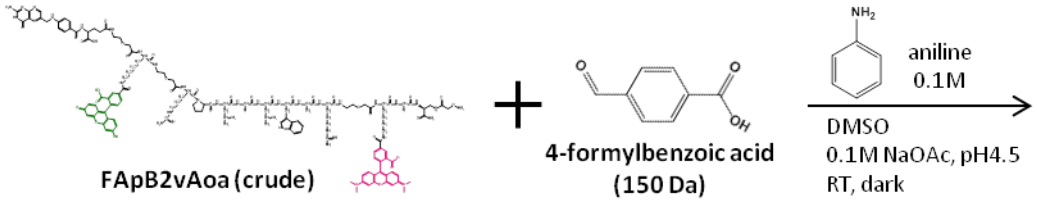

Figure IV-18: Scheme, reaction of FApB2vAoa with 4-formylbenzoic acid

The reaction mix and crude FApB2vAoa peptide starting material were analyzed separately by ESI+ MS for comparison of molecular weights to determine whether the reaction had modified the peptide by oxime ligation. Shown in Figure IV-19, ions representing the triply- and quadruply-charged states of chemical species with the intended mass of FApB2vAoa as well as those with additions of 40 Da, 67 Da, and 107 Da adducts were detected in the crude peptide mixture. An ion 129 Da smaller than FApB2vAoa corresponding to an omission of the DprAoa residue was also apparent, introducing an obvious reason for lack of reactivity. Interestingly, some of the ions present in the peptide mixture were also detected in the reaction mix, whereas others were absent but corresponded with another ion peak increased by 132 Da, the expected mass addition from oxime ligation with 4-formylbenzoic acid. Importantly, FApB2vAoa ions with 40 Da or 107 Da additions or a 129 Da subtraction were found in both the crude peptide and reaction mix samples, indicating no modification of these peptide structures in the reaction. Conversely, FApB2vAoa ions with the expected mass from SPPS with and without 67 Da adducts were not found in reaction mix, but ions with the expected

mass of the oxime ligation product with and without 67 Da adduct were detected, suggesting successful reaction of these peptide structures with 4-formylbenzoic acid.

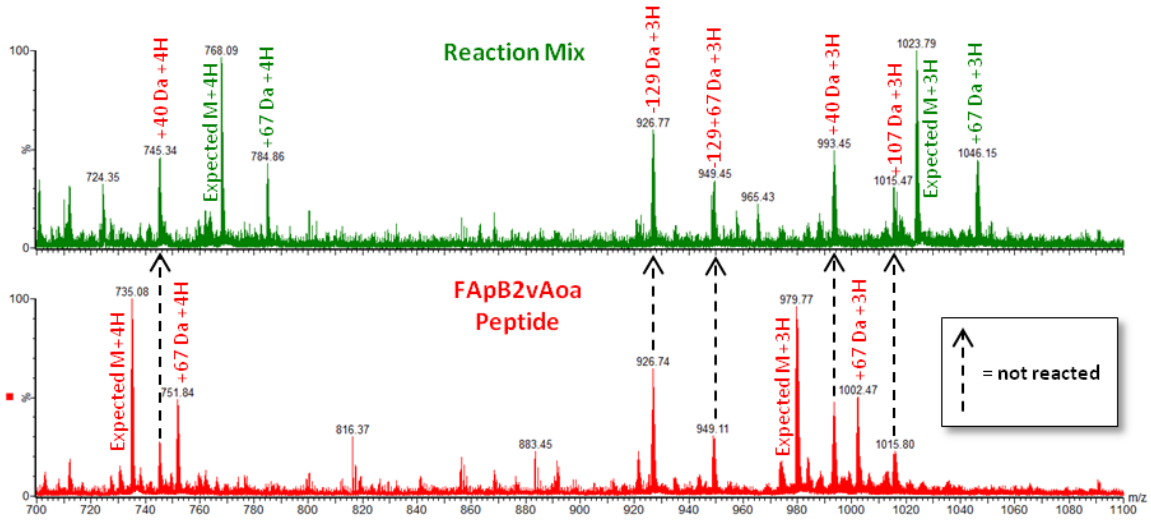

Figure IV-19: ESI+ mass spectra of unpurified FApB2vAoa and reaction mix following oxime ligation with 4-formylbenzoic acid
Dashed arrows and red text indicate ions detected in the unreacted FApB2vAoa sample (red trace, bottom) as well as the reaction mix (green trace, top). Adducts of +40, +67, and +107 Da were detected in the triply (+3H) and quadruply (+4H) charged states. Subtraction of 129 Da from the expected masses corresponds to the absence of C-terminal DprAoa residue in the synthetic peptide.

IV.3.6. Nanobeacon synthesis via Steglich esterification

In parallel with attempts to troubleshoot and optimize oxime ligation, alternative chemistries for C-terminal attachment of peptides to nanoparticles were explored, including a few different reactions requiring a carboxylic acid functional group. For example, Auzély-Velty et al demonstrated the use of Steglich esterification to introduce a modified amino acid residue into a starch polymer, wherein a reaction of carboxyl of the amino acid with the primary and secondary alcohols in the starch polymer was mediated by the carbodiimide DIC and catalyzed by DMAP, as shown in Figure IV-20.

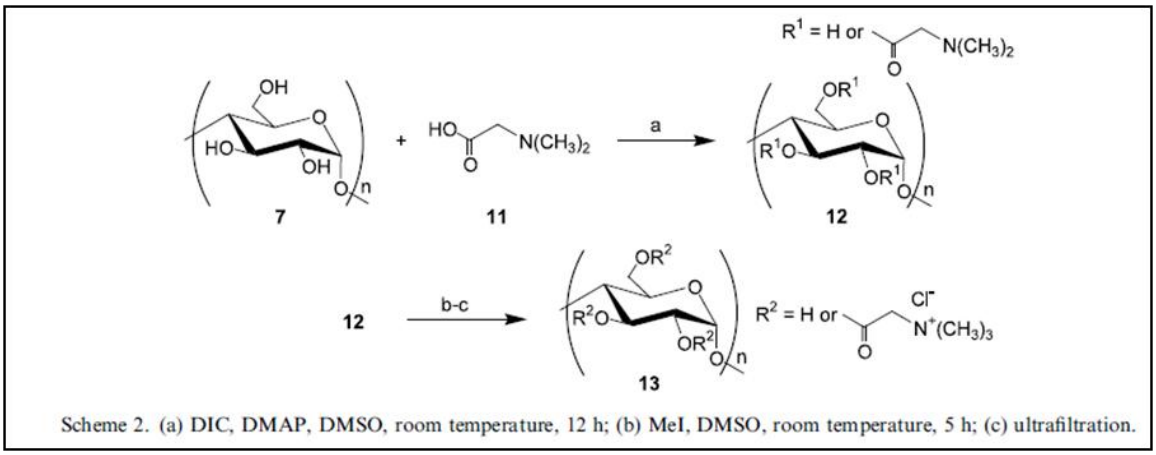

Scheme 2. (a) DIC, DMAP, DMSO, room temperature, 12 h; (b) MeI, DMSO, room temperature, 5 h; (c) ultrafiltration.

Figure IV-20: Scheme, Steglich esterification reaction to modify a starch polymer with a carboxyl-containing mock amino acid residue[148].

Because the dextran coating of IDX nanoparticles consists of lengthy starch polymers with an abundance of secondary alcohols, Steglich esterification of peptides with IDX nanoparticles was attempted. For this purpose, a carboxyl-terminated FRET peptide based on the structure of pB2v with an additional {peg$_1$} spacer, "pB2vp-cooh" [Fmoc-{peg$_1$}K(fam){peg$_1$}RPLGLWAR{peg$_1$}K(tamra){peg$_1$}G-cooh], was synthesized by SPPS (refer to Appendix A for detailed structure). The N-terminus of pB2vp-cooh was acetylated on resin to yield "AcpB2vp-cooh" and the resulting unpurified peptide characterized by LCMS. The crude peptide mixture was found to be composed of a minority product with the expected mass and a majority product 42 Da larger than AcpB2vp-cooh (data not shown), the same size adduct that was found previously on AcpB2vAoa (see III.3.6). Because adducts of the same mass were found on these two peptides with different C-termini, modification of the carboxylic acid group in AcpB2vp-cooh was not suspected. As such, crude AcpB2vp-cooh peptide mixture was reacted overnight with IDX nanoparticles, DIC, and DMAP, all in DMSO, as schematically diagrammed in Figure IV-21.

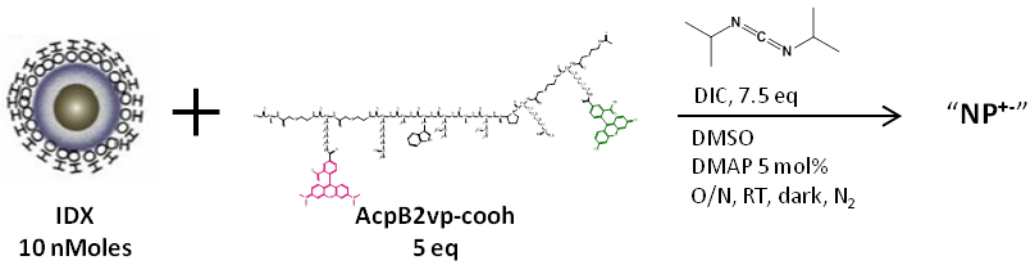

Figure IV-21: Scheme, Steglich esterification reaction of AcpB2vp-cooh peptide with dextran-coated iron oxide nanoparticles (IDX)

Magnetic nanoparticles were precipitated from the Steglich esterification reaction mix by pipetting the reaction mix into ice cold methanol on a magnetic separator device as described previously (see IV.2.5). Peptide attachment to recovered nanoparticles was characterized by UV-visible spectrophotometry as described previously (see IV.2.3). As made apparent by overlaying the absorbance spectra of reaction mix (Figure IV-22a) and recovered nanoparticles (Figure IV-22b) with the spectrum of unreacted IDX nanoparticles scaled to each sample's absorbance at 400 nm, the reaction mix exhibited additional absorbance in visible range characteristic of the peptide-associated dyes, FAM and TAMRA. The recovered magnetic nanoparticles ("Product" in Figure IV-22b, below), did not, as its absorbance spectrum was indistinguishable that of IDX nanoparticles, indicating negligible attachment of pB2vp-cooh to nanoparticles.

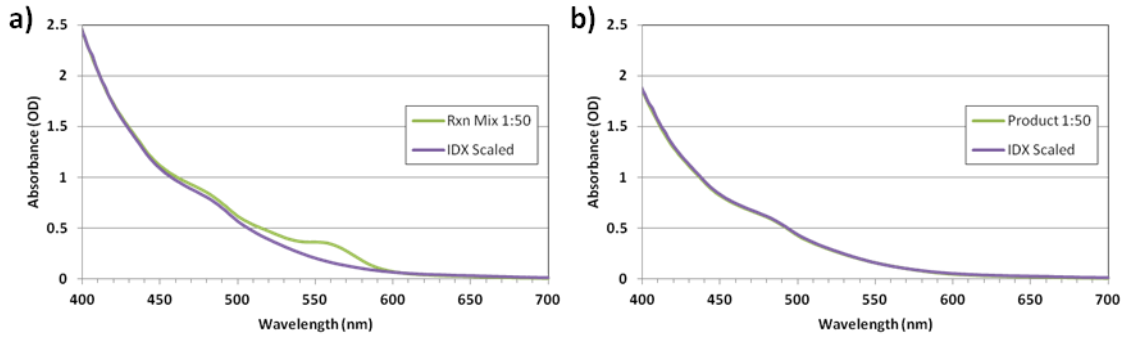

Figure IV-22: Absorbance of reaction mix components from attempted Steglich esterification of AcpB2vp-cooh and IDX nanoparticles
Absorbance of diluted reaction mix (a) and magnetically recovered products of reaction (b) are overlaid with scaled absorbance of parental IDX nanoparticles (purple lines) scaled to absorbance of samples at 400 nm.

The recoveries of peptide in each component of separated reaction mix were calculated from the results of spectrophotometry, as described earlier (see IV.3.4 and Table IV-2), using the peptide-associated (IDX subtracted) absorbance of TAMRA dye in the reaction mix as a basis (Table IV-3). Using TAMRA absorbance as a surrogate measure, approximately 2% of the peptide added to reaction mix was recovered with magnetic nanoparticles, or about 0.1 peptides per nanoparticle on average out of a theoretical maximum of 5 peptides per nanoparticle in the reaction mix.

Table IV-3: Calculated peptide recovery from magnetic separation of Steglich esterification reaction of AcpB2vp-cooh and IDX nanoparticles

Recovered Separation Fraction	Recovery
Reaction Mix (IDX Subtracted)	100%
Supernatant 1	92%
Supernatant 2	2%
Product (IDX Subtracted)	2%

IV.3.7. Nanobeacon synthesis via EDAC coupling

Due to the evident lack of sufficient binding of peptides to iron oxide nanoparticles using oxime ligation or Steglich esterification with peptides produced by SPPS, another

coupling scheme was developed. To eliminate blocking of functional groups on peptides from SPPS or nanoparticle surfaces as a possible cause of non-reactivity, carboxyl-terminated peptides and amine-decorated quantum dot nanoparticles from commercial sources were reacted via a well-studied mechanism of amide bond formation[129]. For this reaction, the 2-color MMP14 substrate, Peptide 13c, and quantum dots decorated with PEG-amine, "Qdot(605)NH_2," were mixed in the presence of EDAC as a mediator of carboxyl-to-amine bioconjugation, as schematically diagrammed in Figure IV-23. Peptide 13c was used in excesses of 100- to 2000-fold relative to quantum dots to allow detection of peptide-nanoparticle conjugation even at low coupling efficiencies. Control reactions replacing either peptide or EDAC with solvent were conducted in parallel.

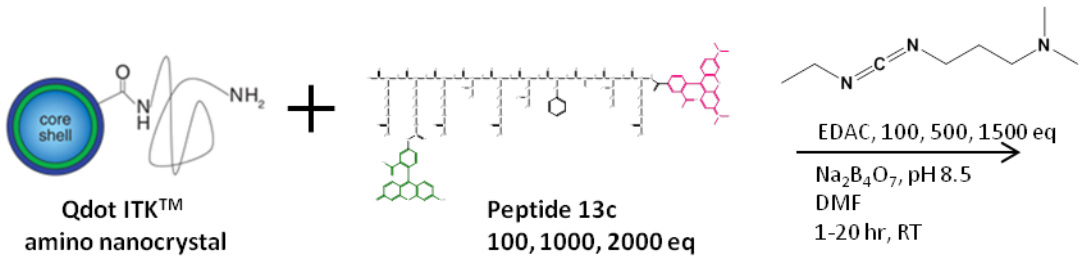

Figure IV-23: Scheme, carbodiimide (EDAC) coupling of Peptide 13c and PEG-NH_2 functionalized quantum dots

Following reactions, qualitative assessment of peptide binding to quantum dots was attempted by measuring the electrophoretic mobility of nanoparticles in 1% agarose gels. As seen in Figure IV-24a, quantum dots migrated toward the cathode at approximately equivalent rates for all reaction conditions except that containing 1000:500:1 molar ratios of peptide:EDAC:Qdot(605)NH_2. Because only one reaction condition appeared to result in retardation of quantum dots, electrophoresis was repeated comparing the previously assessed samples with another reaction mix containing 2000:1500:1 molar ratios to

determine whether a trend could be established. Interestingly, in each gel, quantum dots from the reaction mix omitting EDAC appeared to be partially confined to the sample wells. A qualitative determination of peptides binding to quantum dots could not be made, though, because there was no clear difference in electrophorectic mobility between unreacted quantum dots and those from reaction mixes, as seen in Figure IV-24b.

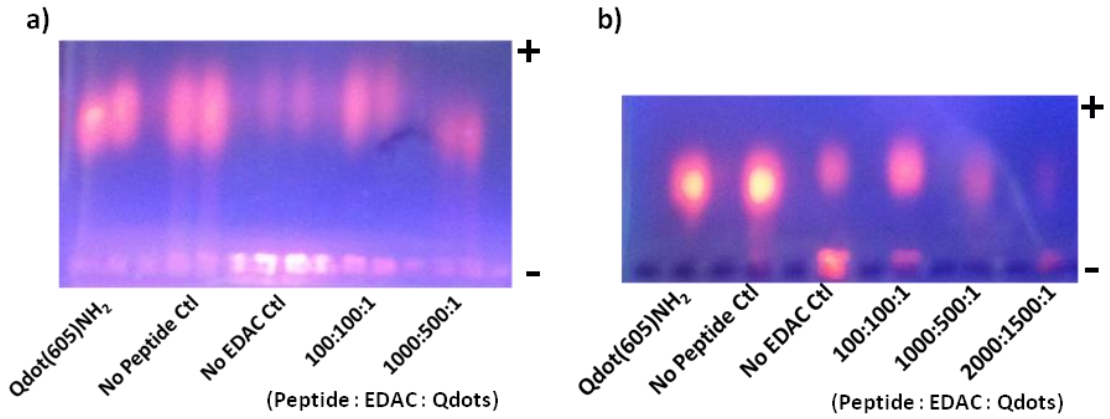

Figure IV-24: Agarose gel electrophoresis of Qdot(605)NH_2 and reaction mixes following attempted carbodiimide (EDAC) coupling with Peptide 13c
Nanoparticle mixtures diluted in sodium borate buffer were pipette in duplicate (a) or singly (b) into wells of freshly cast 1% agarose gels. Bands indicated UV-stimulated fluorescence of Qdots. No Peptide and No EDAC Controls are equivalent to 0:100:1 and 100:0:1 peptide:EDAC:Qdot ratios, respectively.

To provide an alternative means for measuring the attachment of fluorescent peptides to nanoparticles, Peptide 13c was mixed overnight with generation 4 PAMAM dendrimers ("PAMAM-G4") and EDAC, as diagrammed in Figure IV-25, to facilitate carbodiimide-mediated carboxyl-to-amine amide bond formation. A control mixture containing only solvent in place of EDAC ("No Rxn") was also prepared to provide a comparison with a solution in which no covalent attachment of peptides to PAMAM was expected to occur.

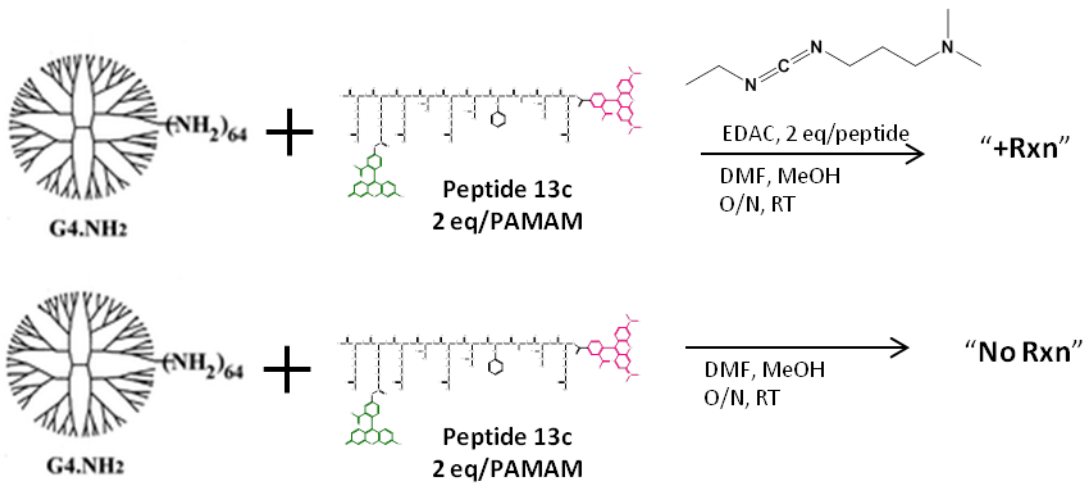

Figure IV-25: Scheme, carbodiimide (EDAC) coupling of Peptide 13c and PAMAM-G4

To separate PAMAM-based macromolecules from unbound reactants in solution following reactions, reaction mixes were diluted in buffer and reconcentrated by repeated ultrafiltration in YM-3 (MWCO 3,000) and YM-10 (MWCO 10,000) centrifugal filter devices. All constituent fractions of reaction mixes recovered from ultrafiltration were analyzed by UV-visible spectrophotometry to allow quantitative determination of the distribution of peptide in each fraction and the amount of peptide attached to PAMAM nanoparticles in each reaction. As shown in Figure IV-26, the absorbance spectra of the reaction mixes and collected retentates from ultrafiltration thereof exhibited peaks corresponding to the peptide-associated dyes, as expected. Calculating peptide recovery from the TAMRA-associated absorbance and volumes of recovered solutions, the retentates from the first separation ("YM-3 Retentate 1," below) represented approximately 19% of the peptide added to reaction mixes, or about 0.4 peptides per PAMAM-G4 (assuming 90% recovery of PAMAM in retentates), regardless of EDAC inclusion in each reaction. Similarly, the final effluents and retentates of YM-3 ultrafiltration were practically no different between reaction mixes with and without

EDAC. As such, no quantitative or qualitative discernment of peptide attachment to nanoparticles could be attributed to covalent amide bonding.

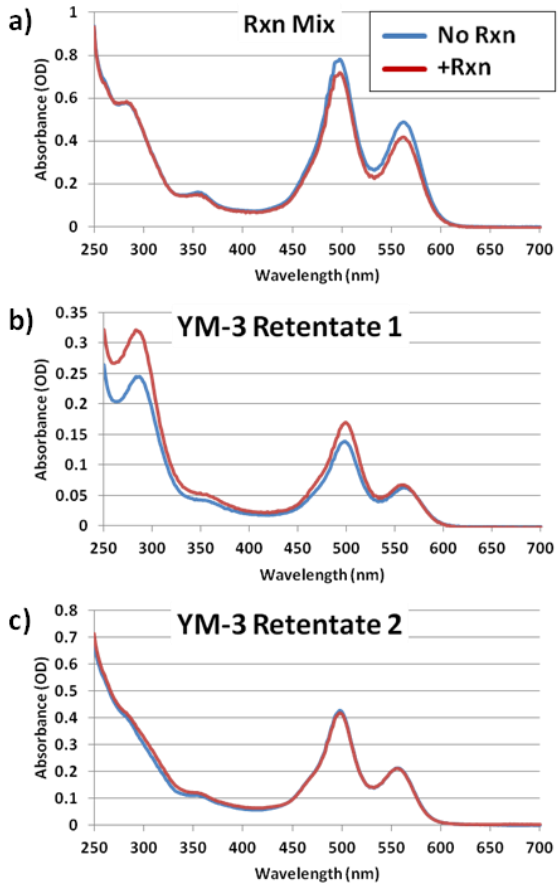

d)

No Rxn

Sample	Peptide Recovery
Reaction Mix	100%
YM-3 Retentate 1	19%
Final YM-3 Effluent	3%
YM-3 Retentate 2	17%

+Rxn

Sample	Peptide Recovery
Reaction Mix	100%
YM-3 Retentate 1	19%
Final YM-3 Effluent	3%
YM-3 Retentate 2	16%

Figure IV-26: UV-visible absorbance of reaction mix components from EDAC coupling of Peptide 13c and PAMAM-G4
Peptide 13c was reacted with PAMAM-G4 either with (red) or without (blue) EDAC carbodiimide coupling reagent. Reaction mix aliquots (a) were collected prior to YM-3 ultrafiltration. YM-3 Retentates 2 (c) represent repeated ultrafiltration of retentates from initial YM-3 ultrafiltration (b). TAMRA-associate absorbance was used to calculate peptide recovery in each fraction (d).

IV.3.8. Synthesis and characterization of pB2vp5C-cooh

We hypothesized that the lack of empirical evidence for covalent bonding of FRET-equipped MMP substrate peptides to different types of nanoparticles using various coupling chemistries could be attributed to steric hindrance of the reactive functional groups on peptides due to the proximity of bulky peptide constituents to the C-terminus

and/or unfavorable conformation of peptides owing to hydrophobic interactions. To address these concerns, a peptide based on pB2v with a relatively long hydrophilic spacer and a cysteine residue at the C-terminus, "pB2vp5C-cooh" [Fmoc-{peg$_1$}K(fam){peg$_1$}RPLGLWAR{peg$_1$}K(tamra){peg$_5$}C-cooh], was synthesized by SPPS (refer to Appendix A for detailed structure). This peptide was deprotected at the N-terminus and folated on resin according to the established standard protocol for folation (see III.2.7) to generate "FApB2vp5C-cooh."

After final deprotection, cleavage from solid support resin, and recovery by precipitation in ice cold Et_2O, crude FApB2vp5C-cooh peptide was characterized by ESI+ MS to determine the molecular weights of recovered peptide products. Unlike previous results from peptides produced by SPPS, the ions most abundant by far in the mass spectrum of crude FApB2vp5C-cooh (Figure IV-27) represented multiple charge states of a parent ion with the expected mass of the peptide without any modifications.

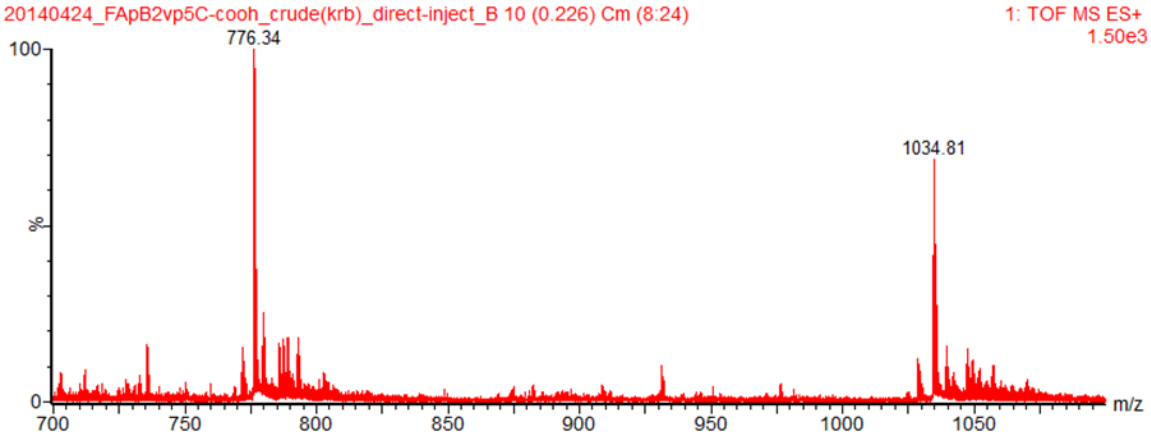

Figure IV-27: ESI+ mass spectrum of unpurified FApB2vp5C-cooh
The most abundant mass peaks represent the triply (1034.81, M+3H) and quadruply (776.34 M+4H) charged states of the expected FApB2vp5C-cooh peptide from SPPS.

The relative purity of crude FApB2vp5C-cooh peptide mixture from SPPS was further investigated by LCMS. While the resulting chromatogram of total ions counted (Figure IV-28) displayed multiple peaks, the first two peaks represented low molecular weight ions not likely to be peptide products of SPPS and the peak of greatest area was characterized by a mass spectrum similar to Figure IV-27, above, indicative of the expected structure of FApB2vp5C-cooh (data not shown).

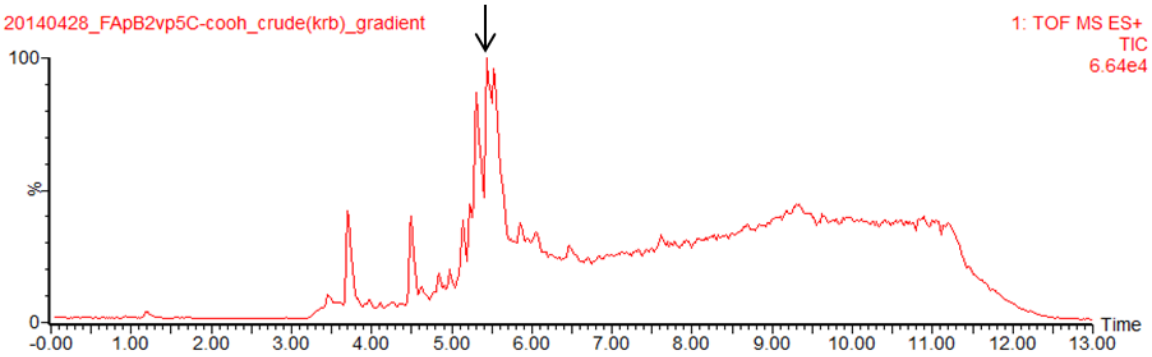

Figure IV-28: LCMS of unpurified FApB2vp5C-cooh
Trace represents total ion count in ESI+ mode following reversed-phase liquid chromatography of crude FApB2vp5C-cooh from SPPS. Arrow indicates the most abundant peak containing ions with the expected molecular weight of the intended peptide.

The intended optical properties of unpurified FApB2vp5C-cooh were confirmed by UV-visible spectrophotometry and plate reader fluorescence spectroscopy. As seen in Figure IV-29a, the crude peptide possessed visible-spectrum absorbance maxima near 495 nm and 560 nm, characteristic of FAM and TAMRA dyes, respectively. Excitation of FApB2vp5C-cooh at 555 nm resulted fluorescence emission near 580 nm, also representative of TAMRA dye, as plotted in Figure IV-29b. Most importantly, excitation at 494 nm resulted in fluorescence emission with a local maximum around 520 nm, characteristic of FAM, but an even greater maximum around 580 nm, suggesting better than 50% FRET efficiency between FAM and TAMRA.

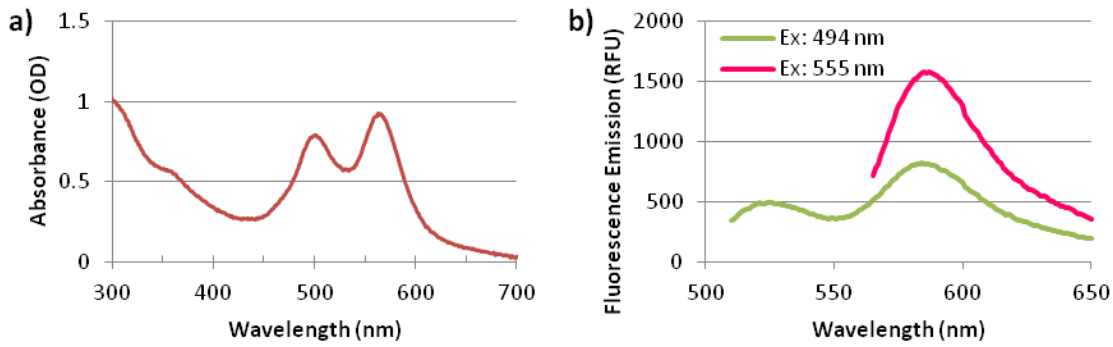

Figure IV-29: Optical properties of FApB2vp5C-cooh peptide
Absorbance (a) and fluorescence (b) spectra of unpurified FApB2vp5C-cooh peptide.

To validate FApB2vp5C-cooh as an optical sensor of MMP-associated proteolysis, the FRET switch of unpurified FApB2vp5C-cooh upon cleavage by MMPs (2, 9, or 14) was measured. As plotted in Figure IV-30, a greater than 10-fold increase in sensor (FAM) fluorescence emission intensity was generated within 60 minutes of incubation with each MMP while continuing to trend upward. The increasing trend continued through approximately 10 hours of uncovered incubation at 37 °C to give 23-, 24-, and 28-fold increases in FApB2vp5C-cooh sensor fluorescence generated by incubation with MMP2, MMP14, and MMP9, respectively (data not shown). MMPs used in this experiment were not characterized for active enzyme content.

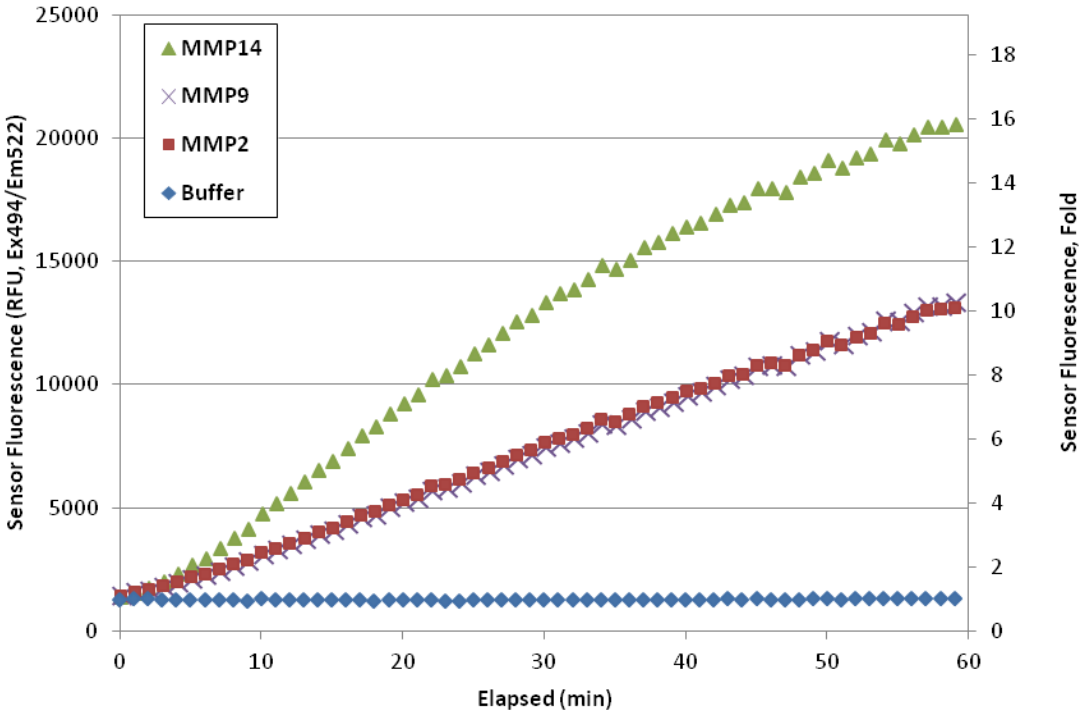

Figure IV-30: FRET switch assay of FApB2vp5C-cooh peptide with MMPs
Sensor fluorescence amplification of FApB2vp5C-cooh upon treatment with MMPs 2, 9, and 14 to cleave peptide substrate. Control samples ("Buffer", blue diamonds) contained an only assay buffer in lieu of enzyme. Values represent average of triplicates. Error bars not shown (SEM; small enough to be obscured by trace markers).

IV.3.9. Synthesis of nanobeacons via reaction of FApB2vp5C-cooh with amine-bearing iron oxide nanoparticles and heterobifunctional linkers

With the MMP-sensing capability of FApB2vp5C-cooh confirmed, a nanoparticle with surface chemistry amenable to bioconjugation involving the C-terminal cysteine residue was required for synthesis of proteolytic nanobeacons. Iron oxide nanoparticles remained an attractive option for nanoparticle cores owing to their ease of recovery by magnetic attraction and the additional imaging modalities they potentially enable, such as MRI contrast and histological staining with Prussian blue. Primary amines provided an adaptable chemistry for bioconjugation with cysteine, as either carbodiimides or any of several commercially available heterobifunctional linkers can mediate covalent bonding of the two [129].

As such, APTES-coated superparamagnetic iron oxide nanoparticles ("FeOx-NH_2") were synthesized by thermal decomposition of iron pentacarbonyl [$Fe(CO)_5$] in oleic acid followed by ligand exchange of APTES for oleic acid by Charleson S. Bell of the Giorgio Laboratory (Dept. of Biomedical Engineering, Vanderbilt University, Nashville, TN, USA). The average particle diameter determined by transmission electron microscopy (TEM) was approximately 17 nm. The presence of surface amines was confirmed by qualitative Ninhydrin test (data not shown, see III.2.4 for general method).

Synthesis of folate-targeted proteolytic nanobeacons was attempted by reacting FApB2vp5C-cooh peptide and FeOx-NH_2 nanoparticles with either Sulfo-SMPB or SIA, two heterobifunctional linkers with amine-reactive succinimidyl groups and sulfhydryl-reactive maleimide or iodoacetyl groups, respectively. Schematically diagrammed in Figure IV-31, FeOx-NH_2 were first "activated" by reaction with SIA or Sulfo-SMPB while FApB2vp5C-cooh was pre-treated with TCEP to reduce and thereby eliminate any disulfide bonds that may have formed in DMSO solution. Activated nanoparticles and reduced peptide solution were then mixed for approximately 21 hours before a solution of mPEG-SH(1k) was added to each reaction to PEGylate any unreacted SIA or Sulfo-SMPB sites, affording FeOx-based "NP^{++}_{SIA}" and "NP^{++}_{SMPB}."

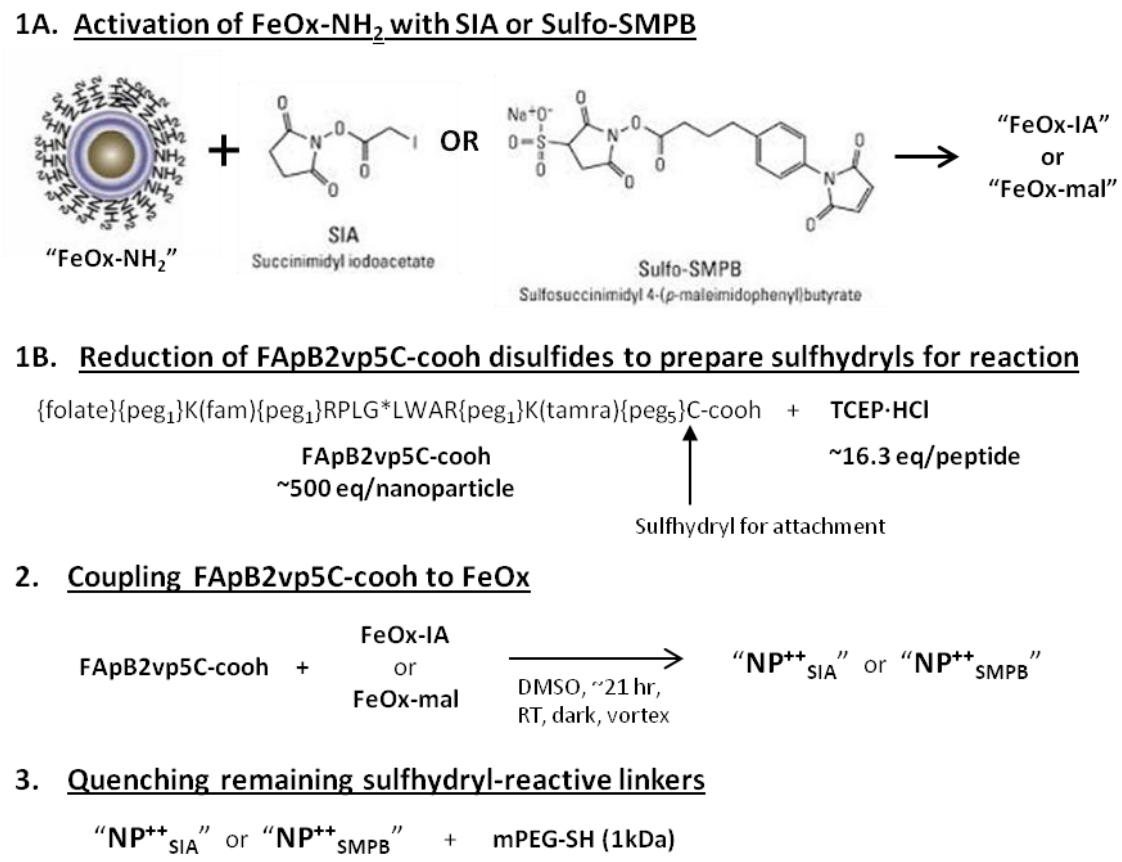

Figure IV-31: Scheme, preparation of FeOx-based NP^{++} nanobeacons
Reactions of FeOx-NH_2 with FApB2vp5C-cooh mediated by amine- and –sulfhydryl-reactive heterobifunctional crosslinkers SIA and Sulfo-SMPB.

The magnetic nanoparticle products of FeOx-based proteolytic nanobeacon synthesis reactions were pelleted by magnetic attraction and the supernatants collected for subsequent analysis. DMSO was added to pellets and magnetic collection repeated, as represented in Figure IV-32.

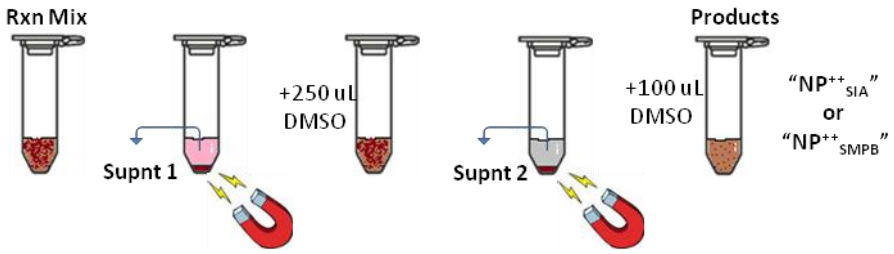

Figure IV-32: Scheme, magnetic separation and recovery of reaction mix components following FeOx-based NP^{++} synthesis

To determine the extent of reaction, the UV-visible absorbance spectra of the recovered component solutions from magnetic separation of reaction mixes were recorded. The absorbance spectra of the magnetically recovered products of syntheses were unobtainable due to rapid flocculation of suspended particulates in DMSO. Several solvents, including water, ethanol, anhydrous DMSO, and chloroform were introduced by solvent exchange to improve the stability of the colloidal suspensions, but none were successful insofar as stabilizing suspensions long enough to obtain absorbance spectra. The supernatants collected from the initial magnetic separation of reaction mix components from each reaction mix ("Supnt 1", above) exhibited visible absorbance spectra characteristic of FApB2vp5C-cooh, as seen in Figure IV-33. The subsequently collected supernatants from the washing of magnetically recovered reaction mix components ("Supnt 2," above), however, where characterized by negligible peptide-associated absorbance.

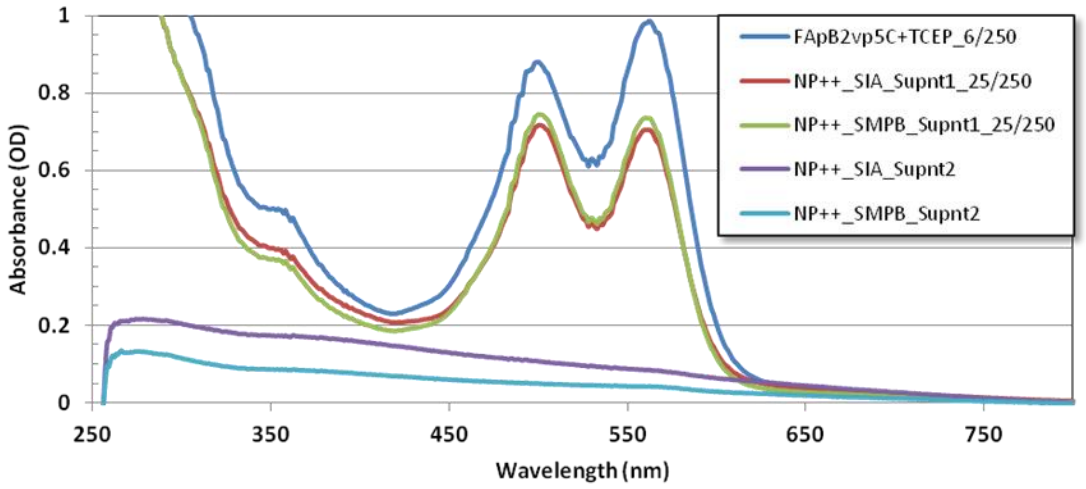

Figure IV-33: Absorbance of FeOx-based NP^{++} reaction mix components recovered from magnetic separation.
Components of reaction mixes from FApB2vp5C-cooh and FeOx-NH_2 with SIA or Sulfo-SMPB were collected following reactions and subsequent magnetic separation. A diluted aliquot of the reduced FApB2vp5C-cooh reactant used in reactions is shown in dark blue. Supernatants 1 (red, green) were collected after pelleting paramagnetic constituents magnetically. Supernatants 2 (purple, light blue) were collected following a DMSO resuspension and magnetic pelleting.

Similar to previous assessments of peptide attachment to nanoparticles using UV-visible absorbance (see IV.3.4, IV.3.6, IV.3.7), peptide recovery was determined by TAMRA-associated absorbance in supernatant samples relative to that in the reaction mix. Representative of peptide recovery, the first supernatant from NP^{++}_{SIA} synthesis exhibited 56% of the TAMRA absorbance in the corresponding reaction mix. The first supernatant from NP^{++}_{SMPB} similarly indicated recovery of 55% of the peptide initially added to the synthesis reaction. As indicated above, the supernatants collected following a wash of magnetic nanoparticles with DMSO possessed negligible peptide-associated absorbance, while measurement of absorbance from magnetically recovered products was not possible. By inference, though, because 55-56% of the peptide-associated TAMRA absorbance from reaction mixes was attributed to recovered supernatants, 44-45%

coupling of FApB2vp5C-cooh to FeOx nanoparticles (or approximately 225 peptides per nanoparticle) was suspected.

To further investigate FApB2vp5C-cooh peptide attachment to FeOx nanoparticles, fluorescence emission spectra of magnetically recovered NP^{++}_{SIA} and NP^{++}_{SMPB} nanoparticles were recorded by plate reader fluorescence spectroscopy. As shown in Figure IV-34a, FeOx-based NP^{++}_{SIA} and NP^{++}_{SMPB} nanoparticles fluoresced weakly upon excitation at 494 nm, exhibiting noisy emission spectra with maxima near 580 nm, indicative of either TAMRA fluorescence or FRET between FAM and TAMRA. Unexpectedly, emission intensity maxima near 520 nm were almost unobservable.

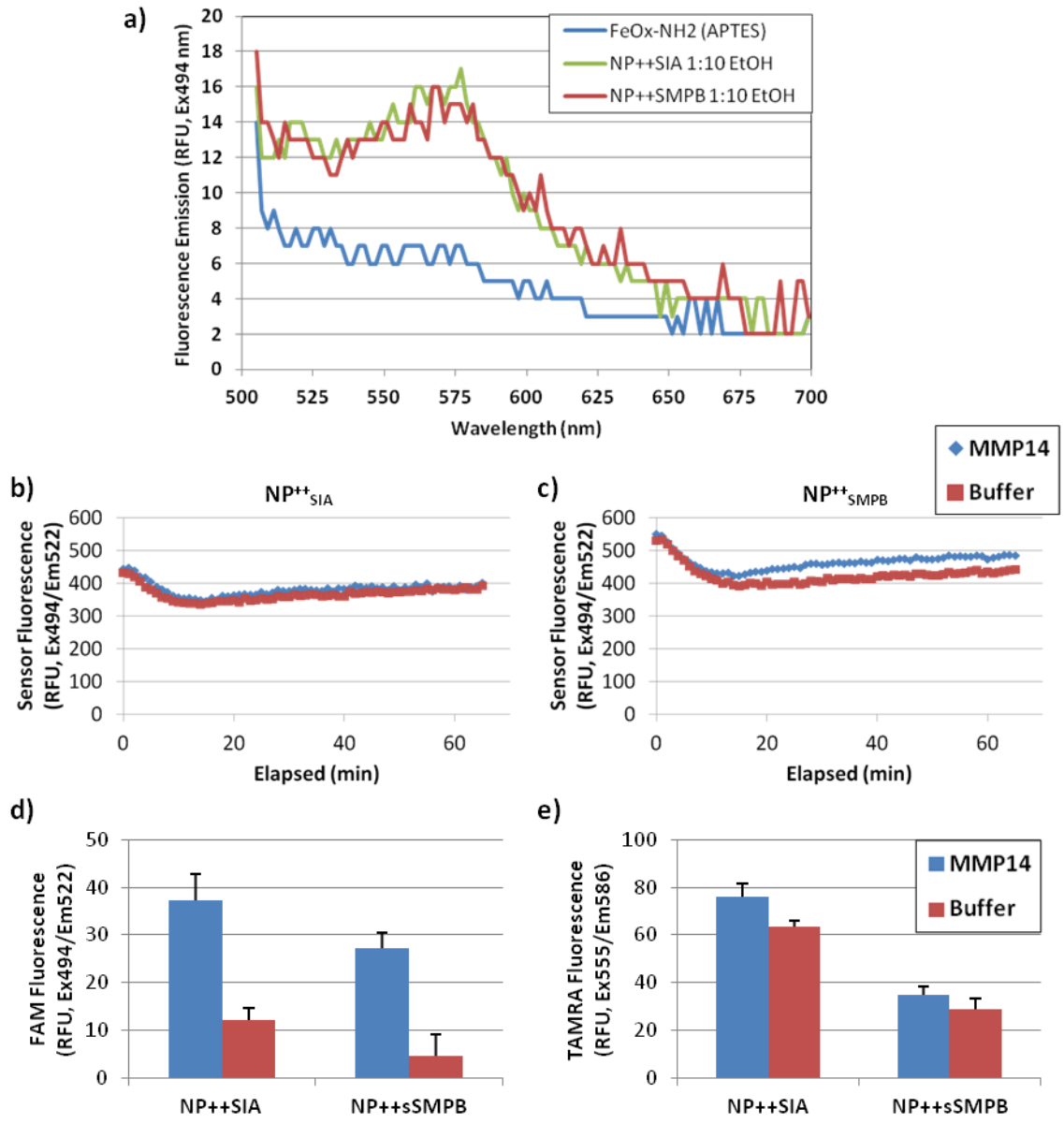

Figure IV-34: Fluorescence and FRET properties of FeOx-based NP^{++}_{SIA} and NP^{++}_{SMPB}. Sensor (FAM) fluorescence emission of magnetically-recovered products from reaction of FApB2vp5C-cooh with FeOx-NH_2 compared to starting nanoparticles (a). Sensor (FAM) fluorescence emission over time upon incubation of NP^{++}_{SIA} (b) or NP^{++}_{SMPB} (c) with MMP-14. Blank-subtracted FAM (d) and TAMRA (e) fluorescence emission of iron-depleted supernatants following incubation with MMP14 or buffer. Values represent mean of triplicates +/-SEM (b-e).

To test the hypothesis that broad absorbance in the UV-visible range by FeOx nanoparticles could be interfering with excitation and emission of the peptide-associated fluorophores, thereby limiting detection of nanobeacon fluorescence, NP^{++}_{SIA} and

NP^{++}_{SMPB} were incubated with or without MMP14 in proteolysis buffer and monitored for FAM fluorescence by plate reader fluorescence spectroscopy over 1 hour, during which flocculated aggregates formed in assay wells. Despite the previously demonstrated FRET switch of FApB2vp5C-cooh with MMP14 (Figure IV-30), incubation of nanoparticle solutions with MMP14 did not result in any significant increase in sensor (FAM) fluorescence, as shown in Figure IV-34b,c. To determine whether depletion of iron from solutions could result in increased FAM fluorescence emission by proteolytically released peptide fragments, the FAM- and TAMRA-associated emission intensities of the assay sample supernatants were subsequently measured. While the FAM intensities of supernatants from samples treated with MMP14 were greater than those from samples containing only assay buffer, as shown in Figure IV-34d, the overall background-subtracted fluorescence intensities represented weak fluorescence, near the limit of detection of the instrument. The TAMRA fluorescence of supernatants (Figure IV-34e) did not exhibit as large a relative difference between MMP14 and assay buffer conditions, although the absolute magnitude of TAMRA emission was greater than FAM emission in all supernatants. Due to the lack of demonstrable FRET switch or sensor fluorescence in iron-depleted supernatants, FeOx-based NP^{++}_{SIA} and NP^{++}_{SMPB} could not be validated for use as proteolytic nanobeacons.

IV.3.10. Synthesis, purification, and characterization of folate-targeted proteolytic nanobeacons from pB2vp5C-cooh and PAMAM-G4 dendrimers

To facilitate optical assessment of FApB2vp5C-cooh peptide attachment to nanoparticles in proteolytic nanobeacon synthesis reactions without the interfering UV-visible absorbance from iron, PAMAM-G4 dendrimers were decorated with FApB2vp5C-cooh peptide using SIA, Sulfo-SMPB, or EDAC to mediate covalent bond

formation between cysteine residues on peptides and primary amines on dendrimers. As schematically diagrammed in Figure IV-35, PAMAM-G4 dendrimers, nominally possessing 64 primary amines each, were prepared by first reacting with PEG5000-NHS to improve water solubility. Aliquots of PEGylated dendrimers ("PAMAM4$(PEG5k)_2$") were then activated with SIA or Sulfo-SMPB to generate sulfhydryl-reactive sites on PAMAM-G4, while FApB2vp5C-cooh peptide was reduced with β-mercaptoethanol to eliminate disulfide dimers that may have formed due to oxidation in solution. Approximately 5 molar equivalents of reduced peptide relative to dendrimers was mixed with either activated PAMAM4$(PEG5k)_2$ or with PAMAM4$(PEG5k)_2$ and EDAC to couple peptides to dendrimers. Following overnight reactions, mPEG-SH (1kDa) was added to the reaction mixes including heterobifunctional linkers SIA or Sulfo-SMPB to convert any remaining sulfhydryl-reactive groups on dendrimer branch termini. The nanoparticle products of reactions were deemed "NP^{++}_{SIA}," "NP^{++}_{SMPB}," or "NP^{++}_{EDAC}" to represent intended folate-targeting and MMP cleavability as well as the mediator of peptide attachment to nanoparticle cores.

1. PEGylation of PAMAM-G4

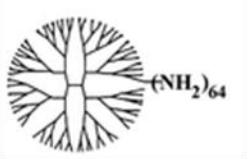

PAMAM-G4

+ PEG5000-NHS ester (2 eq/PAMAM) → $PAMAM4(PEG5k)_2$

2A. Activation of PAMAM

$PAMAM4(PEG5k)_2$ + SIA or Sulfo-SMPB (12.5 eq/PAMAM) → $PAMAM4(PEG5k)_2(IA \text{ or } mal)_{12.5}$

2B. Reduction of FApB2vp5C-cooh

FApB2vp5C-cooh + $HO(CH_2)_2SH$ (1 eq/peptide) → (r)FApB2vp5C-cooh

3A. Coupling reduced FApB2vp5C-cooh to PAMAM via SIA or SMPB

(r)FApB2vp5C-cooh (5 eq/PAMAM) + $PAMAM4(PEG5k)_2(IA \text{ or } mal)_{12.5}$ → $PAMAM4(PEG5k)_2(FApB2vp5C)_x(OH)_y(IA \text{ or } mal)_{12.5-x-y}$

3B. Coupling reduced FApB2vp5C-cooh to PAMAM via carbodiimide (EDAC)

(r)FApB2vp5C-cooh (5 eq/PAMAM) + $PAMAM4(PEG5k)_2$ —EDAC (5 eq/peptide)→ "NP^{++}_{EDAC}"

4. Quenching remaining sulfhydryl-reactive linkers

$PAMAM4(PEG5k)_2(FApB2vp5C)_x(OH)_y(IA \text{ or } mal)_{12.5-x-y}$ + mPEG-SH (1kDa)

→ $PAMAM4(PEG5k)_2(FApB2vp5C)_x(OH)_y(PEG1k)_{12.5-x-y}$

= "NP^{++}_{SIA}" or "NP^{++}_{SMPB}"

Figure IV-35: Scheme, synthesis of PAMAM-based NP^{++}_{EDAC}, NP^{++}_{SIA}, and NP^{++}_{SMPB} from FApB2vp5C-cooh and PAMAM-G4 dendrimer

After completion of PAMAM-G4-based NP^{++} synthesis reactions, reaction mixes were diluted in buffer containing 20% ethanol and reconcentrated by ultrafiltration in YM-10 (MWCO 10,000) centrifugal filter devices, as described above (see IV.3.7). Initial retentates were diluted and reconcentrated a second time with collection of all solutions to allow spectrophotometric quantitation of peptide recovery in each component of separated reaction mixes. Shown in Figure IV-36, the UV-visible absorbance spectra

of all collected solutions diluted in PBS (pH 7.1) were indicative of FAM and TAMRA, possessing absorbance maxima near 495 nm and 560 nm.

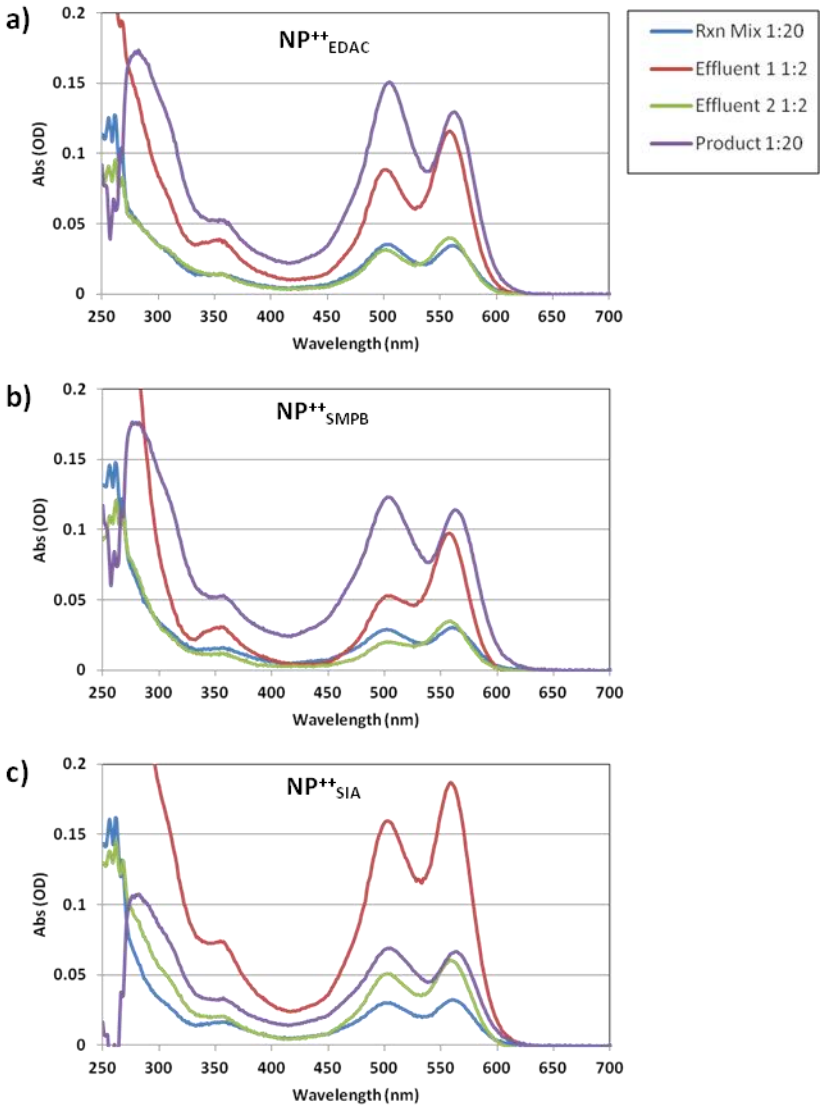

Figure IV-36: Absorbance of recovered PAMAM-based NP^{++} reaction mix components following ultrafiltration.
Absorbance of reaction mixes (blue), effluents (red, green) and retentates (purple, "Product") following YM-10 ultrafiltration of coupling of FApB2vp5C-cooh and PAMAM-G4 via EDAC (a), Sulfo-SMPB (b), or SIA (c).

FApB2vp5C-cooh peptide recovery in final ultrafiltration retentates ("product" in Figure IV-36 and Table IV-4) and effluents were determined by TAMRA-associated

absorbance of each component of reaction mixes. Coupling of peptide with EDAC and Sulfo-SMPB appeared to be more efficient than with SIA, as indicated by 77%, 75%, or 48% recovery in each product, respectively, as seen in Table IV-4. Given the stoichiometry of the reactions, these recoveries represented approximate averages of 3.9 peptides per dendrimer in NP^{++}_{EDAC}, 3.8 in NP^{++}_{SMPB}, and 2.4 in NP^{++}_{SIA}. Substantial and varied TAMRA-associated absorbance in ultrafiltration effluents suggested effective transport of FApB2vp5C-cooh through filters to separate PAMAM-bound from free peptides.

Table IV-4: Calculated peptide recovery in PAMAM-based NP++ reaction mix components

	% Peptide Recovery (TAMRA dye)		
Sample	NP^{++}_{EDAC}	NP^{++}_{SMPB}	NP^{++}_{SIA}
Effluent 1	14%	17%	36%
Effluent 2	9%	8%	16%
Product	77%	75%	48%

To validate PAMAM-based NP^{++} nanoparticles for use as proteolytic nanobeacons, capable of sensing MMP activity, NP^{++}_{EDAC}, NP^{++}_{SMPB}, and NP^{++}_{SIA} were mixed with MMP9 and monitored for FRET switch in comparison with the constituent FApB2vp5C-cooh peptide by plate reader fluorescence spectroscopy. EDTA was included in a control sample with FApB2vp5C-cooh and MMP9 to inhibit metalloproteinase activity. Sensor (FAM) fluorescence emission intensity of the peptide and all NP^{++} products increased roughly linearly over 60 minutes of exposure to MMP9, as shown in Figure IV-37. No FRET switch was observed in any sample not containing MMP9. Inclusion of EDTA completely abrogated FRET switch from FApB2vp5C-cooh peptide (Figure IV-37a,b). After 60 minutes, the relative FRET switch of NP^{++}_{EDAC} was greatest of all samples,

represented by a greater than 12-fold increase in FAM fluorescence emission (Figure IV-37d). NP^{++}_{SMPB} and NP^{++}_{SIA} each also exhibited FRET switches greater than 10-fold after 60 minutes with MMP9.

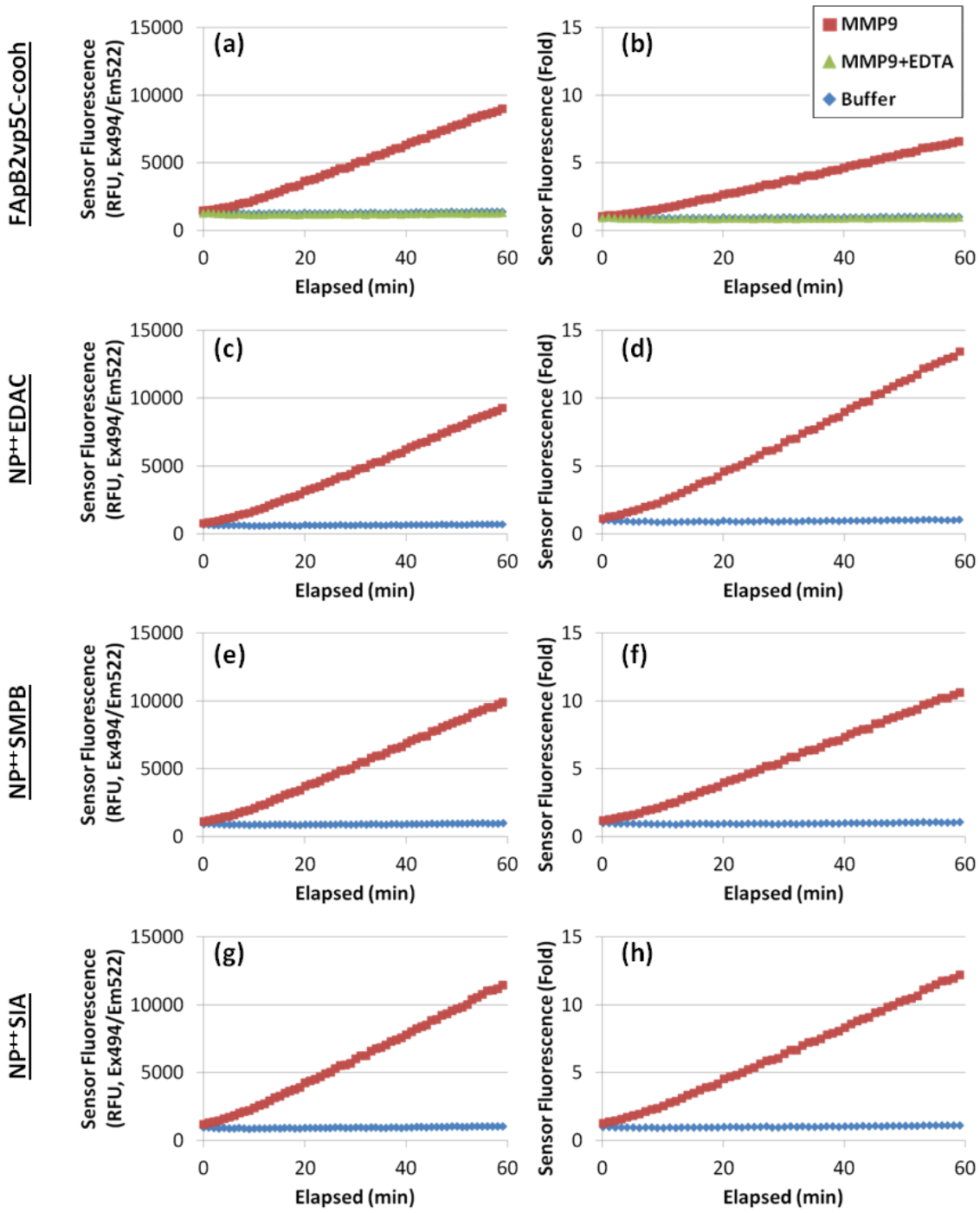

Figure IV-37: FRET switch assay of FApB2vp5C-cooh and PAMAM-based NP++ nanobeacons with MMP9

Sensor fluorescence of FApB2vp5C-cooh peptide (a-b), NP^{++}_{EDAC} (c-d), NP^{++}_{SMPB} (e-f), and NP^{++}_{SIA} (g-h) was measured in real time during incubation with MMP9. Green triangles (a-b) indicate inhibition of MMP9 activity by inclusion of EDTA. Values represent average of triplicates.

Sensor fluorescence of all samples mixed with MMP9 continued to increase for approximately 10 hours before sharply decreasing, presumably due to evaporation of sample solutions. NP^{++}_{EDAC}, which possessed the greatest relative FApB2vp5C-cooh peptide recovery from nanobeacon synthesis (Table IV-4, above), exhibited the greatest maximum FRET switch after 10 hours with a greater than 61-fold increase in FAM emission, as shown in Figure IV-38. Maximum FRET switch was greater for each NP^{++} proteolytic nanobeacon than the constituent FApB2vp5C-cooh peptide. The fluorescence emission intensity of the reference fluorophore (TAMRA) in each sample also increased over time (data not shown). As a result, the maximum FRET switch of NP^{++}_{EDAC} after 10 hours corresponded to an increase in the sensor-to-reference emission ratio (S/R) of 9.4-fold (data not shown).

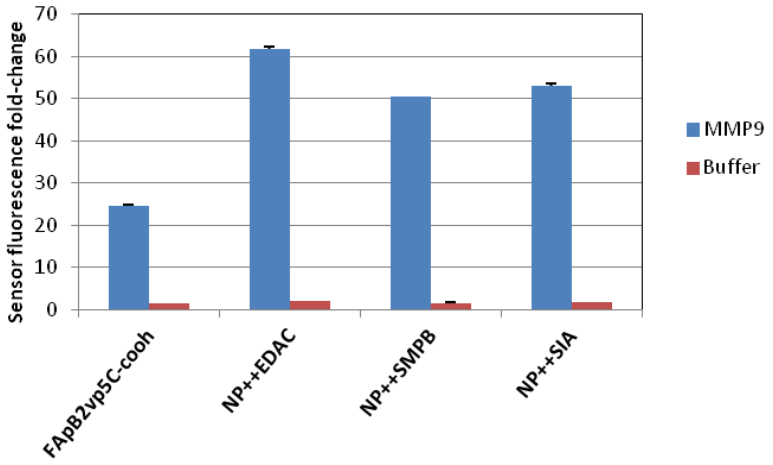

Figure IV-38: Maximum FRET switch of FApB2vp5C-cooh and PAMAM-based NP++ nanobeacons with MMP9
FApB2vp5C-cooh and NP^{++}_{EDAC}, NP^{++}_{SMPB}, and NP^{++}_{SIA} synthesized on PAMAM-G4 were incubated with or without MMP9 in proteolysis buffer. Chart reflects maximum fold-change in sensor fluorescence emission intensity after approximately 10 hours of incubation. Values represent average of triplicates. Error bars: SEM.

IV.3.11. Pilot assessment of MMP- and folate-dependent uptake of proteolytic nanobeacons in vitro

To validate proteolytic nanobeacons *in vitro* with endogenous MMPs and to test the impacts of folate targeting and/or MMP cleavage on cellular uptake of proteloytic nanobeacons, MDA-MB-231 human breast cancer cells were incubated with media containing either intact or MMP14 pre-cleaved NP^{++}_{EDAC} nanobeacons, with or without the addition of folic acid to compete for folate receptors on cell membranes. Following 4 hours of exposure in chamber slide wells, treatment media were collected and cells were washed with fresh PBS prior to imaging by fluorescence microscopy to visualize sensor (FAM) and reference (TAMRA) fluorescence belonging to proteolytic nanobeacons and products of nanobeacon cleavage. The FRET switch of NP^{++}_{EDAC} by recombinant MMP14 in cell culture medium was confirmed by plate reader fluorescence spectroscopy (data not shown). As seen in Figure IV-39, both sensor and reference fluorescence were most prominent in cells treated with intact NP^{++}_{EDAC} without free folic acid competition (Figure IV-39a-d). Interestingly, fluorescence in the sensor channel was found intracellularly in both diffuse and punctate patterns, whereas reference fluorescence was punctate only. Cells in no other treatment conditions exhibited diffuse fluorescence in the sensor channel. Neither sensor nor reference fluorescence was observed in cells treated with intact NP^{++}_{EDAC} and free folic acid (Figure IV-39e-h). Fluorescence puncta in both the sensor and reference channels were found in cells treated with pre-cleaved NP^{++}_{EDAC} in the absence of free folic acid (Figure IV-39i-l), however treatment with pre-cleaved nanobeacons in combination with folic acid resulted in the observation of no intracellular fluorescence (Figure IV-39m-p).

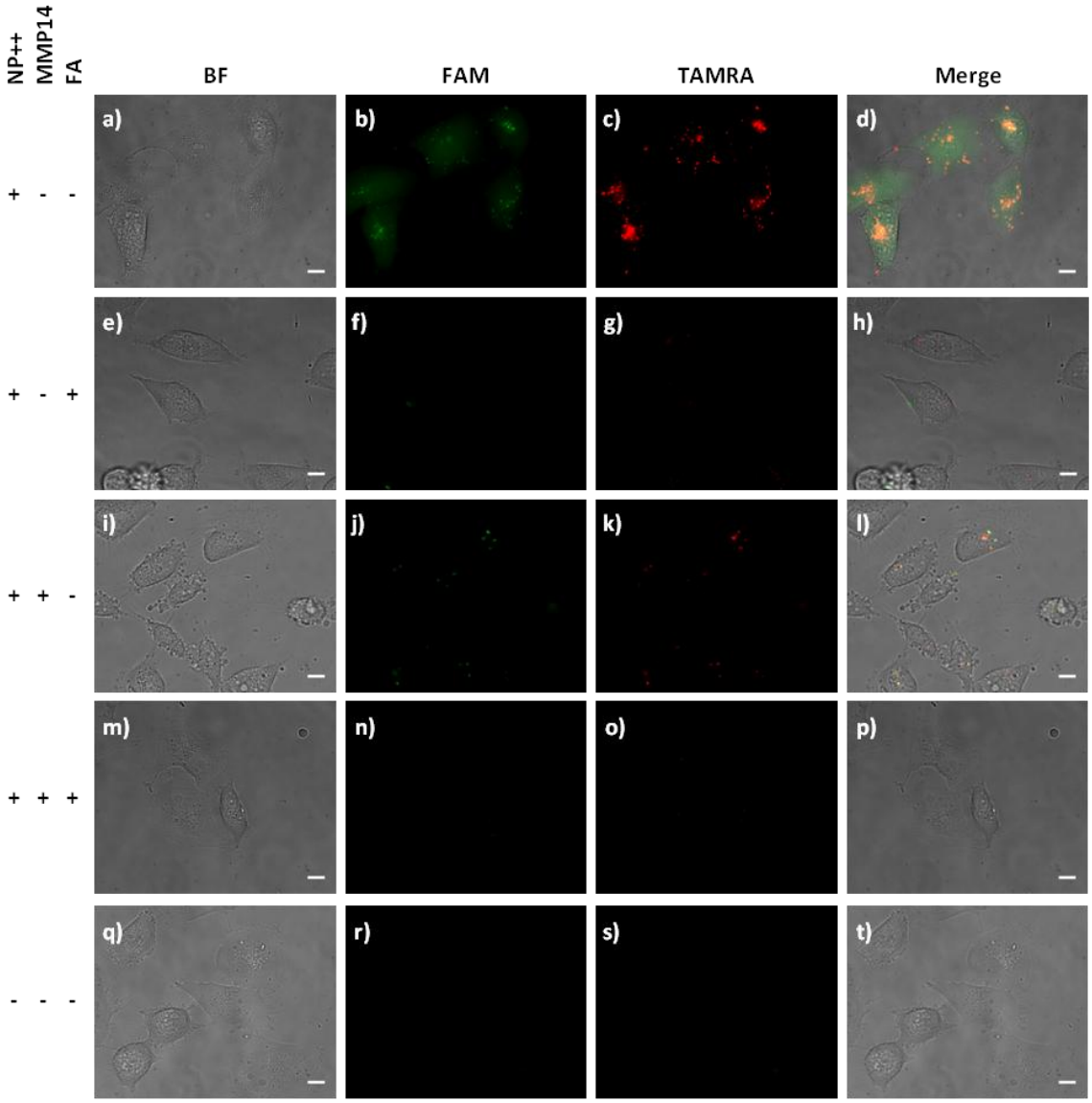

Figure IV-39: Fluorescence microscopy of cell uptake of NP^{++}_{EDAC} by MB231 cells.
MDA-MB-231 cells incubated in folate-free medium containing NP^{++}_{EDAC} (a-p). The additions to each set of culture wells are indicated on the left. NP^{++}_{EDAC} was added either unmodified (a-h) or after pre-incubation with MMP14. Competing folic acid was included (e-h, m-p) or omitted (a-d, i-l) from media during incubation with NP^{++}_{EDAC}. The non-fluorescent no-treatment controls (q-t) were incubated in medium only. Scale bar: 10 µm.

To further quantitate intracellular fluorescence as a measure of cell uptake of nanobeacons, MDA-MB-231 cells were harvested from chamber slides following fluorescence microscopy (above) and analyzed by flow cytometry with 488 nm

excitation. Emission was recorded using filters appropriate for FAM and TAMRA emission, the latter resulting either from minimal excitation of TAMRA at 488 nm or FRET from FAM. As shown in Figure IV-40, both FAM and TAMRA fluorescence emission intensities were about an order of magnitude greater than control in cells treated with NP^{++}_{EDAC} proteolytic nanobeacons in the absence of free folic acid. Cells treated with intact nanobeacons fluoresced more than cells treated with beacons pre-incubated with MMP14 in both emission filters, except when free folic acid was included in treatment media, in which cases cellular fluorescence was no different than controls that were incubated without nanobeacons regardless of proteolytic cleavage.

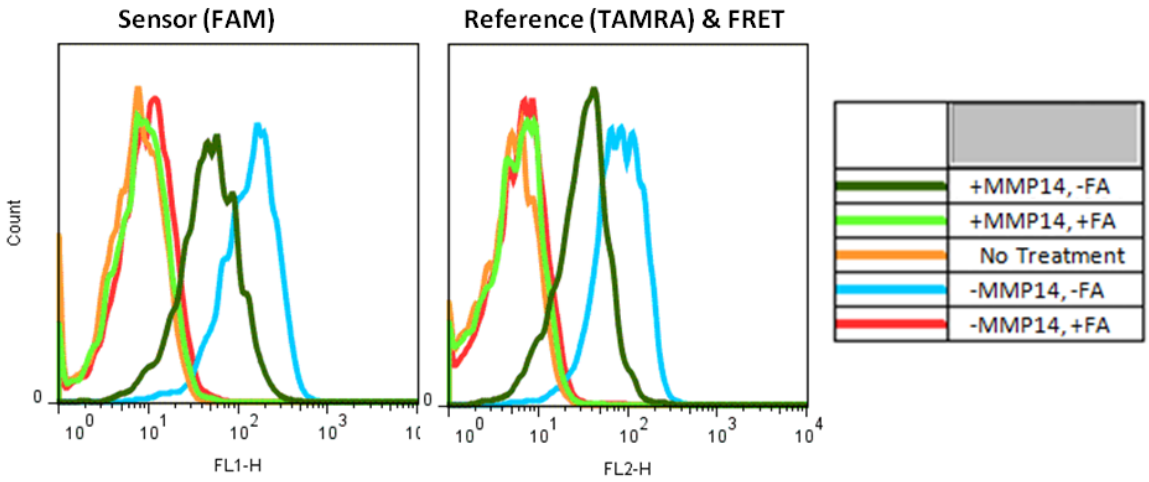

Figure IV-40: Flow cytometry of MDA-MB231 cells following treatment with NP^{++}_{EDAC}. +/-MMP14 indicates whether or not cell culture media containing NP^{++}_{EDAC} were treated overnight with MMP14 prior to cell treatment. +/-FA indicates the inclusion or omission of folic acid during cell incubation with NP^{++}_{EDAC}. No treatment represents incubation of cells with incubation medium only.

Binary gates for FAM and TAMRA fluorescence emission were imposed to calculate the relative number of cells from each treatment condition that were positive for nanobeacon-associated fluorescence. As tabulated in Table IV-5, while less than 1% of control cells were positive for FAM or TAMRA, more than 96% of cells treated with

intact NP^{++}_{EDAC} folate-targeted proteolytic nanobeacons without free folic acid were positive. More than 70% of cells exposed to pre-cleaved nanobeacons in the absence of free folic acid also fluoresced above thresholds for FAM or TAMRA. The vast majority of similarly treated cells that were co-incubated with free folic acid to compete for folate receptors, however, were negative according to the same gates. Taken together with the fluorescence microscopy of cells, cellular association of NP^{++}_{EDAC} appeared to be mostly dependent upon folate-targeting.

Table IV-5: Gated detection of FAM and TAMRA/FRET fluorescence by flow cytometry following NP^{++}_{EDAC} uptake experiment with MDA-MB231 cells

				Live Cells	
Sample	**NP^{++}_{EDAC}**	**MMP14**	**FA**	**FAM+ (%)**	**TAMRA/FRET+ (%)**
No Treatment	-	-	-	0.2	0.9
No pretreat, No FA	+	-	-	96.1	97.8
No pretreat, FA	+	-	+	1.5	3.4
MMP14 Pretreat, No FA	+	+	-	70.1	80.6
MMP14 Pretreat, FA	+	+	+	1.2	2.3

IV.4. Discussion and Conclusions

The research presented in this chapter focused on the synthesis and characterization of folate-targeted proteolytic nanobeacons from the constituent beacon peptides and different types of nanoparticles. As discussed below, the initially proposed synthesis scheme employing oxime ligation of FRET-equipped MMP substrate peptides with FeOx nanoparticles proved unsuccessful in the production of nanobeacons with measurable optical properties for MMP-dependent imaging and delivery applications. Several attempts at alternative syntheses based upon published bioconjugation techniques also resulted in unsuitable nanoparticles, though providing insights into the complexities beacon peptide attachment to nanoparticles. Ultimately, proof-of-concept was accomplished by synthesizing folate-targeted proteolytic nanobeacons using peptides

with hydrophilic PEG5 spacer tails and amine-terminated organic PAMAM dendrimers. The resulting nanoparticles were shown to possess all of the requisite optical and biochemical characteristics necessary for testing of the hypothesis that combined targeting of nanoparticle payloads to folate receptors and proteolysis by MMPs improves selective delivery to solid tumor cells.

Development and troubleshooting of conditions for oxime ligation of the beacon peptides developed in the previous chapters with dextran-coated iron oxide (IDX) nanoparticles provided several insights that informed the successful synthesis of proteolytic nanobeacons. To facilitate this type of bioconjugation with peptides possessing an aminooxy functional group, nanoparticles presenting carbonyl (ketone or aldehyde) groups were required. As indicated by Figure IV-2, introduction of aldehydes on the surfaces of water-soluble IDX nanoparticles was achieved by oxidation with sodium *meta*-periodate as reported previously[129,151,152] and could be detected by modification of a commercial assay for aldehyde concentration in solutions. The number of aldehydes detected per IDX nanoparticle (Table IV-1) correlated with increasing concentration of periodate applied up to 2000 µM, above which IDX nanoparticles rapidly flocculated (data not shown). Oxidation by 500-1000 µM sodium *meta*-periodate over 1 hour was determined to be optimal for maximum introduction of aldehydes without causing noticeable flocculation.

In the pilot attempt to synthesize folate-targeted proteolytic nanobeacons from peptides produced by SPPS, unpurified FApB2vAoa peptide mixture was reacted with oxidized IDX nanoparticles (oIDX-500µM) and 100 µM aniline for nucleophilic catalysis of the reaction[130]. Approximately 3 molar equivalents or 6 molar equivalents of

FApB2vAoa relative to nanoparticles (chosen to be less than the calculated 10.7 aldehydes per nanoparticle on oIDX-500μM) were added in two separate reactions to allow assessment of relative conjugation efficiency in each reaction (abbreviated NP_3^{++} and NP_6^{++}, respectively). UV-visible spectrophotometry was used following ultrafiltration to quantitatively compare the amount of peptides bound to nanoparticles based on the characteristic absorbances of FAM and TAMRA fluorophores incorporated in FApB2vAoa. As seen in Figure IV-4, recovered reaction mixes and concentrates from ultrafiltration of the reactions possessed absorbance spectra shaped differently than the parental oIDX-500μM nanoparticles, especially in the 400-600 nm wavelength range where FAM and TAMRA absorb maximally. The filtrates, on the other hand absorbed very little in the same range, indicating negligible iron and peptide concentrations. Scaling and subtraction of the oIDX-500μM absorbance spectrum from the reaction mixes and ultrafiltration concentrates resulted in residual spectra (Figure IV-5) resembling the absorption of the peptide-associated dyes, confirming FApB2vAoa content in the reaction mixes and suggesting recovery of peptides with nanoparticles retained during ultrafiltration. However, the observation of very little UV-visible absorbance in the filtrates (Figure IV-4c) prompted comparison of the reaction mix concentrates with non-reactive control solutions to which ultrafiltration was also applied. Shown in Figure IV-6, the fluorescence emission intensities corresponding to excitation of FAM and TAMRA dyes were greater in the NP_6^{++} concentrate than NP_3^{++} concentrate, reflective of the difference in the amount of FApB2vAoa peptide added to the reaction mixes. Yet the nearly equivalent emission intensities of NP_3^{++} concentrate and the control concentrates indicated that the majority of the fluorescence signal from NP_3^{++} could not

be attributed to covalently attached peptides. The very faintly detectable fluorescence emission from the NP_6^{++} concentrate following a wash with MeOH (Figure IV-7), in which FApB2vAoa is soluble but IDX nanoparticles are not, further corroborated the suggestion that peptides were not covalently attached and could be removed by solvation. Given the lack of peptide-associated absorption in filtrates, the similarity of NP_3^{++} concentrate fluorescence emission intensity to non-reactive control solutions, and the observation that the ultrafiltration devices were stained following centrifugation (data not shown), FApB2vAoa peptides were not efficiently bioconjugated to oxidized IDX particles in the aforementioned reactions nor did they traverse the filter membranes of the ultrafiltration device as expected. Furthermore, due to aggregation and challenging recovery of iron-containing particles in the devices, ultrafiltration was determined to be unsuitable for the separation of IDX-based nanoparticles and unbound FApB2vAoa.

To explore conditions for improving the efficiency of peptide coupling with surface aldehydes on oxidized IDX nanoparticles, FApB2vAoa crude peptide mixture was mixed with oIDX-1000μM nanoparticles and either aniline or pPDA, a substituted aniline derivative that has been reported to provide an increased rate of oxime catalysis relative to aniline[135]. Characterization of the centrifugally separated particulate products of these reactions by UV-visible spectrophotometry (Figure IV-10) yielded unexpected results. Shown in Figure IV-11, the peptide-associated (oIDX-1000μM subtracted) absorbance spectra of all samples that contained pPDA in their respective reaction mixtures ($NP_n^{++}{}_{pPDA}$, No-Rxn Ctl) were not distinctly representative of FAM and TAMRA absorbance. The spectrum of $NP_6^{++}{}_{An}$, from the reaction employing aniline as the catalyst, did exhibit the absorbance maxima characteristic of the dyes, as expected. This

observation was more obviously portrayed in the absorbance spectra of the recovered supernatants from particulate recovery by centrifugation (Figure IV-12), where the supernatants of $NP_6^{++}{}_{An}$ possessed the two absorbance peaks corresponding FAM and TAMRA in unbound FApB2vAoa and all other samples possessed only one broad absorbance peak corresponding to neither dye. As seen in Figure IV-13, the FAM-associated fluorescence emission intensities of $NP_n^{++}{}_{pPDA}$ recovered particles were all greater than that of $NP_6^{++}{}_{An}$ and correlated with the relative amount of FApB2vAoa added to reaction mixtures, however exhibited almost no detectable TAMRA-associated fluorescence emission. Taken together with the absorbance spectra, these data suggest that while pPDA is likely a more effective catalyst of oxime ligation in the reaction conditions tested, it alters the optical properties of TAMRA. Reactions employing pPDA as a nucleophilic catalyst of oxime ligation were therefore not repeated, as the optical sensing of proteolysis by proteolytic nanobeacons made from the peptides developed in the preceding chapters is dependent upon FRET between FAM and TAMRA.

Modifications of the reaction conditions including solvent system, buffer, and reagent quality for aniline-catalyzed oxime ligation were also attempted with the aim of providing suitable reaction conditions for covalent attachment of FApB2vAoa peptides to oxidized IDX nanoparticles. Reaction of crude FApB2vAoa and oIDX-1000μM in DMSO with 0.1 M sodium acetate (pH 4.5) was performed in consistency with the conditions previously used by our laboratory for bioconjugation of aminooxy terminated peptides with aldehyde terminated dendrons (Scherer and McIntrye, unpublished data). Aniline was sourced from a freshly opened, nitrogen flushed manufacturer's bottle for optimum quality. IDX-based nanoparticles were recovered following reaction by repeated

precipitation in MeOH and centrifugation, as with the syntheses above. The peptide-associated absorbance spectra of initially recovered nanoparticles, shown in Figure IV-15, was characteristic of FAM and TAMRA as expected and indicated approximately 32% recovery of the peptide added to the reaction mix in the recovered nanoparticle sample (see Table IV-2). However, by the same measurement the nanoparticle sample recovered from a control reaction that included non-oxidized IDX nanoparticles instead of oIDX-1000μM also possessed 19% of the peptide added to its reaction mixture, despite the previous finding of less than 1 aldehyde per IDX nanoparticle versus approximately 27 aldehydes per oIDX-1000μM (see Table IV-1). The absorbances of these recovered particle samples at 400 nm and 560 nm corresponds to 5.8 peptides per oIDX-1000μM nanoparticle and 3.0 peptides per IDX nanoparticle.

To determine whether the observation of FApB2vAoa-associated absorption in particulate samples could be attributed to non-covalent inclusion of peptides (e.g. entrapment during precipitation and centrifugation or intercalation in the dextran coating of nanoparticles), the recovered magnetic nanoparticles were washed in MeOH and resuspended in DMSO two additional times, once with recovery by centrifugation and subsequently with recovery by magnetic attraction alone. As indicated in Table IV-2, the calculated recovery of the initial TAMRA absorbance in each type of nanoparticle solution decreased proportionally to one another through each wash and resuspension cycle. Calculations based on iron-associated and TAMRA-associated absorbance after the third recovery correspond to 3.1 and 1.2 peptides per nanoparticle for oIDX-1000μM and IDX nanoparticles, respectively. Interestingly, the repeated MeOH washes of the nanoparticle products without resuspension in DMSO and sonication preceding (Supnt 2,

Supnt 4) did not result in substantial recovery of unbound peptides, suggesting that suspension in DMSO and/or sonication led to the incremental release of peptides from nanoparticle suspensions. This observation corroborates the notion that FApB2vAoa peptides may have been trapped during phase separations or otherwise non-covalently intercalated with IDX-based nanoparticles, as the concentration gradient in a solvent capable of suspending both the nanoparticles and unbound peptides (DMSO) may have driven an equilibrium-based release of peptides. The difference in TAMRA-associated absorptivity of nanoparticles from the second wash-recovery cycle and the third such cycle represented approximately a 50% reduction in the fraction of initial peptide recovered for both oIDX-1000μM and IDX nanoparticles. No further washing of recovered nanoparticle products was performed, as the reactions had resulted in 15% efficiency of FApB2vAoa attachment to oIDX-1000μM nanoparticles at best, and further release of peptides was anticipated.

Because troubleshooting of reaction conditions for oxime ligation and application of conditions previously demonstrated to be robust with commercially obtained peptides did not result in effective bioconjugation, the characteristics of FApB2vAoa from SPPS were revisited. We hypothesized that the unidentified adducts (40 Da, 67 Da) in peptides synthesized with DprAoa as the C-terminal residue could be inhibiting reaction of peptides with aldehydes on nanoparticles, presumably by blocking the required aminooxy group on peptides. As shown in Figure IV-17, LCMS analysis of the mixture resulting from trypsin cleavage of FApB2vAoa indicated the inclusion of the adduct on the C-terminal fragment representing the last four residues of FApB2vAoa, [h_2n-{peg_1}K(tamra)G{Dpr(Aoa)}-$conh_2$], confirming the possibility of attachment to the

aminooxy. To directly assess whether FApB2vAoa could form oxime bonds with aldehydes, FApB2vAoa crude peptide mixture from SPPS was mixed with aniline and a simpler aldehyde-presenting molecule, 4-formylbenzoic acid. Comparison of the mass spectra obtained by ESI+ MS of the crude peptide mixture and the reaction mix was informative. As seen in Figure IV-19, several ions corresponding to the expected M/z of FApB2vAoa with either mass additions of 40 Da or 107 Da or a mass subtraction of 129 Da were detected in both the starting material and the reaction mix, indicating no reaction of these chemical species with the aldehyde. Interestingly, the subtraction of 129 Da corresponds to the omission of the C-terminal Dpr(Aoa) residue from the structure of FApB2vAoa, and no ion with M/z representative of a 129 Da subtraction as well as a 40 Da addition was detected. Furthermore, ions with M/z representative of the expected structure of FApB2vAoa, with or without a 67 Da adduct, were found in the crude peptide mixture but not in the reaction mix. Rather, concordant ions with M/z representing the expected mass addition of 132 Da from reaction with 4-formylbenzoic acid were detected in mass spectrum of the reaction mix, suggesting that the intended FApB2vAoa molecule did react with the aldehyde and that the 67 Da adduct did not interfere. The presence of an ion with M/z representative of the peptide omitting 129 Da but possessing a 67 Da adduct in both samples indicates that the omission of 129 Da was sufficient to block reaction with the aldehyde, corroborating the identity of the omission as Dpr(Aoa). No ions representative of a peptide omitting Dpr(Aoa) but including adducts of 40 Da or 107 Da were detected, suggesting that the 107 Da adduct is likely a combination of the 40 Da and 67 Da adducts and that the 40 Da adduct on other structures was likely attached to the Dpr(Aoa) residue. 40 Da is conspicuously the

expected MW addition if the aminooxy group had reacted with acetone, however the peptide should not have been exposed to substantial concentrations of acetone at any time during synthesis or subsequent workup. Nonetheless, taken together with the inefficiencies of FApB2vAoa oxime ligation reactions with much larger nanoparticles, these data indicate three distinct but possibly overlapping causes for lack of peptide-nanoparticle bioconjugation by oxime formation: (1) lack of an aminooxy functional group due to omission of Dpr(Aoa) in some proportion of peptides from SPPS, (2) blocking of oxime formation due to an unidentified 40 Da adduct on the Dpr(Aoa) residue, and/or (3) steric hindrance of the reactive site by TAMRA dye and relatively large nanoparticles.

Due to the possible inhibition of oxime-based bioconjugation of peptides and nanoparticles by the aforementioned complications related to the Dpr(Aoa) residue, alternative reaction schemes for covalent attachment were pursued in parallel. These strategies relied on the well-characterized and often used reactions of carboxylic acid groups with primary amines mediated by carbodiimides[129]. While this approach is suitable for pB2v-based peptides from SPPS, it limits the adaptability of MMP substrate peptides produced by SPPS by requiring that all primary amines (i.e. the N-terminus and all lysine side chains) be either protected or functionalized at the time of peptide bioconjugation to nanoparticles. Nonetheless, attempts at nanobeacon synthesis using carboxyl-terminated peptides and aminated nanoparticles were instructive.

Carbodiimide-mediated synthesis of nanobeacons was first attempted by reacting a carboxy-terminated pB2v-based peptide (AcpB2vp-cooh, see Appendix A) with IDX nanoparticles and DIC, reproducing reported conditions for the attachment of an amino

acid analogue to starch polymers similar to dextran by Steglich esterification[148]. As shown in Figure IV-22 and Table IV-3, analysis of the magnetically recovered reaction mix components by UV-visible spectrophotometry indicated recovery of 2% or less of the peptide added to the reaction mix, corresponding to about 0.1 peptides per nanoparticle. AcpB2vp-cooh crude peptide mixture did possess a majority product with a 42 Da adduct characterized by LCMS (data not shown), however because an adduct of the same size was detected previously in AcpB2vAoa, attachment to the carboxylic acid functional group was not suspected. The expected mass addition from acetylation is also 42 Da, suggesting that the reaction used for acetylation in solid phase may have imparted two acetyl groups to each intended peptide during synthesis.

To eliminate the blocking of functional groups as a possible cause of non-reactivity, carboxyl-terminated peptides and amine-decorated nanoparticles synthesized and characterized by commercial vendors were reacted in various conditions for carbodiimide-mediated amide bond formation. The 2-color (FAM/TAMRA) MMP14 substrate peptide, Peptide 13c, was reacted with Qdot(605)NH_2 nanoparticles and EDAC in various proportions. The electrophoretic mobilities of the Qdots in the resulting reaction mixes were compared with unreacted Qdots and control solutions. As shown in Figure IV-24a, Qdots from reaction with 1000-fold excess of Peptide 13c and 500-fold excess of EDAC exhibited a trend towards retardation of migration toward the cathode. The tendency of the bands to curve after enough time had elapsed to induce migration of the Qdots confounded interpretation of this gel, though. A repeat electrophoresis experiment including a sample of a reaction mix including even greater excesses of Peptide 13c and EDAC relative to Qdots (Figure IV-24b) did not confirm the trend of

Qdot electrophoretic retardation following reactions. Quizically, samples from a control mixture including Peptide 13c but not EDAC appeared to contain a population of Qdots that were trapped in the loading wells of the 1% agarose gel for an unknown reason. Separate, visibly pink bands in samples containing 1000-fold or greater excesses of Peptide 13c over Qdots were observed to migrate towards the anode, likely indicative of migration of unbound peptides. Unfortunately, not even qualitative evidence of carboxyl-terminated peptide conjugation to Qdot(605)NH_2 nanoparticles could not be gleaned from these experiments.

To quantitatively assess peptide attachment to nanoparticles, a similar reaction was performed with Peptide 13c and organic PAMAM dendrimers using EDAC as the carbodiimide mediator of amide bond formation. The use of these reactants enabled both separation of unbound peptides from nanoparticles by ultrafiltration and direct measurement of peptide content in recovered solutions by UV-visible spectrophotometry because PAMAM dendrimers possess negligible visible-spectrum absorbance. A control solution containing Peptide 13c and PAMAM in amounts equivalent to the reaction mix but omitting EDAC ("No Rxn") was prepared and incubated in parallel with the reaction. The UV-visible absorbance spectra recorded for the reaction mix and the control (Figure IV-26) confirmed equivalent additions of Peptide 13c to each solution with absorbance maxima characteristic of FAM and TAMRA dyes. However, the spectra recorded for diluted solutions of nanoparticles retained during ultrafiltration were unexpectedly also nearly identical in absorptivity. If EDAC had mediated covalent attachment of Peptide 13c to the terminal primary amines of PAMAM dendrimers, as expected, one should have observed much greater peptide-associate absorption from the products of the

reaction than from the control. Rather, in both cases the absorbance at 560 nm corresponded to about 0.3-0.4 peptides per nanoparticle (assuming 90% recovery of peptides from ultrafiltration – McIntyre, unpublished data), or about 16-19% recovery of the peptide added to reaction mixes. As such, EDAC-mediated covalent attachment of peptides to PAMAM dendrimers was not demonstrated.

The lack of evident covalent attachment of FRET-equipped MMP substrate peptides to nanoparticles from various reaction schema employing different functional groups and different types of nanoparticles suggested a systemic problem in our attempts at bioconjugation. We hypothesized that steric hindrance of the reactive site was the primary impedance to effective attachment chemistry. Given our previous findings regarding the effects of steric hindrance of the MMP cleavage site and hydrophobicity of spacer moieties in substrate peptides (see II.4), synthesis of a pB2v-based peptide with the inclusion of a lengthier, hydrophilic PEG_5 spacer isolating a C-terminal cysteine residue (pB2vp5C-cooh) was synthesized by SPPS. Cysteine was selected as the C-terminal residue for its versatility in bioconjugation reactions, as it presents both a sulfhydryl and a carboxylic acid for participation in various types of covalent attachment chemistry. Building on the optimized synthesis of pB2v (see III.3.6), great care was taken to ensure attachment of the initial PEG_5 residue to Fmoc-Cys(Trt)-Wang resin and termination of uncoupled amines following this coupling to block the yield of peptides omitting PEG_5. As a result, mass spectrometry characterization of unpurified peptide mixture following folation, final deprotection, and detachment from the solid support resin (Figure IV-27 and Figure IV-28) indicated a majority of ions with M/z representative of the expected structure of FApB2vp5C-cooh. Unlike previous syntheses

of folated peptides by SPPS, this majority did not correspond to unintended peptide structures including adducts or omitting residues. As seen in Figure IV-29, FApB2vp5C-cooh possessed an absorbance spectrum with maxima around 495 nm and 560 nm, indicative of FAM and TAMRA dye incorporation. Stimulation of fluorescence by excitation at 555 nm and 495 nm resulted in emissions characteristic of TAMRA and FRET between FAM and TAMRA, respectively, confirming the desired optical properties of FApB2vp5C-cooh. Finally, a rapid FRET switch was readily observed from this peptide upon proteolysis by MMPs, as demonstrated in Figure IV-30 by 10-fold to 16-fold increases in FAM emission intensity after exposure to MMPs (2, 9, or 14) for 60 minutes that continued to trend upward for up to 10 hours. Altogether, validation of the optical properties and MMP-cleavability of FApB2vp5C-cooh by spectroscopy and corroboration of its molecular structure by mass spectrometry confirmed that FApB2vp5C-cooh possessed all the attributes necessary for constructing folate-targeted proteolytic nanobeacons and testing our overall hypotheses.

Upon validation of FApB2vp5C-cooh, synthesis of proteolytic nanobeacons using FeOx-based nanoparticles was revisited. Several synthesis schemes and mediators enable bioconjugation of sulfhydryl and carboxylic acid functional groups of cysteine with primary amines[24,37,129,153]. Therefore FeOx nanoparticles with APTES surface decoration, FeOx-NH_2, were synthesized by Charleson S. Bell of the Giorgio Laboratory and characterized by qualitative Ninhydrin assay to confirm availability of primary amines (data not shown). Synthesis of complete nanobeacons from FApB2vp5C-cooh peptide and FeOx-NH_2 nanoparticles was attempted with mediating of covalent bonding by heterobifunctional linkers SIA or Sulfo-SMPB, as diagrammed in Figure IV-31.

Recovery of nanoparticle products by magnetic attraction and characterization of reaction extent by UV-visible spectrophotometry mirrored previous experiments. Shown in Figure IV-33, the absorbance spectra of the nanoparticle-depleted initial supernatants from separated reaction mixes were clearly representative of peptide with dual maxima in the visible portion of the electromagnetic spectrum. These maxima were not observed in supernatants from a DMSO wash of the recovered nanoparticles, though, suggesting that nearly complete removal of unbound FApB2vp5C-cooh from nanoparticles was achieved by the first separation. Unfortunately, reliable UV-visible absorbance spectra of the recovered NP^{++}_{x} nanoparticles could not be recorded due to rapid flocculation of particles in many solvents. However, because the TAMRA-associated absorptivity of the collected supernatants represented only 55-56% of the peptide added to reaction mixes, we inferred that the reactions may have proceeded to a modest extent, attaching 44-45% of starting peptide to nanoparticles (220-225 peptides per nanoparticle). As can be seen in Figure IV-34, excitation of these FeOx-based NP^{++}_{x} nanoparticles at 494 nm resulted in emission spectra with maxima around 520 nm and 580 nm corresponding to FAM and TAMRA dyes, however this emission was only slightly more intense than the background of the non-decorated FeOx-NH_2 nanoparticles and insufficient to be recorded without substantial contributions of noise to the signals. These emission intensities would be insufficient for optical sensing of proteolytic activity, but could be the result of either poor conjugation efficiency or optical interference, the latter of which might be remedied upon separation of cleaved peptide fragments from nanoparticle cores, especially in microscopy experiments. With the hypothesis that the relatively great UV-visible extinction of FeOx might be interfering with excitation and/or emission of FAM and

TAMRA, if present, MMP14-induced FRET switch assays were conducted with fluorescence measurements before and after nanoparticle depletion of samples. No increase in FAM fluorescence emission intensity of either FeOx-based NP^{++}_{x} suspension was associated with proteolysis by MMP14, as shown in Figure IV-34b-c. Interestingly, the MMP14-associated increases in fluorescence emission intensity in nanoparticle-depleted samples were greater for FAM emission than TAMRA emission in each sample (Figure IV-34d-e), perhaps indicative of FRET disruption, but the overall emissions were again scarcely an order of magnitude greater in intensity than the noise of the instrument. Whether or not the bioconjugation reactions proceeded sufficiently to attach FApB2vp5C-cooh to FeOx-NH_2 nanoparticles, MMP-associated FRET switch could not be observed from the resulting product suspensions, rendering them unsuitable for use as proteolytic nanobeacons.

Given the above evidence suggesting possible attachment of peptides to aminated FeOx nanoparticles but the application-limiting optical and solubility properties of the recovered product suspensions, a proof-of-concept synthesis of nanobeacons using nanoparticles transparent to visible-spectrum light was pursued. PAMAM-G4 dendrimers, though somewhat smaller than the ideal range for selective accumulation in solid tumors in vivo via the EPR effect, provided the requisite poly-amine surface and visible-spectrum transparency for this synthesis. As diagrammed in Figure IV-35, FApB2vp5C-cooh crude peptide mixture was mixed with PEGylated PAMAM-G4 separate reactions employing three different mediators of covalent attachment. SIA and Sulfo-SMPB were applied to facilitate reaction with the cysteine sulfhydryl on the peptide and amines on PAMAM-G4, while the carbodiimide EDAC was used to generate

amine-reactive intermediates from the carboxyl termini of peptides for amide bond formation. As with previously attempted PAMAM-based syntheses, unbound peptides were separated from nanoparticles by ultrafiltration and all solutions recovered for analysis by UV-visible spectrophotometry. Calculated from the spectra in Figure IV-36, the FApB2vp5C-cooh peptide recoveries in Table IV-4 are consistent with attachment of peptides to PAMAM-G4 to varying extents. Despite the ability of peptides to traverse the filtration membrane as demonstrated by differing intensities of peptide-associated absorption in the effluent solutions, 48-77% of the peptide added to each reaction mix was recovered in the final retentate solutions. According to the absorbance measurements and calculations, EDAC and Sulfo-SMPB mediation of bioconjugation were comparable and both superior to SIA with respect to the amount of peptide attached to nanoparticles.

While the UV-visible absorbance spectra shown in Figure IV-36 indicated incorporation of the peptide-associated FAM and TAMRA dyes in recovered PAMAM-based NP^{++}_{x} nanoparticle solutions, FRET switch assays with MMP9 (Figure IV-37) validated the functional properties of these prospective proteolytic nanobeacons. NP^{++}_{EDAC}, NP^{++}_{SMPB}, and NP^{++}_{SIA} solutions each exhibited a 10-12-fold increase in FAM fluorescence emission intensity with a still-increasing trend after 60 minutes of incubation with MMP9, constituting the first ever sensing of proteolytic activity by folate-targeted proteolytic nanobeacons. The relative FRET switches of all nanoparticles solutions were greater than that of FApB2vp5C-cooh peptide alone, possibly due to additional intramolecular quenching of FAM by multiple proximal peptides prior to proteolysis. As depicted in Figure IV-38, the disparity in the maximum FRET switches obtained after up to 10 hours incubation was even greater. The TAMRA (reference)

emission intensity of each solution also increased during incubation, though less rapidly, such that the 61-fold increase in the FAM emission intensity of NP^{++}_{EDAC} corresponded to an approximately 9.4-fold increase in S/R ratio. Nonetheless, these relative increases in sensor emission and S/R ratio of each nanoparticle solution in response to proteolysis by MMP9 were sufficient for sensing MMP activation of nanobeacons, especially using fluorescence microscopy.

To validate these nanoparticles as proof-of-concept folate-targeted proteolytic nanobeacons *in vitro*, MDA-MB-231 human metastatic breast cancer cells known to express folate receptor and MMPs (see Appendix C) were incubated with either intact or MMP14 pre-treated NP^{++}_{EDAC} nanoparticles, with or without addition of folic acid to treatment media to compete for cell membrane-anchored folate receptors. This experimental design allowed us to confirm susceptibility of NP^{++}_{EDAC} to cleavage by endogenously expressed MMPs as well as to elucidate the effects of folate targeting and MMP cleavage on cellular internalization of nanobeacons and/or enzymatically released peptide fragments carrying FAM. Bright field and fluorescence microscopy of cells after 4 hours of treatment and exchange of treatment media for PBS (Figure IV-39) indicated that folic acid competition was the most influential factor affecting cell uptake of nanobeacons. Fluorescence in both the FAM and TAMRA channels was found intracellularly when folic acid was not added to treatment media, but almost no fluorescent signal above background was detectable inside cells exposed to free folic acid in addition to nanobeacons. As shown in Figure IV-40 and Table IV-5, quantitation of cellular fluorescence by flow cytometry of cells recovered following microscopy corroborated these observations.

Interestingly, FAM fluorescence was both punctate and diffuse in cells treated with intact NP^{++}_{EDAC} in the absence of competing folic acid (Figure IV-39a-d), whereas only punctate FAM fluorescence was observed in cells incubated with pre-cleaved nanobeacons (Figure IV-39i-l). Intracellular TAMRA fluorescence was only observed to be punctate and in all cases accompanied by FAM, corroborating the suggestion that fluorescence puncta in both channels represent intact peptides or nanobeacons. Concordantly, the diffuse intracellular FAM fluorescence could indicate liberated peptide fragments inclusive of FAM but not TAMRA, as intended following nanobeacon proteolysis by MMPs. However, the absence of diffuse FAM fluorescence in cells treated with pre-cleaved NP^{++}_{EDAC} confounds this suggestion, as the treatment media should have contained a much greater proportion of folate-targeted peptide fragments supposedly represented by diffuse staining. Furthermore, in the absence of competing folic acid, the overall intracellular FAM and TAMRA fluorescence emissions were more intense in cells incubated with intact nanobeacons, as shown in Figure IV-40 and Table IV-5.

While additional experiments are needed to elucidate the reasons for these observations, one explanation could be that the multivalent receptor binding mode of intact nanobeacons results in more efficient association of FAM-carrying nanobeacons with cell surfaces than the monovalent ligand-receptor binding by folate conjugates released from cleaved nanobeacons. The pB2v-based substrate peptide tethering FAM to nanobeacons is cleavable by membrane-bound MMP14 as well as secreted MMPs, concentrations of which are often elevated pericellularly around malignant cells, particularly tumor cells actively invading through surrounding ECM[11,42,110,121,122,154].

Rather than leading to rapid uptake of intact nanoparticles, folate targeting may counterintuitively augment extracellular proteolysis of proteolytic nanobeacons by increasing the overall avidity of nanobeacons for folate receptors displayed on cell membranes, thereby concentrating them in the vicinity of active MMPs.

It is important to emphasize that these observations were made *in vitro* with only one time interval applied for treatment. A 3-dimensional, heterogeneous tumor microenvironment *in vivo* may present additional physical and chemical barriers to cellular internalization of nanobeacons, such that the temporal relationship between extracellular proteolysis and receptor-dependent association of folate-targeted proteolytic nanobeacons with cells could be very different. Conceivably, due to slower diffusion through ECM among other factors, folation could have little impact on the degree to which proteolytic nanobeacons are cleaved extracellularly *in vivo*. Nonetheless, selective delivery to tumor cells may result from this scenario as well, resulting from the intended release of monovalent folate conjugates capable of more rapid diffusion throughout the ECM only in the MMP-rich microenvironment of a tumor. Alternatively, if the fluorescence distributions observed in cells are unrelated to proteolysis of nanobeacons, it is also possible that folate-mediated internalization of intact folate-targeted proteolytic nanobeacons may occur rapidly enough that sufficient time for extracellular proteolysis is not allowed. The diffuse FAM fluorescence observed in MDA-MB-231 cells treated with NP^{++}_{EDAC} nanoparticles indicates that regardless of the mechanisms, some proportion of the sensor moiety was found in the cytoplasm, the aim of delivery for many diagnostic and therapeutic compounds.

While additional experiments are necessary to elucidate the mechanisms and kinetics of delivery and the intracellular fate of such nanoparticles, the troubleshooting presented in this chapter has culminated in the synthesis and characterization of PAMAM-based nanobeacons that are folate-targeted, FRET-equipped, MMP-responsive, and internalized by tumor cells. Folate-targeted proteolytic nanobeacons synthesized from FApB2vp5C-cooh peptides and PAMAM-G4 dendrimers were cleaved by MMPs and internalized in MDA-MB-231 breast cancer cells via a folate-dependent mechanism. We have demonstrated by the syntheses and characterizations above that synthesis of folate-targeted proteolytic nanobeacons is feasible and that the proof-of concept nanoparticles produced may be used to test the hypothesis that our design for dually-targeted nanobeacons allows selective, imageable delivery to tumor cells.

CHAPTER V

SUMMARY AND FUTURE DIRECTIONS

V.1. SUMMARY OF CONCLUSIONS

The research detailed in this dissertation culminated in the synthesis, characterization, and preliminary *in vitro* validation of FTPNBs for the detection of MMP activity and delivery to tumor cells. FTPNBs constitute folate-targeted, MMP-cleavable nanobeacons equipped with visible-spectrum fluorophores that enable a dramatic optical switch upon proteolysis for the detection of MMP activity. Throughout the design, troubleshooting, and optimization of the synthetic and analytical techniques required, several important insights were gained that should inform future work in the field of cancer nanotechnology and optical theranostics.

Complete solid phase synthesis employing standard Fmoc-amino acids, unusual amino acid analogues, folic acid, and HCTU provided a robust and adaptable system for the production of substrate peptides possessing all of the characteristics required for FTPNBs: attachment to FRET-paired sensor and reference fluorophores on opposing sides of an MMP-cleavable peptide bond, N-terminal attachment to folic acid, and unhindered chemical functional groups at the C-terminus for bioconjugation with nanoparticle cores. Key developments and demonstrations in the synthesis of these specialized peptides include:

- attachment of paired fluorophores directly to the substrate peptide for FRET quenching with reproducible efficiency (II.3.2),

- lengthening of the intramolecular spacing between fluorophores using flexible, hydrophilic PEG_1 spacers to enhance cleavage by MMPs that likely results from alleviation of steric hindrance of the MMP cleavage (P1-P1') site by the bulky fluorophores (II.3.4),
- demonstrated optical non-interference and biological non-toxicity of small (40-67 Da), unidentified adducts incorporated during peptide workup (III.3.2),
- optimization of Fmoc-SPPS employing triple-coupling of Fmoc-Lys(5/6-FAM)-OH and Fmoc-Arg(Pbf)-OH to improve yield of the intended peptide products (III.3.6),
- robust and economical bioconjugation of folic acid as a targeting ligand or acetyl as a non-reactive terminus to peptides in solid phase (III.3.3),
- non-interference of folic acid conjugation with fluorescence, FRET, or MMP-associated substrate proteolysis (III.3.6),
- inclusion of a flexible, hydrophilic, intermediate-length PEG_5 spacer separating a C-terminal cysteine residue provided for efficient bioconjugation of peptides to reactive functional groups on nanoparticle cores; the linker is postulated to alleviate potential steric hindrance of the coupling reaction (IV.2.10),
- and successful conjugation of folate-targeted, FRET-equipped, MMP-cleavable substrate peptides to PAMAM nanoparticles utilizing the carboxyl or sulfhydryl functional groups of the C-terminal cysteine with appropriate mediators for covalent attachment to primary amines (IV.2.12).

Other pertinent observations were made during the course of this work that may inform the further development of diagnostic nanoparticles. For example, two different

reagents (2% hydrazine solution and *p*-phenylene diamine) were found to modify TAMRA dye such that its optical properties became unsuitable for use as the quenching reference fluorophore in FTPNBs. In applications where the characteristic optical properties of TAMRA dye are essential, exposure to these chemicals should be avoided, e.g. by altering the sequence of synthesis operations or by chemically protecting TAMRA.

Several factors may have contributed to alack of detectable attachment of aminooxy-functionalized pB2vAoa peptides with aldehyde-bearing oIDX nanoparticles. These include unintended omission of the Dpr(Boc-Aoa) residue during SPPS, blocking of the Aoa residue by an unidentified 40 Da adduct, and steric hindrance of the reactive site. Oxime ligation is nonetheless a useful chemoselective method and could be applicable for development of peptide-decorated nanoparticle probes. This may prove especially important in the development of NIR-emitting FTPNBs, as NIR dyes are often incompatible with the repeatedly applied acid-base deprotection chemistry employed in SPPS. The orthogonality of oxime ligation to amine- and thiol-based bioconjugations allows SPPS and bioconjugation of peptides prior to attachment of NIR dyes, sparing them the harsh conditions of deprotection chemistry. Our laboratory previously has had success employing this strategy to produce NIR-emitting proteolytic beacons (Scherer et al, unpublished). In future syntheses designed for oxime ligation of peptides with nanoparticles or surfaces, one should take care to verify the presence and reactivity of the aminooxy functional group and adequate spacing and solubility to minimize potential steric hindrance of the reaction.

Though there was evidence suggesting some conjugation of peptides to amine-terminated FeOx nanoparticles using SIA or Sulfo-SMPB heterobifunctional linkers (see IV.2.11), the resulting nanoparticles could not be characterized by absorbance and did not exhibit the expected fluorescence properties. In addition to the rapid flocculation of these nanoparticles, the broad UV-visible absorbance of FeOx interfered with optical characterization. FeOx nanoparticles as cores of FTPNBs would provide benefits such as simplified purification by magnetic separation and additional imaging modalities including MRI for tracking biodistribution. Since others have reported the preparation of fluorescent FeOx-based nanoparticles decorated with fluorescein[141,143,155,156], further studies into the development of FeOx-based FTPNBs are merited.

V.2. Significance and Future Directions

The results and conclusions presented in this dissertation are directly applicable to the fields of cancer imaging and drug delivery. Detailed above are the best practices, potential pitfalls, and troubleshooting strategies gleaned from the design, synthesis, and characterization of multiply-targeted, multifunctional nanoparticles for delivery to solid tumors. These insights should prove valuable in the development and application of future diagnostic and therapeutic macromolecules for cancer research and treatment.

FTPNBs evolve a fluorescent optical switch upon proteolytic activation, the source of which is the sensor fluorophore that may subsequently be captured in a tumor cell via a selective, receptor-mediated endocytic mechanism resulting from folate targeting. Sensor-equipped molecules liberated by proteolysis from other macromolecules lacking a targeting ligand, solubility switch, or other mechanism for immobilization may rapidly diffuse out of a tumor or return to circulation. As such, FTPNBs constitute a contribution

toward developing imaging agents useful for analysis of tumor response to therapy, particularly for disease-specific MMPI treatment where quantitative measurements of efficacy have been historically lacking[18,19]. While other imaging agents have been developed, e.g. MMPSense[26], no one agent has overcome all of the challenges associated with clinical assignment/assessment of tumor-associated protease activity by specific protease family members in humans. Ability to selectively image MMP activity in tumors using nanoparticle-mediated delivery of enzyme-selective proteolysis sensors could breathe new life into the interest in MMPs as therapeutic targets in cancer.

FTPNBs developed in this work may also aid in elucidating the mechanisms that determine the intracellular fate of folate-targeted constructs for engineered delivery to tumor cells and overcoming previously unidentified challenges. Whereas many targeting ligands are internalized and trafficked to lysosomes for degradation, folates may be internalized via at least two receptor-mediated routes, one of which directs vesicles to recycling centers where FA may or may not be released from FR before FR is recycled to the cell surface[48,66,67]. The dependence of the intracellular fate of FA-linked particles on multiplicity of FA-FR binding was recently examined, wherein it was shown that folates binding singly were trafficked to mildly acidic (mean pH 6.8-6.95) endosomes whereas particles binding multiple FRs simultaneously were found in lysosomal compartments (mean pH less than 5.0)[48,70].

This could be a critical insight that defines a previously unidentified challenge that many recently developed folate-targeted therapeutic approaches have faced, especially those based on multivalent nanoparticles. For example, Majoros et al developed a dendrimer-based nanoparticle multiply decorated on its surface with FA, a fluorescein-

based fluorescent dye (FITC), and paclitaxel (PXL), a toxic drug that interrupts mitosis in dividing cells. Despite demonstrating the effective targeting of FR-positive KB cells by the nanoparticles, flow cytometry also revealed less than 25% death in targeted cells despite administering 100 nM drug-equipped nanoparticles, the equivalent of 400 nM PXL. Nanoparticle concentrations greater than this were toxic to all cells, regardless of FR status[57]. It is important to note that unlike FTPNBs, the FA, dye, and PXL conjugated to the nanoparticle in that study were each covalently attached directly to the dendrimer on separate branch termini and all by non-cleavable molecular linkers. FTPNBs may overcome this challenge by deploying monovalent folate conjugates only in a permissive, MMP-rich microenvironment such as a solid tumor. Further experiments testing cellular internalization of FTPNBs in conjunction with monitoring of intracellular vesicles using reagents such as LysoTracker dyes could be used to elucidate the intracellular fate of FTPNBs and the folate conjugates released from them by proteolysis.

With slight modifications to the nanoparticles developed in this work, applying the insights detailed above, FTPNBs could provide invaluable developments in the fields of cancer imaging and theranostics. As alluded to above, the oxime ligation chemistry could be combined with conventional amide bond-forming and thiol bond-forming bioconjugations to enable incorporation of NIR dyes or therapeutic molecules on beacon peptides following SPPS. NIR fluorescence permits *in vivo* optical imaging not possible with other fluorophores mostly due to the absorption of lower-wavelength light by hemoglobin and absorption of higher-wavelength light by water outside the NIR window[157]. Furthermore, synthesis of NIR-equipped FTPNBs employing FeOx-based nanoparticle cores in place of PAMAM dendrimers would enable multimodal *in vivo*

imaging using fluorescence as well as MRI. One can envision tracking of nanoparticle accumulation and biodistribution by MRI and assessment of MMP activation by optical imaging. If surgical resection is possible, one could also then quantify tumor and organ accumulation of nanoparticles by Prussian blue staining for iron as well as intracellular delivery of folate conjugates by fluorescence microscopy. If some of the constituent peptides comprising FTPNBs are conjugated with a therapeutic molecule in place of the sensor fluorophore, the resulting nanoparticle becomes a true theranostic agent, one that simultaneously delivers both imaging and therapeutic compounds. The optical fluorescent signal generated upon activation by MMPs would then be a surrogate measure of drug delivery. This strategy has been shown effective in our laboratory by attaching PXL as a pro-drug, which then exerts the full potential of its cyotoxicity following proteolytic activation[109].

The protocols and optimized methods outlined in the preceding chapters are anticipated to have applications well beyond cancer research. The techniques that were developed herein for the synthesis of MMP-cleavable beacon peptides and FTPNBs are highly adaptable to development of substrates for other proteases and enzyme families, attachment of other targeting ligands, and conjugation to other types of nanoparticles. Peptides and nanobeacons with efficient FRET quenching and consequent optical fluorescence switch enable robust interrogation of protease activity *in vitro*, *ex vivo*, and potentially *in vivo*. Mammalian degradomes constitute a massive category within their respective proteomes[126], and proteases alone are thought to comprise 1.7% of the human genome, representing the second largest enzyme family[8]. Indeed, over 570 individual proteases have been identified in the human proteome and linked to over 114 different

hereditary diseases[126]. It is the hope of the author that the methods and results documented in this dissertation may be applied to the research of a plethora of protease-dependent biological processes and disease states and to the development of future diagnostic and therapeutic approaches.

APPENDIX A

PEPTIDE STRUCTURES

Name/Identifier	Amino Acid/Residue Sequence	Page
Peptide #13	fitc{Ahx}RIGF * LRTA{Ahx}C-cooh	228
Peptide #14	fitc{Ahx}PLA * XWAR{Ahx}C-cooh	228
Weiss	Ac-CSGESSN * LFVL{Ahx}-conh$_2$	229
Mucha/Weiss Hybrid	Ac-KWSLN * LFVLC-cooh	229
Ahx-Hybrid	Ac-K{Ahx}WSLN * LFVL{Ahx}C-cooh	229
Broad2	h$_2$n-RPLG * LWARC-cooh	230
TMR-Broad2-FL (TB2F)	tamra-RPLG * LWARC(fam)-cooh	230
FL-Broad2-TMR (FB2T)	fam-RPLG * LWARC(tamra)-cooh	231
Peptide 13c	tamra-RIGF * LRTRK(fitc)R-cooh	232
Peptide 13e	tamra-SGRIGF * LRTAK(fitc)R-conh$_2$	232
Peptide 13g	tamra-{Ahx}SGRIGF * LRTAK(fitc)R-conh$_2$	233
Peptide 13i	Dab-SGRIGF * LRTAK(fitc)R-conh$_2$	233
Ahx-Broad2	h$_2$n-{Ahx}RPLG * LWAR{Ahx}C-cooh	234
Ahx-Broad2-vis	fam-{Ahx}RPLG * LWAR{Ahx}C(tamra)-cooh	234
M9	h$_2$n-{Ahx}AVRW * LLTA{Ahx}C-cooh	235
M9-Folate (M9F)	fa-K{Ahx}AVRW * LLTA{Ahx}C-cooh	235
GG-Broad2-vis	Ac-GGK(fam)GGRPLG * LWARGGK(tamra)G-cooh	236
FA-GG-Broad2-vis	fa-GGK(fam)GGRPLG * LWARGGK(tamra)G-cooh	237
peg-Broad2-vis (pB2v)	h$_2$n-{peg$_1$}K(fam){peg$_1$}RPLG * LWAR{peg$_1$}K(tamra)G-cooh	238
PEPDAB1001	Dab-GPLG * MRGC(fitc)-conh$_2$	239
pB2vAoa	h$_2$n-{peg$_1$}K(fam){peg$_1$}RPLG * LWAR{peg$_1$}K(tamra)G{DprAoa}-cooh	240
FApB2vAoa	fa-{peg$_1$}K(fam){peg$_1$}RPLG * LWAR{peg$_1$}K(tamra)G{DprAoa}-cooh	241
AcpB2vAoa	Ac-{peg$_1$}K(fam){peg$_1$}RPLG * LWAR{peg$_1$}K(tamra)G{DprAoa}-cooh	242
pB2vp-cooh	h$_2$n-{peg$_1$}K(fam){peg$_1$}RPLG * LWAR{peg$_1$}K(tamra){peg$_1$}G-cooh	243
AcpB2vp-cooh	Ac-{peg$_1$}K(fam){peg$_1$}RPLG * LWAR{peg$_1$}K(tamra){peg$_1$}G-cooh	243
pB2vp5C-cooh	h$_2$n-{peg$_1$}K(fam){peg$_1$}RPLG * LWAR{peg$_1$}K(tamra){peg$_5$}C-cooh	244
FApB2vp5C-cooh	FA-{peg$_1$}K(fam){peg$_1$}RPLG * LWAR{peg$_1$}K(tamra){peg$_5$}C-cooh	245
	* designates scissile bond / MMP cleavage	

Note: Standard amino acid side chains are pictured hereafter as conventional neutral residues for simplicity. Due to handling with concentrated TFA, the arginine side chains of peptides produced by SPPS probably carried +1 charge corresponding to protonation.

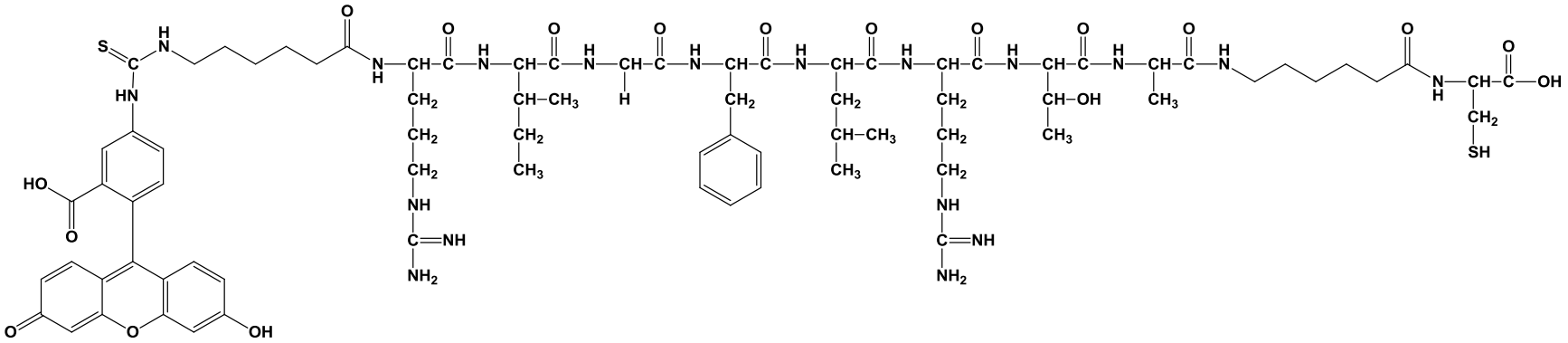

Peptide #13
Chemical Formula: $C_{78}H_{116}N_{18}O_{18}S_2$
Exact Mass: 1656.82

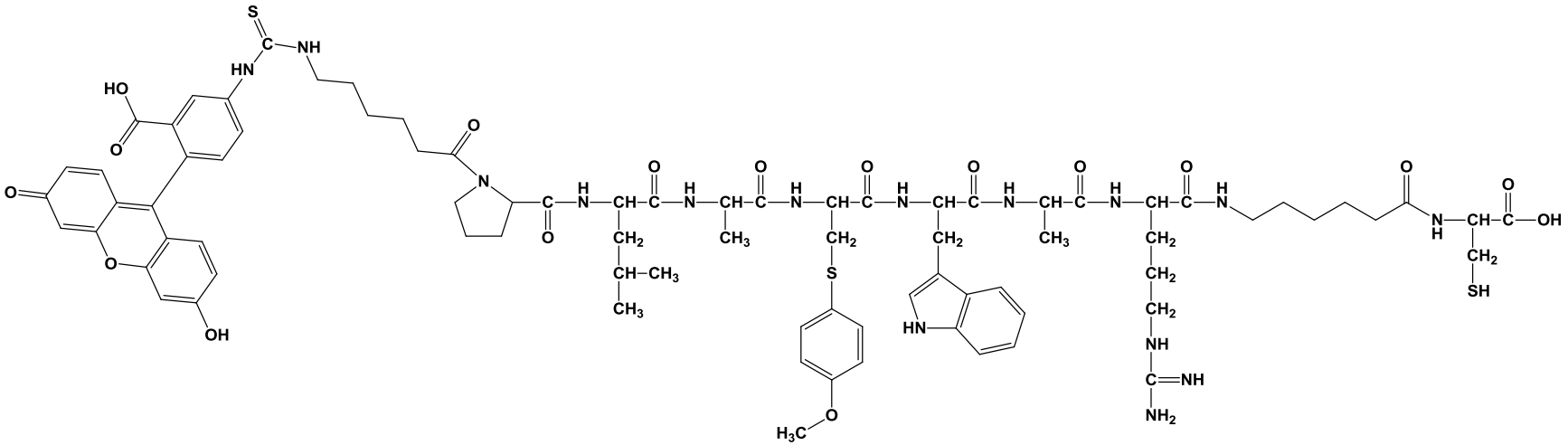

Peptide #14
Chemical Formula: $C_{80}H_{107}N_{15}O_{17}S_3$
Exact Mass: 1645.71

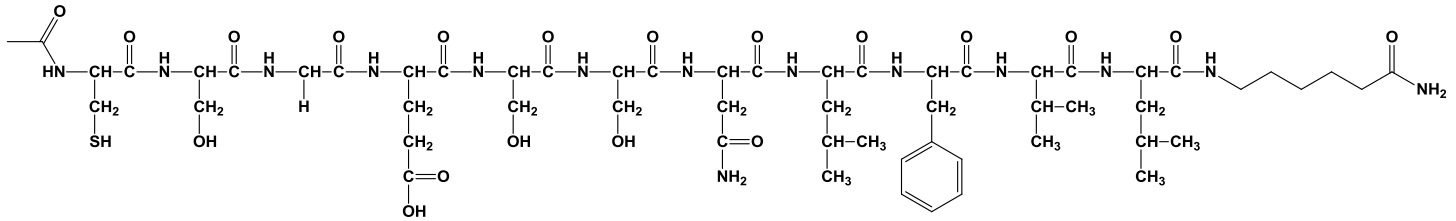

Weiss
Chemical Formula: $C_{57}H_{92}N_{14}O_{19}S$
Exact Mass: 1308.64

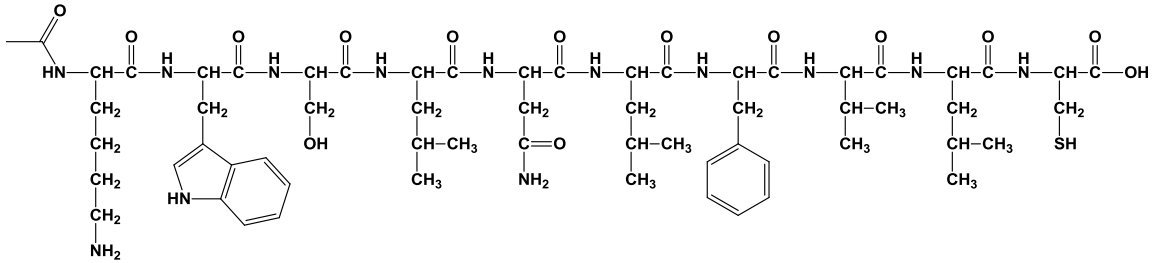

Mucha/Weiss Hybrid
Chemical Formula: $C_{61}H_{93}N_{13}O_{14}S$
Exact Mass: 1263.67

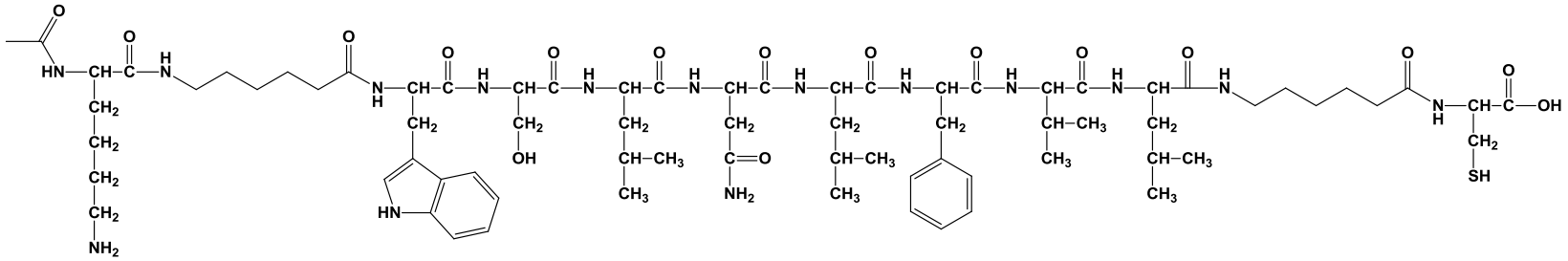

Ahx-Hybrid
Chemical Formula: $C_{73}H_{115}N_{15}O_{16}S$
Exact Mass: 1489.84

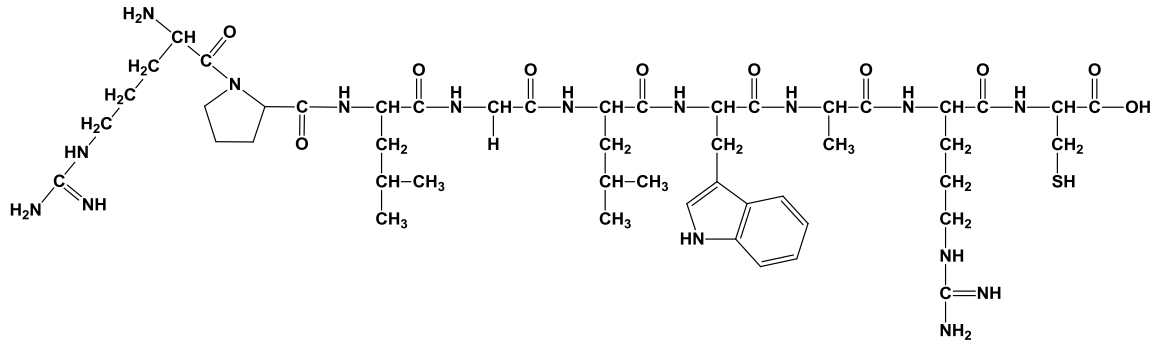

Broad2
Chemical Formula: $C_{48}H_{78}N_{16}O_{10}S$
Exact Mass: 1070.58

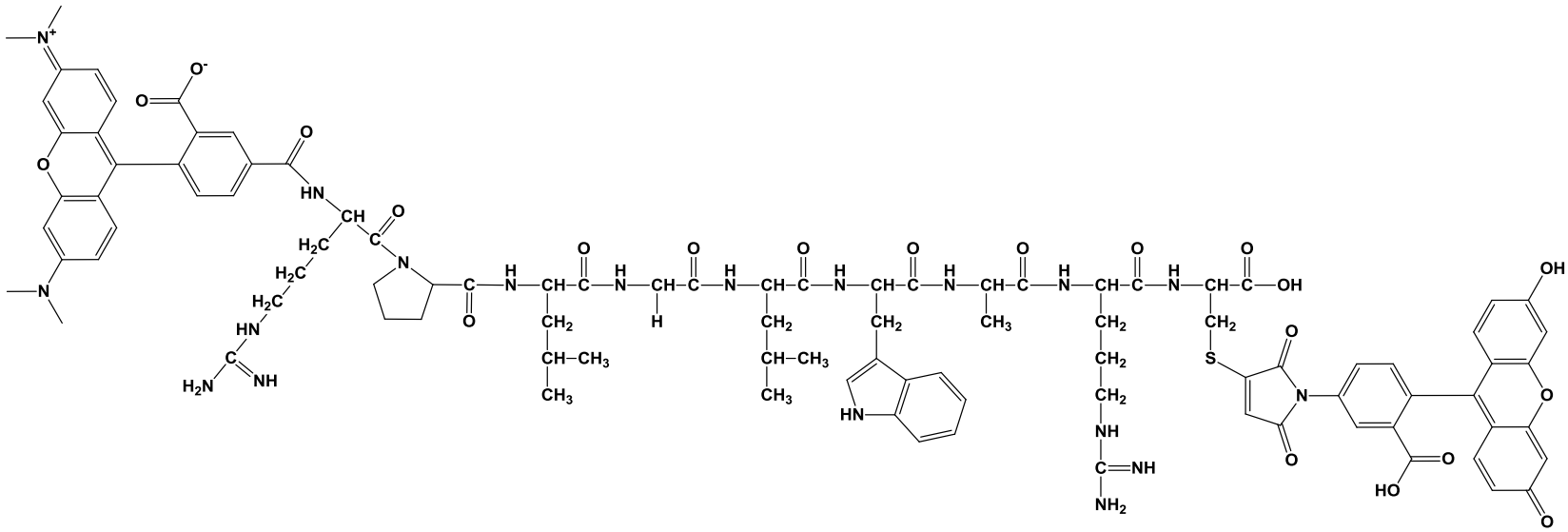

TMR-Broad2-FL
Chemical Formula: $C_{97}H_{109}N_{19}O_{21}S$
Exact Mass: 1907.78

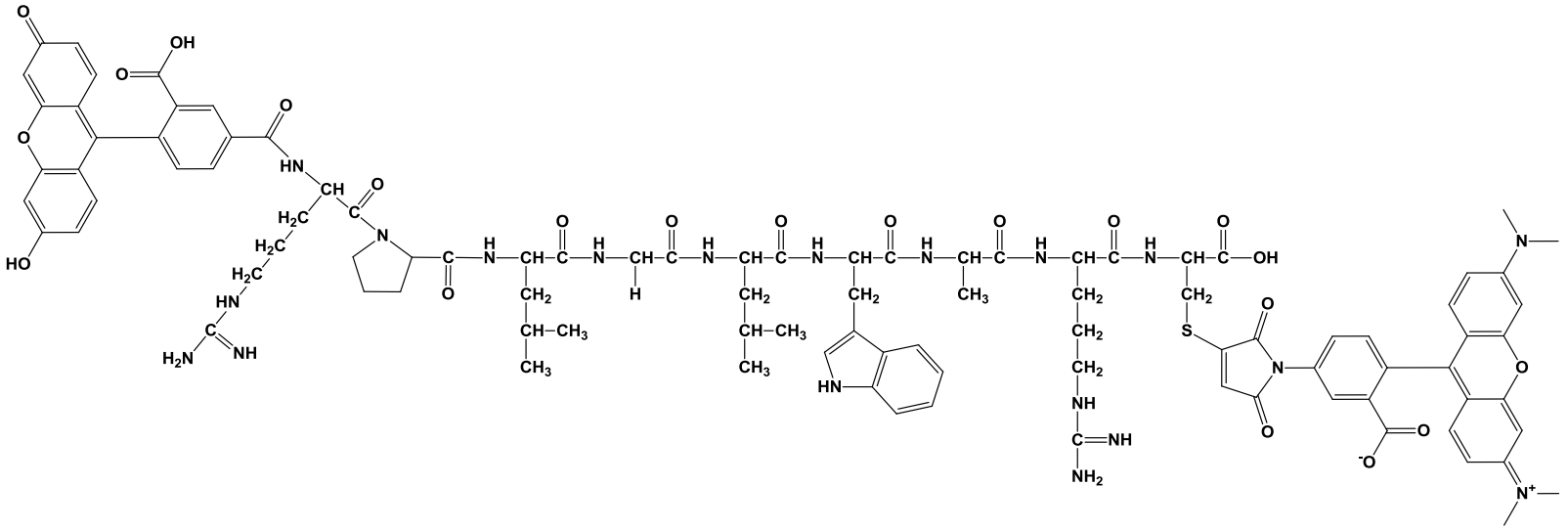

FL-Broad2-TMR
Chemical Formula: $C_{97}H_{109}N_{19}O_{21}S$
Exact Mass: 1907.78

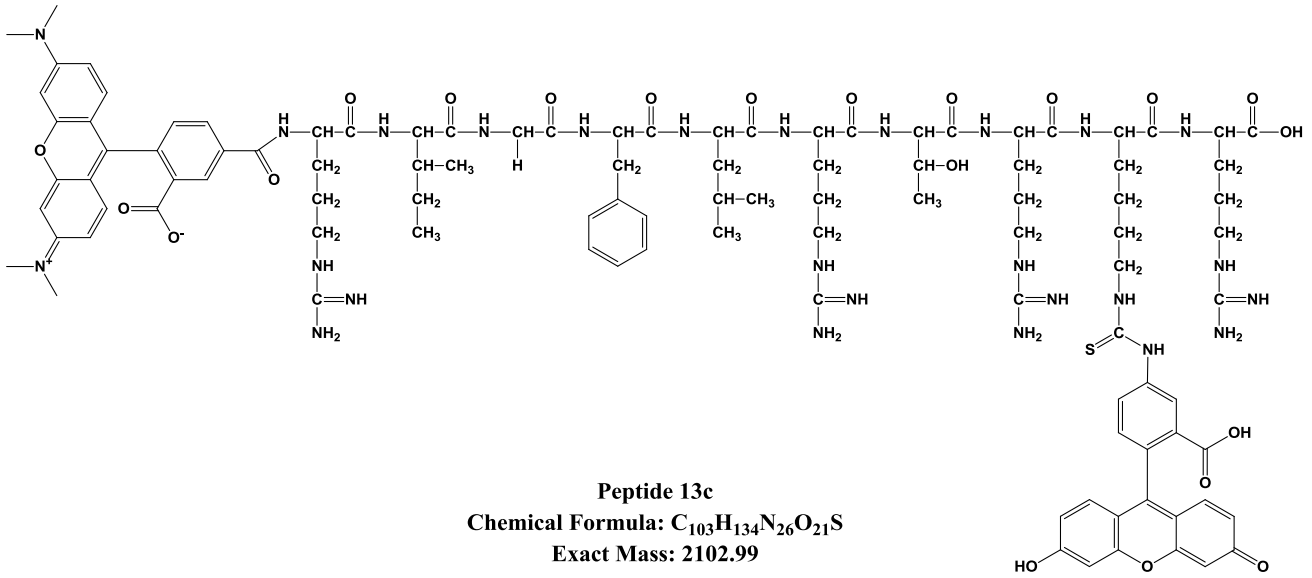

Peptide 13c
Chemical Formula: $C_{103}H_{134}N_{26}O_{21}S$
Exact Mass: 2102.99

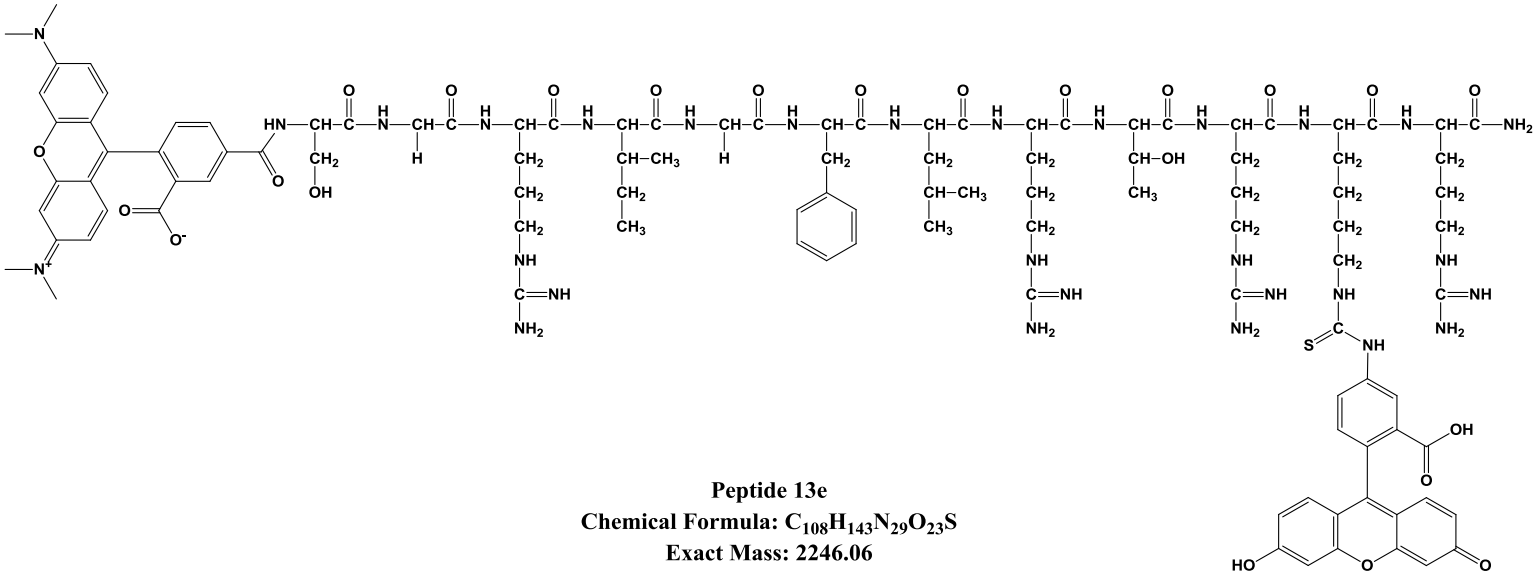

Peptide 13e
Chemical Formula: $C_{108}H_{143}N_{29}O_{23}S$
Exact Mass: 2246.06

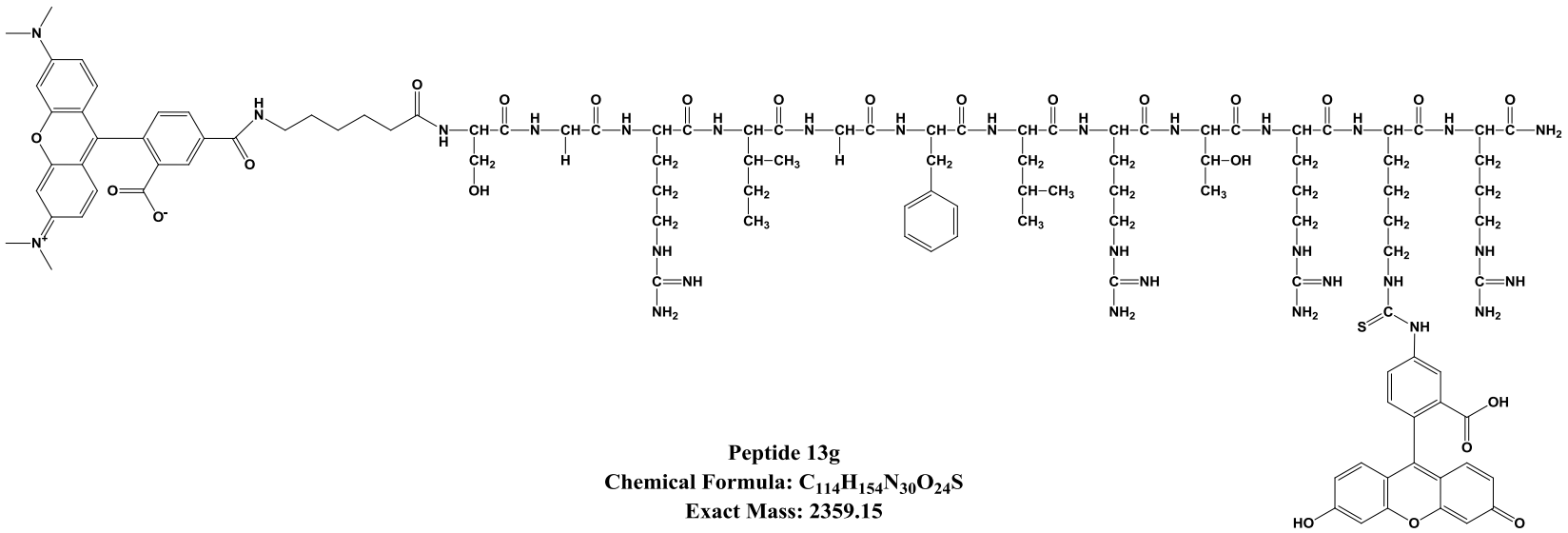

Peptide 13g
Chemical Formula: $C_{114}H_{154}N_{30}O_{24}S$
Exact Mass: 2359.15

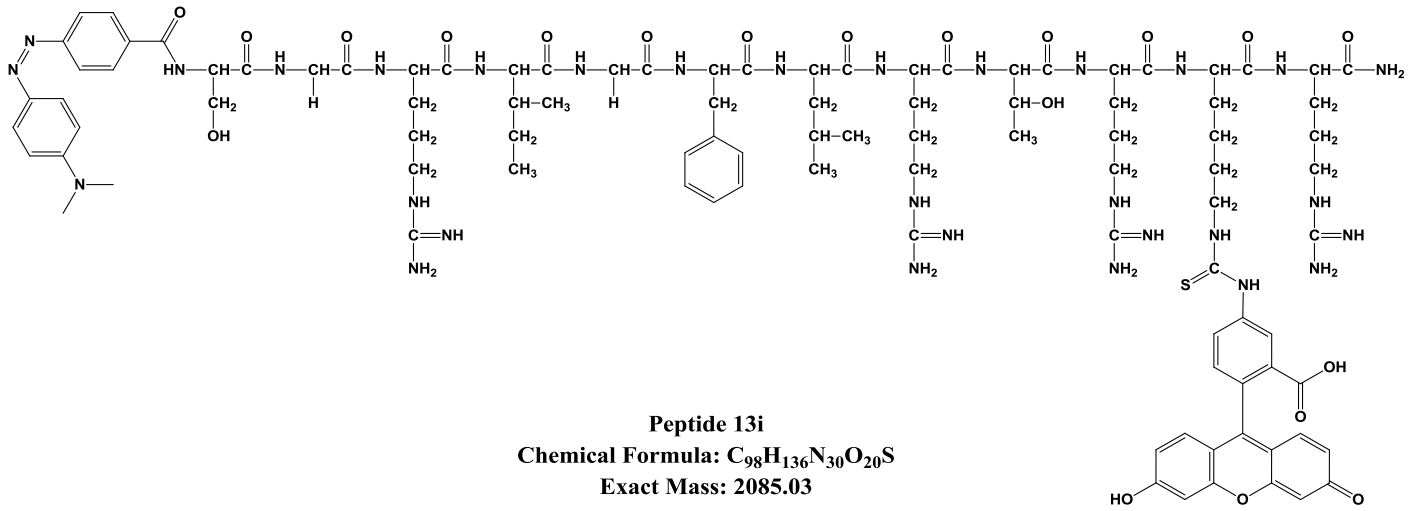

Peptide 13i
Chemical Formula: $C_{98}H_{136}N_{30}O_{20}S$
Exact Mass: 2085.03

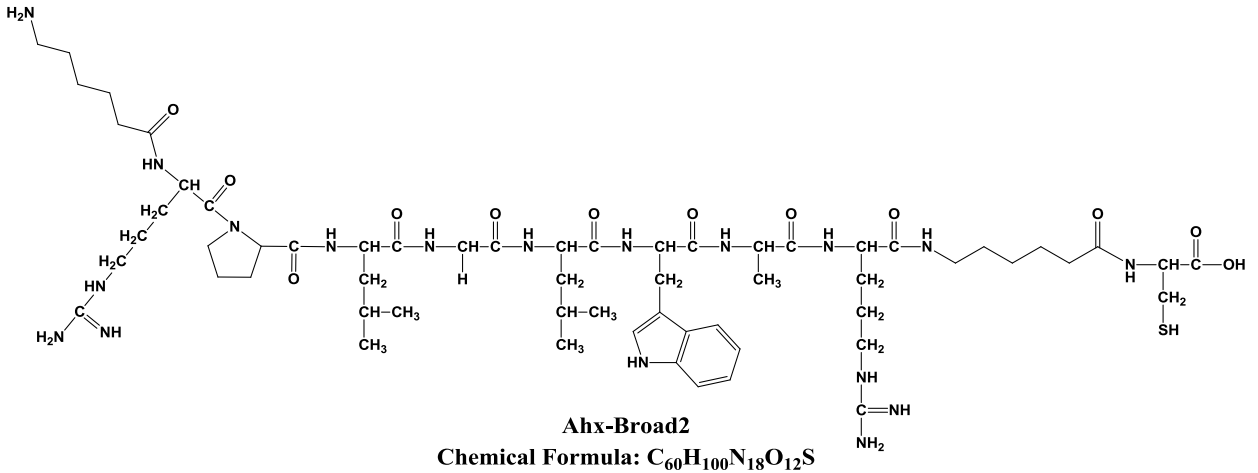

Ahx-Broad2
Chemical Formula: $C_{60}H_{100}N_{18}O_{12}S$
Exact Mass: 1296.75

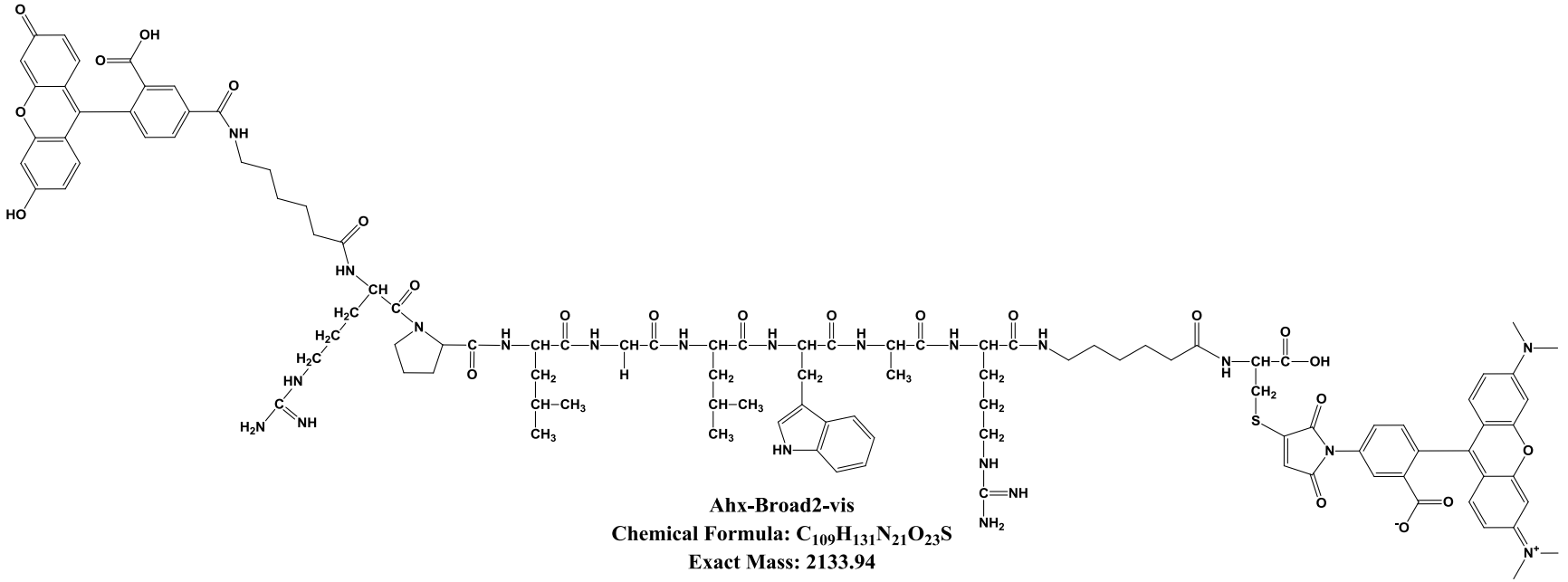

Ahx-Broad2-vis
Chemical Formula: $C_{109}H_{131}N_{21}O_{23}S$
Exact Mass: 2133.94

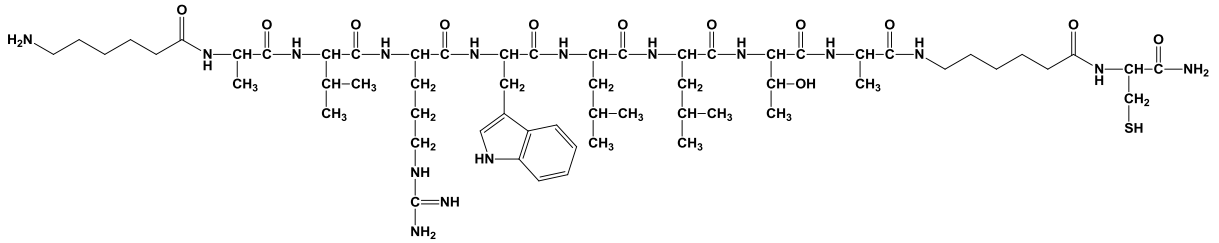

M9
Chemical Formula: $C_{59}H_{100}N_{16}O_{12}S$
Exact Mass: 1256.74

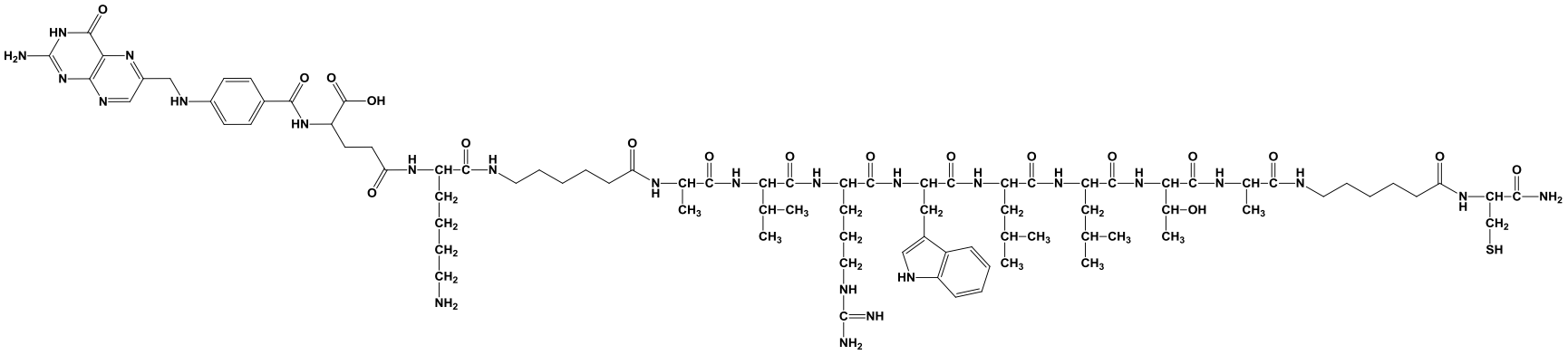

M9-Folate (M9F)
Chemical Formula: $C_{84}H_{129}N_{25}O_{18}S$
Exact Mass: 1807.97

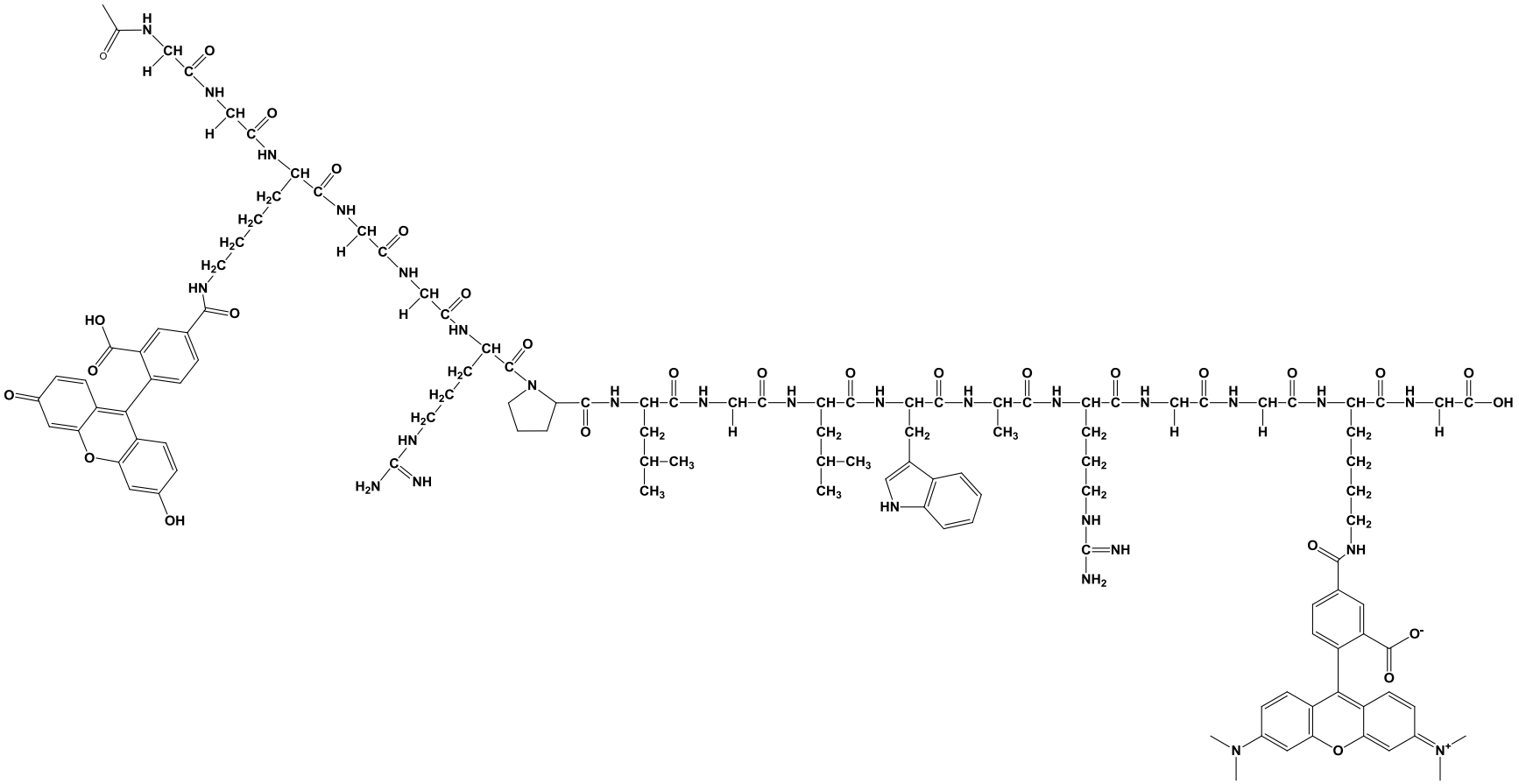

GG-Broad2-vis
Chemical Formula: $C_{119}H_{150}N_{28}O_{29}$
Exact Mass: 2435.11

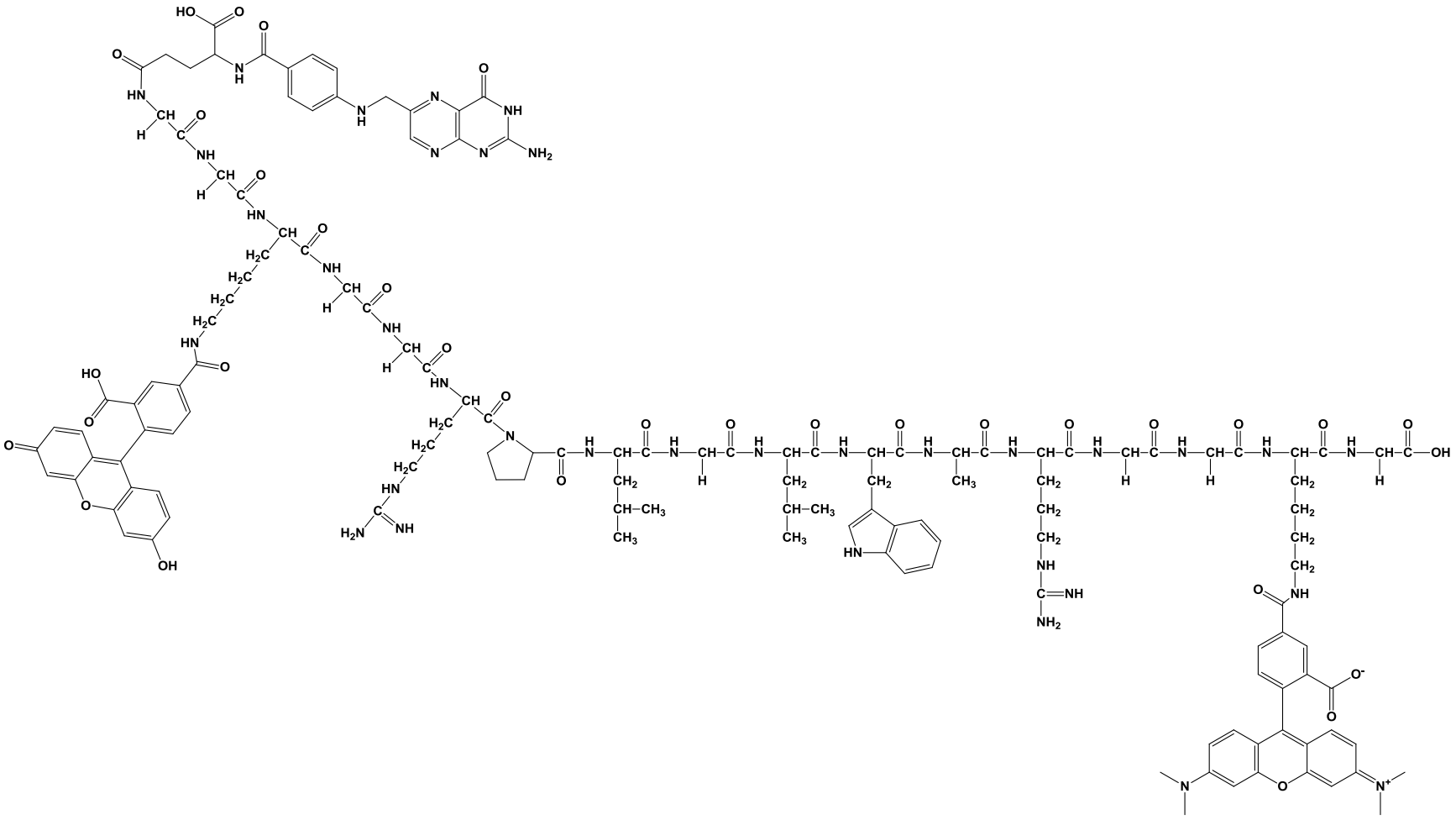

FA-GG-Broad2-vis
Chemical Formula: $C_{136}H_{165}N_{35}O_{33}$
Exact Mass: 2816.23

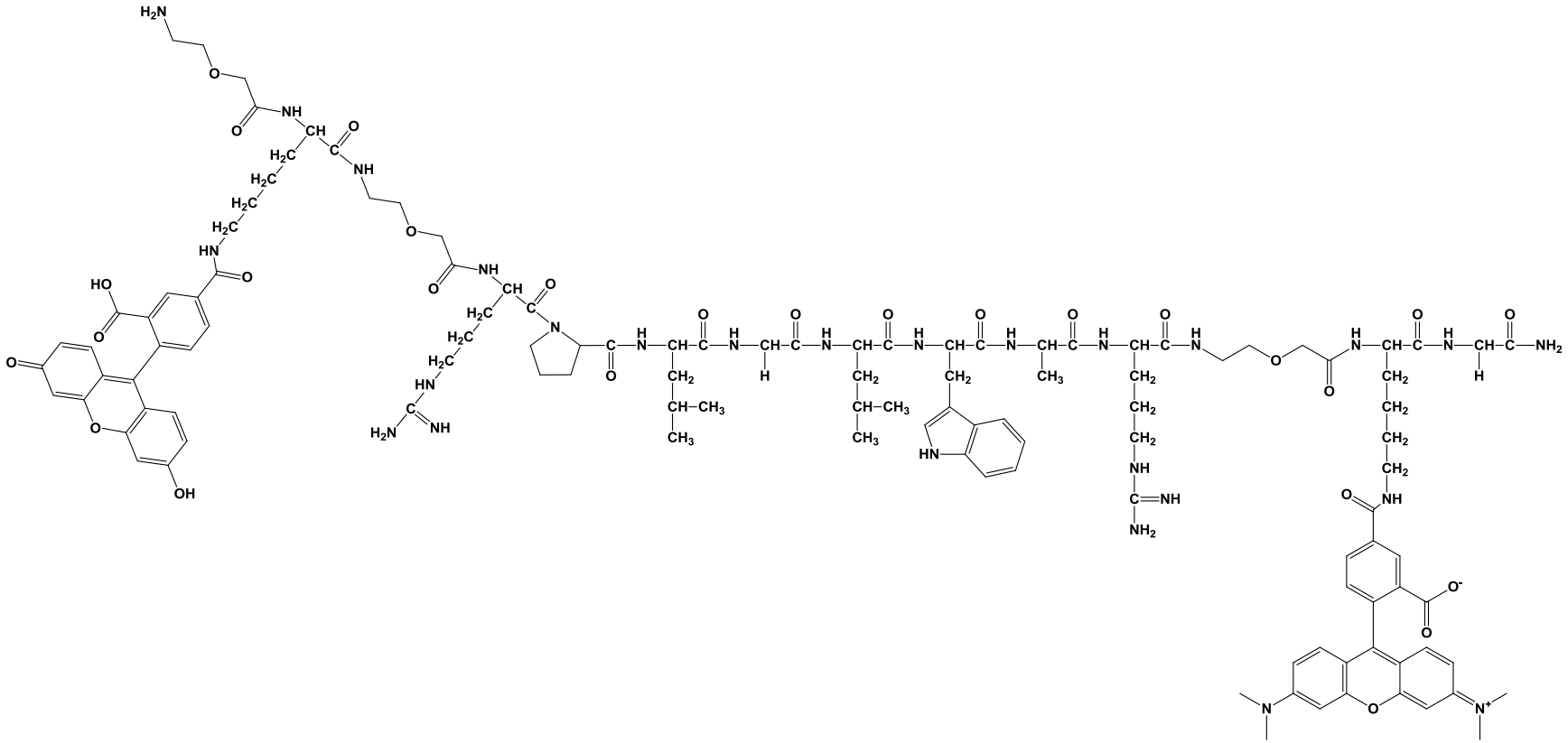

peg-Broad2-vis (pB2v)
Chemical Formula: $C_{117}H_{152}N_{26}O_{27}$
Exact Mass: 2353.13

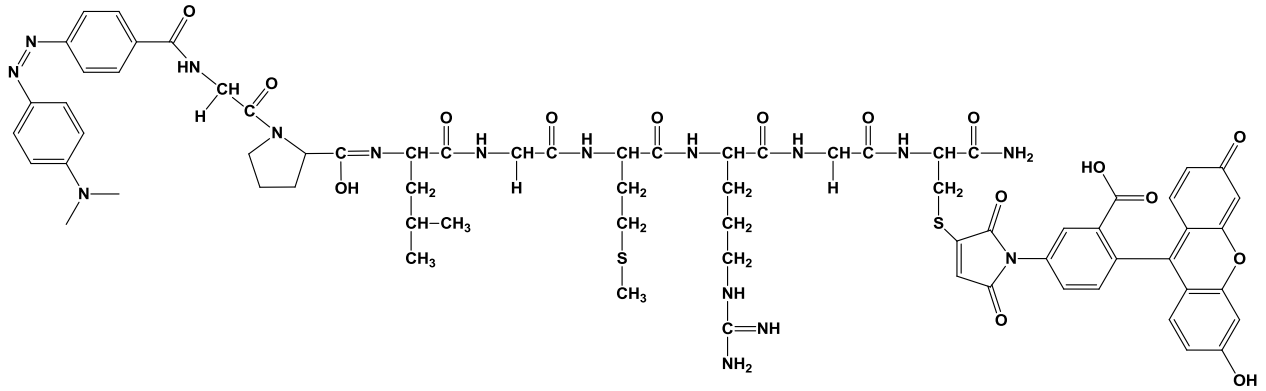

PEPDAB1001
Chemical Formula: $C_{70}H_{80}N_{16}O_{16}S_2$
Exact Mass: 1464.54

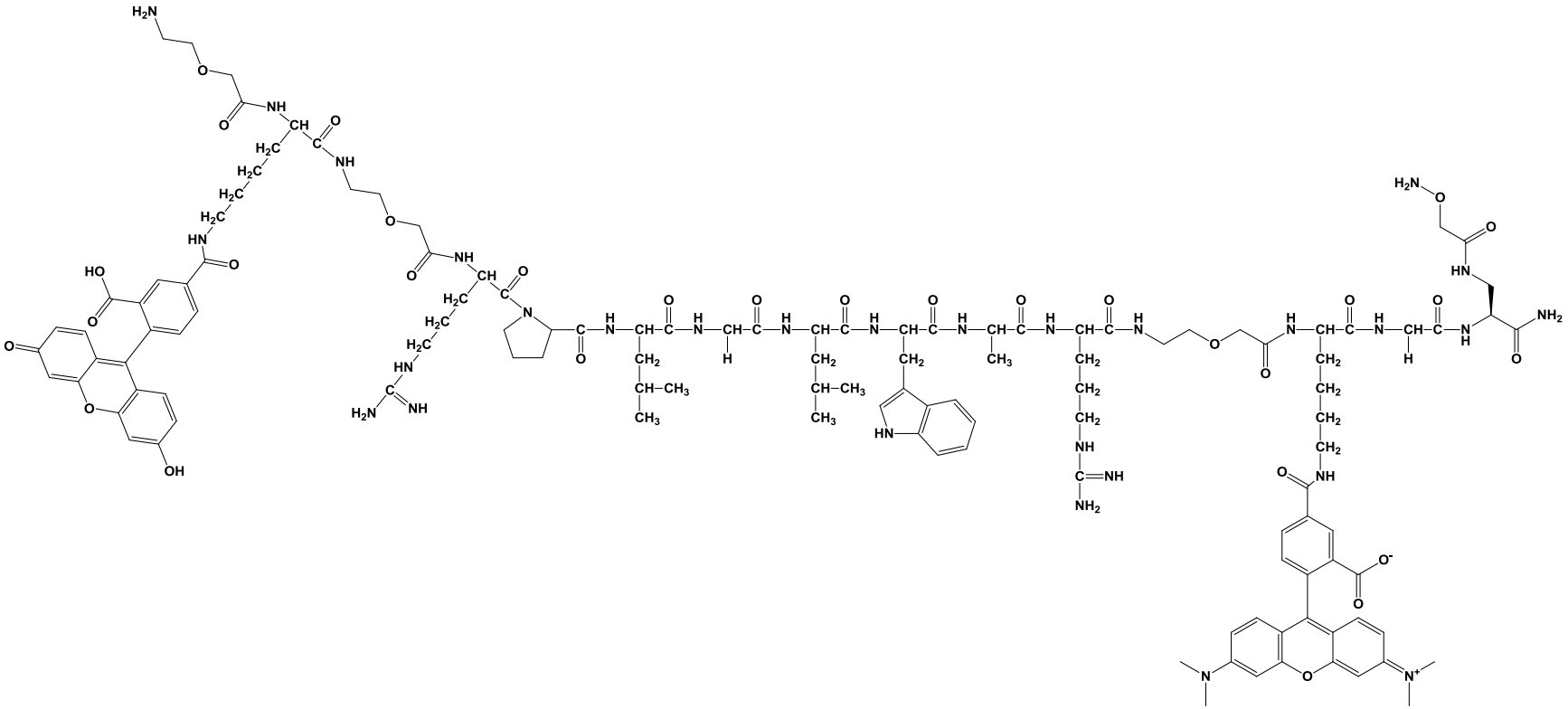

pB2vAoa
Chemical Formula: $C_{122}H_{161}N_{29}O_{30}$
Exact Mass: 2512.20

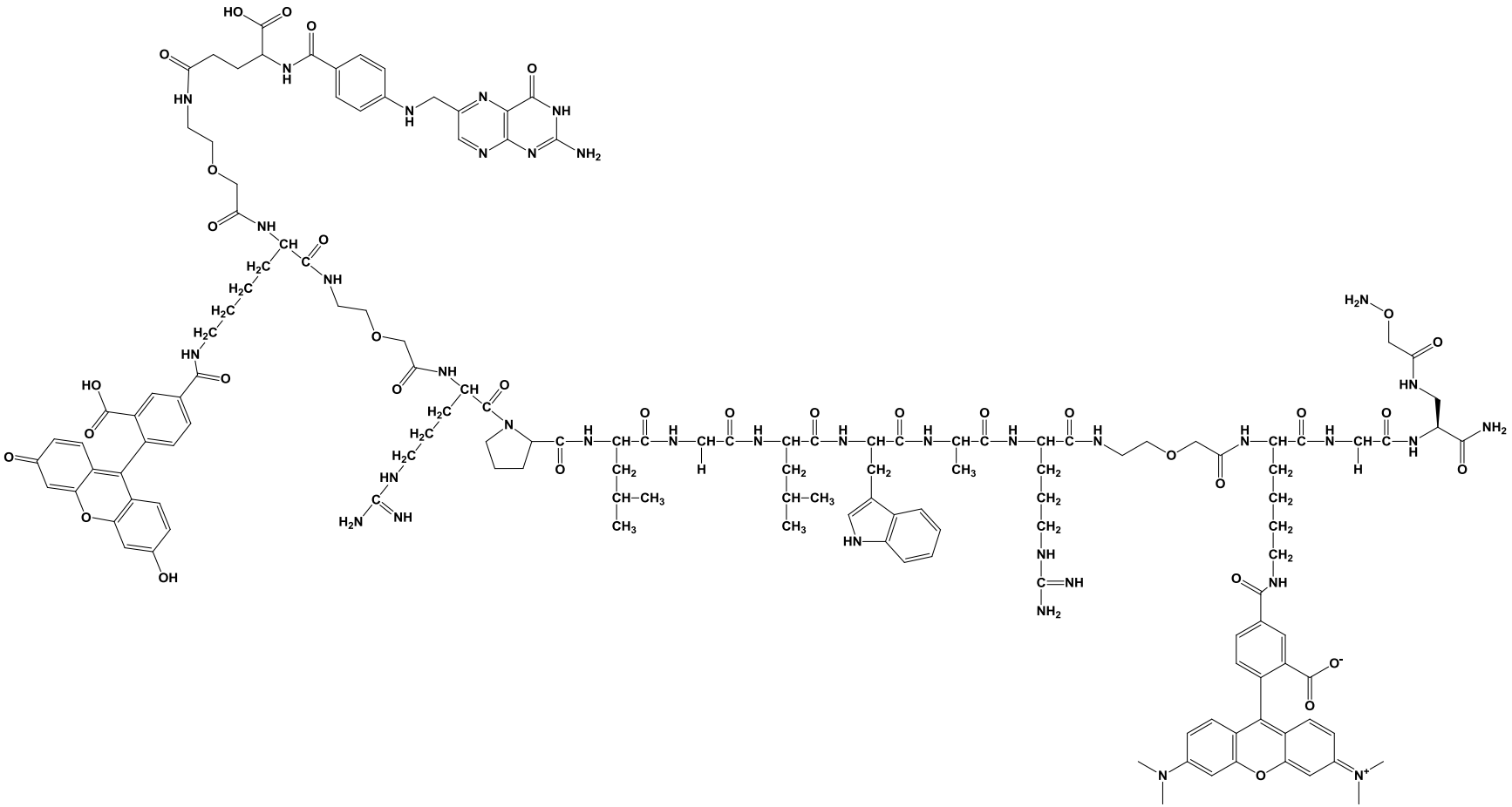

FApB2vAoa
Chemical Formula: $C_{141}H_{178}N_{36}O_{35}$
Exact Mass: 2935.33

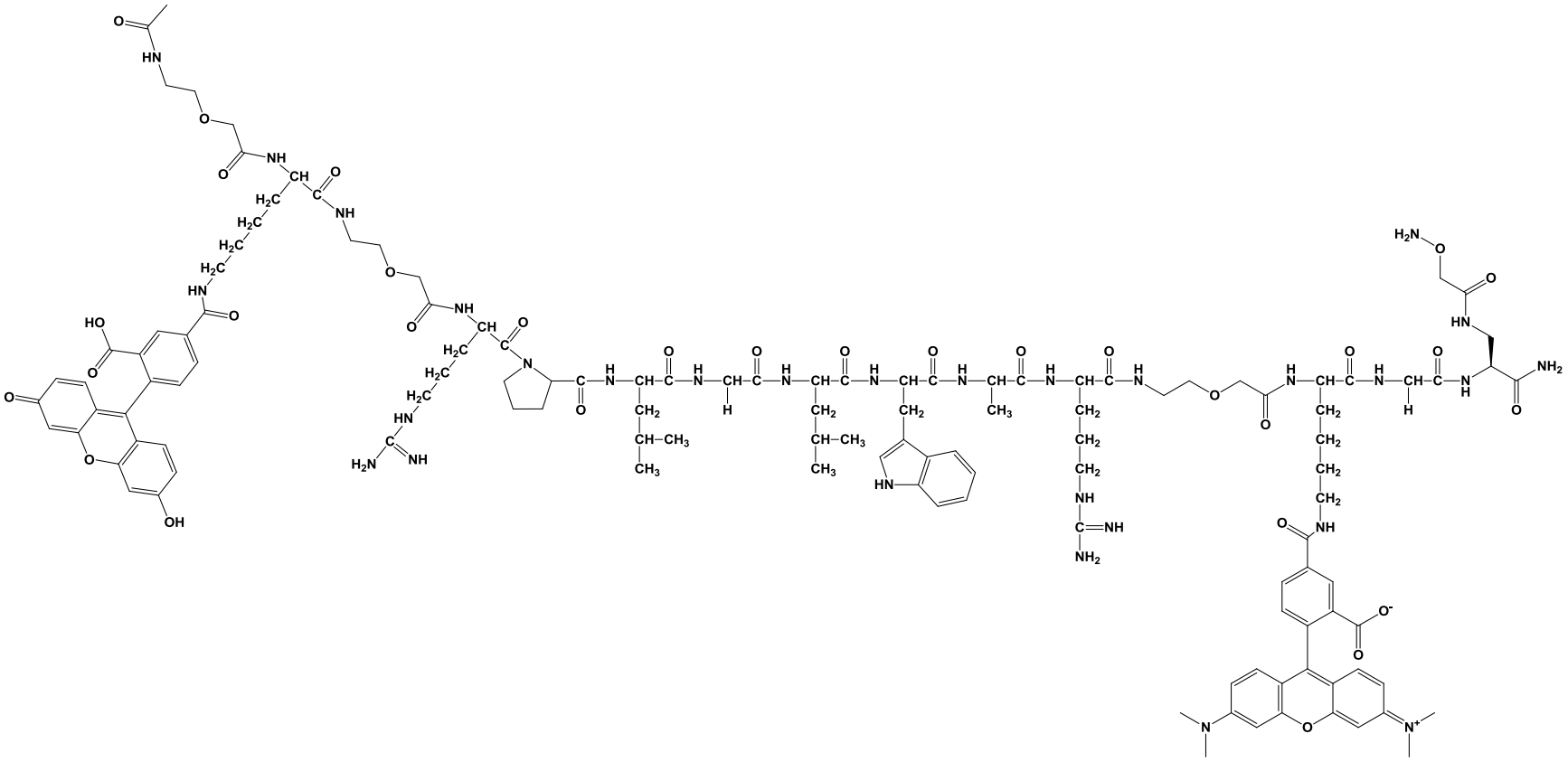

AcpB2vAoa
Chemical Formula: $C_{124}H_{163}N_{29}O_{31}$
Exact Mass: 2554.21

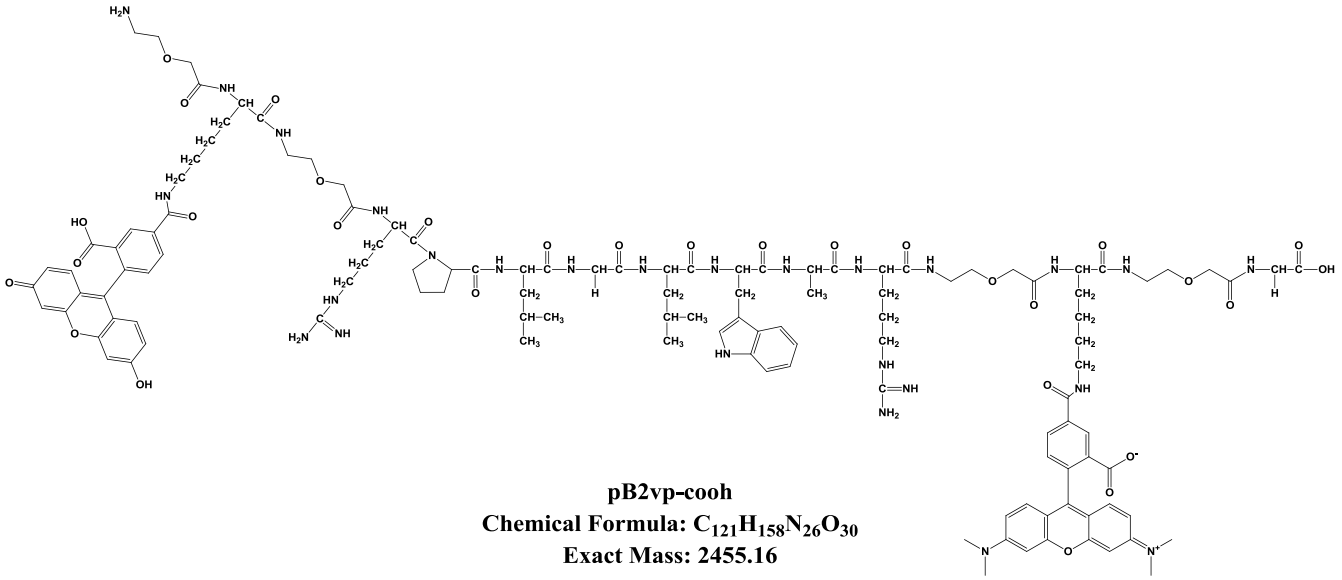

pB2vp-cooh
Chemical Formula: $C_{121}H_{158}N_{26}O_{30}$
Exact Mass: 2455.16

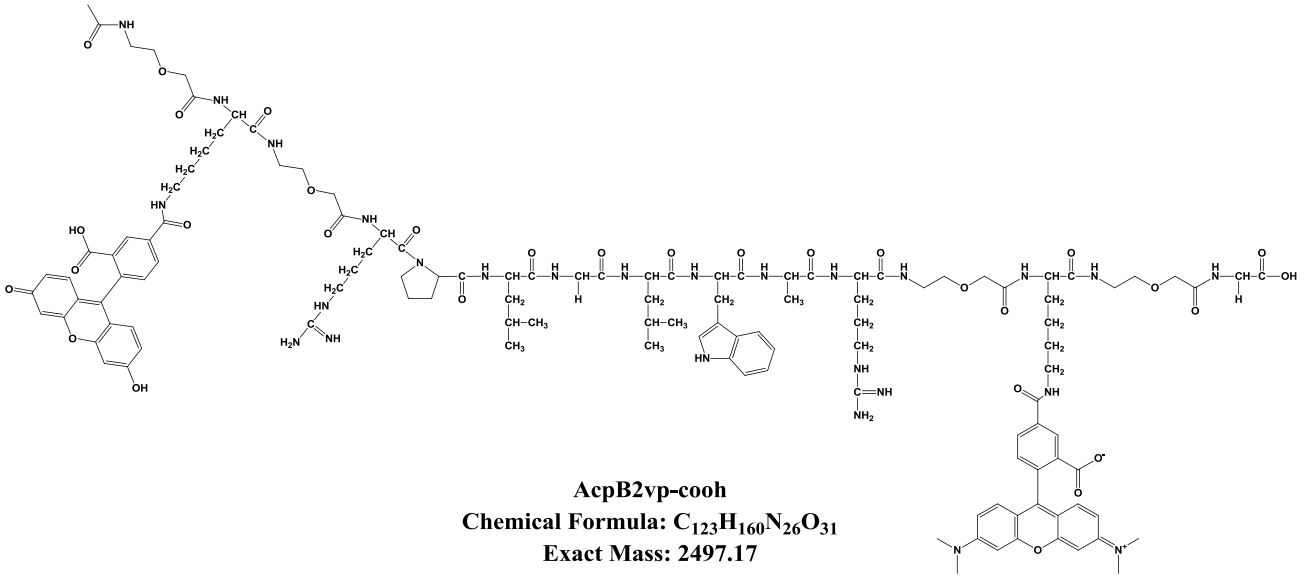

AcpB2vp-cooh
Chemical Formula: $C_{123}H_{160}N_{26}O_{31}$
Exact Mass: 2497.17

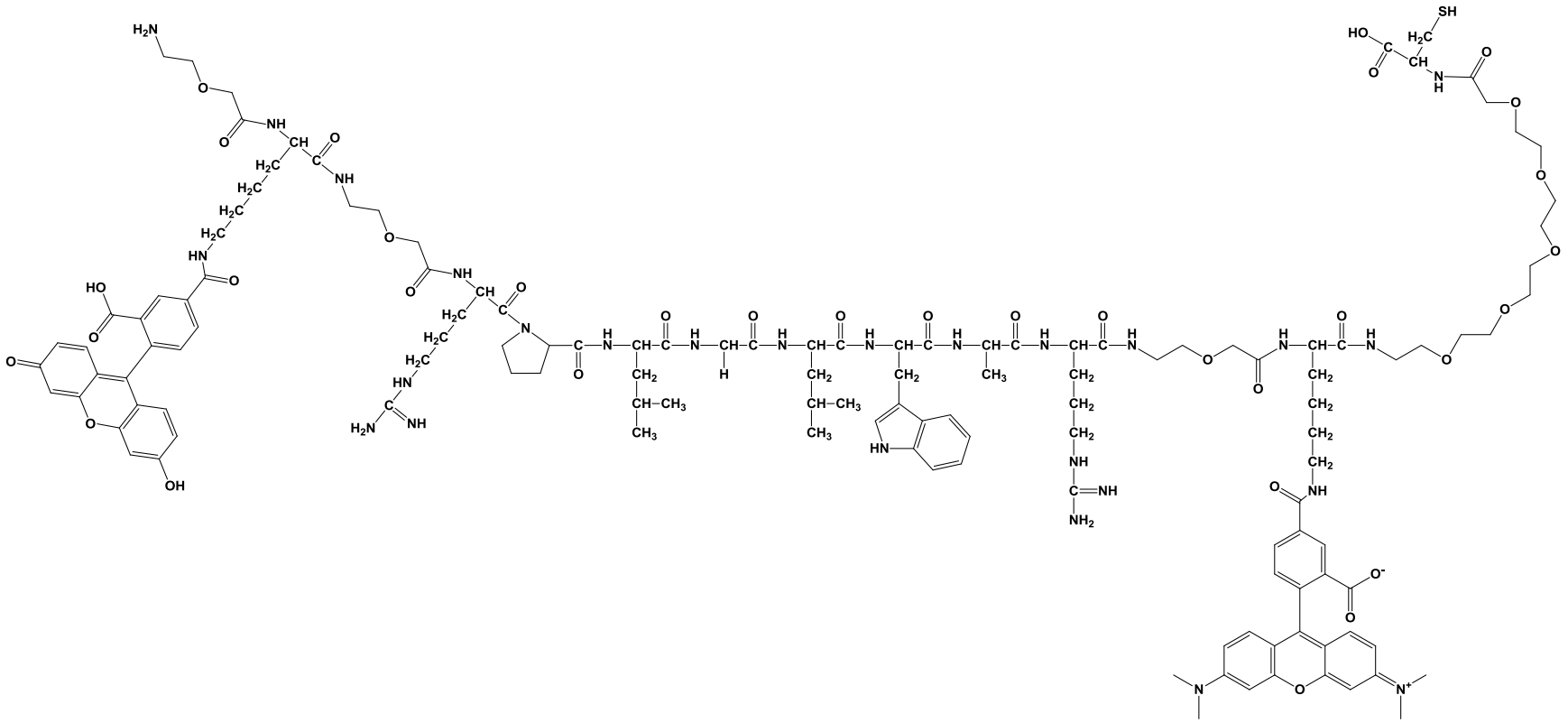

pB2vp5C-cooh
Chemical Formula: $C_{130}H_{176}N_{26}O_{34}S$
Exact Mass: 2677.26

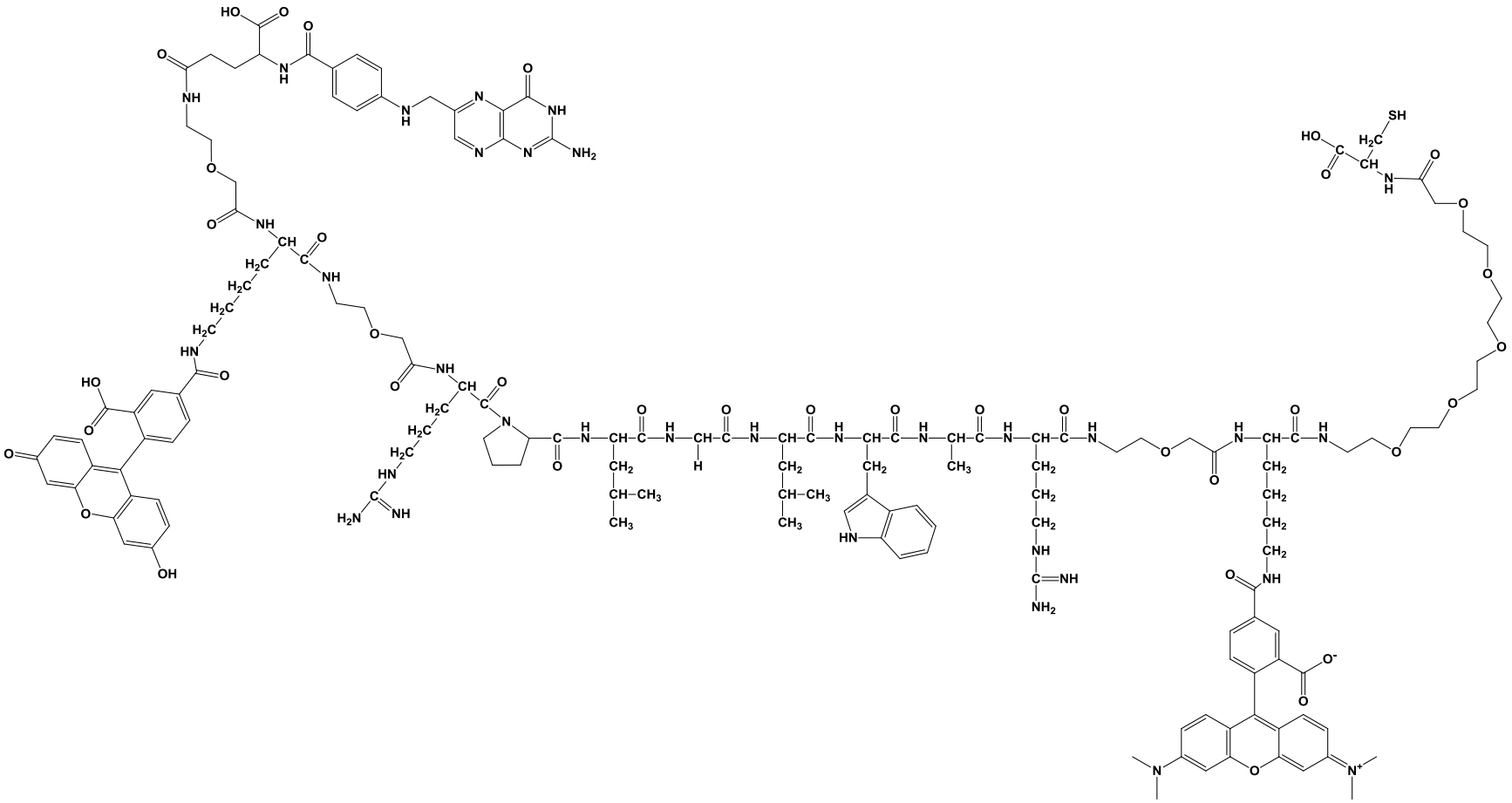

FApB2vp5C-cooh
Chemical Formula: $C_{149}H_{193}N_{33}O_{39}S$
Exact Mass: 3100.39

APPENDIX B

MEASUREMENT OF PEPTIDE CLEAVAGE EFFICIENCY BY MMPs

The relative efficiencies of enzymatic cleavage of peptides by MMPs were compared by calculating the specificity constants (k_{cat}/K_m), as follows:

$$\frac{k_{cat}}{K_m} = \frac{M}{F_e C_e},$$

where M is the initial rate of fluorescence increase, F_e is the maximum fluorescence increase for a particular enzyme-substrate pair and C_e is the concentration of active enzyme[116]. These parameters were indirectly measured by fluorescent FRET switch assay (see II.2.3) of peptides with MMPs, as depicted in Figure B-1.

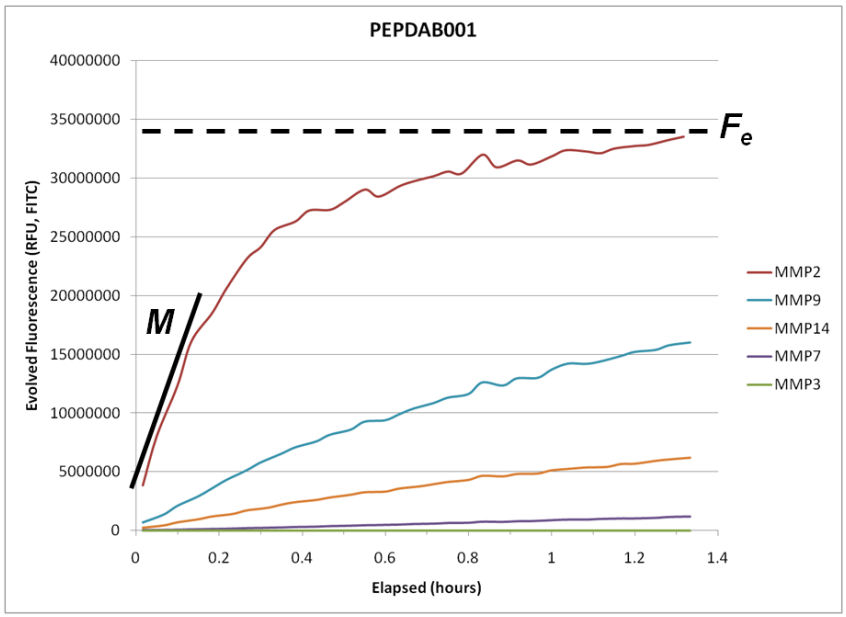

Figure B-1: **Calculation of enzyme-substrate specificity constant by FRET switch assay**
A representative FRET switch assay used to determine the relative efficiency of enzymatic cleavage of PEPDAB1001 peptide by MMPs. The fluorescence emission developed by MMP2-dependent cleavage is used as an example to indicate the parameters used in calculations.

While M and F_e were directly observable from this assay, the concentrations of active MMPs (C_e) had to be determined separately. For this determination, an active site titration assay was performed by incubating MMPs and broadly MMP-cleavable PEPDAB1001 peptide (see Appendix A) in a FRET switch assay with serially diluted GM6001. GM6001 is a broad-spectrum tight-binding inhibitor of MMPs. Active MMP concentrations were then calculated by fitting data to the Morrison equation:

$$V = SA\left([E_0] - \frac{1}{2}\left(\left([E_0] + [I] + K_{i,app}\right) - \sqrt{\left([E_0] + [I] + K_{i,app}\right)^2 - 4[E_0][I]}\right)\right)$$

where V is the observed rate of fluorescence increase, SA is the specific activity of the MMP, $[E_0]$ is the active MMP concentration, $[I]$ is the GM6001 concentration and $K_{i,app}$ is the apparent inhibition constant[158]. An example of the assay and curve-fitting for proteolysis of PEPDAB1001 in the presence of GM6001 to determine the active concentration of a stock of MMP14 is shown in Figure B-2.

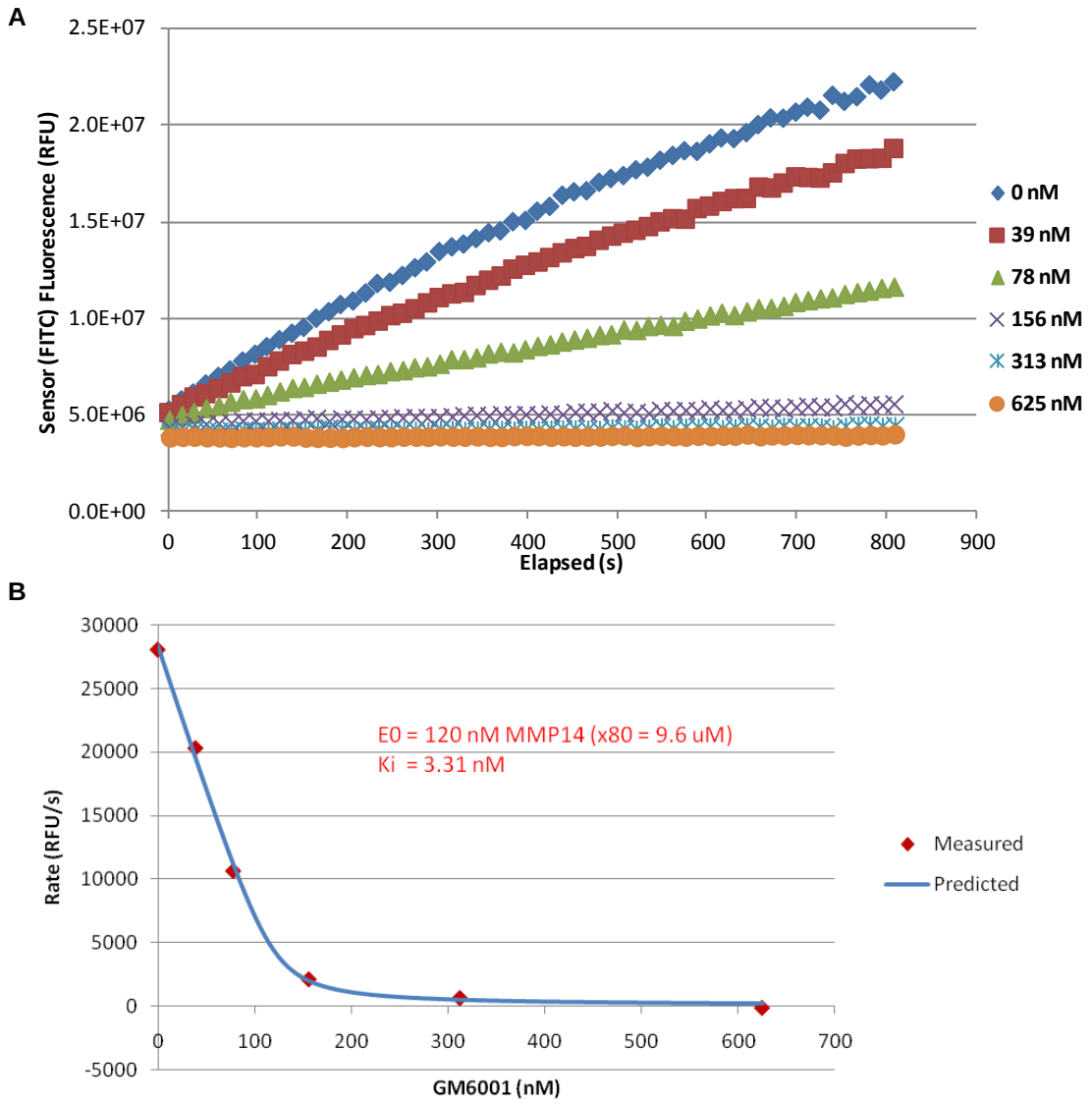

Figure B-2: **Determination of MMP14 stock concentration by inhibitor titration assay (ITA).** PEPDAB1001 peptide was incubated with MMP14 and various concentrations of GM6001 to measure the initial rate of fluorescence increase (A). Initial linear rates of fluorescence increase were plotted against inhibitor concentration (B) and fit to the Morrison equation (blue trace) to calculate the effective inhibition constant (K_i) and active enzyme concentration (E_0 x 80) based on dilution of a purchased stock of MMP14.

APPENDIX C

PREPARATION AND CHARACTERIZATION OF CELL LINES AND CONTRUCTS FOR BIOLOGICAL EXPERIMENTS

Several human and mouse breast cancer cell lines were characterized using common molecular biology techniques to assess their usefulness for *in vitro* and *in vivo* tumor models to facilitate testing of the targeting mechanisms employed by FTPNBs. As a first step, expression of the folate receptor gene, FOLR1, was assessed using reverse transcription polymerase chain reaction (RT-PCR), as shown in Figure C-1.

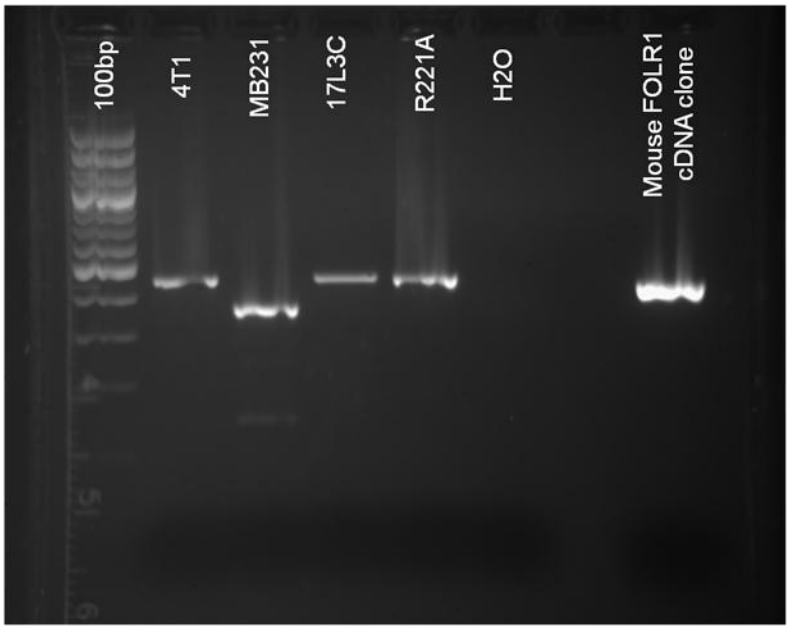

Figure C-1: **Qualitative FOLR1 expression by human and mouse breast cancer cell lines.** An expected 569-bp amplicon from the mouse FOLR1 gene was amplified from mouse breast cancer cell lines (4T1, 17L3C, and R221A) by RT-PCR using: TTGTTGCTCCTGGTGATG, forward primer; and CTGAGCTTGTAGGAGTGA, reverse primer. An expected 360-bp amplicon from the human FORL1 gene was amplified from human breast cancer cell line MDA-MB-231 using: TGGGTGGCTGTAGTAGGGGAG, forward primer; and CAGGGGCACGTTCAGTACC, reverse primer[159]. A water-only (no cDNA) PCR reaction was performed in parallel as a negative control. A mouse FOLR1 cDNA from Sino Biological (Beijing, CN) was used as a positive control. 100 bp DNA Ladder from Life Technologies (Carlsbad, CA, USA) was used to estimate the sizes of DNA oligomers.

4T1 mouse breast cancer cells and MDA-MB-468 human breast cancer cells have been reported to express negligible amounts of FRα[54,160] but substantial levels of MMPs including MMP14[161,162]. These cells presented the potential to develop models allowing testing of folate- and MMP-targeting separately and jointly by manipulating expression of FOLR1 or MMPs. Quantitative RealTime PCR (qPCR) experiments were performed on MB-468 cells in addition to the cell lines introduced above to assess relative expression of the FORL1 and MMP14 genes. Interestingly, these experiments confirmed reported results from 4T1 cells, but indicated that MB-468 cells expressed much more FOLR1 than MB-231 cells and much less MMP14, as shown in Figure C-2.

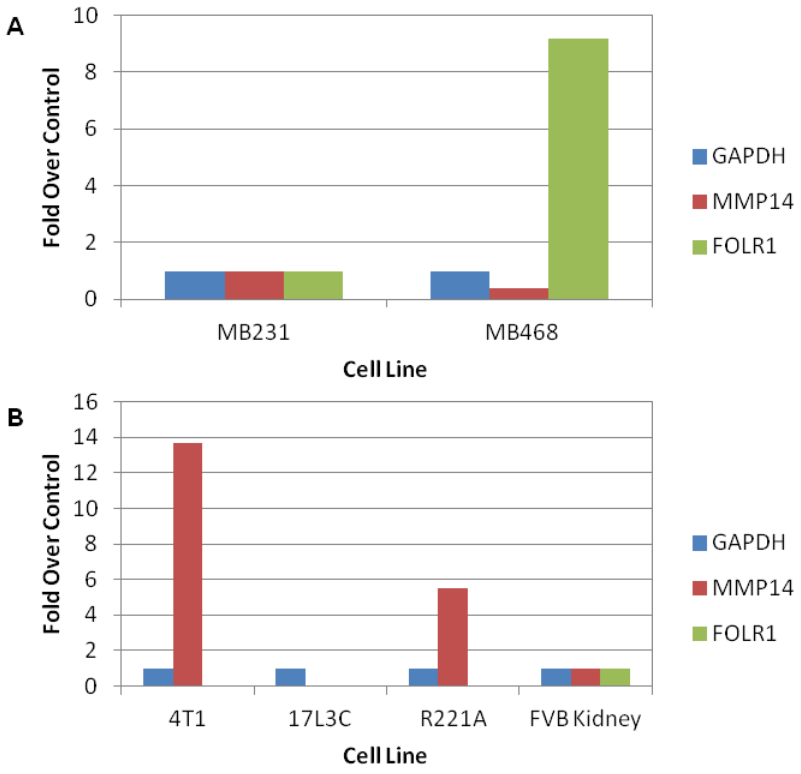

Figure C-2: **Relative expression of FOLR1 and MMP14 in human and mouse breast cancer cells** RealTime PCR was performed using Quantitect Primer Assays from Qiagen (Valencia, CA, USA) to calculate the relative expression of the FOLR1 and MMP14 genes in selected human (A) and mouse (B) breast cancer cell lines. Expression levels were normalized to GAPDH and compared against MB231 (human cells) or FVB mouse kidney tissue lysates (mouse cells). Values represent average of duplicates.

Based upon the above results demonstrating high expression of MMP14 but low-to-negligible expression of FRα in 4T1 cells, construction of a manipulated variant of 4T1 cells expressing exogenous FRα was attempted in order to develop an experimental condition for testing dual-targeted FTPNBs. Briefly, a full-length mouse FOLR1 cDNA clone was obtained from Sino Biologicals (Beijing, CN). This clone was amplified by RT-PCR and validated by restriction enzyme digestion, gel electrophoresis, and sequencing by the Vanderbilt DNA Sequencing Core (data not shown). Mouse FOLR1 cDNA was then used in the Gateway® Cloning System from Life Technologies (Carlsbad, CA, USA) according to supplier instructions to develop a mammalian transfection vector. First, the cDNA was inserted into a pDONR™ 201 entry vector used in the Gateway® system. E. coli bacteria were transformed with the entry vector and grown on kanamycin-supplemented agar plates to select for cells expressing the vector. The pDONR™ entry vector was extracted from the selected E. coli cells and used in an L/R recombination reaction with a pcDNA™ 6.2/V5-DEST Gateway® destination vector according to supplier instructions to construct a mammalian expression vector. Competent bacteria were then transformed with the expression vector and grown on kanamycin-supplemented agar for selection. Individual clones were selected by streaking and expanded in ampicillin-supplemented LB broth. Plasmid DNA was extracted from expanded clonal populations using Plasmid DNA MidiPrep Kits from Life Technologies (Carlsbad, CA, USA) and sequenced by the Vanderbilt DNA Sequencing Core using the T7 promoter. A clone producing the appropriate expression vector for transfection of mammalian cells was selected based on this sequencing, as shown in Figure C-3.

Reverse Complement (Coding Sequence):

CCTTAACATAATTTTTTCCCAGCAAGACGTTGTAAACGACGCCCGTCTTAAGCTCGGCCCCAAATAATGATTTTAT
TTGACTGATAATGACCTGTTCGTTGCAACAAATTGATGAGCAATGCTTTTTCTAATGCCAACTTGTACAAAAAGCA
GGCTCCGCGGCCGCCTTGTTTAACTTTAAGAAGGAGCCCTTCACCATGGCTCACCTGATGACTGTGCAGTTGTTG
CTCCTGGTGATGTGGATGGCCGAATGTGCTCAGTCCAGAGCTACTCGGGCCAGGACTGAACTTCTCAATGTCTG
CATGGATGCCAAACACCACAAAGAAAAACCGGGCCCTGAGGACAATTTACACGACCAGTGCAGCCCCTGGAAG
ACGAATTCCTGCTGTTCCACGAACACAAGCCAGGAAGCACATAAGGACATTTCCTACCTGTACCGGTTCAACTGG
AACCACTGCGGAACTATGACATCCGAATGCAAACGGCACTTTATCCAAGACACCTGCCTCTATGAGTGTTCCCCG
AACTTGGGACCCTGGATCCAGCAGGTGGACCAGAGCTGGCGCAAAGAGCGGATCCTTGATGTTCCCCTGTGCAA
AGAGGACTGTCAGCAGTGGTGGGAGGACTGCCAGAGCTCTTTTACCTGCAAGAGCAATTGGCACAAGGGATGG
AACTGGTCCTCGGGGCATAACGAGTGTCCTGTGGGAGCCTCCTGCCATCCCTTCACCTTCTACTTCCCCACATCTG
CTGCTCTGTGTGAGGAAATCTGGAGTCACTCCTACAAGCTCAGCAACTACAGTCGAGGGAGCGGCCGCTGCATT
CAGATGTGGTTCGACCCAGCCCAGGGCAACCCCAACGAGGAAGTGGCGAGGTTCTATGCCGAGGCCATGAGTG
GAGCTGGGTTTCATGGGACCTGGCCACTCTTGTGCAGCCTGTCCTTAGTGCTGCTCTGGGTGATCAGCTGAAAG
GGTGGGCGCGCCGACCCAGCTTTCTTGTACAAAGTTGGCATTATGGGAAAGCATTGCTTATCAATTTGTGCAACG
AACAGGTCACTATCAGTCAAAATAAATCATATCCATCTAGTAC

Encoded Protein Translation

Mouse FOLR1 protein (NM_008034)

MAHLMTVQLLLLVMWMAECAQSRATRARTELLNVCMDAKHHKEKPGPEDNLHDQCSPWKTNSCCSTNTSQEAH
MAHLMTVQLLLLVMWMAECAQSRATRARTELLNVCMDAKHHKEKPGPEDNLHDQCSPWKTNSCCSTNTSQEAH

KDISYLYRFNWNHCGTMTSECKRHFIQDTCLYECSPNLGPWIQQVDQSWRKERILDVPLCKEDCQQWWEDCQS
KDISYLYRFNWNHCGTMTSECKRHFIQDTCLYECSPNLGPWIQQVDQSWRKERILDVPLCKEDCQQWWEDCQS

SFTCKSNWHKGWNWSSGHNECPVGASCHPFTFYFPTSAALCEEIWSHSYKLSNYSRGSGRCIQMWFDPAQGNP
SFTCKSNWHKGWNWSSGHNECPVGASCHPFTFYFPTSAALCEEIWSHSYKLSNYSRGSGRCIQMWFDPAQGNP

NEEVARFYAEAMSGAGFHGTWPLLCSLSLVLLWVIS
NEEVARFYAEAMSGAGFHGTWPLLCSLSLVLLWVIS

Figure C-3: Sequencing of mouse FOLR1 expression clone and encoded peptide product
A Gateway® expression vector extracted from E.coli grown in ampicillin-supplemented LB broth was sequenced by the Vanderbilt DNA Sequencing Core using the T7 promoter. The protein coding sequence from the plasmid and the encoded protein are highlighted in yellow. The encoded protein is homologous with the reported sequence of protein encoded by the mouse FOLR1 gene (highlighted in green).

Next, transfection of 4T1 cells was attempted using the mouse FOLR1 expression vector validated above. This plasmid was incorporated into transfection complexes and used for transfection using either Lipofectamine® 2000 (Life Technologies, Carlsbad, CA, USA) or SuperFect® (Qiagen, Valencia, CA, USA) according to the suppliers' instructions. Unfortunately, expansion of 4T1 cell culture colonies that remained adherent more than 24 hours subsequent to transfection was not observed. Anecdotally, some cells

appeared to remain viable, but did not remain adherent, seeming to become more like suspension-tolerant cells. To validate successful transfection, 293 human embryonic kidney cells with transiently transfected with the mouse FOLR1 expression vector or a COP-GFP vector, or both vectors simultaneously using Lipofectamine® 2000. As seen in Figure C-4, transient transfection of 293 cells using COP-GFP and mouse FOLR1 together was confirmed by fluorescence microscopy. However, subsequent analysis by qPCR did not detect mouse FOLR1 expression in wild type or transfected 293 cells (data not shown). As such, further attempts at transfection of 4T1 cells with mouse FORL1 were not made.

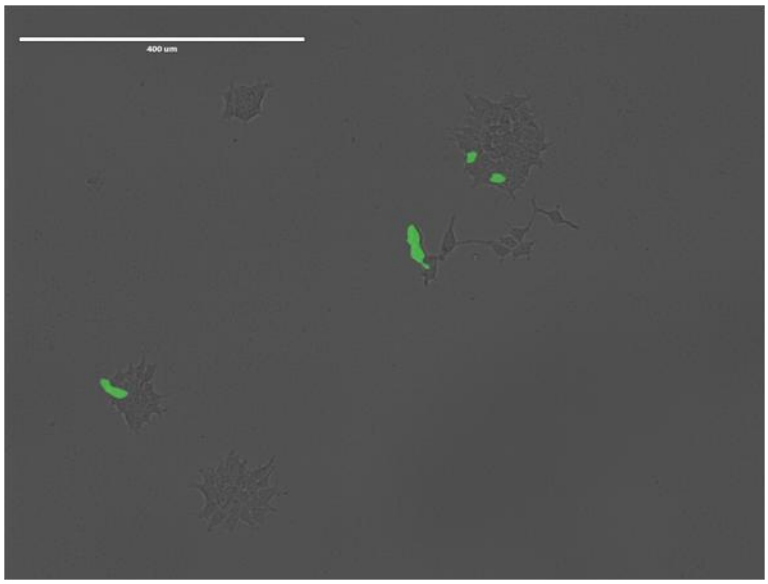

Figure C-4: **Transient transfection of 293 cells with COP-GPF and mouse FOLR1**
293 human embryonic kidney cells well transiently transfected with expression vectors for COP-GFP and mouse FOLR1 using Lipofectamine® 2000 reagent. Cells were imaged following transfection and overnight culture in growth medium using bright field and a green fluorescence filter on an EVOS FL inverted fluorescence microscope (Advanced Microscopy Group, Mill Creek, WA, USA). Scale bar: 400 µm.

Because the attempts at transfection of low FR-expressing 4T1 cells with mouse FOLR1 did not generate a stable construct for experiments on folate targeted compounds, MDA-MB-468 human breast cancer cells were reassessed. In addition to MMP

expression, Figure C-2 above demonstrates relatively high FR expression by MB-468 cells in our laboratory that is contrary to previous reports[160]. Hence, MB-468 cells presented another option for constructing cells with different experimental conditions for folate targeting experiments by knocking down this FR expression. However, before proceeding to manipulate gene expression by these cells, the previous reports of MMP expression levels[161] were also investigated. Shown in Figure C-5, MB-468 cells expressed a substantial amount of MMP7 and much lower levels of MMP2 and MMP9, recapitulating the results reported by Giambernardi et al[161] with the exception of MMP14 expression.

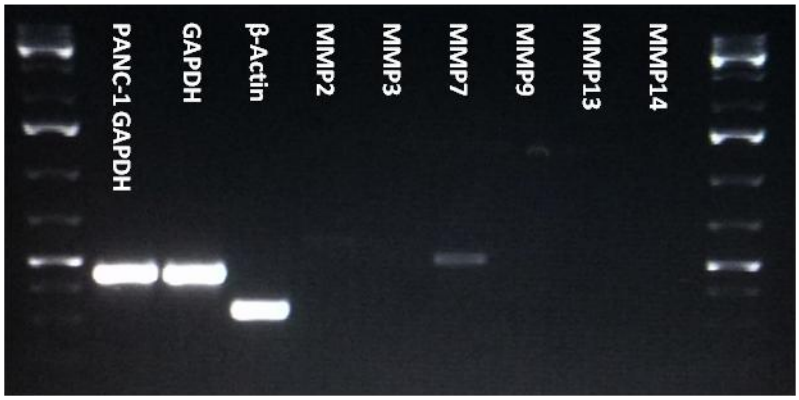

Figure C-5: Expression of selected MMPs by MDA-MB-468 cells
The expression of MMPs 2, 3, 7, 9, 13, and 14 by MDA-MB-468 cells was qualitatively assessed by RT-PCR using the DNA oligo primers and reaction conditions reported by Giambernardi et al[161]. With the exception of a lack of MMP14 expression, these results corroborate the reported findings for MMP expression.

Because relatively high expression of MMP14 by MB-468 cells has been reported[161] and my earlier qPCR experiments detected MMP14 expression by MB-468 cells (Figure C-2), RT-PCR analysis was repeated using different primers and MDA-MB-231 cells as a positive control. In this experiment, MMP14 expression by both MB-231 and MB-468 cell lines was confirmed, as seen in Figure C-6.

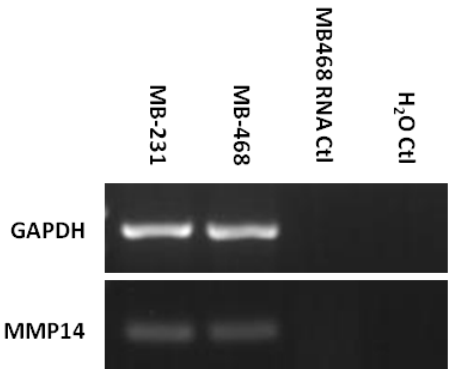

Figure C-6: MMP14 expression by MDA-MB-231 and MDA-MB-468 cell lines
Expression of MMP14 by MDA-MB-231 and MDA-MB-468 metastatic breast cancer cells lines was qualitatively assessed by RT-PCR using primers from the Human MMP14 Quantitect Primer Assay (Qiagen, Valencia, CA, USA). Negative control reactions were performed in parallel using either MB-468 RNA or molecular biology grade water in place of a cDNA template.

With the expression of FRα and MMPs by MB-468 cells confirmed, a strategy was developed to manipulate MB-468 cells to provide different experimental conditions for folate targeting experiments. FR-knockdown cells were constructed by infecting MB-468 cells with lentiviral particles containing vectors encoding short hairpin ribonucleic acid (shRNA) sequences designed to interfere with FOLR1 expression. Mission® shRNA lentiviral transduction particles targeting human FOLR1 knockdown were obtained from Sigma Aldrich (St. Louis, MO, USA). Particles encoding three different targeted shRNA sequences were used to infect MB-468 cells according to the supplier's instructions:

i. #343: CCGGCCCACTGTTCTGTGCAATGAACTCGAGTTCATTGCACA-GAACAGTGGGTTTTTG
ii. #344: CGGGCTTCTCAATGTCTGCATGAACTCGAGTTCATGCAGAC-ATTGAGAAGCTTTTTG
iii. #347: CGGGTGAGCAATGGTGGGAAGATTCTCGAGAATCTTCCCAC-CATTGCTCACTTTTTG

Following lentiviral transduction, infected cells were grown in RPMI-1640 cell culture medium (Life Technologies, Carlsbad, CA, USA) supplemented with 5-10% fetal bovine serum (FBS) and 0.5 μg/mL puromycin to select for cells expressing the shRNA knockdown vectors.

It was also desirable to develop a condition in which the expression of FR by cells was increased above endogenous levels. FR expression and/or folate binding capacity of some cells has been shown to be increased by incubating cells in folate-deficient media[61,163]. For example, the folic acid binding capacity of M109 murine lung carcinoma cells was reportedly increased by as much as 20-80-fold after as little as 24 hours in folate-deficient RPMI-1640 medium[61]. Recapitulating these studies, MB-468 cells were grown in RPMI-1640 and folate-deficient RPMI-1640 media supplemented with 5-10% FBS in parallel.

The expression of FOLR1 and protein levels of FRα in parental and manipulated MB-468 cells were subsequently characterized by qPCR and Western blotting to assess the degree of gene and protein knockdown (see Figure C-7). Cells expressing targeted shRNAs expressed the FORL1 gene at levels 40-75% lower than cells infected with a nonspecific control shRNA. FRα protein levels in lysates from MB-468 cells infected with targeted shRNAs were lower than levels in parental cell lysates. Conversely, cells grown in folate-deficient RPMI-1640 medium (Life Technologies, Carlsbad, CA, USA) exhibited increased levels of FRα protein.

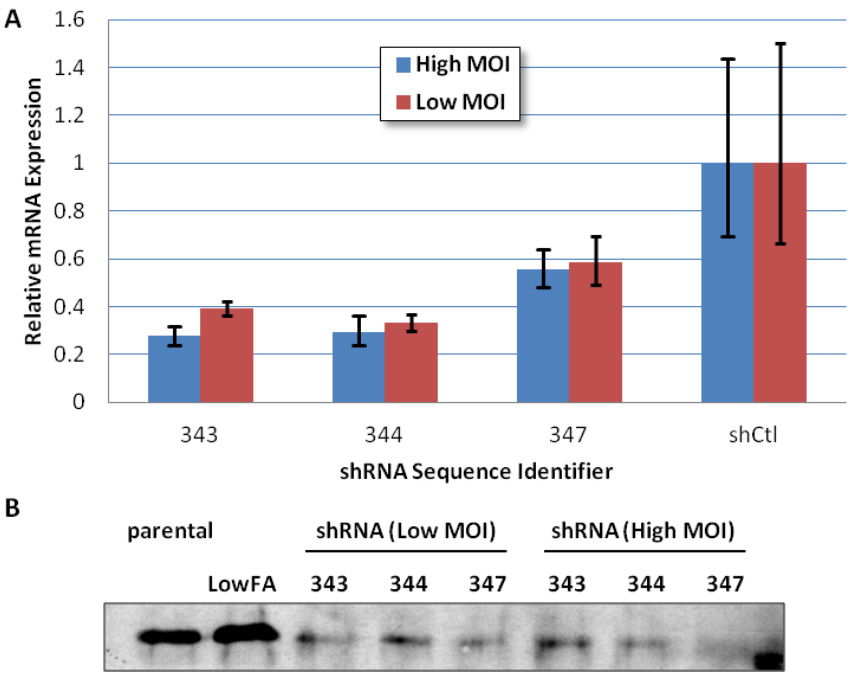

Figure C-7: **Knockdown of FRα expression in MDA-MB-468 cells by shRNA**
MB-468 cells were infected using lentiviral transduction particles carrying vectors for the expression of shRNA directed against the expression of the FOLR1 gene. A non-specific shRNA (shCtl) was used in parallel as a negative control for knockdown effects. (A): Quantitative assessment of gene expression by RealTime PCR indicates 40-75% knockdown of gene expression by MB-468 cells infected with targeted shRNAs. Values represent average of triplicates. Error bars: standard deviation. (B): FRα protein levels in lysates from MB-468 cells infected with targeted shRNAs were lower than levels in parental cell lysates. MB-468 cells grown in folate-deficient RPMI-1640 medium (Life Technologies, Carlsbad, CA, USA) exhibited increased levels of FRα protein. Cell lysate samples were standardized to total protein content as measured by BCA assay. FRα protein was stained using a rabbit anti-FR polyclonal antibody obtained from AbCam (Cambridge, MA, USA).

FRα is a GPI-anchored recycling receptor that is internalized by cells along with any bound ligands (i.e. FA or folates). Previous studies have shown that the high affinity of FA for FR and the rate of internalization of ligand-bound receptors is largely unaffected by FA conjugation to other molecules[136,164]. However, the rate of receptor recycling may vary considerable between different cell types, a factor that may greatly influence the capacity for folate-mediated drug delivery to a particular cell type and may even determine what frequency of dosing is most efficient[136]. Folate binding capacity has previously been reported using radiolabeled ligand assays that require special handling

and safety equipment[61,136,163]. I developed an alternative measure of folate binding capacity using a comparatively more economical strategy employing indirect flow cytometry to measure the amount of FRα present on the surface of cells. Briefly, cells were harvested from subconfluent cultures using enzyme-free cell dissociation buffer (Life Technologies, Carlsbad, CA, USA), rinsed and resuspended in AutoMACs buffer (Miltenyi Biotec, San Diego, CA, USA) containing 3% bovine serum albumin (BSA) and kept on ice during all subsequent steps leading to analysis by flow cytometry. After blocking using a rat anti-CD16/32 (Fcγ III/II) antibody, cells were either labeled with a rabbit anti-FR polyclonal antibody (AbCam, Cambridge, MA, USA) or washed in AutoMACs to provide no-primary controls for secondary antibody staining. For detection by the cytometer, cells were then labeled with a FITC-labeled goat anti-rabbit secondary antibody. Cell suspensions were filtered through 70 μm cell separating filters and then counted using a BD Accuri C6 flow cytometer (BD Biosciences, San Jose, CA, USA).

The effect of growth in folate-deficient medium on cell surface FRα levels of several cell lines was assessed using this assay. As demonstrated in Figure C-8, surface expression of FRα was measurable in these cell lines. Furthermore, the average fluorescence intensities of these cell lines increased subsequent to growth in folate deficient media. With optimization, these techniques for manipulating and measuring the folate binding capacity of cells should prove useful in the design and implementation of experimental tumor models with folate-targeted molecules such as FTPNBs.

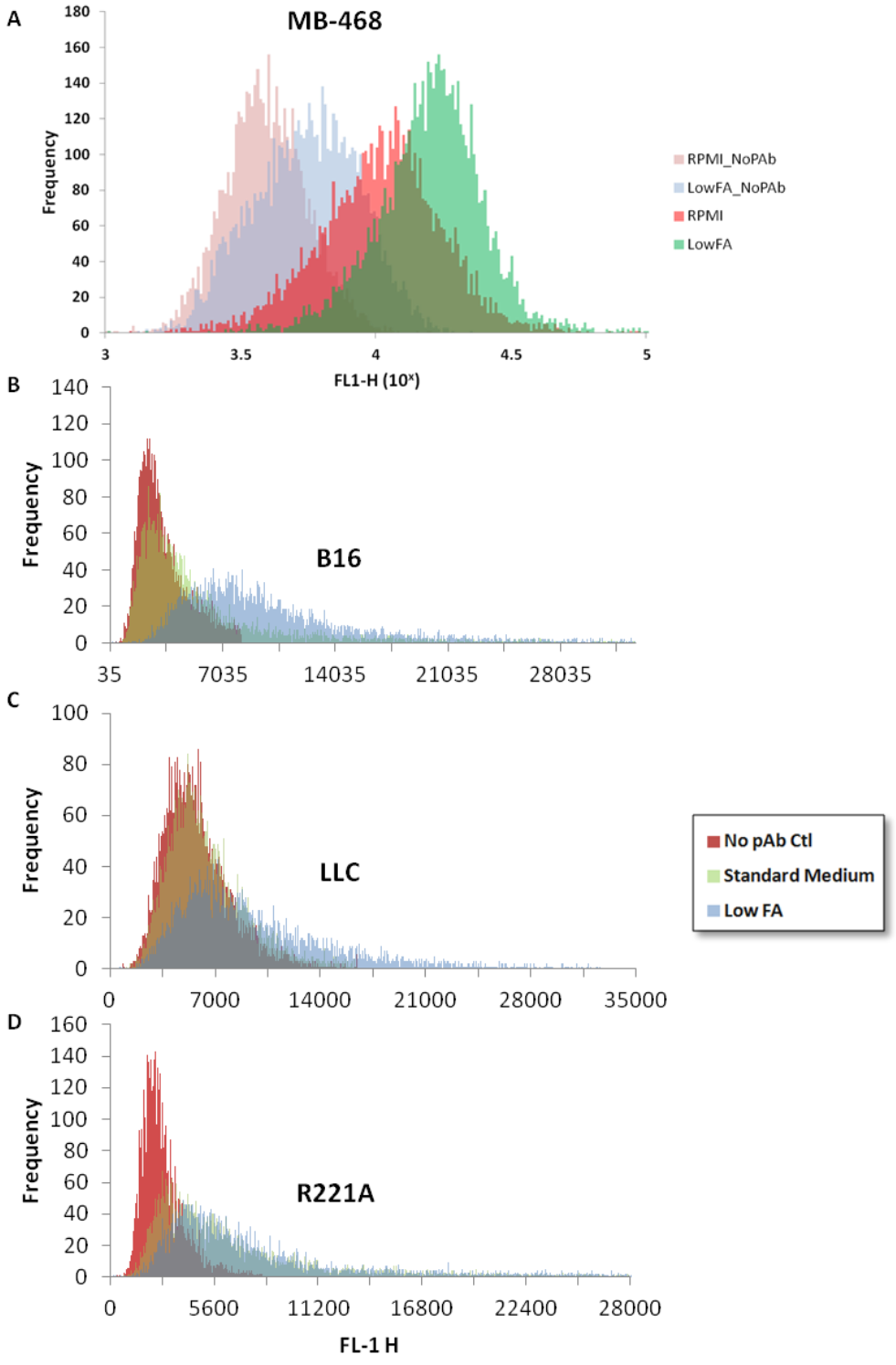

Figure C-8: **Folate binding capacity of cell lines increases after growth in folate-deficient medium** FRα levels on the surfaces of MDA-MB468 human breast cancer (A), B16 mouse melanoma (B), Lewis rat lung carcinoma (LLC)(C), and R221A mouse breast cancer cells (D) were assessed by indirect flow cytometry after growth in standard or low FA RPMI-1640 cell culture media. Control reactions substituting buffer only for anti-FR antibodies were performed in parallel to control for nonspecific fluorescence.

REFERENCES

1. Murphy, S. L., Xu, J. & Kochanek, K. D. Deaths: final data for 2010. *Natl. Vital Stat. Rep.* **61,** 1–117 (2013).
2. Heron, M. Deaths: leading causes for 2010. *Natl. Vital Stat. Rep.* **62,** 1–97 (2013).
3. American Cancer Society. Cancer Facts & Figures 2014. *Cancer Facts Fig.* (2014).
4. Druker, B. J. *et al. Efficacy and safety of a specific inhibitor of the BCR-ABL tyrosine kinase in chronic myeloid leukemia. N. Engl. J. Med.* **344,** 1031–1037 (2001).
5. Dvorak, H. F., Nagy, J. A. & Dvorak, A. M. Structure of solid tumors and their vasculature: implications for therapy with monoclonal antibodies. *Cancer Cells* **3,** 77–85 (1991).
6. Carver, L. A. & Schnitzer, J. E. Caveolae: mining little caves for new cancer targets. *Nat. Rev. Cancer* **3,** 571–581 (2003).
7. McCawley, L. J. & Matrisian, L. M. Matrix metalloproteinases: they're not just for matrix anymore! *Curr. Opin. Cell Biol.* **13,** 534–40 (2001).
8. Overall, C. M. & Dean, R. a. Degradomics: systems biology of the protease web. Pleiotropic roles of MMPs in cancer. *Cancer Metastasis Rev.* **25,** 69–75 (2006).
9. Yan, C. & Boyd, D. D. Regulation of matrix metalloproteinase gene expression. *J. Cell. Physiol.* **211,** 19–26 (2007).
10. Visse, R. & Nagase, H. Matrix metalloproteinases and tissue inhibitors of metalloproteinases: structure, function, and biochemistry. *Circ. Res.* **92,** 827–39 (2003).
11. Barbolina, M. V & Stack, M. S. Membrane type 1-matrix metalloproteinase: substrate diversity in pericellular proteolysis. *Semin. Cell Dev. Biol.* **19,** 24–33 (2008).
12. Fic, P., Zakrocka, I., Kurzepa, J. & Stepulak, A. Matrix metalloproteinases and atherosclerosis. *Postepy Hig. Med. Dosw. (Online)* **65,** 16–27 (2011).
13. Murphy, G. & Nagase, H. Reappraising metalloproteinases in rheumatoid arthritis and osteoarthritis: destruction or repair? *Nat. Clin. Pract. Rheumatol.* **4,** 128–135 (2008).
14. Churg, A., Zhou, S. & Wright, J. L. Matrix metalloproteinases in COPD. *Eur. Respir. J.* **39,** 197–209 (2012).
15. Vihinen, P. & Kähäri, V.-M. Matrix metalloproteinases in cancer: prognostic markers and therapeutic targets. *Int. J. Cancer* **99,** 157–66 (2002).
16. Kessenbrock, K., Plaks, V. & Werb, Z. Matrix metalloproteinases: regulators of the tumor microenvironment. *Cell* **141,** 52–67 (2010).
17. Egeblad, M. & Werb, Z. New functions for the matrix metalloproteinases in cancer progression. *Nat Rev Cancer* **2,** 161–174 (2002).
18. Coussens, L. M., Fingleton, B. & Matrisian, L. M. Matrix metalloproteinase inhibitors and cancer: trials and tribulations. *Science (80-.).* **295,** 2387–92 (2002).
19. Fingleton, B. Matrix metalloproteinase inhibitors for cancer therapy:the current situation and future prospects. *Expert Opin. Ther. Targets* **7,** 385–97 (2003).

20. Roy, R., Yang, J. & Moses, M. a. Matrix metalloproteinases as novel biomarkers and potential therapeutic targets in human cancer. *J. Clin. Oncol.* **27,** 5287–97 (2009).
21. Bramhall, S. R. *et al. Marimastat as maintenance therapy for patients with advanced gastric cancer: a randomised trial. Br. J. Cancer* **86,** 1864–1870 (2002).
22. Akers, W. J. *et al.* Detection of MMP-2 and MMP-9 activity in vivo with a triple-helical peptide optical probe. *Bioconjug. Chem.* **23,** 656–663 (2012).
23. Zhu, L. *et al.* In Vivo Optical Imaging of Membrane-Type Matrix Metalloproteinase (MT-MMP) Activity. *Mol. Pharm.* **8,** 2331–2338 (2011).
24. Scherer, R. L., VanSaun, M. N., McIntyre, O. & Matrisian, L. M. Optical imaging of matrix metalloproteinase-7 activity in vivo using a proteolytic nanobeacon. *Mol. imaging Off. J. Soc. Mol. Imaging* **7,** 118 (2008).
25. Jiang, T. *et al.* Tumor imaging by means of proteolytic activation of cell-penetrating peptides. *Proc. Natl. Acad. Sci. U. S. A.* **101,** 17867–72 (2004).
26. Bremer, C., Tung, C. H. & Weissleder, R. In vivo molecular target assessment of matrix metalloproteinase inhibition. *Nat. Med.* **7,** 743–8 (2001).
27. Pham, W., Choi, Y., Weissleder, R. & Tung, C.-H. Developing a peptide-based near-infrared molecular probe for protease sensing. *Bioconjug. Chem.* **15,** 1403–7 (2004).
28. Weissleder, R., Tung, C. H., Mahmood, U. & Bogdanov, A. In vivo imaging of tumors with protease-activated near-infrared fluorescent probes. *Nat. Biotechnol.* **17,** 375–8 (1999).
29. Lepage, M. *et al.* Noninvasive detection of matrix metalloproteinase activity in vivo using a novel magnetic resonance imaging contrast agent with a solubility switch. *Mol. Imaging* **6,** 393–403 (2007).
30. Lebel, R. *et al.* Novel solubility-switchable MRI agent allows the noninvasive detection of matrix metalloproteinase-2 activity in vivo in a mouse model. *Magn. Reson. Med.* **60,** 1056–1065 (2008).
31. Breyholz, H.-J. *et al.* Radiofluorinated Pyrimidine-2,4,6-triones as Molecular Probes for Noninvasive MMP-Targeted Imaging. *ChemMedChem* **5,** 777–789 (2010).
32. Wagner, S. *et al.* A new 18F-labelled derivative of the MMP inhibitor CGS 27023A for PET: Radiosynthesis and initial small-animal PET studies. *Appl. Radiat. Isot.* **67,** 606–610 (2009).
33. Furumoto, S. *et al.* Tumor detection using 18F-labeled matrix metalloproteinase-2 inhibitor. *Nucl. Med. Biol.* **30,** 119–125 (2003).
34. Watkins, G. A. *et al.* Development of an optimized activatable MMP-14 targeted SPECT imaging probe. *Bioorg. Med. Chem.* **17,** 653–659 (2009).
35. Scherer, R. L., McIntyre, J. O. & Matrisian, L. M. Imaging matrix metalloproteinases in cancer. *Cancer Metastasis Rev.* **27,** 679–90 (2008).
36. Aguilera, T. A., Olson, E. S., Timmers, M. M., Jiang, T. & Tsien, R. Y. Systemic in vivo distribution of activatable cell penetrating peptides is superior to that of cell penetrating peptides. *Integr. Biol. (Camb).* **1,** 371–381 (2009).
37. McIntyre, J. O. *et al.* Development of a novel fluorogenic proteolytic beacon for in vivo detection and imaging of tumour-associated matrix metalloproteinase-7 activity. *Biochem. J.* **377,** 617–28 (2004).

38. Wadsworth, S. J. *et al.* IL-13 and TH2 cytokine exposure triggers matrix metalloproteinase 7-mediated Fas ligand cleavage from bronchial epithelial cells. *J. Allergy Clin. Immunol.* **126,** 366–74, 374.e1–8 (2010).
39. Ouyang, M. *et al.* Visualization of polarized membrane type 1 matrix metalloproteinase activity in live cells by fluorescence resonance energy transfer imaging. *J. Biol. Chem.* **283,** 17740–8 (2008).
40. Li, X. Y., Ota, I., Yana, I., Sabeh, F. & Weiss, S. J. Molecular dissection of the structural machinery underlying the tissue-invasive activity of membrane type-1 matrix metalloproteinase. *Mol. Biol. Cell* **19,** 3221 (2008).
41. Remacle, A., Murphy, G. & Roghi, C. Membrane type I-matrix metalloproteinase (MT1-MMP) is internalised by two different pathways and is recycled to the cell surface. *J. Cell Sci.* **116,** 3905–16 (2003).
42. Hotary, K., Allen, E., Punturieri, a, Yana, I. & Weiss, S. J. Regulation of cell invasion and morphogenesis in a three-dimensional type I collagen matrix by membrane-type matrix metalloproteinases 1, 2, and 3. *J. Cell Biol.* **149,** 1309–23 (2000).
43. Deryugina, E. I., Ratnikov, B. I., Postnova, T. I., Rozanov, D. V & Strongin, A. Y. Processing of integrin alpha(v) subunit by membrane type 1 matrix metalloproteinase stimulates migration of breast carcinoma cells on vitronectin and enhances tyrosine phosphorylation of focal adhesion kinase. *J. Biol. Chem.* **277,** 9749–9756 (2002).
44. Bareford, L. M. & Swaan, P. W. Endocytic mechanisms for targeted drug delivery. *Adv. Drug Deliv. Rev.* **59,** 748–58 (2007).
45. Yu, M. K., Park, J. & Jon, S. Targeting strategies for multifunctional nanoparticles in cancer imaging and therapy. *Theranostics* **2,** 3–44 (2012).
46. Grobmyer, S. R. *et al.* The promise of nanotechnology for solving clinical problems in breast cancer. *J. Surg. Oncol.* **103,** 317–25 (2011).
47. Crisp, J. L. *et al.* Dual targeting of integrin αvβ3 and matrix metalloproteinase-2 for optical imaging of tumors and chemotherapeutic delivery. *Mol. Cancer Ther.* **13,** 1514–25 (2014).
48. Yang, J., Chen, H., Vlahov, I. R., Cheng, J. X. & Low, P. S. Characterization of the pH of folate receptor-containing endosomes and the rate of hydrolysis of internalized acid-labile folate-drug conjugates. *J. Pharmacol. Exp. Ther.* **321,** 462 (2007).
49. Lu, Y. & Low, P. S. Folate-mediated delivery of macromolecular anticancer therapeutic agents. *Adv. Drug Deliv. Rev.* **54,** 675–93 (2002).
50. Farber, S. & Diamond, L. K. Temporary remissions in acute leukemia in children produced by folic acid antagonist, 4-aminopteroyl-glutamic acid. *N. Engl. J. Med.* **238,** 787–793 (1948).
51. Chattopadhyay, S., Moran, R. G. & Goldman, I. D. Pemetrexed: biochemical and cellular pharmacology, mechanisms, and clinical applications. *Mol. Cancer Ther.* **6,** 404–17 (2007).
52. Gonen, N. & Assaraf, Y. G. Antifolates in cancer therapy: structure, activity and mechanisms of drug resistance. *Drug Resist. Updat.* **15,** 183–210 (2012).
53. Coney, L. R. *et al.* Cloning of a tumor-associated antigen: MOv18 and MOv19 antibodies recognize a folate-binding protein. *Cancer Res.* **51,** 6125–6132 (1991).

54. Parker, N. *et al.* Folate receptor expression in carcinomas and normal tissues determined by a quantitative radioligand binding assay. *Anal. Biochem.* **338,** 284–93 (2005).
55. Daldrup-Link, H. E. *et al.* MR imaging of breast and ovarian cancers with folate-receptor targeted contrast agents. in *Contrast Media Mol. Imaging* **304,** 284–285 (2007).
56. Quintana, A. *et al.* Design and function of a dendrimer-based therapeutic nanodevice targeted to tumor cells through the folate receptor. *Pharm. Res.* **19,** 1310–6 (2002).
57. Majoros, I. J., Myc, A., Thomas, T., Mehta, C. B. & Baker, J. R. PAMAM dendrimer-based multifunctional conjugate for cancer therapy: synthesis, characterization, and functionality. *Biomacromolecules* **7,** 572–9 (2006).
58. Moon, W. K. *et al.* Enhanced tumor detection using a folate receptor-targeted near-infrared fluorochrome conjugate. *Bioconjug. Chem.* **14,** 539–45 (2003).
59. Tung, C.-H., Lin, Y., Moon, W. K. & Weissleder, R. A receptor-targeted near-infrared fluorescence probe for in vivo tumor imaging. *Chembiochem* **3,** 784–6 (2002).
60. Kennedy, M. D., Jallad, K. N., Thompson, D. H., Ben-Amotz, D. & Low, P. S. Optical imaging of metastatic tumors using a folate-targeted fluorescent probe. *J. Biomed. Opt.* **8,** 636–41 (2003).
61. Gabizon, A. *et al.* Targeting folate receptor with folate linked to extremities of poly(ethylene glycol)-grafted liposomes: in vitro studies. *Bioconjug. Chem.* **10,** 289–298 (1999).
62. Chen, H., Ahn, R., Van den Bossche, J., Thompson, D. H. & O'Halloran, T. V. Folate-mediated intracellular drug delivery increases the anticancer efficacy of nanoparticulate formulation of arsenic trioxide. *Mol. Cancer Ther.* **8,** 1955–63 (2009).
63. Sun, C., Sze, R. & Zhang, M. Folic acid-PEG conjugated superparamagnetic nanoparticles for targeted cellular uptake and detection by MRI. *J. Biomed. Mater. Res. A* **78,** 550–7 (2006).
64. Hartmann, L. C. *et al.* Folate receptor overexpression is associated with poor outcome in breast cancer. *Int. J. Cancer* **121,** 938–42 (2007).
65. Shia, J. *et al.* Immunohistochemical expression of folate receptor α in colorectal carcinoma: patterns and biological significance. *Hum. Pathol.* **39,** 498–505 (2014).
66. Sega, E. I. & Low, P. S. Tumor detection using folate receptor-targeted imaging agents. *Cancer Metastasis Rev.* **27,** 655–64 (2008).
67. Low, P. S. & Antony, A. C. Folate receptor-targeted drugs for cancer and inflammatory diseases. *Adv. Drug Deliv. Rev.* **56,** 1055–8 (2004).
68. Siegel, B. A. *et al.* Evaluation of 111In-DTPA-folate as a receptor-targeted diagnostic agent for ovarian cancer: initial clinical results. *J. Nucl. Med.* **44,** 700–7 (2003).
69. Sandoval, R. M., Kennedy, M. D., Low, P. S. & Molitoris, B. a. Uptake and trafficking of fluorescent conjugates of folic acid in intact kidney determined using intravital two-photon microscopy. *Am. J. Physiol. Cell Physiol.* **287,** C517–26 (2004).

70. Xia, W. & Low, P. S. Folate-targeted therapies for cancer. *J. Med. Chem.* **53,** 6811–24 (2010).
71. Shen, M. *et al.* Multifunctional drug delivery system for targeting tumor and its acidic microenvironment. *J. Control. Release* **161,** 884–92 (2012).
72. Singh, P., Gupta, U., Asthana, A. & Jain, N. K. Folate and folate-PEG-PAMAM dendrimers: synthesis, characterization, and targeted anticancer drug delivery potential in tumor bearing mice. *Bioconjug. Chem.* **19,** 2239–52 (2008).
73. Goren, D. *et al.* Nuclear delivery of doxorubicin via folate-targeted liposomes with bypass of multidrug-resistance efflux pump. *Clin. Cancer Res.* **6,** 1949–57 (2000).
74. Xie, M., Xu, Y., Liu, J., Zhang, T. & Zhang, H. Preparation and Characterization of Folate Targeting Magnetic Nanomedicine Loaded with Cisplatin. *J. Nanomater.* **2012,** 1–9 (2012).
75. Satyam, A. Design and synthesis of releasable folate-drug conjugates using a novel heterobifunctional disulfide-containing linker. *Bioorg. Med. Chem. Lett.* **18,** 3196–9 (2008).
76. Lu, Y. & Low, P. S. Folate targeting of haptens to cancer cell surfaces mediates immunotherapy of syngeneic murine tumors. *Cancer Immunol. Immunother.* **51,** 153–62 (2002).
77. Lee, Y. Preparation and characterization of folic acid linked poly (L-glutamate) nanoparticles for cancer targeting. *Macromol. Res.* **14,** 387–393 (2006).
78. Endocyte. A Randomized, Open-label Phase 2 Study of EC145 Single-agent and the Combination of EC145 Plus Docetaxel Versus Docetaxel Alone in Participants With Folate-receptor Positive [FR(++)] Second Line NSCLC. *ClinicalTrials.gov* (2014). at <http://www.clinicaltrials.gov/ct2/show/NCT01577654>
79. Vlahov, I. R. & Leamon, C. P. Engineering folate-drug conjugates to target cancer: from chemistry to clinic. *Bioconjug. Chem.* **23,** 1357–69 (2012).
80. Longmire, M., Choyke, P. L. & Kobayashi, H. Clearance properties of nano-sized particles and molecules as imaging agents: considerations and caveats. *Nanomedicine* **3,** 703–717 (2008).
81. Choi, H. S. *et al.* Renal clearance of quantum dots. *Nat. Biotechnol.* **25,** 1165–1170 (2007).
82. Maeda, H., Wu, J., Sawa, T., Matsumura, Y. & Hori, K. Tumor vascular permeability and the EPR effect in macromolecular therapeutics: a review. *J. Control. Release* **65,** 271–284 (2000).
83. Maeda, H. The enhanced permeability and retention (EPR) effect in tumor vasculature: the key role of tumor-selective macromolecular drug targeting. *Adv. Enzyme Regul.* **41,** 189–207 (2001).
84. Matsumura, Y. & Maeda, H. A new concept for macromolecular therapeutics in cancer chemotherapy: Mechanism of tumoritropic accumulation of proteins and the antitumor agent smancs. *Cancer Res.* **46,** 6387–6392 (1986).
85. Maeda, H. & Matsumura, Y. Tumoritropic and lymphotropic principles of macromolecular drugs. *Crit. Rev. Ther. Drug Carrier Syst.* **6,** 193–210 (1989).
86. Bazzoni, G. Endothelial tight junctions: Permeable barriers of the vessel wall. *Thromb. Haemost.* **95,** 36–42 (2006).
87. Maeda, H. Tumor-selective delivery of macromolecular drugs via the EPR effect: background and future prospects. *Bioconjug. Chem.* **21,** 797–802 (2010).

88. Maeda, H. Macromolecular therapeutics in cancer treatment: The EPR effect and beyond. *J. Control. Release* **164,** 138–44 (2012).
89. Noguchi, Y. *et al.* Early Phase Tumor Accumulation of Macromolecules: A Great Difference in Clearance Rate between Tumor and Normal Tissues. *Cancer Sci.* **89,** 307–314 (1998).
90. Tang, L., Fan, T., Borst, L. & Cheng, J. Synthesis and biological response of size-specific, monodisperse drug–silica nanoconjugates. *ACS Nano* 3954–3966 (2012).
91. Tang, L., Gabrielson, N. P. N., Uckun, F. M. F., Fan, T. M. & Cheng, J. Size-Dependent Tumor Penetration and in Vivo Efficacy of Monodisperse Drug–Silica Nanoconjugates. *Mol. Pharm.* **10,** 883–892 (2013).
92. Torchilin, V. Tumor delivery of macromolecular drugs based on the EPR effect. *Adv. Drug Deliv. Rev.* **63,** 131–135 (2011).
93. Prabhakar, U. *et al.* Challenges and Key Considerations of the Enhanced Permeability and Retention Effect for Nanomedicine Drug Delivery in Oncology. *Cancer Res.* **73 ,** 2412–2417 (2013).
94. Duncan, R. *et al.* Validation of tumour models for use in anticancer nanomedicine evaluation: the EPR effect and cathepsin B-mediated drug release rate. *Cancer Chemother. Pharmacol.* **72,** 417–27 (2013).
95. Newton, K. & Dixit, V. M. Signaling in innate immunity and inflammation. *Cold Spring Harb. Perspect. Biol.* **4,** (2012).
96. Seong, S.-Y. & Matzinger, P. Hydrophobicity: an ancient damage-associated molecular pattern that initiates innate immune responses. *Nat. Rev. Immunol.* **4,** 469–478 (2004).
97. Avila-Olias, M., Pegoraro, C., Battaglia, G. & Canton, I. Inspired by nature: fundamentals in nanotechnology design to overcome biological barriers. *Ther. Deliv.* **4,** 27–43 (2013).
98. Murray, P. J. & Wynn, T. A. Protective and pathogenic functions of macrophage subsets. *Nat. Rev. Immunol.* **11,** 723–737 (2011).
99. Li, S. & Huang, L. Pharmacokinetics and Biodistribution of Nanoparticles. *Mol. Pharm.* **5,** 496–504 (2008).
100. Sewell, S. L. & Giorgio, T. D. Synthesis and enzymatic cleavage of dual-ligand quantum dots. *Mater. Sci. Eng. C* **29,** 1428–1432 (2009).
101. Subramani, K., Hosseinkhani, H., Khraisat, A., Hosseinkhani, M. & Pathak, Y. Targeting Nanoparticles as Drug Delivery Systems for Cancer Treatment. *Curr. Nanosci.* **5,** 135–140 (2009).
102. Wang, W. *et al.* The decrease of PAMAM dendrimer-induced cytotoxicity by PEGylation via attenuation of oxidative stress. *Nanotechnology* **20,** 105103 (2009).
103. Cheng, Y., Zhao, L., Li, Y. & Xu, T. Design of biocompatible dendrimers for cancer diagnosis and therapy: current status and future perspectives. *Chem. Soc. Rev.* 2673–2703 (2011). doi:10.1039/c0cs00097c
104. Li, S. & Huang, L. Pharmacokinetics and Biodistribution of Nanoparticles. *Mol. Pharm.* **5,** 496–504 (2008).
105. Levchenko, T. S., Rammohan, R., Lukyanov, A. N., Whiteman, K. R. & Torchilin, V. P. Liposome clearance in mice: The effect of a separate and combined presence of surface charge and polymer coating. *Int. J. Pharm.* **240,** 95–102 (2002).

106. Alexis, F., Pridgen, E., Molnar, L. K. & Farokhzad, O. C. Factors Affecting the Clearance and Biodistribution of Polymeric Nanoparticles. *Mol. Pharm.* **5,** 505–515 (2008).
107. Verma, A. & Stellacci, F. Effect of surface properties on nanoparticle-cell interactions. *Small* **6,** 12–21 (2010).
108. Smith, R. A., Sewell, S. L. & Giorgio, T. D. Proximity-activated nanoparticles : in vitro performance of specific structural modification by enzymatic cleavage. *Int. J. Nanomedicine* **3,** 95 (2008).
109. Samuelson, L. E., Scherer, R. L., Matrisian, L. M., McIntyre, J. O. & Bornhop, D. J. Synthesis and in vitro efficacy of MMP9-activated NanoDendrons. *Mol. Pharm.* **10,** 3164–74 (2013).
110. Sabeh, F. *et al.* Tumor cell traffic through the extracellular matrix is controlled by the membrane-anchored collagenase MT1-MMP. *J. Cell Biol.* **167,** 769–781 (2004).
111. Osenkowski, P., Toth, M. & Fridman, R. Processing, shedding, and endocytosis of membrane type 1-matrix metalloproteinase (MT1-MMP). *J. Cell. Physiol.* **200,** 2–10 (2004).
112. Hakulinen, J., Sankkila, L., Sugiyama, N., Lehti, K. & Keski-Oja, J. Secretion of active membrane type 1 matrix metalloproteinase (MMP-14) into extracellular space in microvesicular exosomes. *J. Cell. Biochem.* **105,** 1211–1218 (2008).
113. Kridel, S. J. *et al.* A unique substrate binding mode discriminates membrane type-1 matrix metalloproteinase from other matrix metalloproteinases. *J. Biol. Chem.* **277,** 23788–93 (2002).
114. Mucha, A. *et al.* Membrane type-1 matrix metalloprotease and stromelysin-3 cleave more efficiently synthetic substrates containing unusual amino acids in their P1' positions. *J. Biol. Chem.* **273,** 2763–8 (1998).
115. Knight, C. G. G., Willenbrock, F. & Murphy, G. A novel coumarin-labelled peptide for sensitive continuous assays of the matrix metalloproteinases. *FEBS Lett.* **296,** 263–266 (1992).
116. Rasmussen, F. H. *et al.* Use of a multiple-enzyme/multiple-reagent assay system to quantify activity levels in samples containing mixtures of matrix metalloproteinases. *Biochemistry* **43,** 2987–95 (2004).
117. Chen, E. I. *et al.* A unique substrate recognition profile for matrix metalloproteinase-2. *J. Biol. Chem.* **277,** 4485–91 (2002).
118. Fisher, J. & Mobashery, S. Recent advances in MMP inhibitor design. *Cancer Metastasis Rev.* **25,** 115–136 (2006).
119. Pei, P. *et al.* Reduced nonprotein thiols inhibit activation and function of MMP-9: Implications for chemoprevention. *Free Radic. Biol. Med.* **41,** 1315–1324 (2006).
120. Bogani, P., Canavesi, M., Hagen, T. M., Visioli, F. & Bellosta, S. Thiol supplementation inhibits metalloproteinase activity independent of glutathione status. *Biochem. Biophys. Res. Commun.* **363,** 651–655 (2007).
121. Deryugina, E. I. & Quigley, J. P. Matrix metalloproteinases and tumor metastasis. *Cancer Metastasis Rev.* **25,** 9–34 (2006).
122. Linder, S. The matrix corroded: podosomes and invadopodia in extracellular matrix degradation. *Trends Cell Biol.* **17,** 107–17 (2007).

123. Hofmann, U. B., Eggert, A. A. O., Blass, K., Bröcker, E. B. & Becker, J. C. Expression of Matrix Metalloproteinases in the Microenvironment of Spontaneous and Experimental Melanoma Metastases Reflects the Requirements for Tumor Formation. *Cancer Res.* **63,** 8221–8225 (2003).
124. Stack, M. S. & Gray, R. D. Comparison of vertebrate collagenase and gelatinase using a new fluorogenic substrate peptide. *J. Biol. Chem.* **264,** 4277–81 (1989).
125. Gupta, S. P. & Patil, V. M. Specificity of binding with matrix metalloproteinases. *EXS* **103,** 35–56 (2012).
126. Quesada, V., Ordóñez, G. R., Sánchez, L. M., Puente, X. S. & López-Otín, C. The Degradome database: mammalian proteases and diseases of proteolysis. *Nucleic Acids Res.* **37 ,** D239–D243 (2009).
127. Martin, M. D. *et al.* Effect of ablation or inhibition of stromal matrix metalloproteinase-9 on lung metastasis in a breast cancer model is dependent on genetic background. *Cancer Res.* **68,** 6251–9 (2008).
128. Chan, W. & White, P. *Fmoc solid phase peptide synthesis: a practical approach*. 376 (Oxford University Press, 2000).
129. Hermanson, G. *Bioconjugate Techniques*. 1202 (Academic Press, 2008).
130. Dirksen, A., Hackeng, T. M. & Dawson, P. E. Nucleophilic catalysis of oxime ligation. *Angew. Chem. Int. Ed. Engl.* **45,** 7581–4 (2006).
131. Fischer, R., Mader, O., Jung, G. & Brock, R. Extending the applicability of carboxyfluorescein in solid-phase synthesis. *Bioconjug. Chem.* **14,** 653–60 (2003).
132. Díaz-Mochón, J. J., Bialy, L. & Bradley, M. Full orthogonality between Dde and Fmoc: the direct synthesis of PNA--peptide conjugates. *Org. Lett.* **6,** 1127–9 (2004).
133. Landmark, K. J. *et al.* Synthesis, characterization, and in vitro testing of superparamagnetic iron oxide nanoparticles targeted using folic Acid-conjugated dendrimers. *ACS Nano* **2,** 773–83 (2008).
134. Lempens, E. H. M., Helms, B. a, Merkx, M. & Meijer, E. W. Efficient and chemoselective surface immobilization of proteins by using aniline-catalyzed oxime chemistry. *Chembiochem* **10,** 658–62 (2009).
135. Wendeler, M., Grinberg, L., Wang, X., Dawson, P. E. & Baca, M. Enhanced Catalysis of Oxime-Based Bioconjugations by Substituted Anilines. *Bioconjug. Chem.* (2013). doi:10.1021/bc400380f
136. Paulos, C. M., Reddy, J. A., Leamon, C. P., Turk, M. J. & Low, P. S. Ligand binding and kinetics of folate receptor recycling in vivo: impact on receptor-mediated drug delivery. *Mol. Pharmacol.* **66,** 1406 (2004).
137. Wang, S. & Low, P. S. Folate-mediated targeting of antineoplastic drugs, imaging agents, and nucleic acids to cancer cells. *J. Control. Release* **53,** 39–48 (1998).
138. Malik, N. *et al.* Dendrimers: relationship between structure and biocompatibility in vitro, and preliminary studies on the biodistribution of 125I-labelled polyamidoamine dendrimers in vivo. *J. Control. Release* **65,** 133–48 (2000).
139. Malkoch, M., Malmström, E. & Hult, A. Rapid and Efficient Synthesis of Aliphatic Ester Dendrons and Dendrimers. *Macromolecules* **35,** 8307–8314 (2002).

140. Hawker, C. & Fréchet, J. M. J. A new convergent approach to monodisperse dendritic macromolecules. *J. Chem. Soc. Chem. Commun.* 1010 (1990). doi:10.1039/c39900001010
141. Tassa, C., Shaw, S. Y. & Weissleder, R. Dextran-coated iron oxide nanoparticles: a versatile platform for targeted molecular imaging, molecular diagnostics, and therapy. *Acc. Chem. Res.* **44,** 842–52 (2011).
142. Tang, L. & Cheng, J. Nonporous Silica Nanoparticles for Nanomedicine Application. *Nano Today* **8,** 290–312 (2013).
143. Medarova, Z., Rashkovetsky, L., Pantazopoulos, P. & Moore, A. Multiparametric monitoring of tumor response to chemotherapy by noninvasive imaging. *Cancer Res.* **69,** 1182–9 (2009).
144. Kresse, M. *et al.* Targeting of ultrasmall superparamagnetic iron oxide (USPIO) particles to tumor cells in Vivo by using transferrin receptor pathways. *Magn. Reson. Med.* **40,** 236–242 (1998).
145. Choi, H., Choi, S. R., Zhou, R., Kung, H. F. & Chen, I.-W. Iron oxide nanoparticles as magnetic resonance contrast agent for tumor imaging via folate receptor-targeted delivery. *Acad. Radiol.* **11,** 996–1004 (2004).
146. Kobukai, S. *et al.* Magnetic nanoparticles for imaging dendritic cells. *Magn. Reson. Med.* **63,** 1383–1390 (2010).
147. Gyergyek, S., Huskić, M., Makovec, D. & Drofenik, M. Superparamagnetic nanocomposites of iron oxide in a polymethyl methacrylate matrix synthesized by in situ polymerization. *Colloids Surfaces A Physicochem. Eng. Asp.* **317,** 49–55 (2008).
148. Auzély-Velty, R., Rinaudo, M. & Auze, R. Synthesis of starch derivatives with labile cationic groups. *Int. J. Biol. Macromol.* **31,** 123–129 (2003).
149. Bell, C. S., Yu, S. S. & Giorgio, T. D. The Multistrata Nanoparticle: an FeOx/Au Core/Shell Enveloped in a Silica–Au Shell. *Small* **7,** 1158–1162 (2011).
150. Meadows, D. L., Shafer, J. S. & Schultz, J. S. Determining the extent of labeling for tetramethylrhodamine protein conjugates. *J. Immunol. Methods* **143,** 263–272 (1991).
151. Högemann, D., Josephson, L., Weissleder, R. & Basilion, J. P. Improvement of MRI probes to allow efficient detection of gene expression. *Bioconjug. Chem.* **11,** 941–6 (2000).
152. Moore, A., Basilion, J. P., Chiocca, E. A. & Weissleder, R. Measuring transferrin receptor gene expression by NMR imaging. *Biochim. Biophys. Acta* **1402,** 239–49 (1998).
153. Kircher, M. F., Weissleder, R. & Josephson, L. A dual fluorochrome probe for imaging proteases. *Bioconjug. Chem.* **15,** 242–8 (2004).
154. Weaver, A. M. Invadopodia: specialized cell structures for cancer invasion. *Clin. Exp. Metastasis* **23,** 97–105 (2006).
155. Nickels, M., Xie, J., Cobb, J., Gore, J. C. & Pham, W. Functionalization of iron oxide nanoparticles with a versatile epoxy amine linker. *J. Mater. Chem.* **20,** 4776–4780 (2010).
156. Moore, A., Medarova, Z., Potthast, A. & Dai, G. In vivo targeting of underglycosylated MUC-1 tumor antigen using a multimodal imaging probe. *Cancer Res.* **64,** 1821–7 (2004).

157. Weissleder, R. A clearer vision for in vivo imaging. *Nat Biotech* **19,** 316–317 (2001).
158. Williams, J. & Morrison, J. The kinetics of reversible tight-binding inhibition. *Methods Enzymol.* **63,** 437–467 (1979).
159. Simmons, G. *et al.* Folate Receptor Alpha and Caveolae Are Not Required for Ebola Virus Glycoprotein-Mediated Viral Infection. *J. Virol.* **77 ,** 13433–13438 (2003).
160. Meier, R. *et al.* Breast Cancers: MR Imaging of Folate-Receptor Expression with the Folate-Specific Nanoparticle P1133. *Radiology* **255,** 527–535 (2010).
161. Giambernardi, T. a *et al.* Overview of matrix metalloproteinase expression in cultured human cells. *Matrix Biol.* **16,** 483–96 (1998).
162. Tester, A. M., Ruangpanit, N., Anderson, R. L. & Thompson, E. W. MMP-9 secretion and MMP-2 activation distinguish invasive and metastatic sublines of a mouse mammary carcinoma system showing epithelial-mesenchymal transition traits. *Clin. Exp. Metastasis* **18,** 553–560 (2000).
163. Leamon, C. P. *et al.* Impact of High and Low Folate Diets on Tissue Folate Receptor Levels and Antitumor Responses Toward Folate-Drug Conjugates. **327,** 918–925 (2008).
164. Leamon, C. P. *et al.* Synthesis and Biological Evaluation of EC20: A New Folate-Derived, 99mTc-Based Radiopharmaceutical. *Bioconjug. Chem.* **13,** 1200–1210 (2002).